Free vibration and dynamic instability analyses of doubly-tapered rotating laminated composite beams

Saemul Seraj

A thesis

in

the Department

of

Mechanical and Industrial Engineering

Presented in Partial Fulfillment of the Requirements

For the Degree of

Master of Applied Science (Mechanical Engineering) at

Concordia University

Montreal, Quebec, Canada

July 2016

CONCORDIA UNIVERSITY
School of Graduate Studies

This is to certify that the thesis prepared

By: Saemul Seraj

Entitled: Free vibration and dynamic instability analyses of doubly-tapered rotating laminated composite beams

and submitted in partial fulfillment of the requirements for the degree of

Master of Applied Science (Mechanical Engineering)

complies with the regulations of the University and meets the accepted standards with respect to originality and quality.

Signed by the final examining committee:

Dr. C. Moreau _____ Chair

Dr. M. Hojjati _____ Examiner

Dr. C. Marsden _____ Examiner

Dr. R. Ganesan _____ Supervisor

Approved by _____
Chair of Department or Graduate Program Director

_____
Dean of Faculty

Date July 26, 2016

ABSTRACT

Free vibration and dynamic instability analyses of doubly-tapered rotating laminated composite beams

Saemul Seraj

Due to the outstanding engineering properties, such as high strength/stiffness to weight ratios, capability to be stiff at one location and flexible at another location and favorable fatigue characteristics, doubly-tapered composite beam is used in the rotating structures such as helicopter rotor blades and wind turbine blades. Due to its distinct characteristics from static beam and wide range of applications, rotating beam requires a comprehensive research to understand its dynamic response. Design of mechanical components using doubly-tapered composite beams requires a better understanding of their behavior in free vibration and their dynamic instability. In the present thesis, free vibration and dynamic instability analyses of doubly-tapered rotating cantilever composite beams are conducted considering three different types of vibrations (out-of-plane bending, in-plane bending and axial). Rayleigh-Ritz approximate method based on classical lamination theory has been employed to formulate the free vibration problem and solve it. Bolotin's method is applied to determine the instability regions. Numerical and symbolic computations have been performed using the software MATLAB. The results for natural frequencies have been validated using Finite Element Analysis (FEA) tool ANSYS. A comprehensive parametric study is conducted in order to understand the effects of various design parameters. Moreover, critical speed of doubly-tapered rotating composite beam is determined and change of critical speed due to double-tapering is investigated. Also, change in maximum deflection due to rotational velocity and double-tapering is observed in this thesis. The material chosen in this thesis for numerical calculations is NCT-301 graphite-epoxy prepreg.

iii

ACKNOWLEDGEMENT

First of all I would like to express my invaluable gratitude to Almighty creator who gave me the ability to complete this thesis. Then I wish to express my most sincere gratitude to my supervisor Dr. Rajamohan Ganesan for his time, patience, tolerance and keen guidance especially for the thesis writing corrections. In a word he enhanced the value and experience of my graduate research immeasurably.

I would also like to thank Mohammad Amin Fazili, Chirag Delvadiya and Mehdi Darabi who supported me by sharing ideas and discussion during my research studies. I would also thank and appreciate to my officemates with whom I shared a lot time for many ideas as a good friend.

I gratefully acknowledge the funding sources for my master's thesis provided by the NSERC and Concordia University.

Thank You.

Table of Contents

Chapter-1: Introduction, literature review and scope of the thesis

Chapter-2: Free vibration and dynamic instability analyses of doubly-tapered rotating laminated composite beams for out-of-plane bending vibration

Chapter-4: Comparative study between out-of-plane bending and in-plane bending vibrations of doubly-tapered rotating composite beam

Chapter-5: Conclusion and future work

List of Figures

List of Tables

Nomenclature

L	Length of the beam
h_0	Thickness of the beam at fixed side
h_L	Thickness of the beam at free side
b_0	Width of the beam at fixed side
b_L	Width of the beam at free side
R	Hub radius
Ω	Rotational velocity
$\Omega(t)$	Periodic rotational velocity
x	Longitudinal direction of composite beam
y	Width direction of composite beam
z	Thickness direction of composite beam
σ_{xx}	Stress along x direction
ε_{xx}	Total strain along x direction
σ_{yy}	Stress along y direction
ε_{yy}	Total strain along y direction
τ_{xy}	Shear stress acting on $x - y$ plane
γ_{xy}	Shear strain along $x - y$ plane
σ_{zz}	Stress along z direction
γ_{xz}	Shear strain acting on $x - z$ plane
γ_{yz}	Shear strain along $y - z$ plane
N	Total number of layers in the laminate
k	Lamina order in the laminate
U	Strain energy
$b(x)$	Variable width of the beam
h_k	Distance from top surface of the ply to mid-plane
h_{k-1}	Distance from bottom surface of the ply to mid-plane
h_{ply}	Ply thickness
θ	Fiber angle

φ	Laminate taper angle
$[Q^k]$	Transformed reduced stiffness matrix of a composite ply
$[Q_{resin}]$	Transformed reduced stiffness matrix of a composite ply
u_0	Mid-plane displacement in x direction
v_0	Mid-plane displacement in y direction
w_0	Mid-plane displacement in z direction
$[\varepsilon^0]$	Mid-plane strain matrix
$[k]$	Curvature matrix
$D_{11}(x)$	First coefficient of variable bending stiffness matrix
$A_{11}(x)$	First coefficient of stretching stiffness matrix
$\emptyset_i(x)$	Approximate shape function for out-of-plane bending deformation
$\emptyset_{2i}(x)$	Approximate shape function for axial deformation
$\emptyset_{3i}(x)$	Approximate shape function for in-plane bending deformation
$q_i(t)$	Generalized coordinate for out-of-plane bending deformation
$q_{2i}(t)$	Generalized coordinate for axial deformation
$q_{3i}(t)$	Generalized coordinate for in-plane bending deformation
t	Time
m	Number of terms in displacement function
K_{ij}	Coefficient of global stiffness matrix for out-of-plane bending deformation
$K_{ij}{}^u$	Coefficient of global stiffness matrix for axial deformation
$K_{ij}{}^v$	Coefficient of global stiffness matrix for in-plane bending deformation
$[K]$	Global stiffness matrix for out-of-plane bending
ds	Deformed arc length of the infinitesimal beam element
$P(x)$	Variable centrifugal force of the beam
W	Work done by centrifugal force
ρ_k	Mass density of ply
$K^C{}_{ij}$	Coefficient of centrifugal stiffness matrix for out-of-plane bending deformation
$K_{1ij}{}^{cv}$	Coefficient of centrifugal stiffness matrix for in-plane bending deformation
$[K^C]$	Centrifugal bending stiffness matrix for out-of-plane bending deformation
$[K^{cv}]$	Centrifugal bending stiffness matrix for in-plane bending deformation

ρ_L	Mass per unit length per unit width of the laminated beam
T	Kinetic energy
$\vec{V}$	Velocity vector
$\vec{r}$	Position vector after deformation
$\hat{i}$	Unit vector in x direction
$\hat{j}$	Unit vector in y direction
$\hat{k}$	Unit vector in z direction
M_{ij}	Coefficient of global mass matrix for out-of-plane bending deformation
$M_{ij}{}^u$	Coefficient of global mass matrix for axial deformation
$M_{ij}{}^v$	Coefficient of global mass matrix for in-plane bending deformation
$K_{ij}{}^{cu}$	Coefficient of centrifugal softening matrix for axial deformation
$K_{2ij}{}^{cv}$	Coefficient of centrifugal softening matrix for in-plane bending deformation
$[M]$	Global mass matrix for out-of-plane bending deformation
$[M^u]$	Global mass matrix for axial deformation
$[M^v]$	Global mass matrix for in-plane bending deformation
$\{q\}$	Displacement vector for out-of-plane bending vibration
$\{q_2\}$	Displacement vector for axial vibration
$\{q_3\}$	Displacement vector for in-plane bending vibration
$\{Q\}$	Mode shape (eigen) vector for out-of-plane bending vibration
$\{\tilde{Q}\}$	Mode shape (eigen) vector for coupled in-plane bending and axial vibration
ω	Natural frequency of free vibration
S	Number of ply drop-off
r_b	Width ratio
H	Thickness of the uniform laminate
D_{11}	First coefficient of bending stiffness matrix of uniform composite laminate
ω_f	Forcing frequency
n	Number of vane in a rotating element
Ω_0	Mean value of periodic rotational velocity
β	Amplitude factor
θ_p	Parametric resonance frequency

Chapter-1

Introduction, literature review and scope of the thesis

1.1   Vibration analysis of rotating structure

Numerous engineering applications involve high speed rotating structures, which rotate about a symmetrical axis. Especially aerospace industries and wind energy plants use such structures. Due to distinct alteration from static beam and wide range of applications, rotating beam required a comprehensive research to understand the dynamic response of this physical system. The fundamental difference between rotating and non-rotating beams is the presence of centrifugal acceleration and Coriolis effects due to angular velocity, which significantly affect the dynamic behavior of rotating beam. Importantly vibration characteristic is altered due to the consideration of angular velocity.

Vibration is a time dependent undesirable fluctuating motion from a state of equilibrium. More explicitly vibration may cause fatigue failure in a machine element due to repetitive stress development in a structure. In the case of rotating structures such as wind turbines, gas turbines, helicopter rotors and aircraft propellers that are often idealized as rotating beams, vibration increases fiercely due to rotating unbalance. In rotating beam, uneven distributed load due to rotation, displaces the center of pressure which results in unpleasant vibration. Free vibration of a rotating element referred to as vibration due to initial displacement which does not undergo any external force. Whenever this natural frequency of free vibration coincides with the frequency of external load (forced vibration) a resonance may occur which accelerates the vibration excessively

and leads to failure of the structure. This devastating effect can be avoided by analyzing vibration properly.

1.2   Dynamic instability analysis of rotating structure

Dynamic instability is a problem concerning with the structural behavior due to parametric vibration. This is a new branch of research study that provides engineers for the design of a structural member considering time-dependent load referred to as parametric excitation. In a rotating beam, parametric excitation can be caused by in-plane periodic load or by introducing periodic rotational velocity. Mechanical structures that operate within the instability region, will experience parametric resonance. This incident reduces the durability of structure and leads to unpredictable failure.

Especially in an aircraft engine or in wind turbine, rotating blade experiences periodic aerodynamic load which changes the constant angular velocity to pulsating angular velocity. The excitation frequency involve in pulsating load may coincide with the natural frequency of free vibration and blade becomes dynamically unstable from nominal position.

Dynamic instability analysis has opened a new way to accurately design an engineering application, which is more similar to a practical appearance in the field. Although parametric vibration might not have an immediate effect, but it is a future threat for fatigue failure, if they continue to act. Therefore, dynamic instability analysis introduces a method to prevent the parametric vibration which is necessary to design a structure precisely which is out of immediate maintenance.

1.3   Composite material in rotating structure

A structural material where two or more constituents composed at macroscopic level and constituents are not soluble in each other is called composite material. One of the constituents in

composite material generally is continuous phase, called matrix and another is discontinuous phase called reinforcing material that may be in the form as fibers, particles or flakes. Fiber reinforced composite materials are often made in the form of a thin layer, which is called lamina. The different layers of the lamina are permanently bonded together under heat and pressure using a hot press or autoclave. Fiber orientation in each lamina and stacking sequences of layers can be chosen so as to achieve the desired strength and stiffness for specific applications. Nowadays composite materials are widely used in different applications such as aircraft and space structures, automobiles, submarine structure, sports equipment and medical prosthetic devices, in the structural form of bar, beam and plate.

The use of composite structure in the design of mechanical systems has been increasing fast during the last few years due to the recent technological advances. Composite material has outstanding engineering properties, such as high strength/stiffness to weight ratios and favorable fatigue characteristics and due to this reason composite material is used in the design of rotating structure such as aircraft engine blades, helicopter rotor blades and wind turbine blades. Some specific applications such as helicopter blades, robot arms, turbine blades and satellite antenna need to be stiff at one location and flexible at another location. A typical example is a helicopter rotor blade, where a progressive variation in the thickness of the blade is required to provide high stiffness at the hub and flexibility in the middle of blade length to accommodate for flapping. This type of structure is formed by terminating or dropping off plies at the specified location to reduce the stiffness of that structure which is called tapered composite structure [6]. These elastic tailoring properties and more significant weight saving than commonly used laminated components allow an increasing use of tapered composite in commercial and military aircrafts. The first commercial composite rotor blade yoke assembly made of glass-fiber (S-2 glass)/epoxy composite was

3

fabricated at Bell helicopter Textron that provides more safety and endures several times more flight hours than traditional titanium or steel. The structural configuration possibilities provided by fiber reinforced composite materials are vital to enhance the dynamic behavior of rotating beams operating in complex environmental conditions. As a result of the mentioned advances in composite materials, the structural design concepts have changed substantially.

1.4   Rayleigh-Ritz method

Deriving the governing differential equations of a physical system is a complicated task and finding exact solutions to the governing differential equations is usually even more formidable. In order to solve such equations, approximate methods of analysis provide a convenient, alternative method for finding solutions. The Rayleigh-Ritz method is such a method, typically used in the literature and referred to as classical variational method.

Lord Rayleigh was an English Physicist, published his renowned book *Theory of Sound* in 1877. He explained the calculation method to determine fundamental natural frequency of a continuous system such as strings, bars, beams, membranes and plate in his book. The principle of Rayleigh's method is based on assuming the mode shape and equating the maximum potential and kinetic energies in a cycle of motion.

In 1908, Walter Ritz used principle of multiple admissible displacement functions to determine the frequencies and mode shapes of any structural member. He demonstrated his method by determining the natural frequency of a completely free square plate. Consequently, Rayleigh used the same principle in his book and another publication. After a while, many researchers used this method some calling it the 'Ritz method' and others the 'Rayleigh-Ritz' method.

Rayleigh-Ritz method has gained the popularity in last few decades to accurately determine the natural frequencies and mode shapes of vibration of continuous systems, especially if the exact

solution is not available. This method becomes more applicable after the discovery of digital computer. The success of this method in a boundary value problem or in an eigenvalue problem depends on accurately assuming the solution in the form of series of approximate displacement functions which must satisfy the geometric boundary conditions.

The mathematical basis of Finite Element Method (FEM) first comes from Rayleigh-Ritz method. The Rayleigh-Ritz (R-R) method discretize the structure by assuming solution in form of series instead of discretization by dividing into elements (FEM). One of the disadvantages of Finite Element Method is that one can only compute the displacement at locations where elements are connected (called 'nodes') and the displacement within the element is unknown. The Rayleigh-Ritz method overcome this problem by assuming single displacement field that spans the entire structure.

This thesis uses the Rayleigh-Ritz method to solve the eigenfrequency problem of a rotating composite beam and uses Finite Element Analysis tool – ANSYS to validate the results.

1.5   Finite Element Method

Since structural configurations were changing rapidly during the last few years, the existing methods were generally insufficient to deal with the variety and complexity of the new structural shapes. It was in this circumstance that the Finite Element Method (FEM) emerged as recognizable modern method in the mid-1980s.

The greatest advantage of FEM is its ability to deal with arbitrary geometry, boundary conditions as well as arbitrary shape of non-homogeneous materials that are made up of numerous different material regions. The analysis of laminated composite beam is usually based on four approaches those are classical theory of elasticity, theory of mechanics of materials, variational statement and strain energy statement. The governing equations of motions are generally non-

linear partial differential equations those are difficult to solve in the closed form. But the powerful numerical technique, Finite Element Method (FEM) made possible the analysis of complex structures such as tapered composite beam with the help of modern digital computers. The basic idea of the Finite Element Method is to find the approximate solution of complicated problem by replacing it with a simpler one. The speed of convergence and accuracy of the results obtained by finite element method are strongly dependent on the selected element type. In Conventional Finite Element (CFE), a beam element is modeled using two nodes at the ends where each node has two degrees of freedom (displacement and rotation). The beam should be divided into a large number of elements to achieve the accurate results. Higher-order Finite Element (HOFE) overcomes these difficulties considering four degrees of freedom (displacement, rotation, curvature and gradient of curvature) per node. In this thesis work, ANSYS® software is used which solves vibrational problems of complex structural shapes using Finite Element Method.

1.6   Literature review

A detailed literature review can be made to explore the contributions of researchers analyzing the vibration and stability of rotating beam. Composite material is a new inclusion on this specific type of engineering application. Before usage of composite material, homogeneous material has been used by researcher/engineer to build any complex machine structure but methodology to analyze has been revealed. In recent years researcher using composite material to design and analyze a rotating blade but geometry of a blade was restricted in uniform shape in most of the works. Researchers started analyzing tapered composite beam or plate but they are also limited to static condition. Following topic presents prehistory of vibration and dynamic instability analysis of rotating composite beam.

1.6.1 Free vibration analysis of rotating composite beam

Southwell and Gough [46] were the first to estimate the modal characteristics of rotating cantilever beams, using the energy method. This method was simple and widely used by engineers who want to design rotating blades. In 1958, Scilhansl [47] used Ritz method and derived the equations of motion of rotating cantilever beams and obtained more accurate model to estimate the natural frequencies. These analytical models were introduced in the early stage of the rotating beam research. Using this method large number of numerical analysis have been performed by many researchers around the world (see, for instance, Putter and Manor [48], Yoo and Shin [23], Kuo and Lin [49]). However, all these results are involved with rotating beams problem that is made of isotropic material.

Vibration characteristics of non-rotating composite structures were investigated in many previous works (Abarcar and Cunniff [50], Miller and Adams [51]), where most of the works were conducted for out-of-plane bending (transverse) vibration and rotary inertia effect has been ignored. Few researchers (Hodges et al [22], Krishnaswamy et al [52]) included shear deformation and rotary inertia effect in their analysis. Reddy [3], Berthelot [2] and Jones [4] have found the exact solutions for the free vibrations of uniform laminated composite beams. Few works have been found those are conducted for in-plane bending vibration (Hassan et al [40] and Vebil [41]).

Several engineering components, such as turbine blade or helicopter rotor blade usually have non-uniform geometry. Therefore, determination of dynamic characteristics of non-uniform rotating composite beam has greater practical importance. Ganesan and Zabihollah [11] analyzed the free vibration and buckling of uniform-width thickness-tapered composite beams using both conventional and advanced finite element formulations. They used two nodes per element and four degrees of freedom per node (deflection, slope, curvature, derivative of curvature) in the advanced

finite element formulations. Nabi and Ganesan [53] developed a general finite element formulation based on a first-order shear deformation theory with 16 degrees of freedom per element to study the free vibration characteristics of laminated composite beams. They also conducted a parametric study on the influence of beam geometry and boundary conditions on the natural frequencies of the beam. Eftakher [14] conducted free and forced vibration analysis of uniform-width thickness-tapered laminated composite beams using Rayleigh-Ritz method and conventional and advanced finite element formulations. He used two nodes per element and four degrees of freedom per node in the advanced finite element formulation. Vijay [54], Pooya [13] and Mohammad [55] conducted the free and forced vibration analysis of thickness-tapered width-tapered laminated composite beams using Rayleigh-Ritz method, Conventional Finite Element Method and Hierarchical Finite Element Method, respectively.

Most of the vibration analyses of rotating composite beam were restricted to uniform shape. Yoo et al [23] investigated the flap wise bending vibration of uniform composite laminated beam using Rayleigh-Ritz method in conjunction with Timoshenko beam theory. Chandiramani et al. [26] also conducted research on rotating composite beam using higher order shear deformation theory for hollow boxed beam. Coriolis effect has been ignored in their work. Kim et al. [24] considered Coriolis effect on a piezoelectric fiber composite beam to analyze the free vibration. Finite Element Method has been used in that case. Kaya et al. [21, 25] used differential transformed method to determine natural frequencies of axial and bending vibrations of rotating uniform Piezolaminated composite beam. Carrera [20] established a refined structural theory called Carrera Unified Formulation to do analysis for free vibration of rotating composite beam. Bakhtiari-Nejad et al. [19] determined fundamental frequency of free vibration considering nonlinear Von-Karman displacement theory. They have used differential transformed method to formulate the problem.

8

1.6.2 Dynamic instability analysis of rotating composite beam

Dynamic instability analysis of a beam subjected to periodic loads is an important and advanced research topic. A number of research works can be traced to parametric resonance or dynamic instability of isotropic non-rotating beam. Bolotin [31] first comprehensively reviewed the research of dynamic instability problems in case of bar, plate and shell. Hyun and Yoo [56] studied the dynamic stability of an axially oscillating cantilever beam considering the stiffness variation. The dynamic stability of a rotating beam subjected to base excitation was investigated by Tan et al. [57].

With a few exceptions, most of these studies have addressed the axially oscillating problem. On the other hand, Yoo et al. [58] analyzed the dynamics of a rotating cantilever beam. They presented a linear modeling method for the dynamic analysis of a flexible beam undergoing overall motion. Based on this modeling method, Chung and Yoo [38] derived the partial differential equations of motion for a rotating cantilever beam and discretized by the Galerkin method to investigate the natural frequencies and time responses. This study investigates the dynamic stability for the flap wise motion of a cantilever beam by using the method of multiple scales, when the beam oscillates in the rotational direction.

In relation to composite materials, Saravia et al. [34] first investigated the dynamic stability behavior of thin-walled rotating composite beams using Finite Element Method. Lin and Chen [35] studied the dynamic stability of a rotating composite beam with a constrained damping layer subjected to axial periodic loads. Chen et al. [59] investigated the dynamic stability of rotating composite shafts under axial periodic loads. Chattopadhyay and Radu [36] studied the dynamic instability of composite laminates using a higher order theory.

1.7   Objective of this thesis

The main objectives of the present study are the following:

1. To investigate the free vibration response in out-of-plane bending, in-plane bending and axial vibrations of doubly-tapered rotating cantilever composite beam using Rayleigh-Ritz method and FEA tool ANSYS.

2. To investigate the dynamic instability due to periodic rotational velocity of doubly-tapered rotating cantilever composite beam considering out-of-plane bending, in-plane bending and axial vibrations.

3. To conduct a comprehensive parametric study on the effects of rotational velocity, hub radius, double-taper ratio, taper configuration and laminate configurations on the free vibration and dynamic instability of the doubly-tapered rotating cantilever composite beams.

4. To perform a detailed comparative study between out-of-plane bending and in-plane bending vibrations, in order to identify the fundamental frequency, first critical speed, maximum displacement and width of instability region.

1.8   Layout of this thesis

The present chapter provides a brief introduction and literature survey on free vibration and dynamic instability analysis of laminated composite beams.

Chapter-2 is dedicated for free vibration and dynamic instability analyses of out-of-plane bending vibration of doubly-tapered rotating cantilever laminated composite beams using Rayleigh-Ritz method based on classical lamination theory. In the first part of Chapter 2, free vibration analysis is conducted considering different parameters such as rotational velocity, hub radius to beam length ratio, ply drop-off, double-taper ratio, stacking sequence and different taper configurations. Mode shapes and critical speed are also determined for doubly-tapered composite

beam. Determined natural frequencies are compared and validated with existing results obtained using Conventional Finite Element Method (CFEM) and FEA tool ANSYS. In the second part of this chapter dynamic instability analysis using Bolotin's method is carried out for out-of-plane bending vibration of doubly-tapered composite beam subjected to time varying rotational speed. Boundaries between stable and unstable regions are determined in terms of resonance frequency and amplitude factor. Variation of width of instability region is compared for different parameters such as rotational velocity, double-taper ratio and stacking sequence.

In Chapter-3, free vibration and dynamic instability analyses for in-plane and axial vibrations of doubly-tapered rotating laminated composite beam are carried out using Rayleigh-Ritz method. Results for natural frequencies are compared and validated with existing reference and Finite Element Analysis tool ANSYS. Coriolis term and rotary inertia effect have been ignored. Variation of natural frequency and the width of instability region have been analyzed for different parameters changes. Mode shapes and critical speed are also determined in this chapter.

In Chapter-4, a detailed comparative study is presented between out-of-plane bending and in-plane bending vibrations, in order to identify the fundamental frequency, critical speed, maximum displacement and largest width of instability region. Different taper configurations are also considered for this analysis.

Chapter 5 brings the thesis to its end by providing an overall conclusion of the present work and some recommendations for future work.

Chapter-2

Free vibration and dynamic instability analyses of doubly-tapered rotating laminated composite beams for out-of-plane bending vibration

2.1   Introduction

Free vibration and dynamic instability analyses of rotating laminated composite beam is an engineering research field of extensive interest. Laminated composite beam has the property to keep the required strength by having less weight, which has foremost importance in aerospace, mechanical and automotive structures. Recently, composite laminate which has a taper profile in both thickness and width throughout its length is increasingly being used in aerospace industry and wind energy sector as rotating element such as helicopter blade or wind turbine blade. Geometric non-linearity in the composite beam provides the provision to control the vibration. In this chapter, free vibration analysis for out-of-plane bending of thickness-and-width-tapered laminated composite beam is conducted using Rayleigh-Ritz method and also the dynamic instability analysis is carried out. Commercial Finite Element Analysis tool ANSYS is used to validate the results. NCT-301 Graphite/Epoxy prepreg has been chosen to conduct the numerical analysis, which is available in the laboratory of Concordia Centre for Composites (CONCOM).

2.2   Description of the rotating beam

Consider a laminated composite beam of length L, which is attached to a hub of radius R, as shown in the Figure 2.1 in Cartesian coordinates. The hub rotates about its axis at a constant angular speed Ω rad/s. The origin for the coordinates is taken at the edge of the hub. The x-axis coincides with the neutral axis of the beam, the z-axis is parallel to the axis of rotation and the y-axis lies in the plane of rotation.
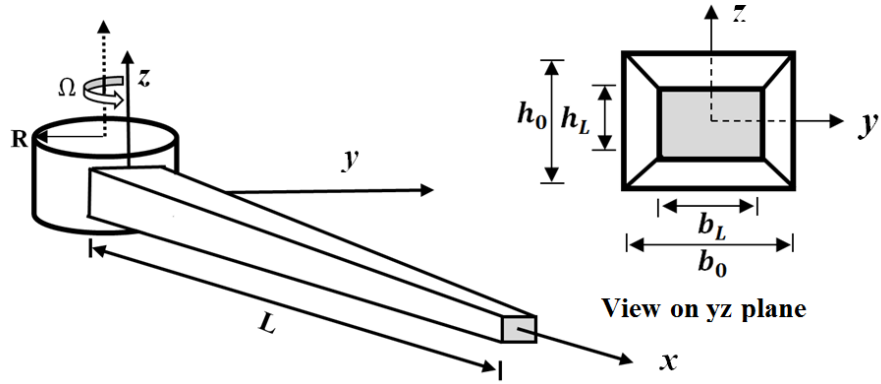
Figure 2.1 Doubly-tapered rotating composite beam

View on y-z plane illustrates beam changing the thickness from h_0 to h_L and changing its width from b_0 to b_L over the length L. The laminated composite beam consists of N layers, numbered from the lower to the upper face. To study the out-of-plane bending vibration, x-y plane is chosen as mid-surface and reference plane. Half of the layers of laminated beam are in positive z-direction and the other half are in negative z-direction. Half of the width is in positive y-direction and the other half is in negative y-direction.

Any system with mass and elasticity can undergo free vibration. Free vibration analysis of the above composite beam requires associated equation of motion. The Lagrange's equation can be used to obtain the equation of motion of this physical system. To use this equation, total strain energy, including work done by the centrifugal force and kinetic energy of the system, needs to be determined. Energies of any complex system can be formulated using approximated solution methods such as Galerkin method or Rayleigh-Ritz method to determine the natural frequencies in free vibration. In this thesis, Rayleigh-Ritz method is used to determine the natural frequencies of doubly-tapered rotating laminated composite beam. This method uses series of shape functions to obtain fundamental frequencies more accurately. The success of this method depends on the choice of the shape functions that should satisfy the geometric boundary conditions.

2.3   Energy formulation using Rayleigh-Ritz method

2.3.1   Strain energy

Strain energy is the energy stored by a system undergoing deformation. Considering that the beam's length to thickness ratio is high, Classical Laminate Theory (CLT) can be used to determine the strain energy which assumes that transverse shear strains are zero and neglects z-direction stress, that is $\sigma_{zz}{}^k = 0$, and $\gamma_{xz}{}^k = \gamma_{yz}{}^k = 0$. Therefore, strain energy for a laminate with N layers can be written as:

$$U = \sum_{k=1}^{N} \frac{1}{2} \iiint (\sigma_{xx}{}^k \varepsilon_{xx}{}^k + \sigma_{yy}{}^k \varepsilon_{yy}{}^k + \tau_{xy}{}^k \gamma_{xy}{}^k) \, dx \, dy \, dz \tag{2.1}$$

where $\sigma_{xx}{}^k$ and $\sigma_{yy}{}^k$ denote the stresses in corresponding layer along the x and y directions, respectively, $\varepsilon_{xx}{}^k$ and $\varepsilon_{yy}{}^k$ denote the strain in corresponding layer along x and y directions, respectively. $\tau_{xy}{}^k$ is shear stress and $\gamma_{xy}{}^k$ is shear strain in the corresponding layer acting on the x-y plane.

As shown in the Figure 2.1, a doubly-tapered laminated composite beam has length L, width of ply changes from b_0 to b_L and the ply lies between h_k and h_{k-1}, then the strain energy equation can be written as:

$$U = \sum_{k=1}^{N} \frac{1}{2} \int_0^L \int_{-\frac{b(x)}{2}}^{\frac{b(x)}{2}} \int_{h_{k-1}}^{h_k} (\sigma_{xx}{}^k \varepsilon_{xx}{}^k + \sigma_{yy}{}^k \varepsilon_{yy}{}^k + \tau_{xy}{}^k \gamma_{xy}{}^k) \, dz \, dy \, dx \tag{2.2}$$

Here, for linearly width-tapered beam the variable width $b(x)$ can be defined as:

$$b(x) = b_0 - \frac{(b_0 - b_L)}{L} x \tag{2.3}$$

For a thickness-tapered laminated beam, h_k is the distance from mid-plane to top of the k-th lamina and h_{k-1} is the distance from mid-plane to bottom of the k-th lamina. Expressions for h_k and h_{k-1} depend on different types of internal mid-plane tapered laminates obtained by configuring the ply drop-off at different locations of the laminate (see Appendix-A).

Considering plane stress assumption [5], stresses in the *k-th* ply are written as follows:

$$
\begin{bmatrix} \sigma_{xx}{}^k \\ \sigma_{yy}{}^k \\ \tau_{xy}{}^k \end{bmatrix} = [Q^k] \begin{bmatrix} \varepsilon_{xx}{}^k \\ \varepsilon_{yy}{}^k \\ \gamma_{xy}{}^k \end{bmatrix} \tag{2.4}
$$

here,
$$
[Q^k] = \begin{bmatrix} Q_{11}{}^k & Q_{12}{}^k & Q_{16}{}^k \\ Q_{21}{}^k & Q_{22}{}^k & Q_{26}{}^k \\ Q_{61}{}^k & Q_{62}{}^k & Q_{66}{}^k \end{bmatrix} \tag{2.5}
$$

$[Q^k]$ is transformed reduced stiffness matrix of a composite ply, which is a function of mechanical properties of composite material and the transformation matrices due to fiber angle (θ) and laminate taper angle (φ) [12]. For resin plies in taper configurations, $[Q^k]$ is replaced with $[Q_{resin}]$, which can be defined by the mechanical properties of resin as:

$$
[Q_{resin}] = \begin{bmatrix} \dfrac{E}{1-v^2} & \dfrac{vE}{1-v^2} & 0 \\ \dfrac{vE}{1-v^2} & \dfrac{E}{1-v^2} & 0 \\ 0 & 0 & \dfrac{E}{2(1+v)} \end{bmatrix} \tag{2.6}
$$

In equation (2.4) strains in a ply for out-of-plane bending deformation can be defined as:

$$
\begin{bmatrix} \varepsilon_{xx}{}^k \\ \varepsilon_{yy}{}^k \\ \gamma_{xy}{}^k \end{bmatrix} = [\varepsilon^0] + z[k] = \begin{bmatrix} \dfrac{\partial u_0}{\partial x} \\ \dfrac{\partial v_0}{\partial y} \\ \dfrac{\partial u_0}{\partial y} + \dfrac{\partial v_0}{\partial x} \end{bmatrix} + z \begin{bmatrix} -\dfrac{\partial^2 w_0}{\partial x^2} \\ -\dfrac{\partial^2 w_0}{\partial y^2} \\ -2\dfrac{\partial^2 w_0}{\partial x \partial y} \end{bmatrix} \tag{2.7}
$$

where $[\varepsilon^0]$ is mid-plane strain matrix and $[k]$ is curvature matrix for out-of-plane bending deformation. u_0, v_0 and w_0 are mid-plane displacements corresponding to x, y and z directions, respectively.

Substituting equation (2.7) into equation (2.4), the stress-strain relation leads to:

$$
\begin{bmatrix} \sigma_{xx}{}^k \\ \sigma_{yy}{}^k \\ \tau_{xy}{}^k \end{bmatrix} = [Q^k] [\varepsilon^0] + z[Q^k] [k] \tag{2.8}
$$

Substituting $\sigma_{xx}{}^k$, $\sigma_{yy}{}^k$ and $\tau_{xy}{}^k$ in equation (2.2), strain energy equation becomes:

$$U = \sum_{k=1}^{N} \frac{1}{2} \int_0^L \int_{-\frac{b(x)}{2}}^{\frac{b(x)}{2}} \int_{h_{k-1}}^{h_k} (Q_{11}{}^k(\varepsilon_{xx}{}^k)^2 + Q_{22}{}^k(\varepsilon_{yy}{}^k)^2 + Q_{66}{}^k(\gamma_{xy}{}^k)^2 + 2Q_{12}{}^k \varepsilon_{xx}{}^k \varepsilon_{yy}{}^k +$$

$$2Q_{16}{}^k \varepsilon_{xx}{}^k \gamma_{xy}{}^k + 2Q_{26}{}^k \varepsilon_{yy}{}^k \gamma_{xy}{}^k) \, dz \, dy \, dx \tag{2.9}$$

For pure out-of-plane bending deformation, $\varepsilon_{yy}{}^k$ and $\gamma_{xy}{}^k$ are can be neglected. Also neglecting small axial mid-plane displacement u_0, strain energy expression simplifies to:

$$U = \sum_{k=1}^{N} \frac{1}{2} \int_0^L \int_{-\frac{b(x)}{2}}^{\frac{b(x)}{2}} \int_{h_{k-1}}^{h_k} Q_{11}{}^k (-z \frac{\partial^2 w_0}{\partial x^2})^2 \, dz \, dy \, dx \tag{2.10}$$

From Classical Laminate Theory:

$$\sum_{k=1}^{N} \int_{h_{k-1}}^{h_k} z^2 Q_{11}{}^k dz = D_{11}(x) \tag{2.11}$$

where, $D_{11}(x)$ is the first coefficient of bending stiffness matrix for out-of-plane bending. Using equation (2.11) and integrating with respect to y across the width of the laminate, equation (2.10) becomes:

$$U = \frac{1}{2} \int_0^L b(x) D_{11}(x) (\frac{\partial^2}{\partial x^2} w_0(x,t))^2 dx \tag{2.12}$$

To use Rayleigh-Ritz method, out-of-plane bending displacement is assumed as:

$$w_0(x,t) = \sum_{i=1}^{m} \emptyset_i(x) q_i(t) \tag{2.13}$$

where, $\emptyset_i(x)$ is approximate shape function for out-of-plane bending deformation. Any compact set of admissible functions that satisfy the geometric boundary conditions of the beam can be used as the shape functions and $q_i(t)$ is generalized coordinate where t refers to time and m is number of terms in w_0. After using Rayleigh-Ritz approximation for out-of-plane bending displacement, equation (2.12) leads to:

$$U = \sum_{i=1}^{m} \sum_{j=1}^{m} \frac{1}{2} \int_0^L b(x) D_{11}(x) \left(\frac{\partial^2}{\partial x^2} \emptyset_i(x) \right) \left(\frac{\partial^2}{\partial x^2} \emptyset_j(x) \right) q_i(t) q_j(t) dx \tag{2.14}$$

Finally,

$$U = \sum_{i=1}^{m} \sum_{j=1}^{m} \frac{1}{2} q_i K_{ij} q_j \tag{2.15}$$

Here,

$$K_{ij} = \int_0^L b(x) D_{11}(x) \emptyset_i''(x) \emptyset_j''(x) dx \tag{2.16}$$

2.3.2 Work done by the centrifugal force

When the free end of a cantilever rotating beam deflects transversely (out-of-plane bending), particles of the beam have a small axial displacement due to centrifugal force. The work done by this centrifugal force and corresponding axial displacement produces centrifugal stiffening that has effects on the natural frequency of free vibration. This axial displacement can be expressed in terms of transverse displacement as:

$$du = ds - dx = \sqrt{(dx)^2 + \left(\frac{\partial w_0}{\partial x} dx\right)^2} - dx = dx\left(\sqrt{1 + \left(\frac{\partial w_0}{\partial x}\right)^2} - 1\right) \approx \frac{1}{2}\left(\frac{\partial w_0}{\partial x}\right)^2 dx \tag{2.17}$$

Here dx is the length of an undeformed infinitesimal beam element and ds is the deformed arc length of the infinitesimal beam element shown in the Figure 2.2.
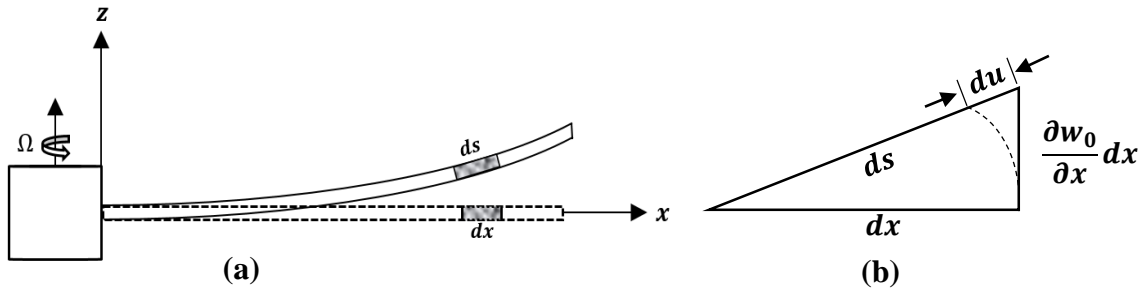
Figure 2.2 (a) Transversely deflected cantilever beam, (b) Geometrical representation

If $P(x)$ is the centrifugal force at any point x, then work done by this centrifugal force in doubly-tapered laminated composite beam can be written as:

$$W = P(x) * u \tag{2.18}$$

17

Or:

$$W = \frac{1}{2}\int_0^L P(x)(\frac{\partial}{\partial x}w_0(x,t))^2 dx \qquad (2.19)$$

Here, $P(x)$ for the doubly-tapered laminate can be written as:

$$P(x) = \int_0^{L-x} b(\delta)\,\rho_L(\delta)\Omega^2(R+x+\delta)d\delta \qquad (2.20)$$

Here, $b(\delta) = b(x) - \frac{b(x)-b_L}{L-x}\delta$ is variable width of a ply within x and L (shown in Figure 2.3),

$\rho_L(\delta) = \sum_{k=1}^N \rho_k\big(h_k(\delta) - h_{k-1}(\delta)\big)$, where $\big(h_k(\delta) - h_{k-1}(\delta)\big)$ is variable distance between top

and bottom faces of a ply within x and L (see Appendix-D) and ρ_k is mass density of ply.
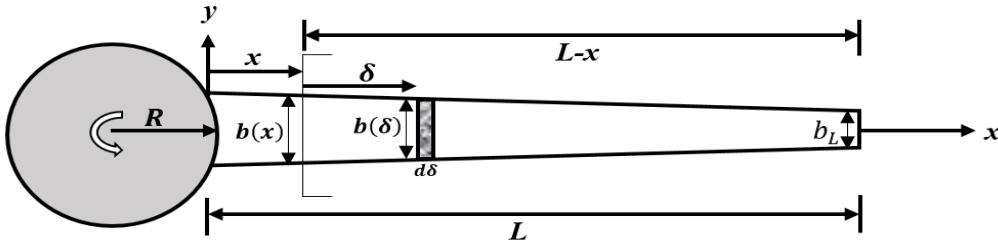
Figure 2.3 Doubly-tapered rotating composite beam (x-y plane view)

Substituting Rayleigh-Ritz approximate function, equation (2.19) can be written as:

$$W = \sum_{i=1}^m \sum_{j=1}^m \frac{1}{2}\int_0^L P(x)\frac{\partial}{\partial x}\emptyset_i(x)\frac{\partial}{\partial x}\emptyset_j(x)q_i(t)q_j(t)dx \qquad (2.21)$$

Finally,

$$W = \sum_{i=1}^m \sum_{j=1}^m \frac{1}{2}q_i K^C_{ij}q_j \qquad (2.22)$$

Here,

$$K^C_{ij} = \int_0^L P(x)\emptyset_i{}'(x)\emptyset_j{}'(x)dx \qquad (2.23)$$

2.3.3 Kinetic energy

The kinetic energy of an elastic body depends on the mass of the body as well as its velocity. The kinetic energy of a doubly-tapered rotating composite beam can be expressed as:

$$T = \frac{1}{2} \int_0^L \int_{-\frac{b(x)}{2}}^{\frac{b(x)}{2}} \rho_L b(x) \left(V_x^2 + V_y^2 + V_z^2 \right) dy \, dx \tag{2.24}$$

Here, $\rho_L = \sum_{k=1}^N \rho_k (h_k - h_{k-1})$ denotes the mass per unit length per unit width of the laminated beam and V_x, V_y and V_z are the velocity components in x, y and z directions, respectively. The velocity vector gives the velocity components of an object with its direction. The velocity vector of any point in a rotating composite beam can be expressed as [16]:

$$\vec{V} = \frac{\partial \vec{r}}{\partial t} + \Omega \hat{k} \times \{ (R + x + u_0)\hat{i} + v\hat{j} + w\hat{k} \} = \frac{\partial u}{\partial t}\hat{i} + \frac{\partial v}{\partial t}\hat{j} + \frac{\partial w}{\partial t}\hat{k} + \Omega \hat{k} \times \{ (R + x + u_0)\hat{i} +$$

$$v\hat{j} + w\hat{k} \} \tag{2.25}$$

where u, v and w are the displacements in x, y and z directions, respectively and $\vec{r}$ is position vector after deformation. $\hat{i}, \hat{j}$ and $\hat{k}$ are unit vectors in x, y and z directions, respectively. Neglecting displacement in y direction and applying vector cross-product formula ($\hat{k} \times \hat{k} = 0, \hat{k} \times \hat{i} = \hat{j}, \hat{k} \times \hat{j} = -\hat{i}$), equation (2.25) can be written as:

$$\vec{V} = \frac{\partial u}{\partial t}\hat{i} + \Omega(R + x + u_0)\hat{j} + \frac{\partial w}{\partial t}\hat{k} \tag{2.26}$$

Therefore, velocity components in three directions are:

$$V_x = \frac{\partial u}{\partial t}, \ V_y = \Omega(R + x + u_0) \text{ and } V_z = \frac{\partial w}{\partial t} \tag{2.27}$$

From Classical Laminate Theory and neglecting small axial mid-plane displacement one can get:

$$u(x,t) = -z\frac{\partial w_0(x,t)}{\partial x} \tag{2.28}$$

$$w(x,t) = w_0(x,t) \tag{2.29}$$

Using equation (2.27) to (2.29) into the equation (2.24), the kinetic energy equation of a doubly-tapered rotating laminated composite beam becomes:

$$T = \frac{1}{2} \int_0^L \rho_L b(x) \{ \left(\frac{\partial w_0}{\partial t}\right)^2 + \Omega^2(R + x)^2 + (-z\frac{\partial^2 w_0}{\partial x \partial t})^2 \} dx \tag{2.30}$$

19

According to Euler-Bernoulli theory for thin beam, rotary inertia terms can be neglected [3], then the equation (2.30) for kinetic energy becomes:

$$T = \frac{1}{2}\int_0^L \rho_L b(x)\left\{\left(\frac{\partial w_0}{\partial t}\right)^2 + \Omega^2(R+x)^2\right\}dx \tag{2.31}$$

After using Rayleigh-Ritz approximation, equation (2.31) simplifies to

$$T = \sum_{i=1}^m \sum_{j=1}^m \frac{1}{2}\int_0^L \rho_L b(x)\emptyset_i(x)\emptyset_j(x)\dot{q}_i(t)\dot{q}_j(t)dx + \frac{1}{2}\int_0^L \rho_L b(x)\Omega^2(R+x)^2 dx \tag{2.32}$$

Finally,

$$T = \sum_{i=1}^m \sum_{j=1}^m \frac{1}{2}\dot{q}_i(t)M_{ij}\dot{q}_j(t) + \frac{1}{2}\int_0^L \rho_L b(x)\Omega^2(R+x)^2 dx \tag{2.33}$$

Here,

$$M_{ij} = \int_0^L \rho_L b(x)\emptyset_i(x)\emptyset_j(x)dx \tag{2.34}$$

2.3.4 Equation of motion

Equation of motion describes a physical system as a function of time. For this particular free vibration problem, Lagrange's equation can be written as [44]:

$$\frac{d}{dt}\left(\frac{\partial T}{\partial \dot{q}_i}\right) - \frac{\partial T}{\partial q_i} + \frac{\partial (U+W)}{\partial q_i} = 0, i = 1..m \tag{2.35}$$

Substituting U, W and T from equations (2.15), (2.22) and (2.33), respectively into the equation (2.35), gives a set of m equations that can be written in matrix form as

$$[M]\{\ddot{q}\} + ([K] + [K^C])\{q\} = \{0\} \tag{2.36}$$

where, $[M], [K], [K^C]$ and $\{q\}$ are mass matrix, stiffness matrix, stiffness matrix due to centrifugal action and system displacement vector, respectively (see Appendix-C).

To find the natural frequency of a structure, the solution of the equation (2.36) can be assumed as

$$\{q\} = \{Q\}e^{\sqrt{-1}\omega t} \tag{2.37}$$

where, $\{Q\}$ is the mode shape (eigen) vector and ω is the natural frequency of the out-of-plane bending vibration. Using equation (2.37), equation (2.36) leads to:

$$((\lbrack K \rbrack + \lbrack K^C \rbrack) - {\omega_i}^2 \lbrack M \rbrack)\lbrace Q \rbrace e^{\sqrt{-1}\omega t} = \lbrace 0 \rbrace \qquad (2.38)$$

Equation (2.38) is an eigenvalue problem and can be solved to determine the natural frequencies of the doubly-tapered rotating cantilever laminated composite beam.

2.4   Boundary condition and approximate shape function

Rayleigh-Ritz method uses series of shape functions where each function gives the result for each mode, which means that the number of natural frequencies and modes depend on the number of shape functions used. This method serves best depending on the choice of the shape functions that must satisfy the geometric boundary conditions.

Rotating structure such as helicopter rotor blade or wind turbine blade is usually attached with the hub at one side and the other side is free. For a beam of length L, that is fixed at one end and free at the other end, the boundary conditions are [2,3]:

$$w_{0(x=0)} = 0, w_{0(x=L)} \neq 0, \left.\frac{\partial w_0}{\partial x}\right|_{(x=0)} = 0 \ and \ \left.\frac{\partial w_0}{\partial x}\right|_{(x=L)} \neq 0 \qquad (2.39)$$

Various trial functions can satisfy this boundary condition. One of the simple polynomial functions is [10]:

$$\emptyset_i(x) = \left(\frac{x}{L}\right)^{i+1}, \ i = 1,2,3 \dots m \qquad (2.40)$$

2.5   Validation and results

Rayleigh-Ritz formulation for free vibration analysis described above has been developed using MATLAB for validation and numerical analysis. Validation of results have been performed by comparing the existing results available in the literature and the results obtained using ANSYS. Results available for non-rotating tapered composite beam have been compared with the results of the present work for free vibration response. In the case of rotating composite beam, ANSYS result has been compared with the present work. First three natural frequencies are taken into account to

perform the validation. Four different taper configurations (see Appendix-A) are considered for validation and numerical analysis. Validation of results for isotropic material are given in Appendix-E. Following flowchart is considered as a required step to validate the final result.

STEP 1		STEP 2		STEP 3
Result verification for rotating uniform composite beam	▷	Result verification for thickness-tapered rotating composite beam	▷	Result verification for doubly-tapered rotating composite beam
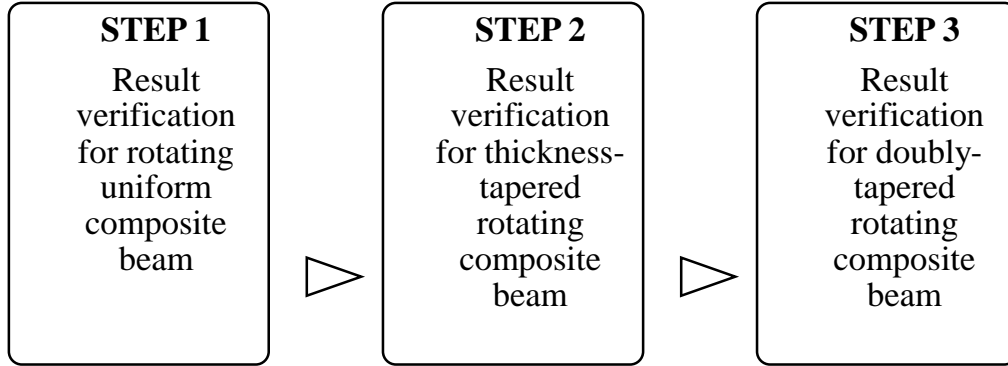
Figure 2.4 Flowchart for required validation steps

The geometric parameters and mechanical properties of the material used are listed below.

Table 2.1 Mechanical properties of unidirectional NCT-301 graphite-epoxy prepreg [55]

Longitudinal modulus (E_1)	113.9 GPa
Transverse modulus (E_2)	7.985 GPa
$E_3 = E_2$	7.985 GPa
In-plane shear modulus (G_{12})	3.137 GPa
Out-of-plane shear modulus (G_{23})	2.852 GPa
Density of fiber (ρ_f)	1480 kg/m^3
Major Poisson's ratio (ν_{12})	0.288
Minor Poisson's ratio (ν_{21})	0.018

Table 2.2 Mechanical properties of resin material [55]

Elastic modulus (E)	3.93 GPa
Shear modulus (G)	1.034 GPa
Density of resin (ρ_r)	1000 kg/m^3
Major Poisson's ratio (υ)	0.37

Rotational and geometric parameters used for steps 1 to 3 are given below:

Table 2.3 Rotational parameters used in validation and numerical analysis

Rotational Velocity, Ω	0, 50, 100, 200 rad/s
Hub radius, R	0.025 m

Table 2.4 Geometric properties used in validation and numerical analysis

Length of beam, L	0.25 m
Individual ply thickness, h_{ply}	0.000125 m
Width of beam, b_0	0.02 m
Laminate stacking sequence	$[0/90]_{9s}$, $[0]_{18s}$, $[90]_{18s}$, $[0/45/-45]_{6s}$

All the laminates used in this thesis have symmetrical stacking sequence. In this thesis thickness-tapering in the laminated beam is described by the number of ply drop-off (S). Thickness taper angle and number of ply drop-off are related by the following equation:

$$\varphi = tan^{-1}(\frac{\left(\frac{S}{2}\right) h_{ply}}{L}) \tag{2.41}$$

Here, φ is thickness taper angle, S is number of ply drop-off, L is length of the beam and h_{ply} is individual ply thickness.

Width-tapering is described by width-ratio (r_b) as:

$$r_b = \frac{b_L}{b_0} \tag{2.42}$$

Here, b_0 is width of beam at fixed side and b_L is width of beam at free side.

2.5.1 Finite element program-ANSYS

The commercial finite element program ANSYS 15.0 Workbench platform has been chosen to perform the modal analysis. Modal analysis for a rotating beam problem is a pre-stressed analysis where static analysis has to be done before modal analysis to set up the boundary condition and rotational load. ANSYS Composite PrepPost (ACP) has been used to model the different taper configurations in laminated composite beams. Four-node layered shell element (SHELL 181) is

23

employed in the modeling to describe the bending vibrations of laminated beams. The beams are discretized using the finite element (SHELL 181) shown in Figure 2.5, available in the commercial package ANSYS 15.0. This element has 4 nodes (I, J, K and L are shown in Figure 2.5) and six degrees of freedom at each node: translations in the nodal x, y and z directions and rotations about the nodal x, y, and z-axes. The circled number in Figure 2.8 represents the element faces. The choice of SHELL 181 element type is based on layered applications of a structural shell model and the type of results that need to be calculated.
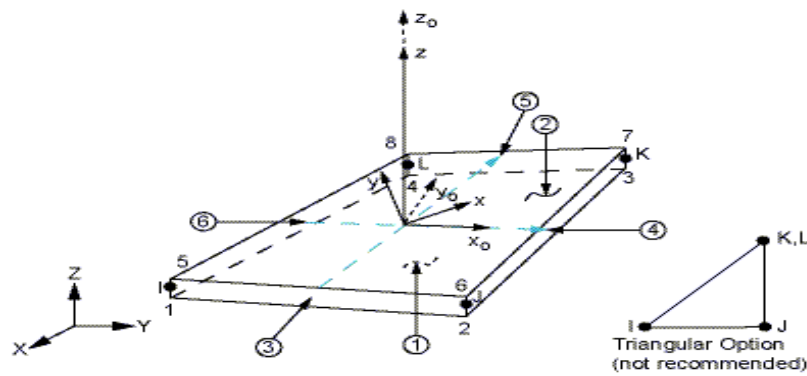
Figure 2.5 Geometry of finite element- SHELL181 [28]

2.5.2 Validation step-1: Rotating uniform composite beam

In this validation step non-rotating and rotating uniform composite beams are considered. In Table 2.5, first three out-of-plane bending natural frequencies determined for non-rotating clamped-free uniform composite beam using Rayleigh-Ritz (R-R) method, are compared with the exact solution, ANSYS results and existing results obtained using Conventional Finite Element Method (CFEM). Results obtained using different number of terms in Rayleigh-Ritz approximate shape function are also listed in Table 2.5. It shows that as the number of terms increases the results become more accurate. In Table 2.6, first three out-of-plane bending natural frequencies for rotating clamped-free uniform composite beam have been compared with ANSYS results. Beam length, width, thickness of the lamina and hub radius are given in Tables 2.3 and 2.4. Mechanical

24

properties of composite material are given in Table 2.1. Different stacking sequences are considered to compare the results. The mode shapes associated with the frequencies of $[0/90]_{9s}$ and $[0/45-45]_{6s}$ non-rotating laminated beams are illustrated in Figures 2.6 and 2.7 respectively, and these are deduced from ANSYS for the first three out-of-plane bending natural frequencies.

Table 2.5 Natural frequencies (Hz) of non-rotating uniform cantilever composite beam

Stacking Sequence	Mode	R-R solution (3 terms)	R-R solution (7 terms)	R-R solution (8 terms)	CFEM [13]	Exact solution	ANSYS
$[0/90]_{9s}$	1st	77.49	77.47	77.47	77.51	77.99	77.34
	2nd	489.9	485.5	485.5	485.6	485.4	481.2
	3rd	2603.1	1359.8	1359.4	1360.1	1359.2	1333.4
$[90]_{18s}$	1st	27.09	27.08	27.08	27.06	27.08	27.02
	2nd	171.2	169.7	169.6	169.8	169.7	169.5
	3rd	909.9	475.3	474.8	475.4	475.2	476.2
$[0]_{18s}$	1st	102.3	102.3	102.3	102.3	102.3	101.8
	2nd	646.7	640.9	640.6	641.1	640.9	629.0
	3rd	3436.5	1795.1	1793.23	1795.4	1794.8	1725.5
$[0/45/-45]_{6s}$	1st	77.56	77.57	77.69	77.67	77.58	69.78
	2nd	490.5	486.1	486.7	486.2	487.4	434.9
	3rd	2606.6	1361.6	1362.3	1361.9	1361.4	1211.0

In Table 2.5, the formula for exact solution given by [2]

$$\omega_i = \frac{\mu_i}{2\pi L^2}\sqrt{\frac{D_{11}}{\rho H}} \tag{2.43}$$

has been used where, $\mu_{i=1,2,3} = 3.516, 22.034, 61.701$ for first three natural frequencies, L is the length of the beam, H is the thickness of the laminate, ρ is the mass density of the composite material and D_{11} is the first coefficient in bending stiffness matrix of composite laminate. The comparison has been made with the existing results [13], that used Conventional Finite Element Method considering the cylindrical bending theory. Total of 10 elements were used to get the convergence in the result with exact solution, considering two degrees of freedom per node and four degrees of freedom per element.
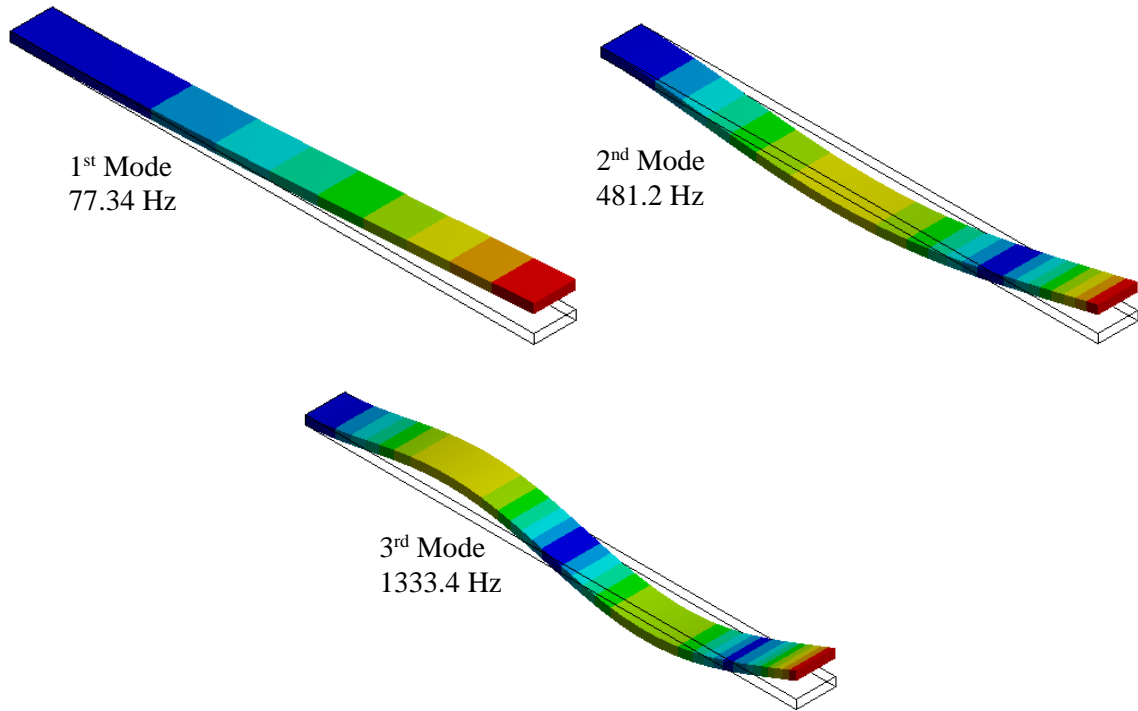
Figure 2.6 The first three out-of-plane bending vibration modes of non-rotating uniform cantilever composite beam with $[0/90]_{9s}$ stacking sequence
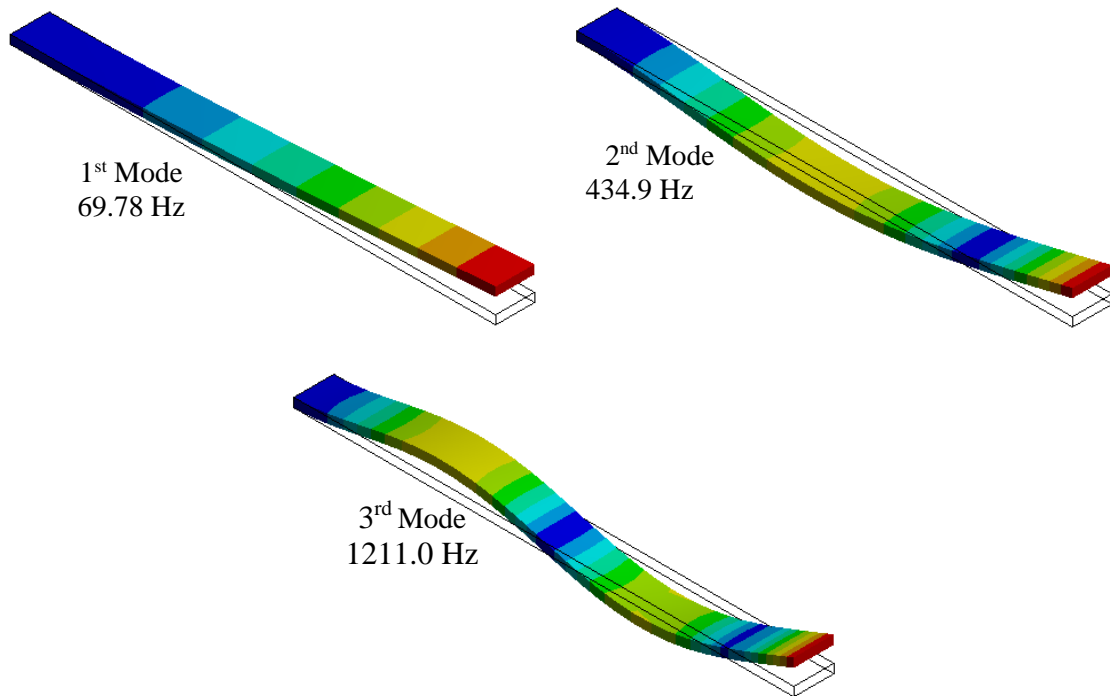
Figure 2.7 The first three out-of-plane bending vibration modes of non-rotating uniform cantilever composite beam with $[0/45/-45]_{6s}$ stacking sequence

Table 2.6 Natural frequencies (Hz) of rotating uniform cantilever composite beam

| Stacking Sequence | Mode | Ω = 50 rad/s | | Ω = 100 rad/s | | Ω = 200 rad/s | |
		R-R Solution (8 terms)	ANSYS	R-R Solution (8 terms)	ANSYS	R-R Solution (8 terms)	ANSYS
[0/90]$_{9s}$	1st	78.02	77.89	79.65	79.52	85.83	85.70
	2nd	486.0	481.7	487.4	483.13	493.1	488.9
	3rd	1360.3	1334.0	1361.7	1335.4	1367.3	1341.2
[90]$_{18s}$	1st	28.61	28.55	32.77	32.72	45.62	45.58
	2nd	171.1	170.9	175.1	174.9	190.4	190.2
	3rd	476.7	477.5	480.7	481.5	496.5	497.3
[0]$_{18s}$	1st	102.7	102.2	103.9	103.5	108.8	108.3
	2nd	641.3	629.4	642.4	630.5	646.7	634.9
	3rd	1795.5	1725.8	1796.5	1726.9	1800.8	1731.4
[0/45/-45]$_{6s}$	1st	78.12	70.39	79.75	72.19	85.92	78.99
	2nd	486.6	435.5	488.1	437.1	493.7	443.4
	3rd	1362.1	1211.5	1363.5	1213.1	1369.2	1219.5

As expected, results for both non-rotating and rotating uniform composite beams are showing very good agreement between the results obtained from R-R method, ANSYS and other sources.

2.5.3 Validation step-2: Thickness-tapered rotating cantilever composite beam

In this validation step, thickness-tapering in beam profile is considered. In Table 2.7, first three out-of-plane bending natural frequencies obtained using Rayleigh-Ritz method for a non-rotating thickness-tapered uniform-width composite beam are validated with ANSYS and existing results obtained using CFEM. The comparison has been performed for a clamped-free beam which has 20 plies at the fixed side and 4 plies have been dropped to obtain Taper Configuration-A (See Appendix A). The beam length, beam width and thickness of lamina are given in Table 2.4. Mechanical properties of composite and resin material are given in Table 2.1 and 2.2, respectively. Number of terms used in R-R method, in this case, is 8. Figure 2.8 shows the first three mode shapes associated with the natural frequencies given in Table 2.7.

Table 2.7 Natural frequencies (Hz) of non-rotating thickness-tapered cantilever composite beam

Stacking Sequence	No. of ply drop-off, S	Mode	R-R Solution	ANSYS	CFEM [13]
$[0/90]_{5s}$	4	1st	45.631	45.510	39.950
		2nd	263.74	261.82	229.02
		3rd	720.93	715.40	624.68

1st Mode
45.51 Hz

2nd Mode
261.82 Hz

3rd Mode
715.40 Hz
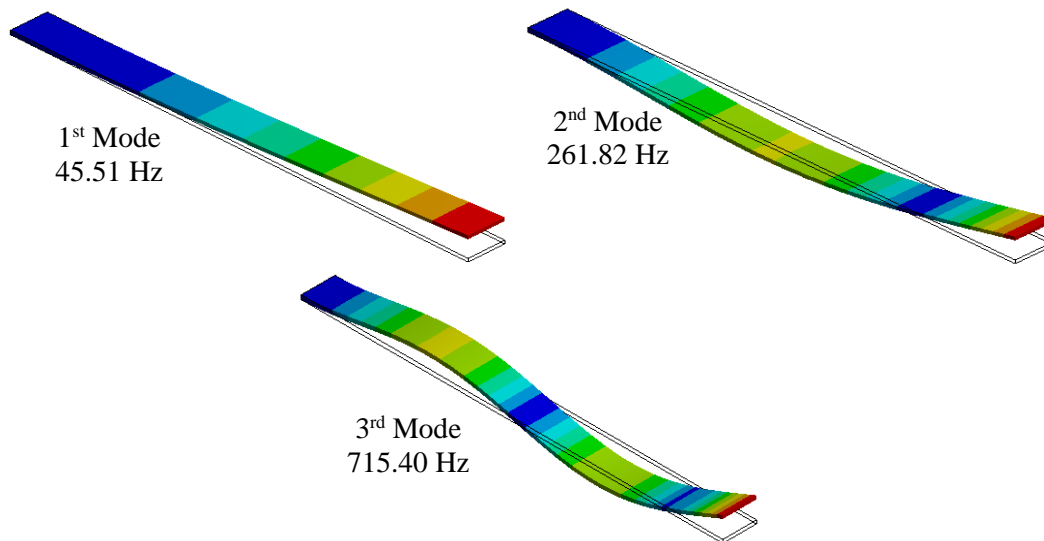
Figure 2.8 The first three out-of-plane bending vibration modes of non-rotating thickness-tapered cantilever composite beam with $[0/90]_{5s}$ stacking sequence

In Table 2.7, results from the R-R method are showing excellent agreement with ANSYS results. Table 2.8 provides further comparison between ANSYS and R-R solutions for first three natural frequencies of non-rotating clamped-free beam with taper Configuration-A. Three different numbers of ply drop-off are considered, validating the results for two different stacking sequences. In this case, the number of terms in approximate shape function is 8.

Table 2.8 Natural frequencies (Hz) of non-rotating thickness-tapered cantilever composite beam for Configuration-A

Stacking Sequence	S	Mode	R-R solution	ANSYS	Stacking Sequence	S	Mode	R-R solution	ANSYS
[0/90]$_{9s}$	2	1st	78.15	77.88	[90]$_{18s}$	2	1st	27.30	27.22
		2nd	479.2	473.8			2nd	167.4	166.9
		3rd	1333.2	1304.5			3rd	465.6	465.6
	6	1st	79.64	79.03		6	1st	27.80	27.81
		2nd	466.2	458.4			2nd	162.5	161.9
		3rd	1279.3	1245.3			3rd	445.8	445.0
	10	1st	81.24	80.26		10	1st	28.36	28.77
		2nd	452.1	444.6			2nd	157.4	157.7
		3rd	1221.8	1189.9			3rd	424.9	425.8

Following Tables 2.9 and 2.10 compare the results for thickness-tapered beam for rotating condition considering three different numbers of ply drop-off. Table 2.9 shows the results for Configuration-A and Table 2.10 is for Configurations B, C and D. Stacking sequence for both tables are [90]$_{18s}$. Hub radius is taken as 0.025 m. Results are compared for three different rotational velocities. All four configurations show that first natural frequency increases when the number of ply drop-off increases and second and third natural frequencies decrease as the number of ply drop-off increases except for Configuration-D. Figures 2.9 and 2.10 show the mode shapes of first three out-of-plane bending natural frequencies for Configurations B and D, respectively, when thickness-tapered beam rotating at 200 rad/s with 10 drop-off plies.

Table 2.9 Natural frequencies (Hz) of rotating thickness-tapered cantilever composite beam for

Configuration-A

No. of ply drop-off, S	Mode	R-R solution	ANSYS	R-R solution	ANSYS	R-R solution	ANSYS
		$\Omega = 50$ Rad/s		$\Omega = 100$ Rad/s		$\Omega = 200$ Rad/s	
2	1st	28.83	28.77	32.98	32.93	45.82	45.78
	2nd	168.7	168.55	172.8	172.6	188.1	187.9
	3rd	466.9	467.86	471.0	471.91	486.8	487.7
6	1st	29.32	29.30	33.45	33.40	46.27	46.20
	2nd	163.9	163.7	168.0	167.8	183.5	183.3
	3rd	447.8	448.0	451.3	452.07	467.2	468.0
10	1st	29.87	29.80	33.98	33.92	46.78	46.70
	2nd	158.8	158.6	162.9	162.7	178.6	178.4
	3rd	426.3	427.0	430.4	431.1	446.5	447.2

Table 2.10 Natural frequencies (Hz) of thickness-tapered rotating composite beam for

Configurations B, C and D

Configuration	S	Mode	R-R solution	ANSYS	R-R solution	ANSYS	R-R solution	ANSYS
			$\Omega = 0$ rad/s		$\Omega = 50$ rad/s		$\Omega = 200$ rad/s	
B	6	1st	27.61	27.69	29.14	29.21	46.14	46.19
		2nd	163.6	161.1	165.0	162.5	184.9	182.0
		3rd	450.5	442.8	451.9	444.2	472.2	464.2
	10	1st	28.09	28.18	29.61	29.70	46.59	46.67
		2nd	159.8	154.8	161.2	156.2	181.5	176.0
		3rd	434.4	418.4	435.8	419.7	456.6	439.9
C	6	1st	27.61	27.69	29.14	29.22	46.14	46.20
		2nd	163.5	161.1	165.0	162.5	184.8	182.1
		3rd	450.4	442.9	451.8	444.5	472.2	464.2
	10	1st	28.07	28.21	29.60	29.73	46.58	46.69
		2nd	159.7	154.9	161.1	156.3	181.4	176.1
		3rd	434.1	418.6	435.6	420.0	456.3	440.1
D	6	1st	29.57	27.66	31.0	29.19	47.36	46.18
		2nd	175.5	161.0	176.8	162.4	195.5	182.0
		3rd	483.5	442.7	484.8	444.0	503.9	464.0
	10	1st	31.25	28.11	32.62	29.63	48.56	46.62
		2nd	179.7	154.6	181.0	156.0	199.28	175.7
		3rd	490.2	417.7	491.4	419.1	510.0	439.3
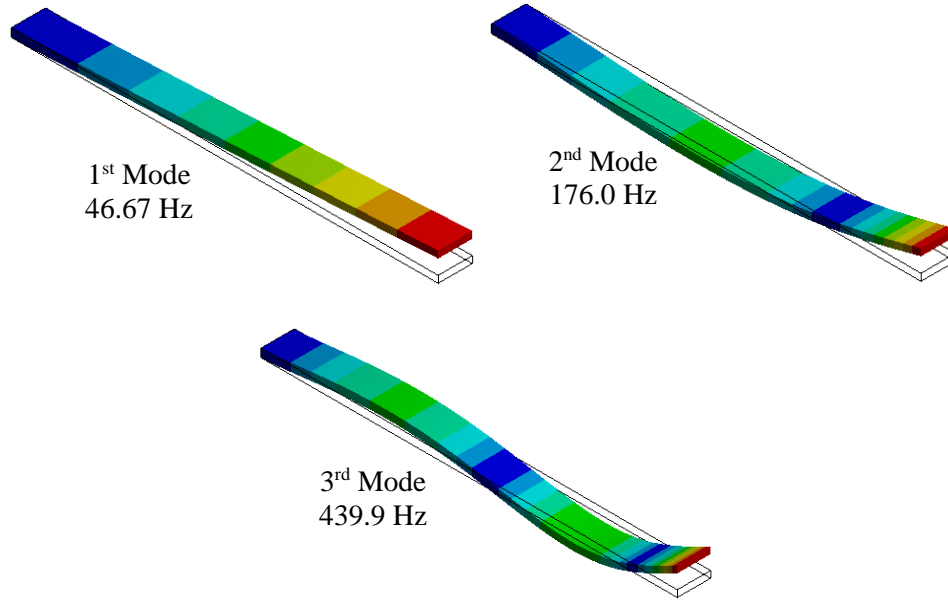
Figure 2.9 The first three out-of-plane bending vibration modes of rotating (200 rad/s) thickness-tapered cantilever composite beam ($[90]_{18s}$) with Configuration-B
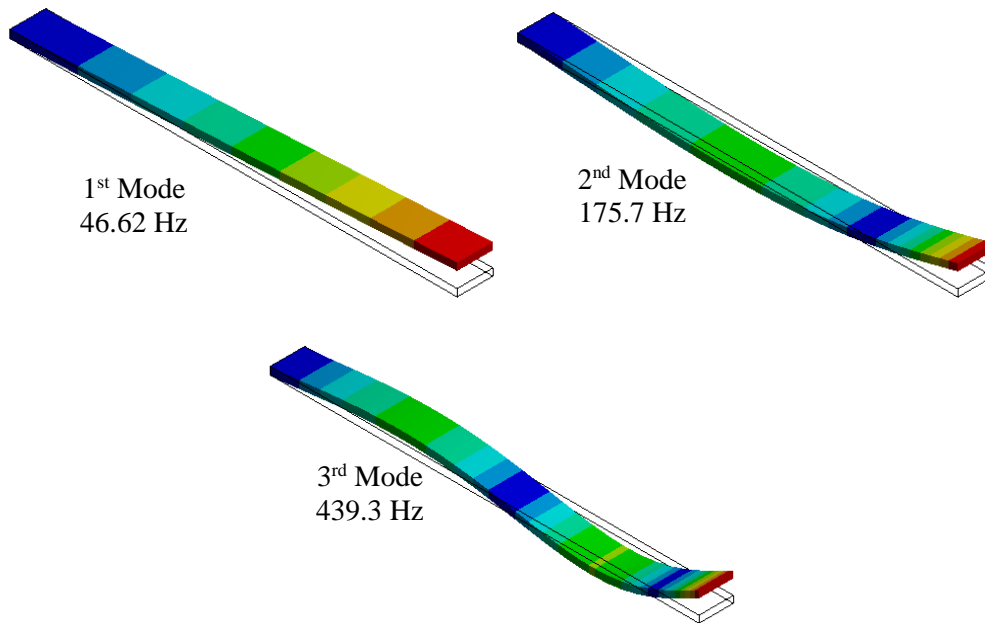
Figure 2.10 The first three out-of-plane bending vibration modes of rotating (200 rad/s) thickness-tapered cantilever composite beam ($[90]_{18s}$) with Configuration-D

2.5.4 Validation step-3: Doubly-tapered rotating cantilever composite beam

In the last validation step, width-tapering is included in beam geometry along with the thickness-tapering. Results for beam with 18 ply drop-off have been compared with ANSYS for different values of width-ratio and for different thickness-taper configurations. The length of the clamped-free beam is 25 cm and width at fixed side is 2 cm. Stacking sequence is $[90]_{18s}$. Rotational velocity is 200 rad/s. In Tables 2.11 and 2.12, '0 rad/s' as rotational velocity is describing the non-rotating condition. Unit width-ratio ($r_b = 1$) and '0' drop-off ply are describing the uniform-width and uniform-thickness in the beam, respectively. Table 2.11 compares the results for taper Configuration-A and Table 2.12 compares the results for the other three configurations. One fact to be noted is that up to 2 ply drop-off, all configurations are same as Configuration-A and number of ply drop-off in Configuration-D cannot be more than half of total plies. Both Tables 2.11 and 2.12 show that first three natural frequencies increase as the width-ratio decreases. For any specific width-ratio, second and third natural frequencies decrease as the thickness-tapering increases while the first natural frequency increases with thickness-tapering. For both tables, number of terms in approximate shape function is 8.

Table 2.11 Natural frequencies (Hz) of doubly-tapered rotating cantilever composite beam for Configuration-A

No. of ply drop-off, S			0				18			
Configura-tion	r_b	Mode	R-R	ANSYS	R-R	ANSYS	R-R	ANSYS	R-R	ANSYS
			$\Omega = 0$ rad/s		$\Omega = 200$ rad/s		$\Omega = 0$ rad/s		$\Omega = 200$ rad/s	
A	0.1	1st	46.75	46.62	60.09	59.98	49.99	49.82	63.41	63.27
		2nd	210.2	209.6	222.7	222.1	180.9	180.3	194.8	194.2
		3rd	524.7	523.3	536.8	535.5	420.2	419.2	433.8	432.9
	0.5	1st	33.23	33.15	49.85	49.80	35.94	35.83	52.53	52.44
		2nd	181.1	180.8	198.4	198.1	155.3	154.9	173.9	173.6
		3rd	486.8	486.4	504.1	503.7	388.1	387.9	406.9	406.7
	1.0	1st	27.08	27.02	45.62	45.58	29.66	29.56	48.00	47.92
		2nd	169.7	169.5	190.4	190.2	145.5	145.3	167.3	167.1
		3rd	475.3	476.2	496.4	497.3	377.8	378.5	400.0	400.7

Table 2.12 Natural frequencies (Hz) of doubly-tapered rotating cantilever composite beam for Configurations B, C and D

Number of ply drop-off, S			18			
Configuration	Width ratio, r_b	Mode	R-R Solution	ANSYS	R-R Solution	ANSYS
			$\Omega = 0$ rad/s		$\Omega = 200$ rad/s	
B	0.1	1st	49.57	49.25	63.04	62.85
		2nd	187.0	175.6	201.2	189.6
		3rd	440.9	406.4	455.0	420.1
	0.5	1st	35.13	35.65	51.90	52.36
		2nd	160.5	150.9	180.1	169.5
		3rd	408.2	375.7	427.9	394.3
	1.0	1st	28.86	29.44	47.40	47.88
		2nd	150.5	141.4	173.5	163.1
		3rd	397.5	366.4	421.1	388.4
C	0.1	1st	49.50	49.44	63.00	63.01
		2nd	186.1	176.0	200.4	190.0
		3rd	438.4	407.3	452.6	421.0
	0.5	1st	35.07	35.78	51.88	52.46
		2nd	159.8	151.3	179.4	169.9
		3rd	405.9	376.5	425.7	395.2
	1.0	1st	28.82	29.55	47.39	48.00
		2nd	149.8	141.8	172.9	163.4
		3rd	395.4	367.3	419.0	389.2
D	0.1	1st	49.18	48.72	62.53	62.41
		2nd	194.8	174.2	208.4	188.3
		3rd	468.1	403.7	481.5	417.5
	0.5	1st	34.88	35.29	51.52	52.09
		2nd	167.4	149.8	186.2	168.5
		3rd	433.7	373.2	452.5	391.9
	1.0	1st	28.59	29.11	47.05	47.65
		2nd	156.9	140.4	179.0	162.2
		3rd	422.8	363.8	445.4	386.0

Figures 2.11 and 2.12 show the mode shapes for taper Configuration-A with width-ratio 0.5 and for taper Configuration-C with width-ratio 0.1, respectively. Both beams are rotating at 200 rad/s with 18 drop-off ply. From Tables 2.11 and 2.12, it can be stated that results from R-R method have very good agreement with ANSYS results, which offers further analysis to study the influence of different parameters (related to beam's geometry and composite configuration) on natural frequency.
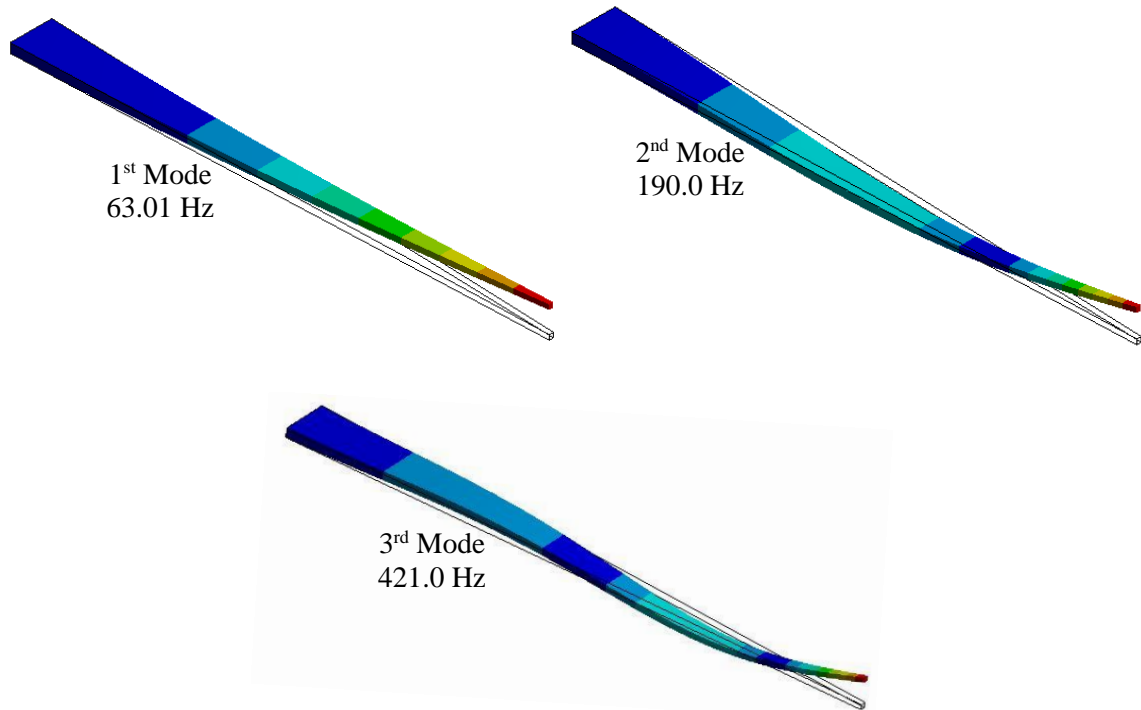
Figure 2.11 The first three out-of-plane bending vibration modes of doubly-tapered ($S = 18, r_b = 0.1$) rotating (200 rad/s) cantilever composite beam ($[90]_{18s}$) with Configuration-C
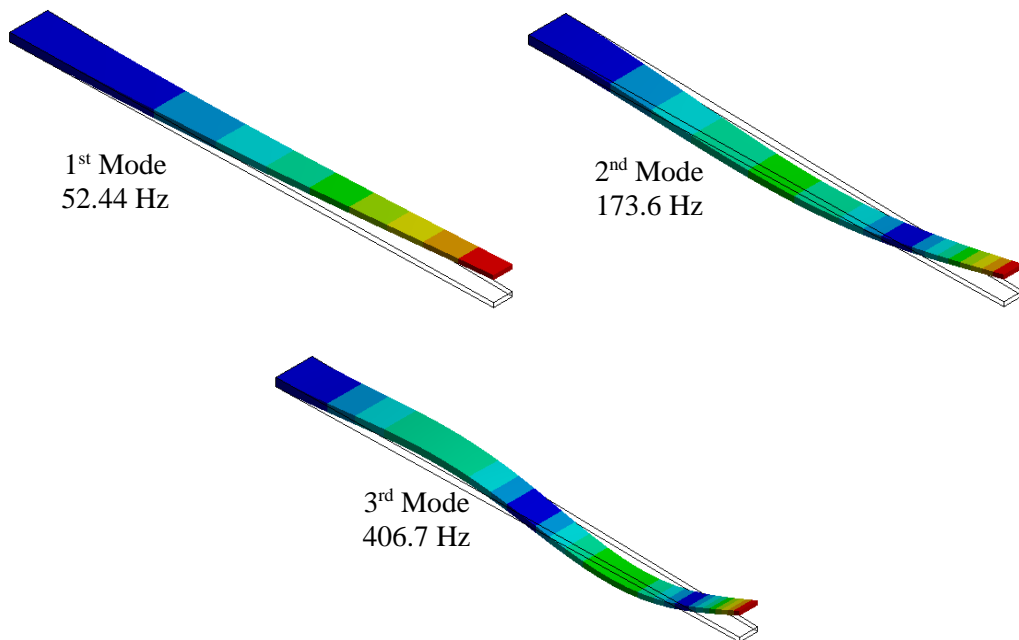
Figure 2.12 The first three out-of-plane bending vibration modes of doubly-tapered ($S = 18, r_b = 0.5$) rotating (200 rad/s) cantilever composite beam ($[90]_{18s}$) with Configuration-A

2.6 Mode shapes determination

Having the eigenvectors obtained from equation (2.38), one can have the mode shapes of doubly-tapered cantilever laminated composite beams. From Figures 2.13 to 2.15, first three mode shapes of non-rotating and rotating (200 rad/s) doubly-tapered ($S = 18, r_b = 0.1$) cantilever laminated composite beams (Configuration-A) are compared with non-rotating and rotating (200 rad/s) uniform cantilever composite beams. The length of the clamped-free beam is 25 cm, width at fixed side is 2 cm and hub radius is .025 m. Stacking sequence is $[90]_{18s}$. It shows, that except for the first mode of the uniform beam, mode shapes are same for non-rotating and rotating conditions. Also, one can observe that for the first and second modes, maximum displacement of the uniform beam is higher than that of the doubly-tapered beam and for the third mode doubly-tapered beam has higher maximum displacement than that of the uniform beam. In Figures 2.13 to 2.15, bold solid straight lines represent the neutral position of the beam.
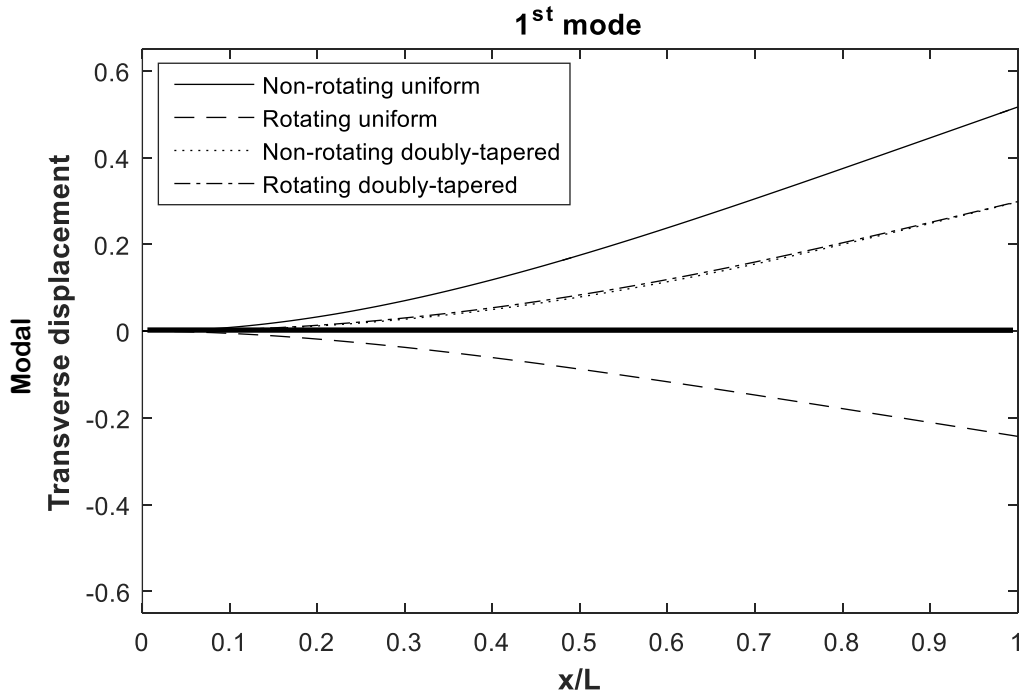
Figure 2.13 First mode shape of uniform and doubly-tapered cantilever composite beams for non-rotating and rotating conditions

35
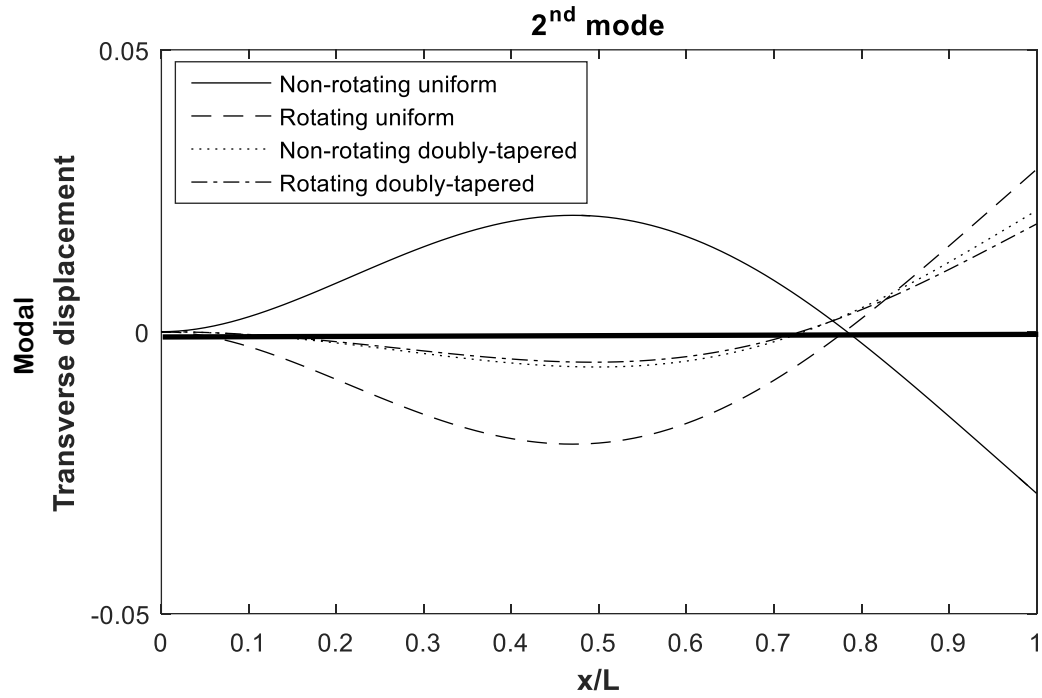
Figure 2.14 Second mode shape of uniform and doubly-tapered cantilever composite beams for non-rotating and rotating conditions
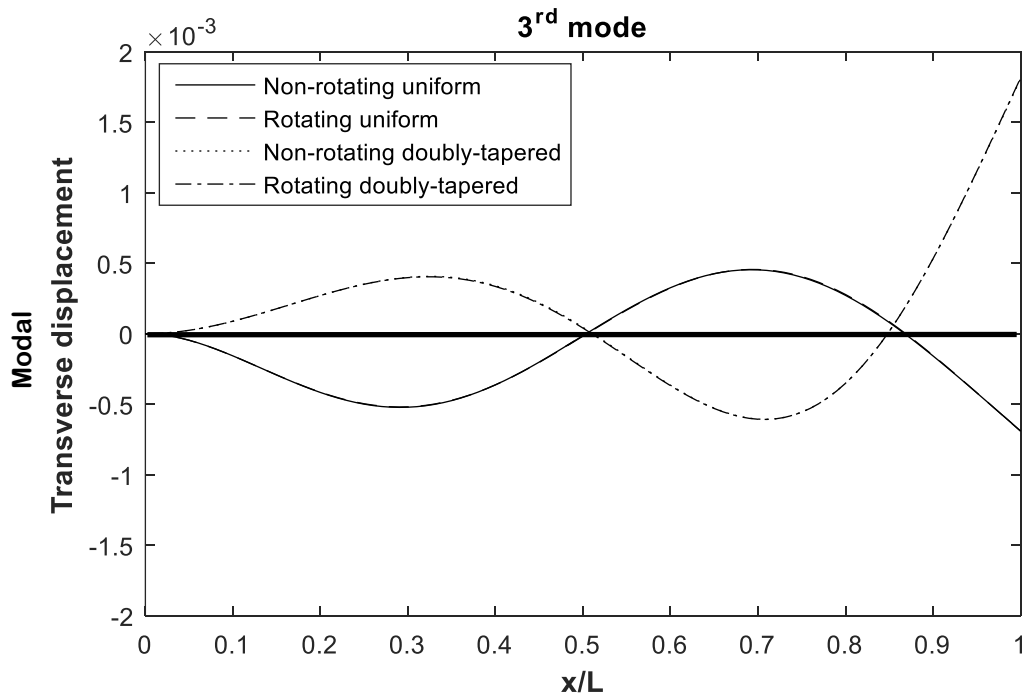
Figure 2.15 Third mode shape of uniform and doubly-tapered cantilever composite beams for non-rotating and rotating conditions

Figure 2.16 illustrates the mode shapes for rotating (200 rad/s) doubly-tapered cantilever laminated composite beam considering different taper configurations. It shows that for first three modes, maximum displacement for Configuration-D is highest and maximum displacement for Configuration-C is the lowest among all the configurations considered. In Figure 2.16, bold solid straight line represents the neutral position of the beam.
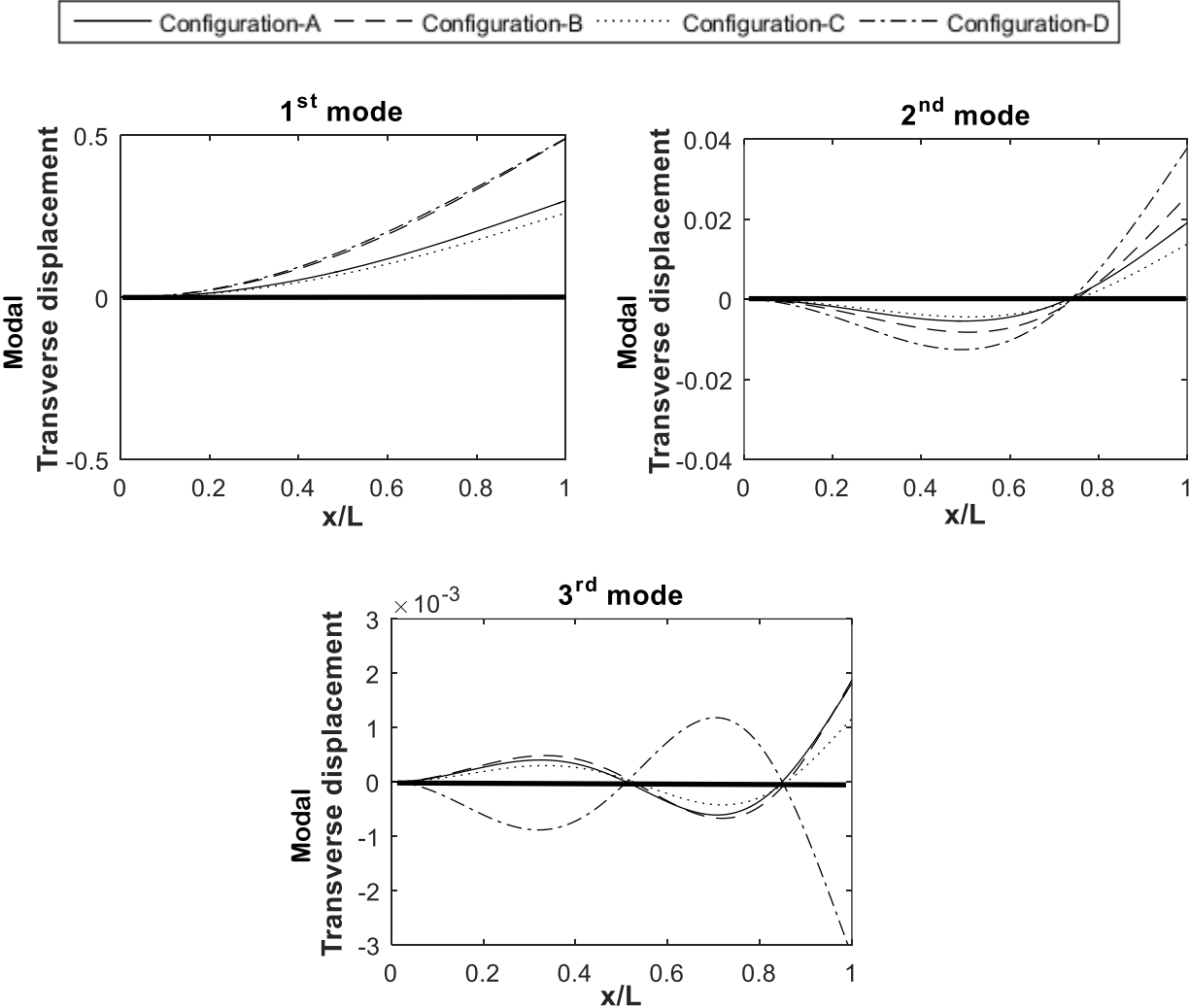
Figure 2.16 First three mode shapes of rotating doubly-tapered cantilever composite beams for different taper configurations

2.7   Free vibration analysis

Natural frequencies of free vibration for doubly-tapered cantilever rotating laminated composite beam are influenced by different parameters associated with the geometry of the beam and the rotational velocity. Different graphs can be plotted to understand the behavior of natural frequency with respect to different parameters. Mechanical properties of materials used to do the analysis are given in Tables 2.1 and 2.2.

2.7.1   Effect of rotational velocity

To understand the influence of rotational velocity on natural frequencies, five different types of beams are considered where one has uniform-thickness and uniform-width, and four others are doubly-tapered ($S = 18, r_b = 0.1$) beams with four different configurations. All the beams have same length. One end of 25 cm long beam is mounted on a hub of radius 0.025 m and the other end is free. The beam width is 2 cm at fixed side. Stacking sequence of the laminated beam is $[90]_{18s}$ at fixed side.

Figures 2.17 to 2.19 show the variation of first three natural frequencies of 5 selected beams for various rotational velocities. It can be stated from the Figures 2.17 to 2.19 that natural frequencies for all the selected beams increase as the rotational velocity increases. Figure 2.17 for first natural frequency shows that doubly-tapered beams with any configuration have much higher natural frequency than uniform-thickness and uniform-width composite beam. Also, it can be stated that taper Configuration-A has the highest natural frequency of the first mode in both non-rotating and rotating conditions. Figures 2.18 and 2.19 for second and third natural frequencies, respectively, show uniform beam has the highest natural frequency at high rotational velocity wherein for third natural frequency uniform beam has highest natural frequency in both rotating and non-rotating conditions.
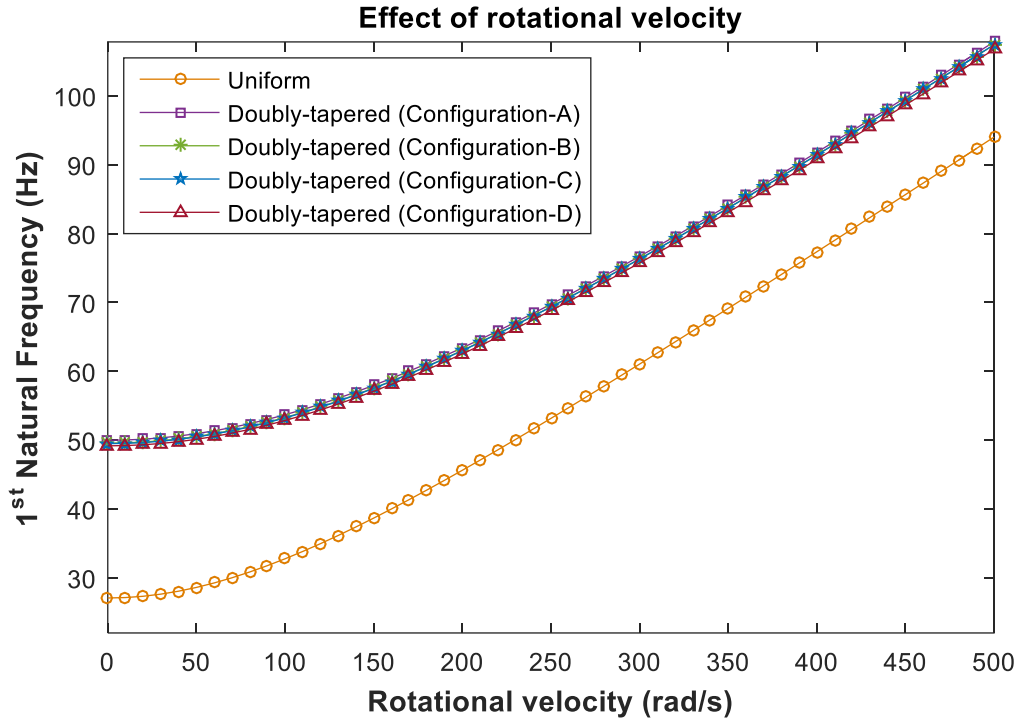
Figure 2.17 Effect of rotational velocity on first natural frequency
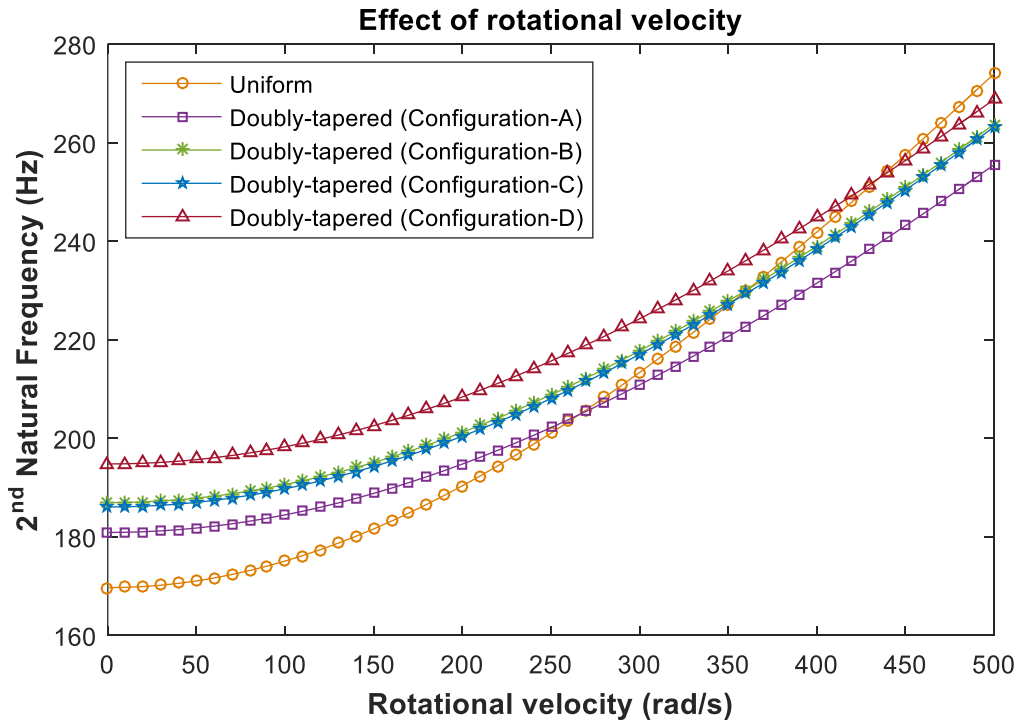
Figure 2.18 Effect of rotational velocity on second natural frequency
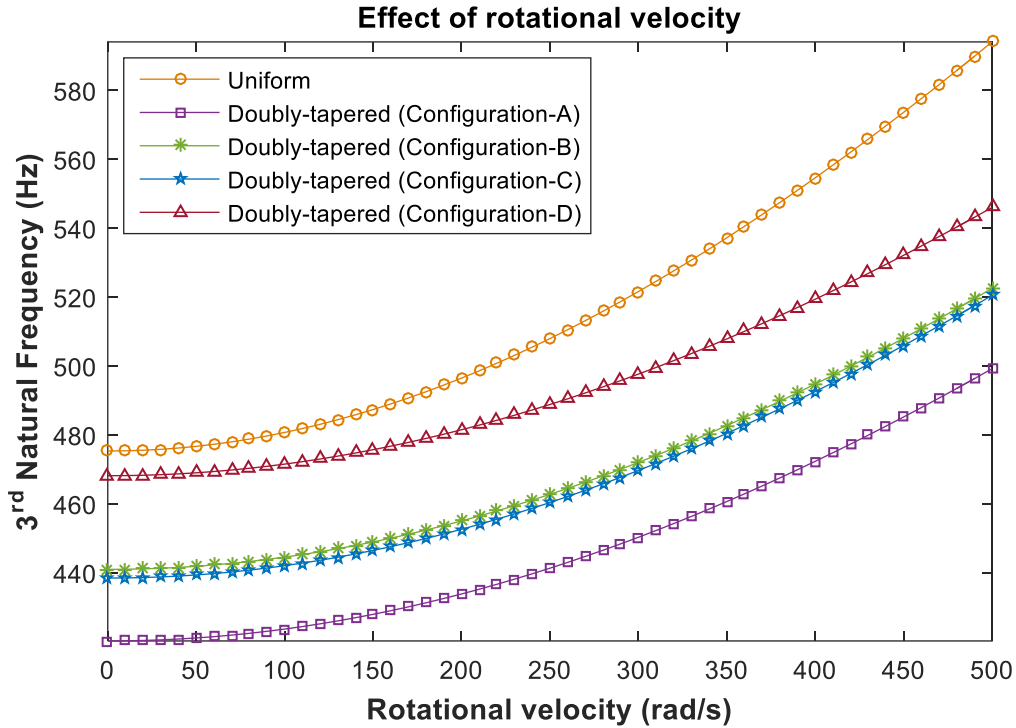
Figure 2.19 Effect of rotational velocity on third natural frequency

2.7.2 Effect of hub radius to beam length ratio

Figures 2.20 to 2.22 show the behavior of natural frequencies with respect to different values of hub radius to beam length ratio (R/L). This analysis is conducted on a doubly-tapered ($S = 18, r_b = 0.1$) rotating beam which has same length, same stacking sequence, same width at fixed side and same boundary condition as that of previous analysis discussed in section 2.7.1. The variation of first three natural frequencies is shown for different hub radius. The hub is constantly rotating at 200 rad/s. Four different taper configurations are considered for this analysis.

From Figures 2.20 to 2.22 it can be understood that natural frequencies increase with increase of hub radius to beam length ratio. For the first natural frequency, Configuration-A is giving the highest value while Configuration-D gives the highest value for the second and third natural frequencies.
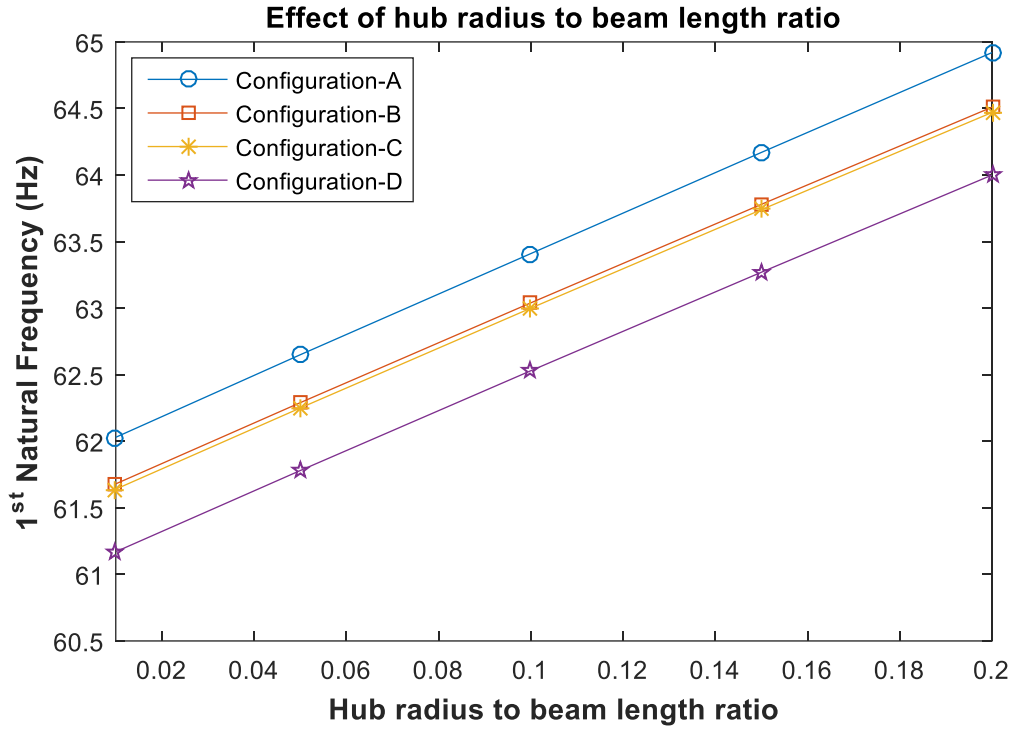
Figure 2.20 Effect of hub radius to beam length ratio on first natural frequency
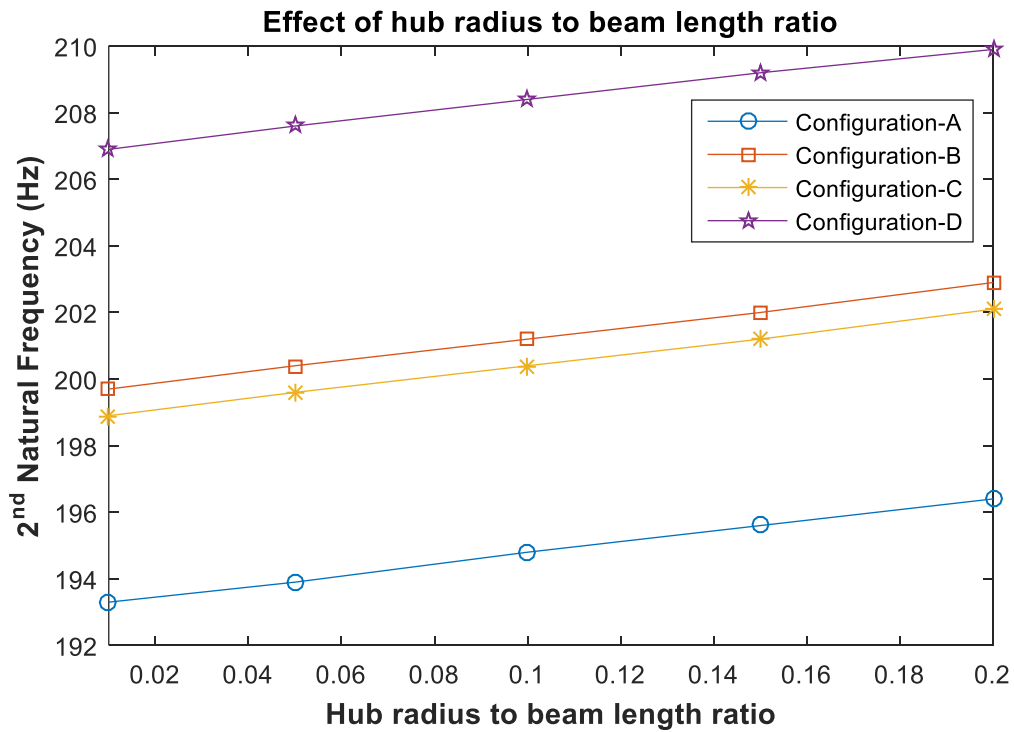
Figure 2.21 Effect of hub radius to beam length ratio on second natural frequency
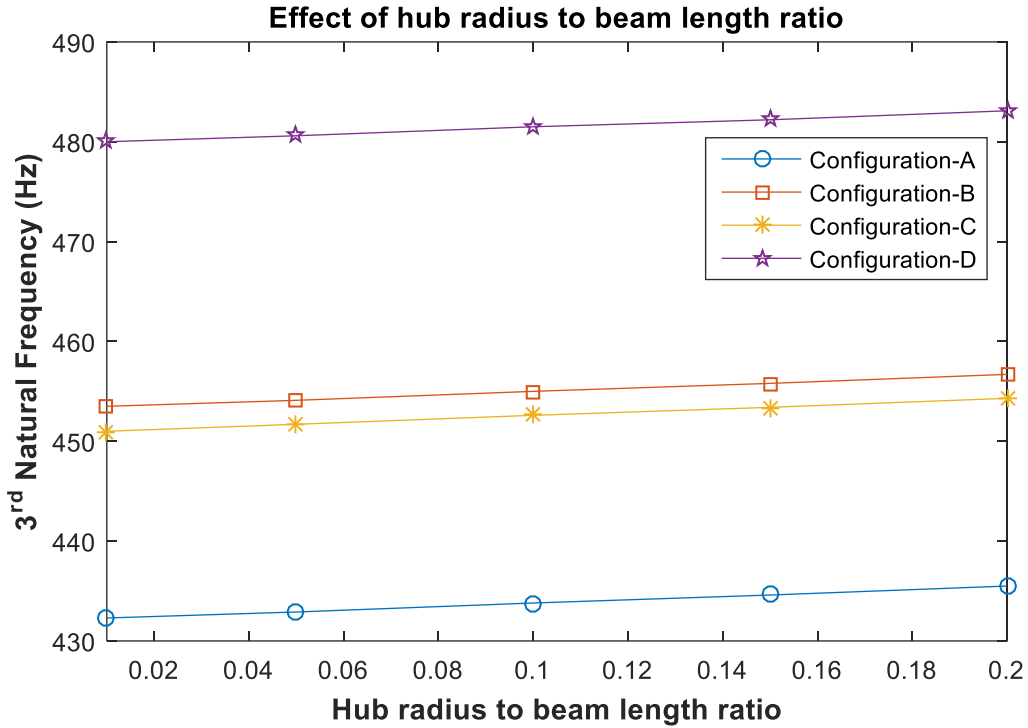
Figure 2.22 Effect of hub radius to beam length ratio on third natural frequency

2.7.3 Effect of ply drop-off (thickness-tapering)

Thickness-tapering in composite laminate can provide variable stiffness through the length of the beam. Also, the thickness that is gradually decreasing towards the tip gives better design to handle the aerodynamic load. Following Figures 2.23 to 2.25 show the variation of the first three natural frequencies of a thickness-tapered-and-uniform-width rotating composite beam with respect to number of ply drop-off. The relation between the number of ply drop-off and thickness taper angle is given by equation (2.41). The beam length, stacking sequence at fixed side, beam width at fixed side and boundary condition are taken as that of previous analysis discussed in section 2.7.2. In this case, the width - ratio is 1 (uniform-width). Hub radius is 0.025 m, which is rotating at 200 rad/s. The variation is plotted for 0 to 30 ply drop-off.

42

From Figures 2.23 to 2.25 for first three natural frequencies, one can observe that Configuration-D has highest natural frequency as long as the ratio between overall stiffness to mass of plies increases. Overall stiffness of composite laminate of Configuration-D starts to decrease after 12 ply drop-off as the resin pocket, takes place near to the outer surface of the laminate. Number of ply drop-off in Configuration-D is limited to half of the total number of plies. Figure 2.23 depicts that first natural frequency of Configuration-A, B and C increase with number of ply drop-off, but Figures 2.24 and 2.25 for second and third natural frequencies, respectively, for Configuration-A, B and C show that natural frequencies decrease as the number of ply drop-off increases.
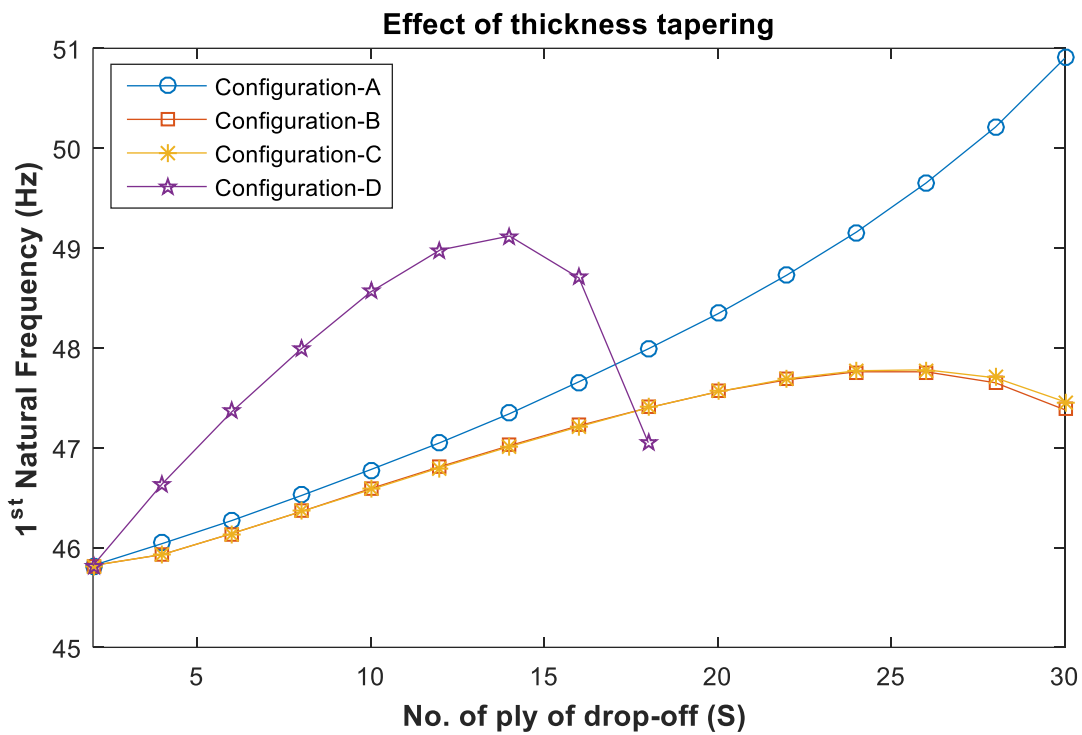
Figure 2.23 Effect of thickness tapering on first natural frequency
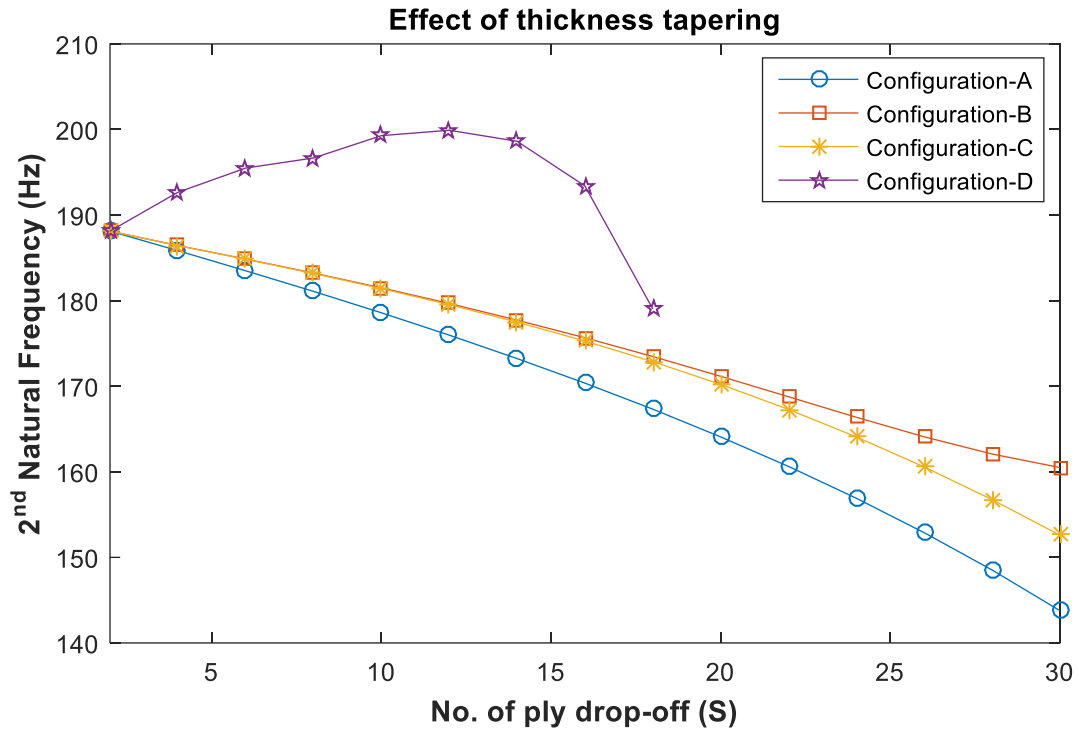
Figure 2.24 Effect of thickness tapering on second natural frequency
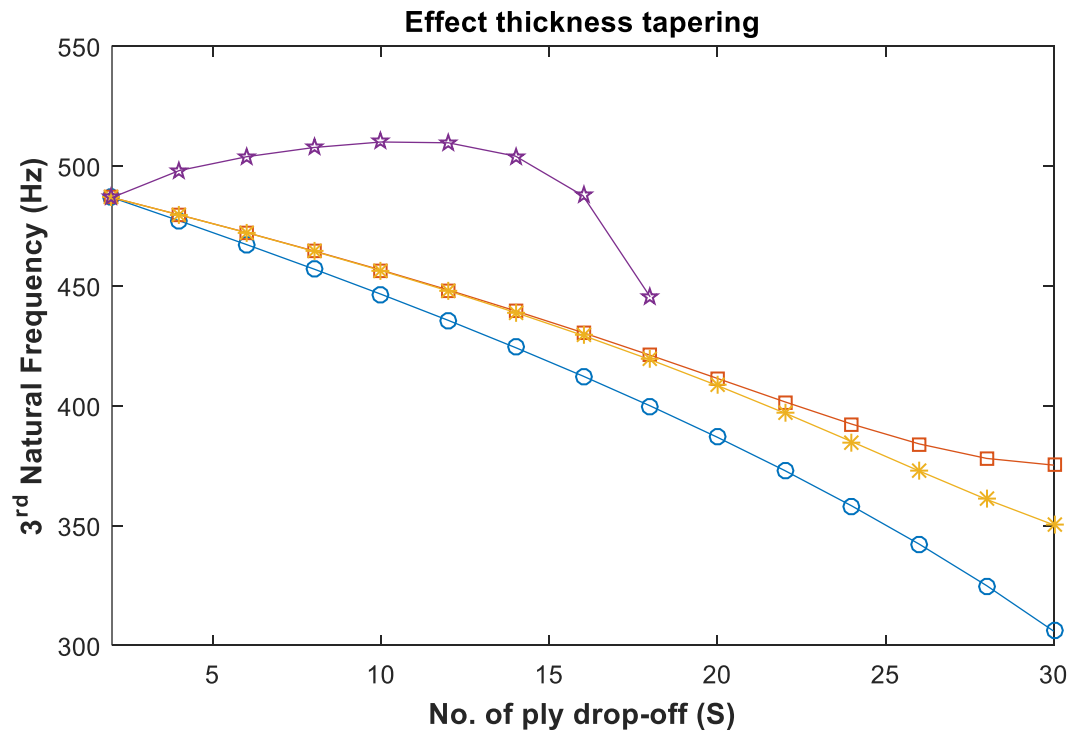
Figure 2.25 Effect of thickness tapering on third natural frequency

2.7.4 Effect of double-tapering

Double-tapering affects the natural frequency of rotating beam. Especially width-tapering can remove more material from the beam compared to thickness-tapering. This has an effect on the overall stiffness and mass of the beam. Following Figures 2.26 to 2.28 show the effect on natural frequencies due to double-tapering in a rotating composite beam. This beam has same length, stacking sequence, hub radius and rotational velocity as that of previous analysis for thickness tapering in section 2.7.3. The width of the beam is 2 cm on the fixed side. Figures 2.26 to 2.28 illustrate the variation of natural frequencies for double tapering in which, double-tapering is described as

$$Double\ taper\ ratio = \frac{S}{r_b} \tag{2.44}$$

where, r_b is width-ratio and S is number of ply drop-off. Number of ply drop-off and corresponding width-ratio used in Figures 2.26 to 2.28 are listed below:

Table 2.13 Number of ply drop-off and corresponding width-ratio to obtain double-taper ratio

Number of ply drop-off, S	Width-ratio, r_b	Double-taper ratio
2	0.9	2.222
4	0.8	5.000
6	0.7	8.571
8	0.6	13.33
10	0.5	20.00
12	0.4	30.00
14	0.3	46.67
16	0.2	80.00
18	0.1	180.0

Figure 2.26 shows that first natural frequency for all configurations increase as the double-tapering increases. Among all the taper configurations, Configuration-D has the highest value for first three natural frequencies. Figures 2.27 and 2.28 for second and third natural frequencies, respectively, indicate that natural frequencies for Configuration-D start to decrease after certain double-taper ratio, which is due to dominating effect of thickness-tapering on natural frequencies (see Figures 2.24 and 2.25). Also, from Figures 2.27 and 2.28, one can see that second and third natural frequencies for Configuration-A, B and C start to increase after certain double-taper ratio, which is due to dominating effect of width-tapering on natural frequencies. One can see from Tables 2.11 and 2.12 that width-tapering significantly increases the first three natural frequencies of out-of-plane bending vibration.
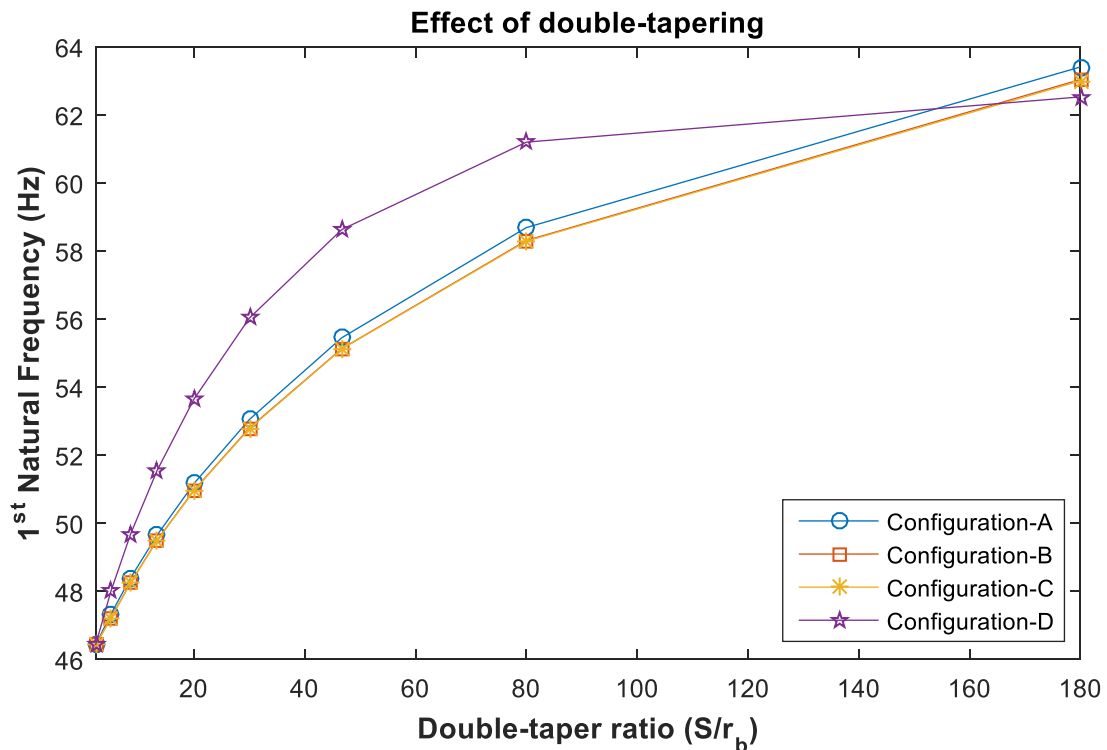
Figure 2.26 Effect of double-tapering on first natural frequency
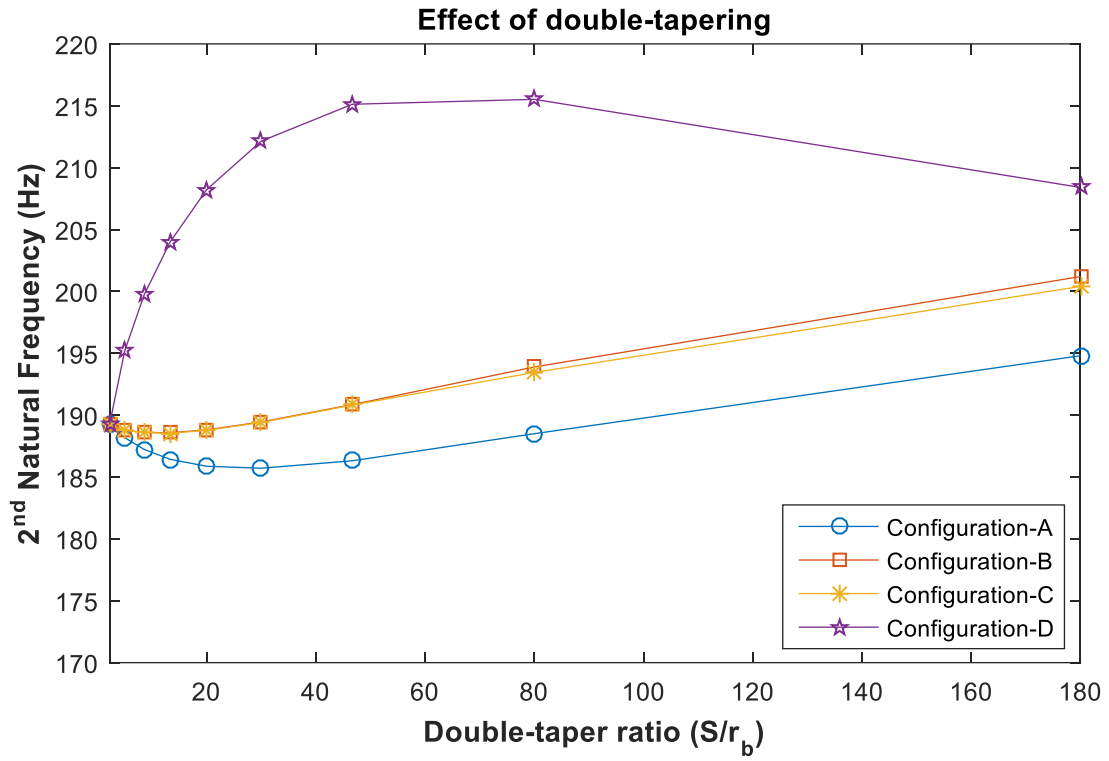
Figure 2.27 Effect of double-tapering in second natural frequency
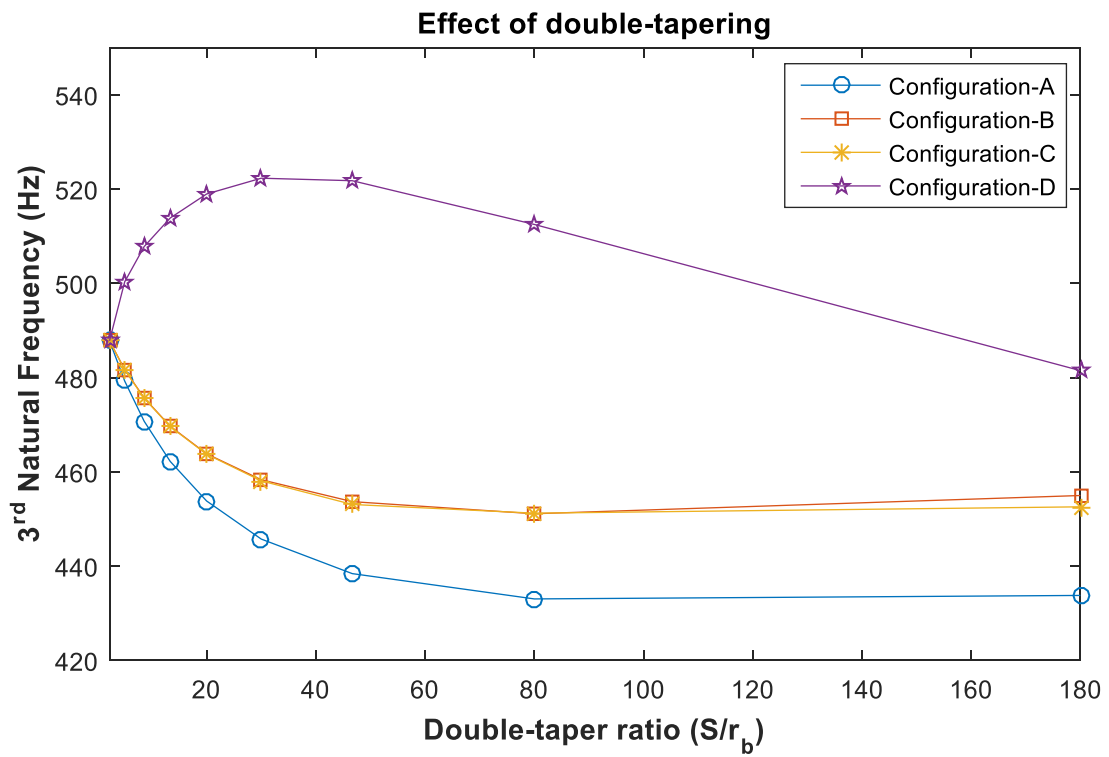
Figure 2.28 Effect of double-tapering in third natural frequency

47

2.8　Critical speed determination

Critical speed is a certain rotating speed that excites the natural frequency of a rotating structure, which can be a rotating blade, gear or shaft. At the critical speed, angular velocity of a rotating structure approaches the natural frequency and structure starts to resonate which exceedingly increases the vibration.

Campbell diagram is one of the methods to obtain the critical speed of a rotating object. Campbell diagram plot the natural frequency of the object for various rotating speeds, where the intersection of the natural frequency curve and forcing frequency line, is the critical speed. Forcing frequency is the frequency of a rotating part which is equal to the number of vanes/blades of the rotating part times the RPM. Besides the Campbell diagram, there is another method to determine the critical speed, which is called direct method. In the direct method, the critical speeds are taken when one of the natural frequencies at a specific speed is equal to the forcing frequency. The forcing frequency can be written in terms of rotating speed as [44]:

$$\omega_f = n\Omega \tag{2.45}$$

where, n is number of rotating blade. For example, in a four-bladed helicopter rotor $n = 4$.

To determine the critical speed using direct method, equation (2.36) can be written as:

$$[M]\{\ddot{q}\} + ([K] + \Omega^2[K^{*C}])\{q\} = \{0\} \tag{2.46}$$

where, $\Omega^2[K^{*C}]$ is stiffness matrix due to centrifugal action. The solution of the equation (2.46) can be assumed as:

$$\{q\} = \{Q_0\}e^{i\omega_f t} \tag{2.47}$$

Using equations (2.45), (2.46) and (2.47), one can get

$$([K] + \Omega^2([K^{*C}]) - n^2\Omega^2[M])\{Q_0\}e^{in\Omega t} = \{0\} \tag{2.48}$$

The above equation has a nontrivial solution if $|[K] + \Omega^2([K^C] - n^2[M]|$ becomes singular. As a result, the equation can be simplified as the generalized eigenvalue problem and takes the form as:

$$\Omega^2(n^2[M] - [K^{*C}])\{Q_0\} = [K]\{Q_0\} \tag{2.49}$$

The eigenvalues Ω are in complex form; the real part of Ω gives the critical speed.

2.8.1   Numerical results and Campbell diagram

To study the critical speed of doubly-tapered rotating cantilever composite beam, four different types of beams are taken as follows: 1) Uniform-thickness and Uniform-width (U-U), 2) Uniform-thickness and Width-taper (U-W), 3) Thickness-and-Width taper (doubly-tapered) (T-W) and 4) Thickness-taper and Uniform-width (T-U). All four beams are 25 cm in length, attached to a hub of radius 0.025 m and width is 2 cm at fixed side. For width-tapered beams (U-W and T-W), width-ratio is 0.1. For thickness-tapered beams (T-W and T-U) ply drop-off number is 18. All the beams have $[90]_{18s}$ stacking sequence. The Campbell diagram is drawn for first natural frequency to obtain the first critical speed.

In Figure 2.29 one can observe that thickness-and-width taper (doubly-tapered) beam has highest critical speed that means operating speed for doubly-tapered beam is higher than other types of beams. From Figure 2.29, it can also be stated that doubly-tapered beam with Configuration-A has the highest operating speed. Critical speeds obtained using the direct method and Campbell diagram are listed in Table 2.14.

In Figure 2.30, only beam with Configuration-A (T-W) is considered to understand the effect of stacking sequences in critical speed. It can be understood from the Campbell diagram and results from direct method (listed in Table 2.15) that stacking sequence with unidirectional ply ($[0]_{18s}$) has the highest critical speed and stacking sequence ($[90]_{18s}$) has the lowest critical speed.
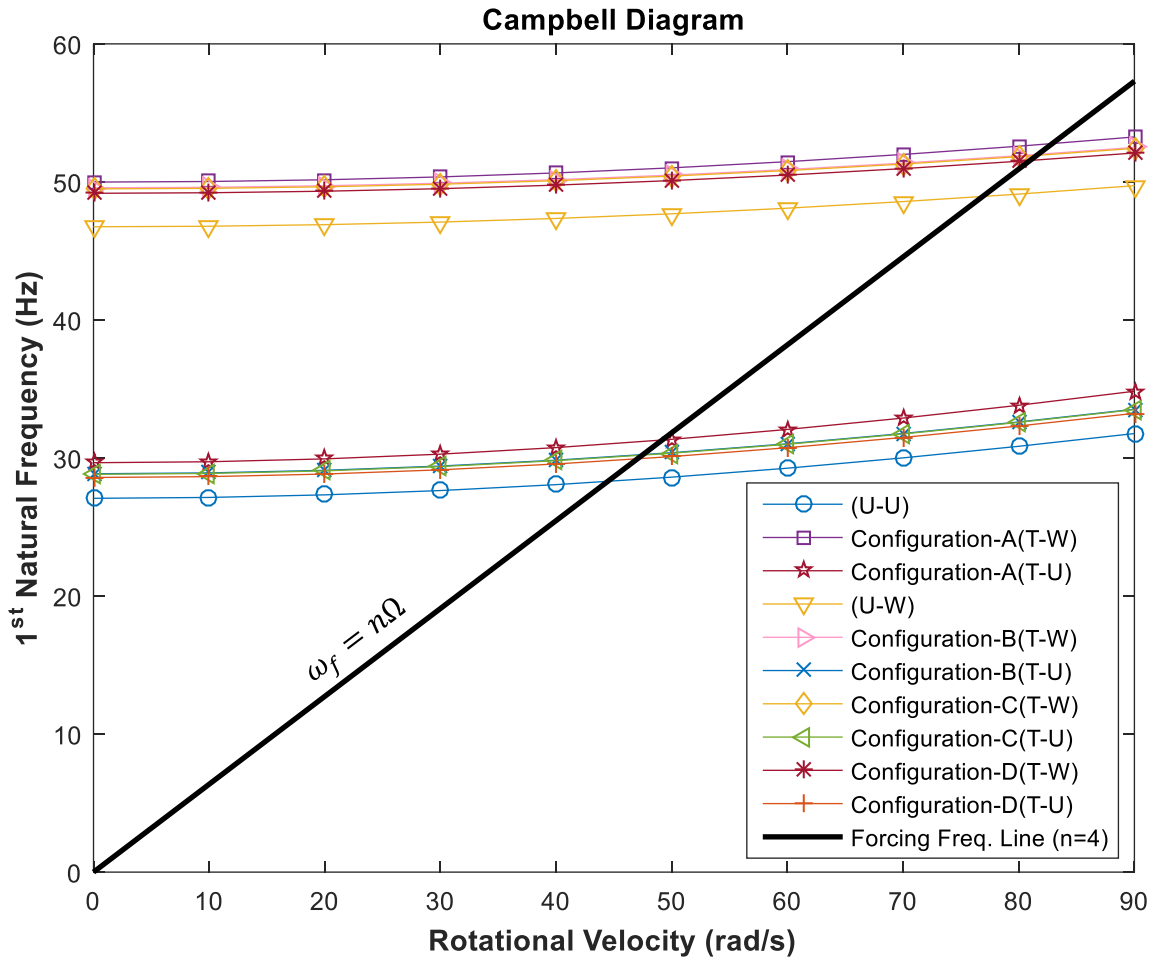
Figure 2.29 Critical speed determination using Campbell diagram

Table 2.14 Critical speeds (rad/s) obtained using different methods

Type of beam	Direct method	Campbell diagram
U-U	44.45	44.46
U-W	76.88	76.90
Configuration-A (T-W)	82.90	82.91
Configuration-A (T-U)	49.16	49.19
Configuration-B (T-W)	81.67	81.69
Configuration-B (T-U)	47.50	47.53
Configuration-C (T-W)	81.55	81.56
Configuration-C (T-U)	47.44	47.46
Configuration-D (T-W)	80.98	80.98
Configuration-D (T-U)	47.02	47.04
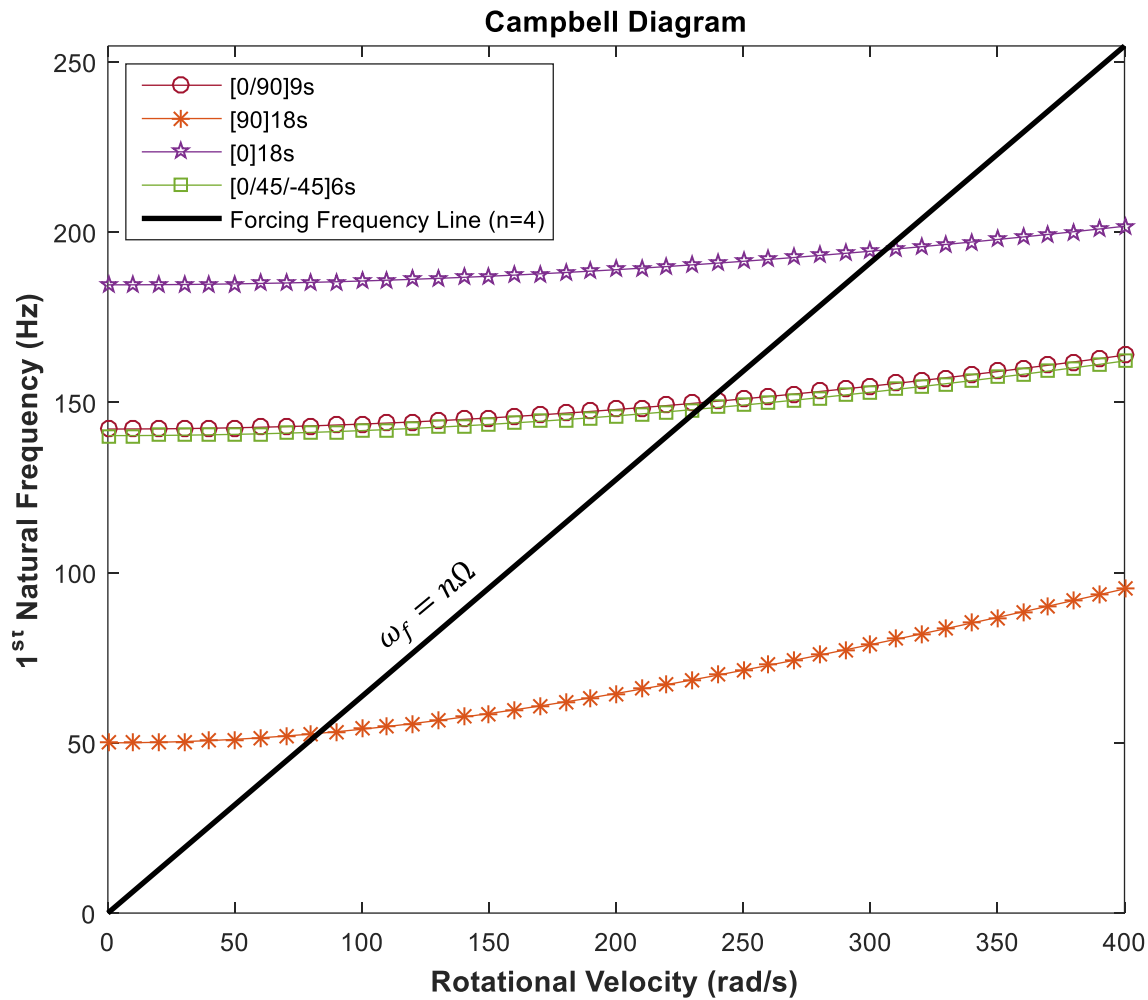
Figure 2.30 Campbell diagram for doubly-tapered beam with different stacking sequences

Table 2.15 Critical speeds (rad/s) for different stacking sequences

Stacking sequence	Direct method	Campbell diagram
$[0/90]_{9s}$	235.68	235.70
$[90]_{18s}$	82.900	82.910
$[0]_{18s}$	305.90	305.90
$[0/45/-45]_{6s}$	232.46	232.50

2.9   Dynamic instability analysis

A rotating structure can experience dynamic instability due to periodic rotational velocity. When a cantilever beam swings periodically, that is oscillating about the axis of rotation, the dynamic bending stiffness varies harmonically that causes transverse vibrations with gradually increasing amplitudes that are often called dynamic instability or parametric instability. This large amplitude vibration could damage the rotating structure. A cantilever beam with time-dependent rotary oscillation can be regarded as a parametric excitation system [31].

The periodic rotational velocity ($\Omega(t)$) can be employed in equation of motion instead of constant rotational velocity Ω. In equation (2.36), square of constant rotational velocity is multiplied with all the coefficients of stiffness matrix $[K^C]$ that is due to centrifugal action. Introducing periodic rotational velocity in equation (2.36) leads to:

$$[M]\{\ddot{q}\} + ([K] + \Omega^2(t)[K^{*C}])\{q\} = \{0\} \tag{2.50}$$

where, $\Omega^2(t)[K^{*C}]$ is time dependent stiffness matrix due to centrifugal action.

If periodic rotational velocity is considered for the system, dynamic instability can be observed. The periodic rotational velocity can be written in terms of static and dynamic rotational terms and parametric resonance frequency.

$$\Omega(t) = \Omega_0 + \Omega_1 sin\theta_p t \tag{2.51}$$

Here, Ω_0 is mean or static value of periodic rotational velocity, Ω_1 is amplitude of periodic rotational velocity, θ_p is parametric resonance frequency and t is time. The amplitude of periodic rotational velocity (Ω_1) can be defined by a measure of the mean value of rotational velocity (Ω_0) as:

$$\Omega_1 = \beta \, \Omega_0 \tag{2.52}$$

where, β is amplitude factor. Therefore, periodic rotational velocity can be expressed as:

52

$$\Omega(t) = \Omega_0 + \beta\,\Omega_0 sin\theta_p t \tag{2.53}$$

Substituting $\Omega(t)$ in equation (2.50) one can get:

$$[M]\{\ddot{q}\} + \left([K] + \left(\Omega_0{}^2 + 2\Omega_0{}^2\beta sin\theta_p t + \frac{\Omega_0{}^2\beta^2}{2}(1 - cos2\theta_p t)\right)[K^{*C}]\right)\{q\} = 0 \tag{2.54}$$

This is a Mathieu type equation that can describe the instability behavior of a rotating beam with a periodic rotational load. Dynamic instability occurs only within certain regions on the resonance frequency-driving amplitude plane. The boundaries of the regions of instability on this plane represent periodic solutions of the equations of motion. Dynamic instability region separated from stable region by periodic solutions with period $T = \frac{2\pi}{\theta_p}$ and $2T = \frac{4\pi}{\theta_p}$. The solutions with period $2T$ are of greater practical importance as the widths of these unstable regions are usually larger than those associated with the solutions having period of T [32].

To find the periodic solution with period $2T$, Bolotin's first approximation [31] can be considered. The periodic solutions with period $2T$ can be sought in the form:

$$\{q\} = \sum_{r=1,3,5\dots}^{\infty} \left[\{a_r\} sin\left(\frac{r\theta_p t}{2}\right) + \{b_r\} cos\left(\frac{r\theta_p t}{2}\right)\right] \tag{2.55}$$

Taking one-term solution and differentiating two times with respect to time t,

$$\{\ddot{q}\} = \left[-\frac{\theta_p{}^2}{4}\{a_1\} sin\left(\frac{\theta_p t}{2}\right) - \frac{\theta_p{}^2}{4}\{b_1\} cos\left(\frac{\theta_p t}{2}\right)\right] \tag{2.56}$$

After substituting $\{q\}$ and $\{\ddot{q}\}$ in equation (2.55) and simplifying through trigonometric formula (see Appendix B) and finally comparing the coefficients of $sin\left(\frac{\theta_p t}{2}\right)$ and $cos\left(\frac{\theta_p t}{2}\right)$ in the governing equation, two equations can be found:

For $sin\left(\frac{\theta_p t}{2}\right)$:

$$-\frac{\theta_p{}^2}{4}[M]\{a_1\} + [K]\{a_1\} + [K^{*C}]\Omega_0{}^2\{a_1\} + [K^{*C}]\Omega_0{}^2\beta\{b_1\} + \frac{\Omega_0{}^2\beta^2}{2}[K^{*C}]\{a_1\} = 0 \tag{2.57}$$

53

For $\cos\left(\frac{\theta_p t}{2}\right)$:

$$-\frac{\theta_p{}^2}{4}[M]\{b_1\} + [K]\{b\}_1 + [K^{*C}]\Omega_0{}^2\{b_1\} + [K^{*C}]\Omega_0{}^2\beta\{a_1\} + \frac{\Omega_0{}^2\beta^2}{2}[K^{*C}]\{b_1\} = 0 \qquad (2.58)$$

Equations (2.58) and (2.59) can be written in the matrix form as

$$\begin{bmatrix} -\frac{\theta_p{}^2}{4}[M] + [K] + [K^{*C}]\Omega_0{}^2 + \frac{\Omega_0{}^2\beta^2}{2}[K^C] & [K^{*C}]\Omega_0{}^2\beta \\ [K^{*C}]\Omega_0{}^2\beta & -\frac{\theta_p{}^2}{4}[M] + [K] + [K^{*C}]\Omega_0{}^2 + \frac{\Omega_0{}^2\beta^2}{2}[K^{*C}] \end{bmatrix}\begin{bmatrix}\{a_1\} \\ \{b_1\}\end{bmatrix} = \{0\}$$

$$(2.59)$$

For non-trivial solution determinant of the matrix coefficients must be zero.

$$det\begin{bmatrix} -\frac{\theta_p{}^2}{4}[M] + [K] + [K^{*C}]\Omega_0{}^2 + \frac{\Omega_0{}^2\beta^2}{2}[K^{*C}] & [K^{*C}]\Omega_0{}^2\beta \\ [K^{*C}]\Omega_0{}^2\beta & -\frac{\theta_p{}^2}{4}[M] + [K] + [K^{*C}]\Omega_0{}^2 + \frac{\Omega_0{}^2\beta^2}{2}[K^{*C}] \end{bmatrix} = 0$$

$$(2.60)$$

After expanding the determinant and solving for $\theta_p{}^2$, two equations can be found as:

$$\theta_p{}^2 = (4[K^{*C}]\Omega_0{}^2 + 4[K^{*C}]\Omega_0{}^2\beta + 2[K^{*C}]\Omega_0{}^2\beta^2 + 4[K])/[M] \qquad (2.61)$$

and $\qquad \theta_p{}^2 = (4[K^{*C}]\Omega_0{}^2 - 4[K^{*C}]\Omega_0{}^2\beta + 2[K^{*C}]\Omega_0{}^2\beta^2 + 4[K])/[M] \qquad (2.62)$

Equations (2.61) and (2.62) can be solved as eigenvalue problems where each eigenvalue $\theta_p{}^2$ is the square of parametric resonance frequency which gives the boundary between stable and unstable regions in resonance frequency-driving amplitude plane. Equations (2.61) and (2.62) give upper and lower boundaries of the instability region, respectively.

2.9.1 Validation

To investigate the accuracy of above formulation a graph has been plotted using MATLAB to find the instability region where the upper and lower boundaries are determined from the eigenvalues of equations (2.61) and (2.62), respectively. In this graph vertical axis represents the

parametric ratio $(\frac{\theta_p}{2\omega_i})$ which is the resonance frequency of the parametric exciting system divided by doubled fundamental frequency of free vibration. Subscript 'i' is mode number. The horizontal axis represents the amplitude of the periodic rotational velocity.

Figures 2.31, 2.33 and 2.34 show the instability regions for first three out-of-plane bending vibration modes for a doubly-tapered rotating cantilever composite beam with different taper configurations. The mean value of angular velocity is 50 rad/s. The beam is 25 cm long and has 2 cm width at fixed side and the width-ratio is 0.1. The hub radius is taken as 0.025 m. The ply thickness is 0.125 mm and stacking sequence is $[90]_{18s}$ with 18 ply drop-off. Mechanical properties chosen for composite and resin materials are given in Tables 2.1 and 2.2, respectively.

From Figures 2.31, 2.33 and 2.34, one can see that area inside the upper and lower boundary lines are unstable regions where the width of instability region increases with amplitude factor. If any parametric point $(\beta, \frac{\theta_p}{2\omega_i})$ of the structural system is in these unstable regions, the system becomes dynamically unstable. In order to verify such a statement, the modal response $q_i(t)$ of the beam can be determined for any parametric point using Mathieu-Hill equation (2.54). Modal response $q_i(t)$ should keep increasing with time when the beam is unstable. The Mathieu-Hill equation given in (2.54) can be converted to the first order matrix differential form as:

$$\begin{bmatrix} \{\ddot{q}\} \\ \{\dot{q}\} \end{bmatrix} = \begin{bmatrix} [0] & -[M]^{-1}[K^*] \\ [I] & [0] \end{bmatrix} \begin{bmatrix} \{\dot{q}\} \\ \{q\} \end{bmatrix} \tag{2.63}$$

where, $[K^*] = [K] + \left(\Omega_0{}^2 + 2\Omega_0{}^2 \beta sin\theta_p t + \frac{\Omega_0{}^2 \beta^2}{2}\left(1 - cos2\theta_p t\right) \right)[K^{*C}]$, and $[I]$ is $m \times m$ identity matrix. Setting $Y = \begin{bmatrix} \{\dot{q}\} \\ \{q\} \end{bmatrix}$ in equation (2.63), yields:

$$\dot{Y} = f(Y, t) \tag{2.64}$$

First order matrix differential equation (2.64) can be solved using fourth-order Runge-Kutta method [33, 45]. The solution gives the time response q_i for 1 to m modes.

In Figure 2.32, modal responses of three different points (P1, P2 and P3 shown in Figure 2.31) are given for first vibrational mode, where points P1($\theta_p = 653.96 \frac{rad}{s}, \beta = 0.4$), P3 ($\theta_p = 634.73 \frac{rad}{s}, \beta = 0.6$) are located in the stable region and P2($\theta_p = 644.35 \frac{rad}{s}, \beta = 0.5$) is located in unstable region for the doubly-tapered beam with Configuration-A. The modal response of points P1 and P2 are confined in a scope of about 0.02 m, while that of point P2 increases rapidly and exceeds 10 m in the same duration. Hence, the structural system corresponding to points P1 and P3 is dynamically stable, but that corresponding to point P2 is dynamically unstable. Also, it can be understood from Figures 2.31, 2.33 and 2.34, that beam with Configuration-D has smallest width of instability region among all the tapered configurations considered and Configuration-A has largest width of instability region.
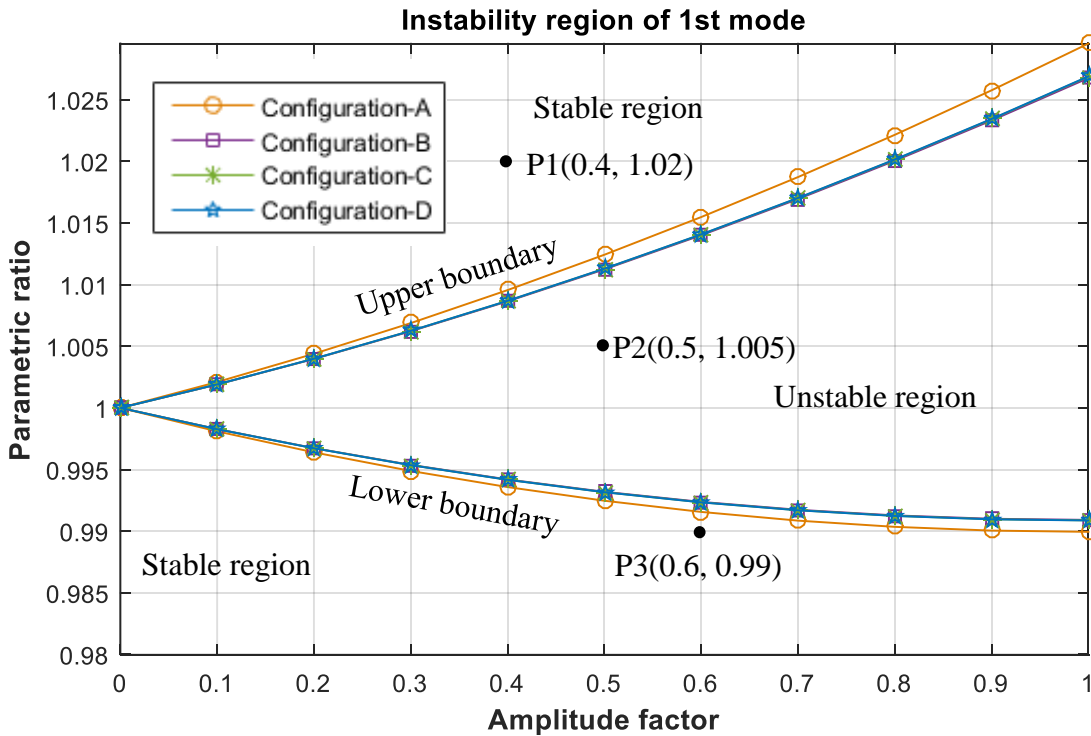
Figure 2.31 Instability region for first out-of-plane bending mode of doubly-tapered beam
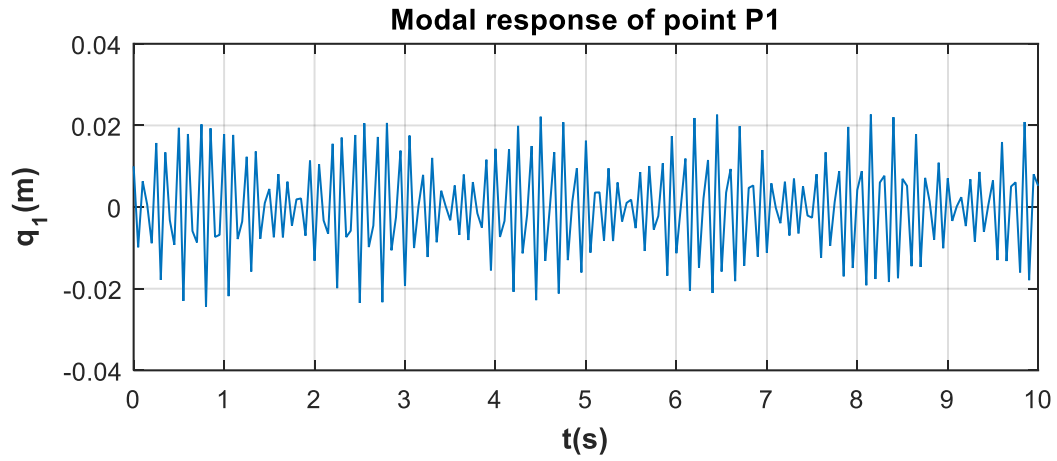
a) Point P1
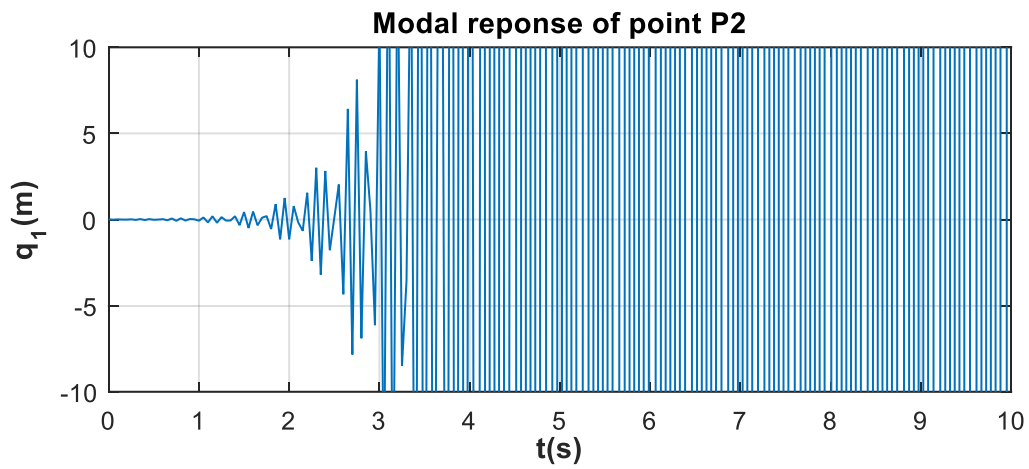
b) Point P2
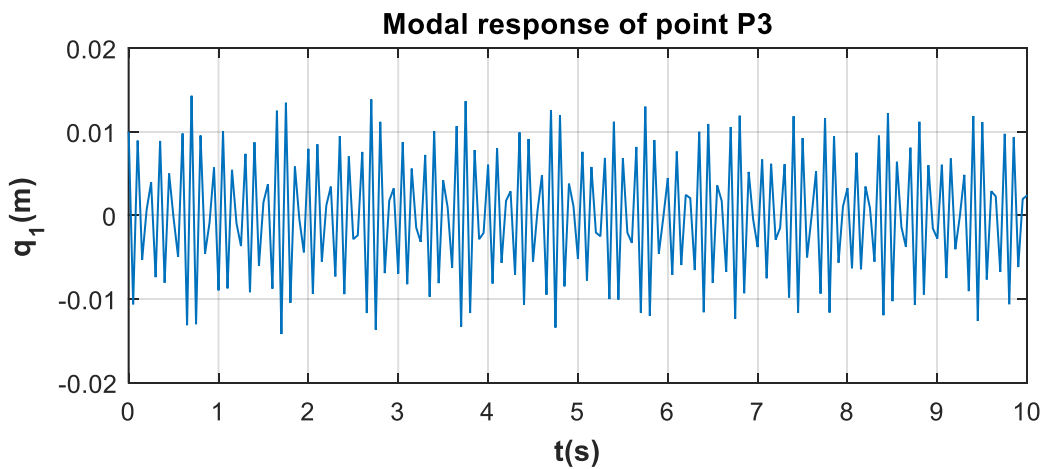
c) Point P3

Figure 2.32 Modal response $q_1(t)$ for the parametric points P1, P2 and P3
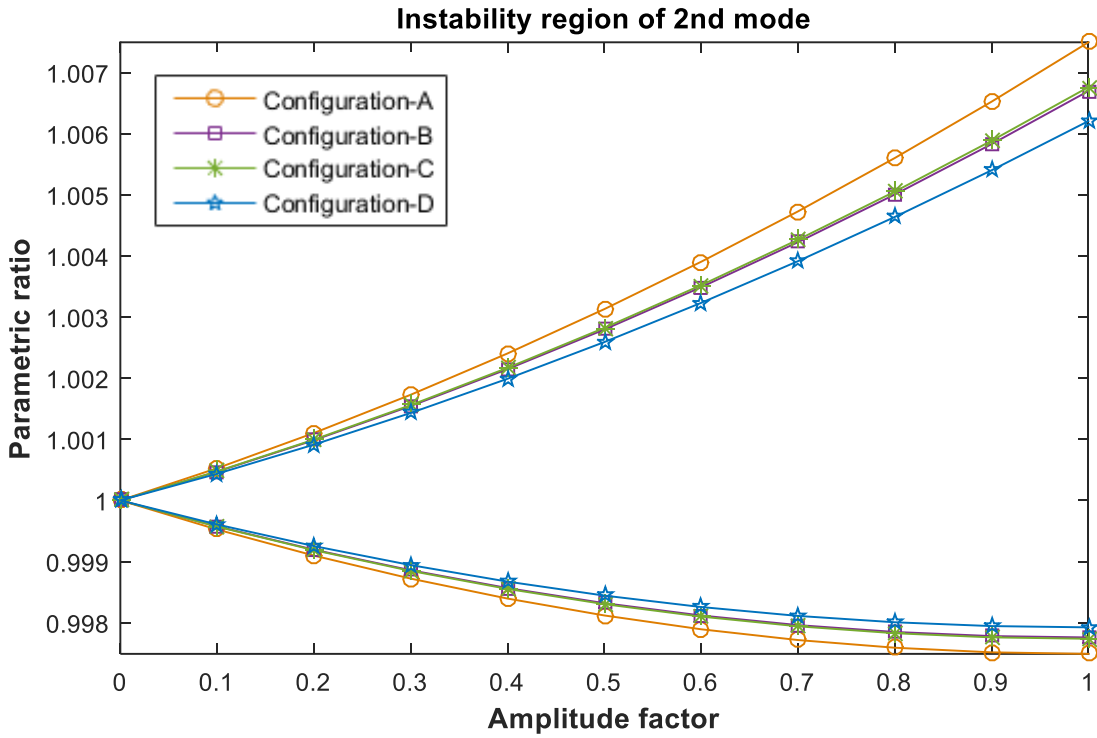
Figure 2.33 Instability region for second out-of-plane bending mode of doubly-tapered beam
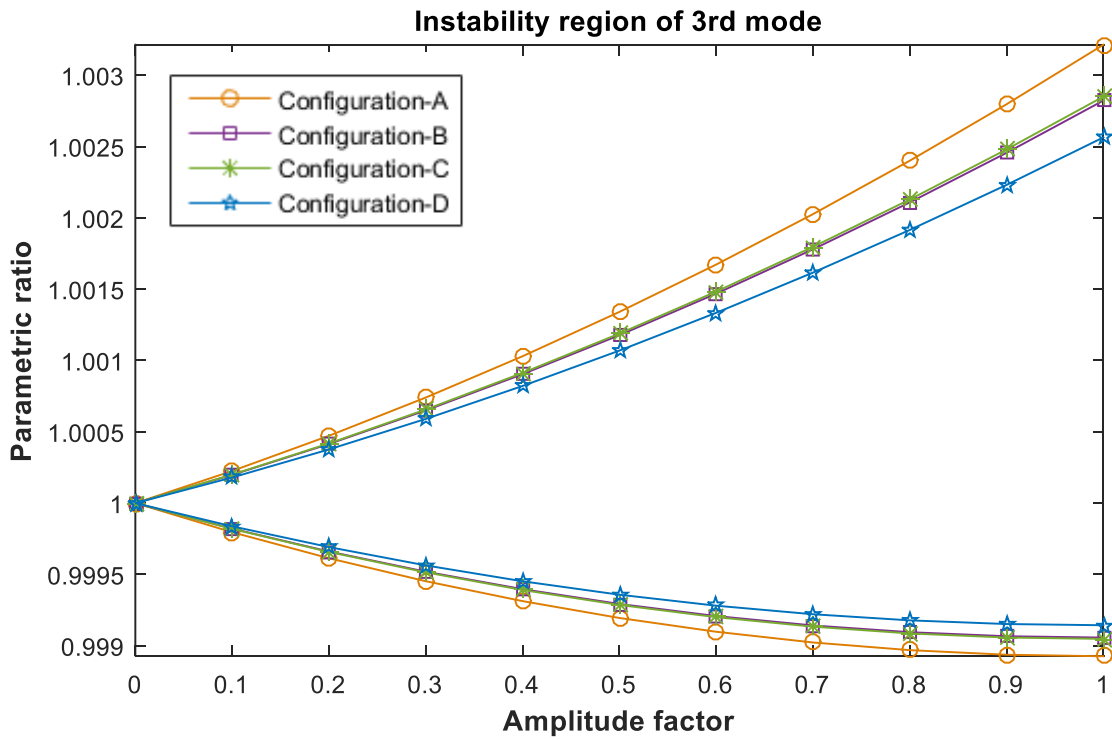
Figure 2.34 Instability region for third out-of-plane bending mode of doubly-tapered beam

58

2.10   Instability analysis considering different system parameters

In addition, to the dynamic and static parameters of rotation, the stability of a doubly-tapered composite cantilever beam is also affected by different geometric parameters such as length, hub radius, thickness-taper angle and width-ratio. The stacking sequence also has an effect on instability region. Following graphs will show the effect on the instability region with respect to different parameters. The analysis is conducted by considering taper Configuration-A and Configuration-D. Also, the analysis is conducted for first three modes which have greater practical importance because of their corresponding three lowest natural frequencies and parametric resonance frequencies. Mechanical properties of materials used to do the analysis are given in Tables 2.1 and 2.2.

2.10.1 Effect of mean rotational velocity

The increase of mean rotational velocity in time-varying rotational load increase the resonance frequency in a doubly-tapered rotating cantilever beam that affects the dynamic instability characteristics. Figures 2.35 to 2.37 show the effect on dynamic instability due to change in mean rotational velocity. In this case, a 25 cm long doubly-tapered ($S = 18, r_b = 0.1$) rotating cantilever composite beam is mounted on a hub. Hub radius is taken as 0.025 m. The beam width is 2 cm at fixed side. The stacking sequence is $[90]_{18s}$ at fixed side. The individual ply thickness is 0.125 mm.

The following three graphs for first three modes of out-of-plane bending vibration clearly show that instability region increases as the mean rotational velocity increases. It means that the mean rotational velocity increases rotating beam becomes more unstable. Also, following three graphs for first three modes of out-of-plane bending vibration show that the width of instability region for Configuration-D is smaller than the width of instability region for Configuration-A.

59
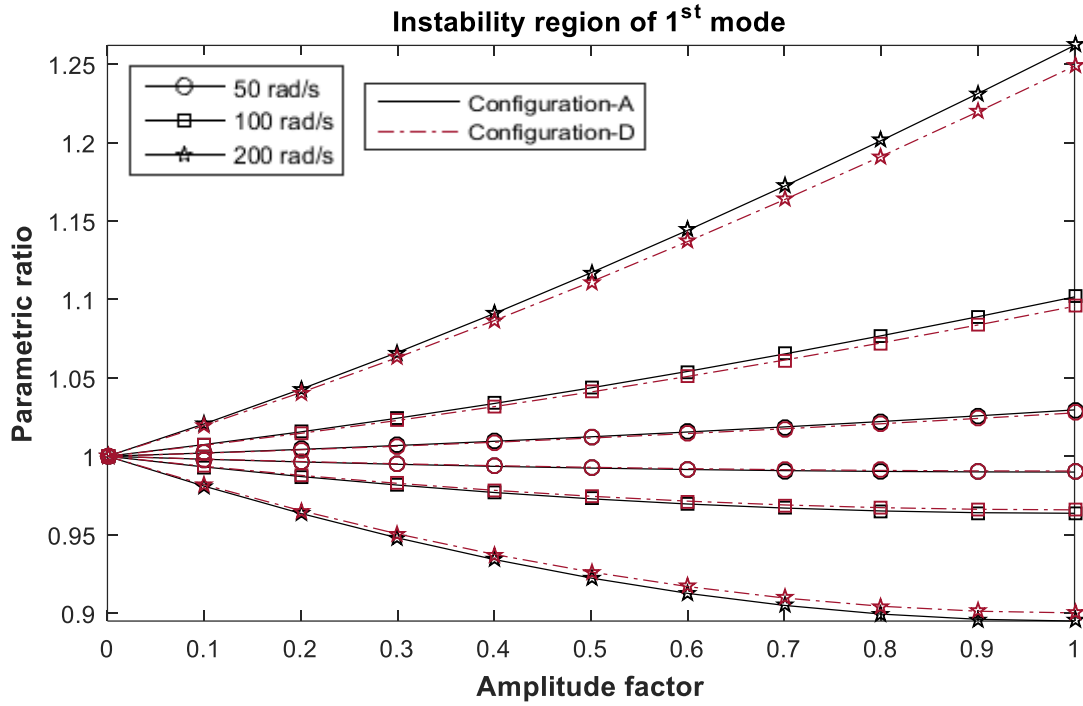
Figure 2.35 Effect of mean rotational velocity on instability region of first mode
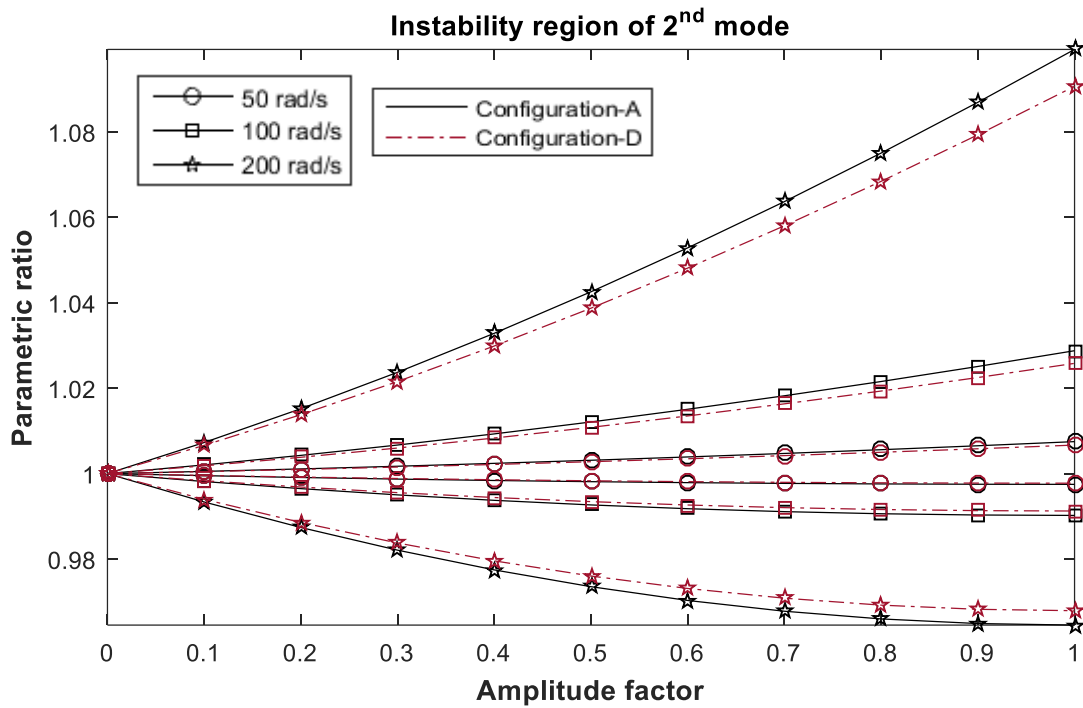
Figure 2.36 Effect of mean rotational velocity on instability region of second mode
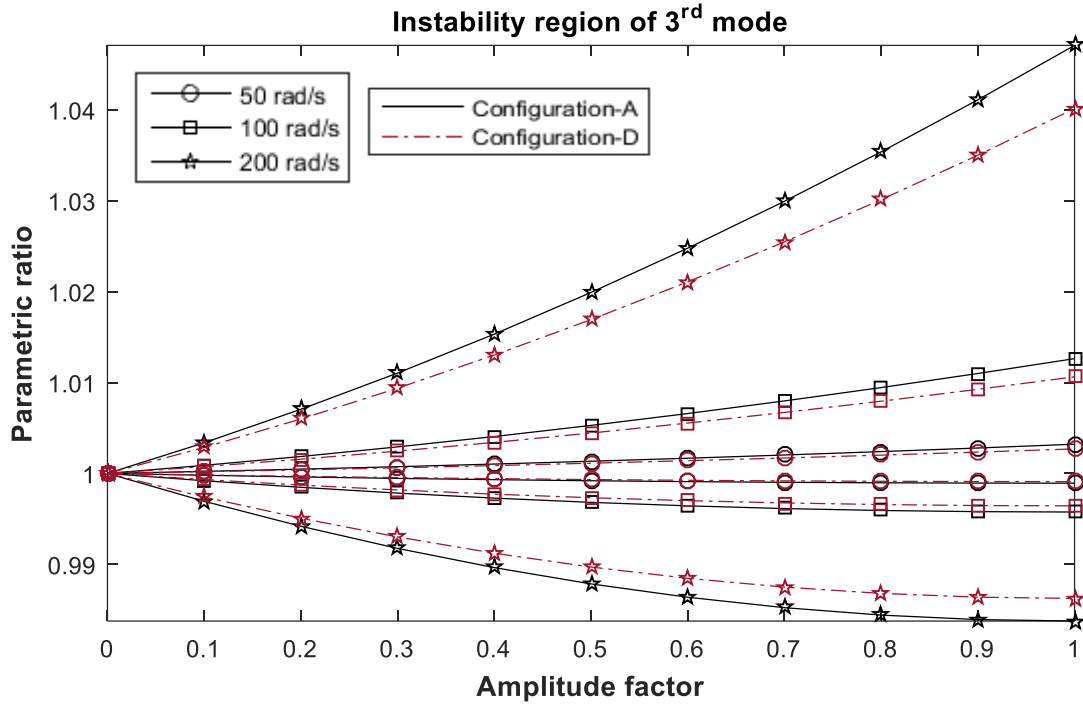
Figure 2.37 Effect of mean rotational velocity on instability region of third mode

2.10.2 Effect of hub radius to beam length ratio

Although hub radius has no effect on the mass of the rotating beam, but it has an effect on the stiffness caused by centrifugal action. Therefore final result changes due to change of hub radius. Figures 2.38 to 2.40, illustrate the variation of instability region due to change in the ratio of hub radius over beam length (R/L). The doubly-tapered beam $(S = 18, r_b = 0.1)$ has same length, same stacking sequence, same width at fixed side and same boundary condition as that of previous section 2.10.1. The mean rotational velocity in this case is 50 rad/s.

The following three graphs for first three modes of out-of-plane bending vibration show that width of instability region increases as the ratio of hub radius to beam length increases and the width of instability region for Configuration-D is smaller than the width of instability region for Configuration-A.
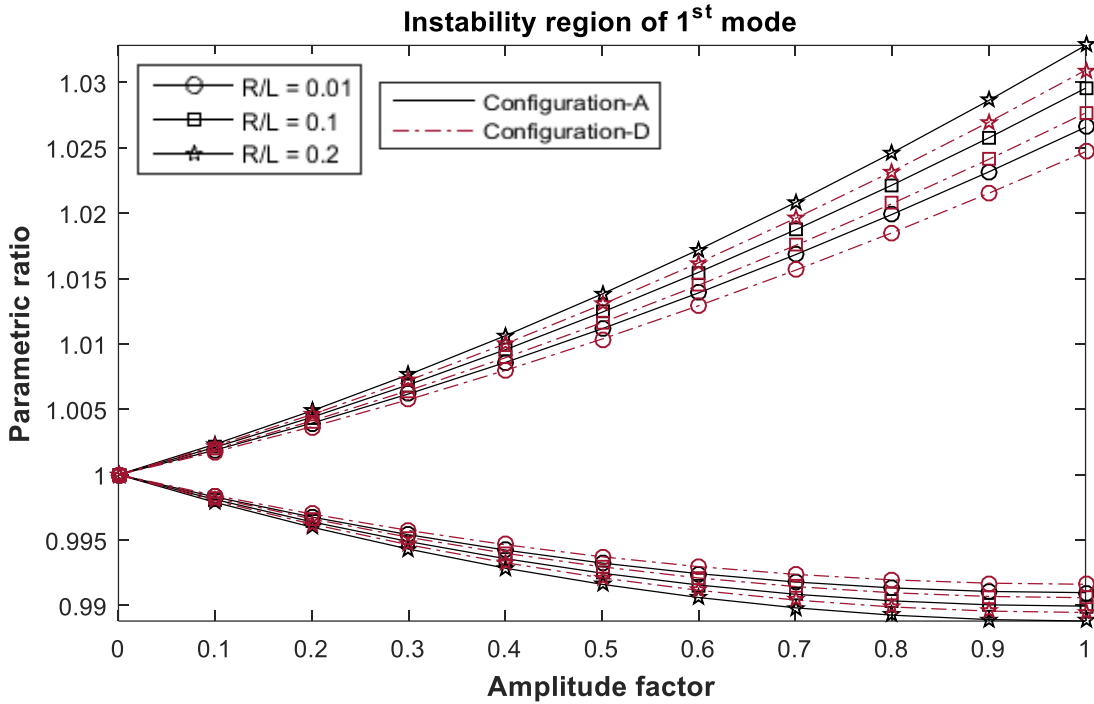
Figure 2.38 Effect of hub radius to beam length ratio on instability region of first mode
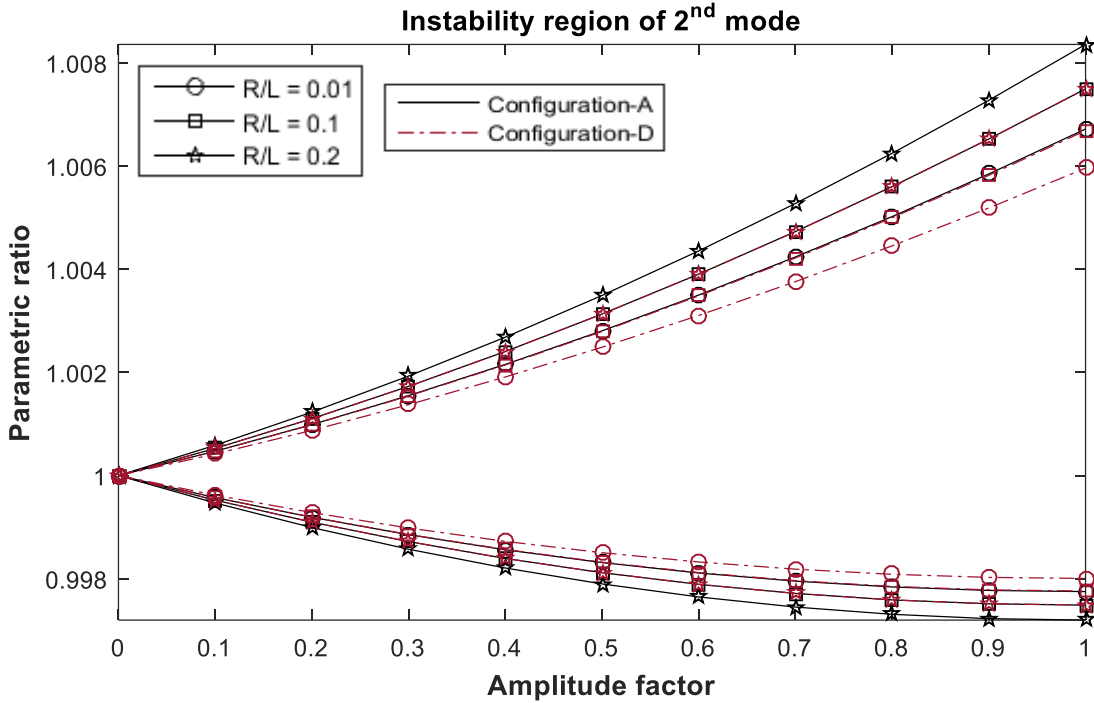
Figure 2.39 Effect of hub radius to beam length ratio on instability region of second mode
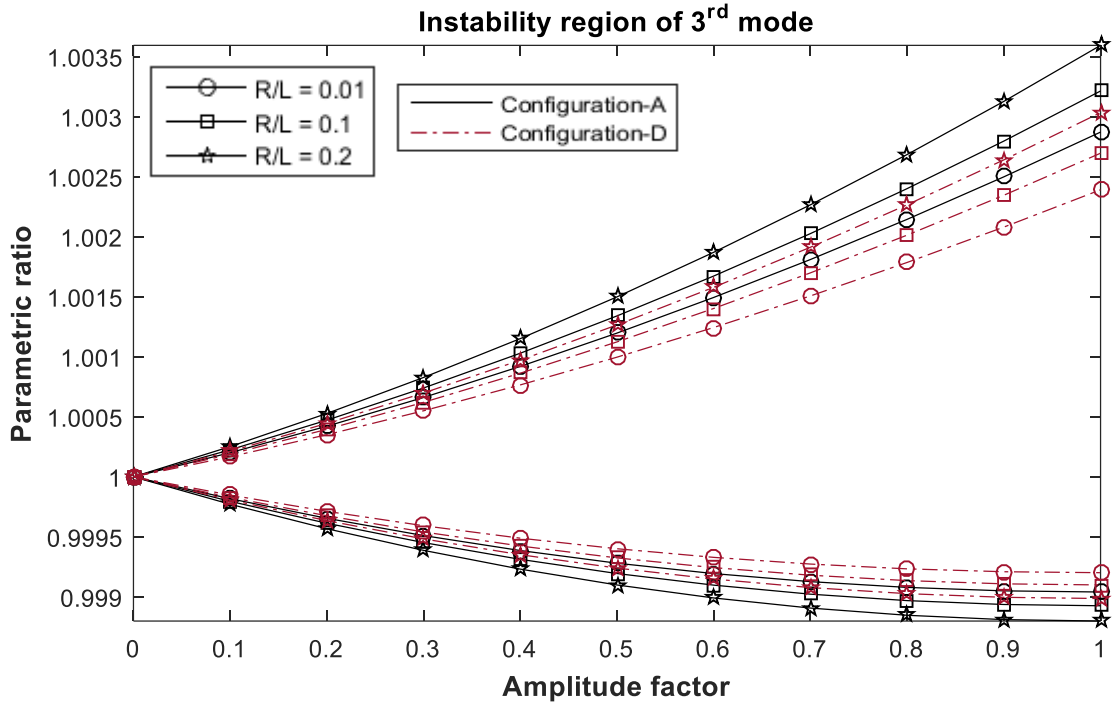
Figure 2.40 Effect of hub radius to beam length ratio on instability region of third mode

2.10.3 Effect of double-tapering

To understand the effect of double tapering on dynamic instability, double-taper ratio has been introduced again in this section. Double-taper ratio is defined in equation (2.44). Figures 2.41 to 2.43 show the variation of instability region for three different values of double-taper ratio. The beam length, width at fixed side, stacking sequence and mean rotational velocity is taken as same as that of previous section 2.10.2. The hub radius, in this case, is 0.025 m.

From Figures 2.41 to 2.43 it can be easily stated that increase of double-taper ratio decreases the width of instability region for first three modes of out-of-plane bending vibration. More clearly, increase of double-tapering decreases the risk of dynamic instability for out-of-plane bending vibration. Also, following three graphs for first three modes of out-of-plane bending vibration show that the width of instability region for Configuration-D is smaller than the width of instability region for Configuration-A.
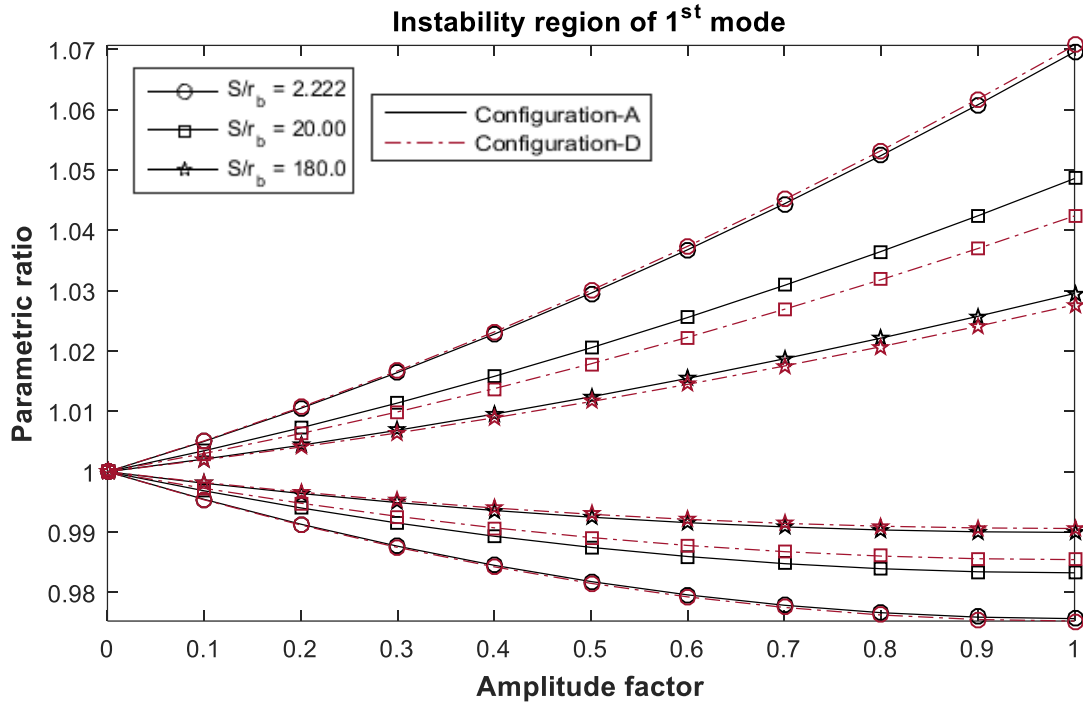
Figure 2.41 Effect of double-tapering on instability region of first mode
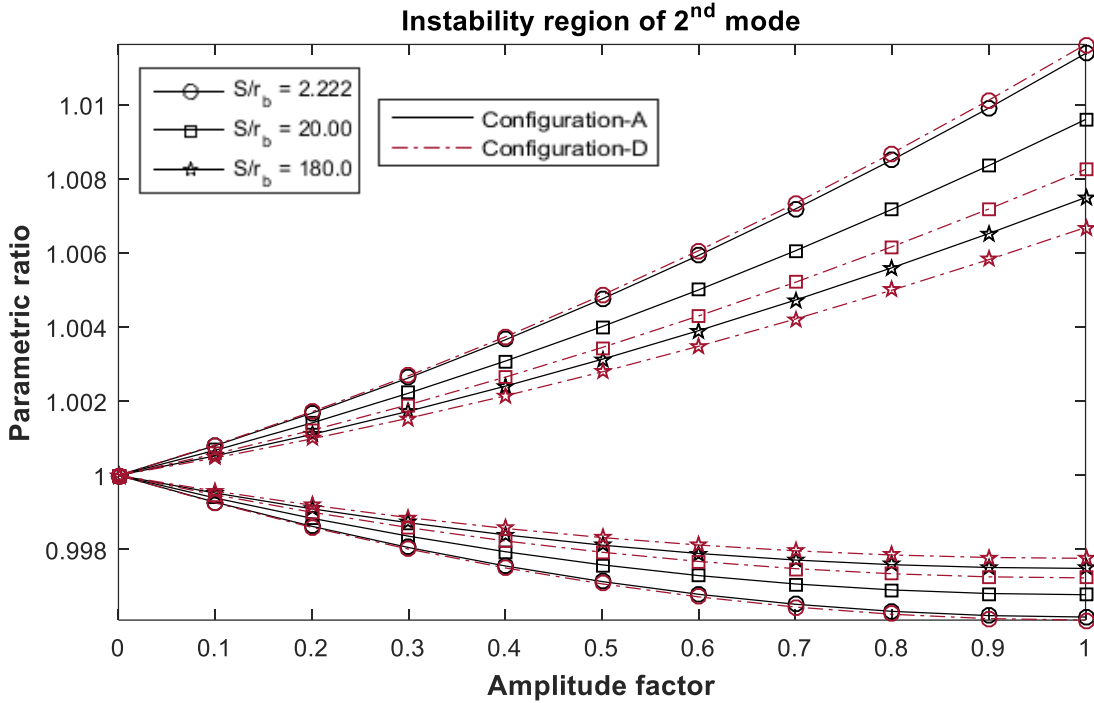
Figure 2.42 Effect of double-tapering on instability region of second mode
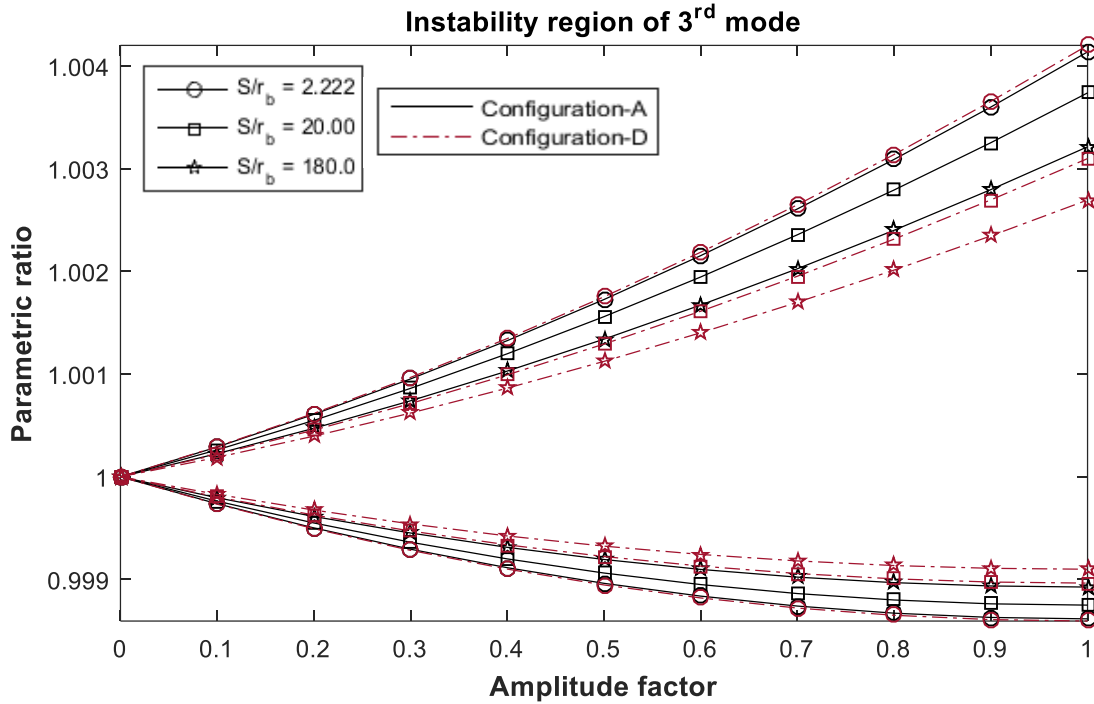
Figure 2.43 Effect of double-tapering on instability region of third mode

2.10.4 Effect of stacking sequence

To understand the influence of stacking sequence on dynamic instability of a doubly-tapered beam, four different stacking sequences were considered in this section. The doubly-tapered ($S = 18, r_b = 0.1$) rotating cantilever composite beam is considered in this section which has same length, same width at fixed side, same hub radius and same mean rotational velocity as that of previous section 2.10.3.

From Figures 2.44 to 2.46, it can be observed that for both Configuration-A and Configuration-D, unidirectional ply stacking sequence ($[0]_{18s}$) has less width of instability region whereas $[90]_{18s}$ has highest width of instability region. Cross-ply laminate $[0/90]_{9s}$ and angle-ply laminate $[-45/45/0]_{6s}$ stacking sequences have the almost same width of instability regions, but greater than that of unidirectional stacking sequence and less than that of $[90]_{18s}$ stacking sequence.
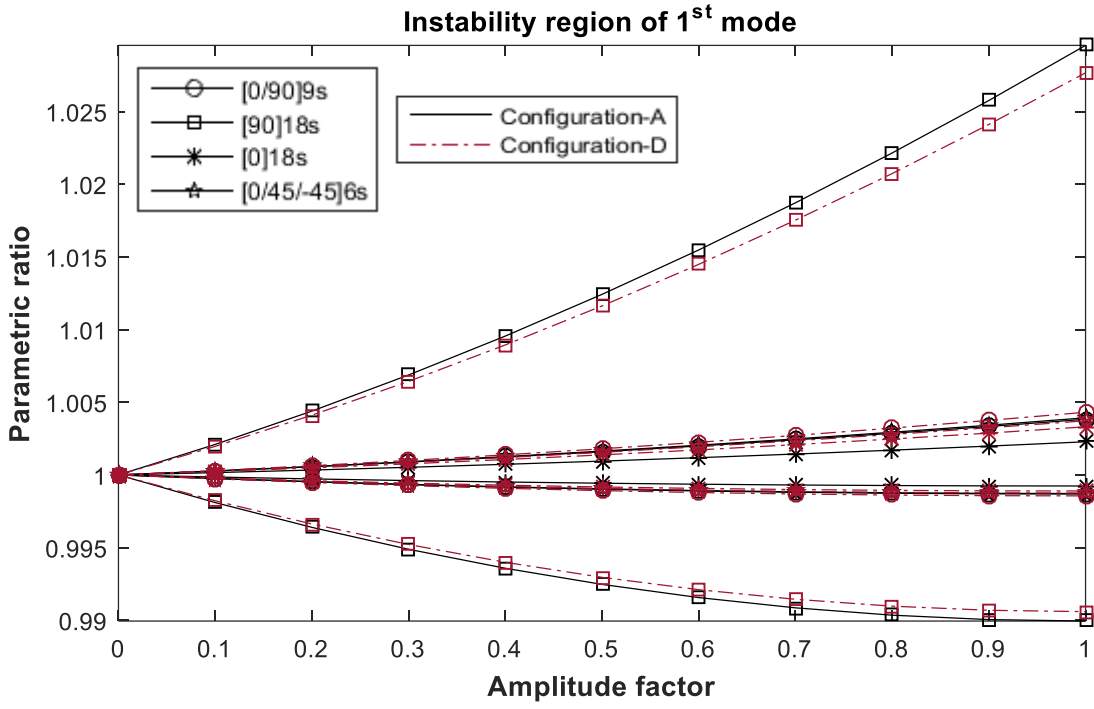
Figure 2.44 Effect of stacking sequence on instability region of first mode
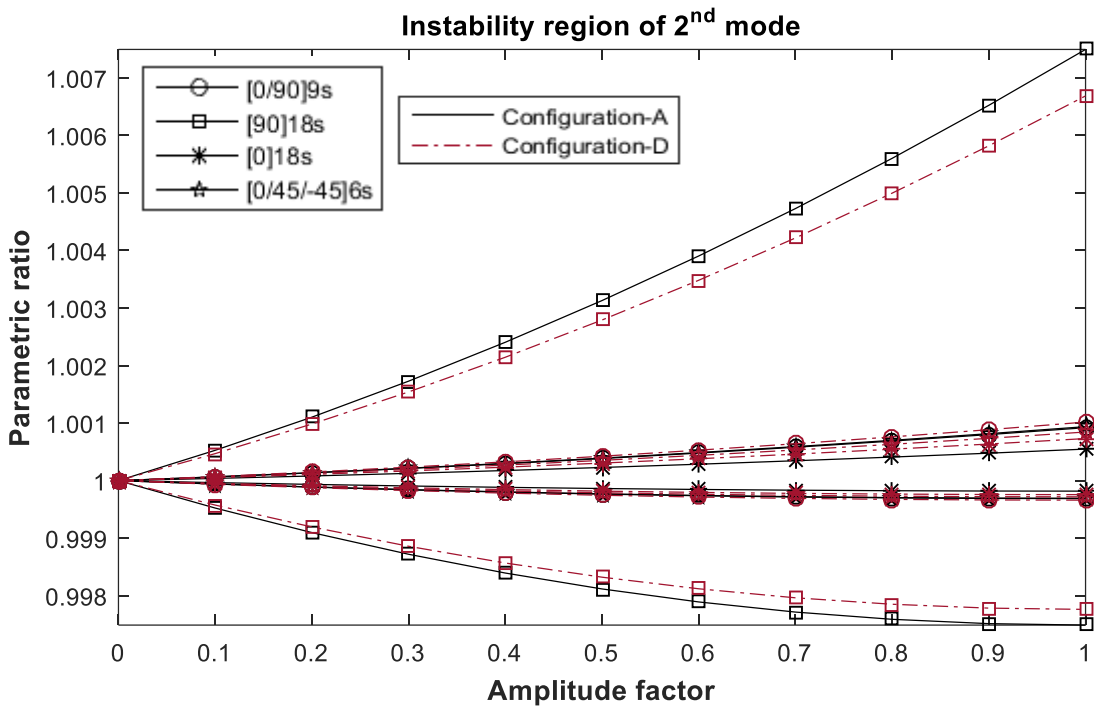
Figure 2.45 Effect of stacking sequence on instability region of second mode
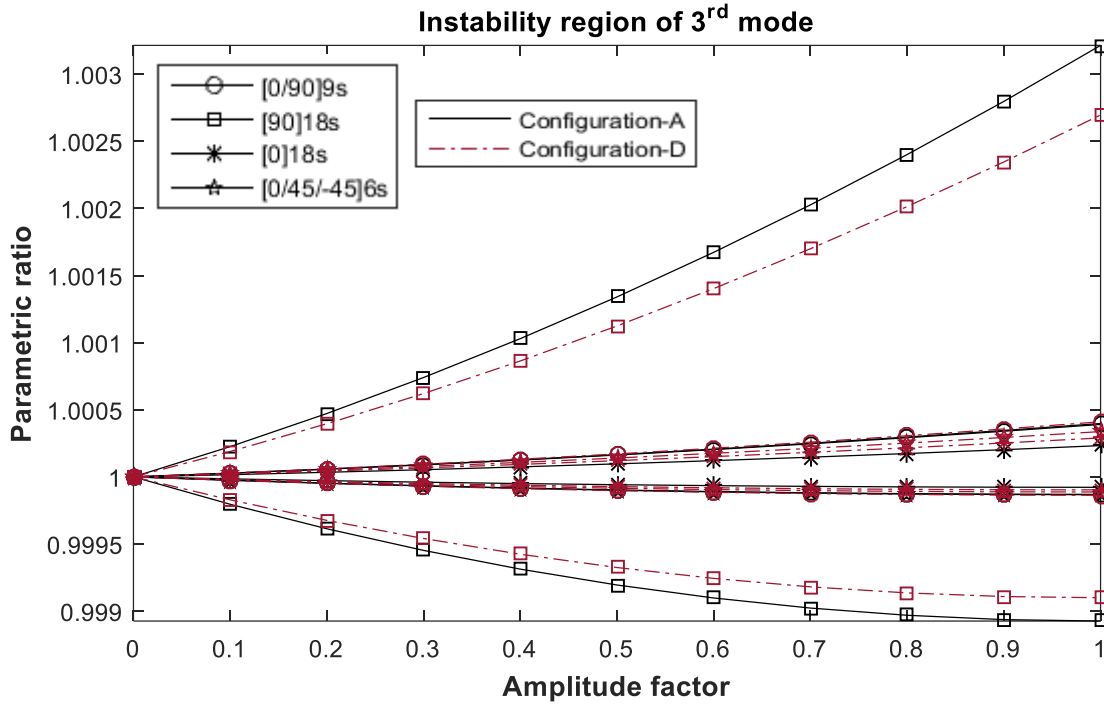
Figure 2.46 Effect of stacking sequence on instability region of third mode

2.11   Summary

In this chapter, first, free vibration analysis for out-of-plane bending has been carried out for a doubly-tapered rotating cantilever composite beam. Rayleigh-Ritz approximate method based on Classical Lamination Theory has been employed to formulate the free vibration problem. The results for first three natural frequencies are validated with existing reference and FEA software ANSYS. Upon completing the validation, effects of different parameters such as ply drop-off, width-taper ratio, rotational velocity and stacking sequence of laminate have been investigated. Based on the results obtained, Configuration-A (See Appendix-A) has lowest natural frequency as this configuration has largest amount of resin pockets among the four configurations, which results in the lowest stiffness and Configuration-D has highest natural frequency as this configuration has lower volume of resin pockets and also they are placed farther from the center that leads to higher contribution to the stiffness. As expected, natural frequencies increase with the

rotational velocity. As the double-tapering increase, natural frequency also increases. After free vibration analysis, critical speed has been determined for various types of beams. In this case, doubly-tapered beam has the highest critical speed (operating speed) than uniform beam. Also, beam with unidirectional ply stacking sequence has highest critical speed.

In the second part of this chapter, dynamic instability analysis for out-of-plane bending vibration has been performed for a periodic rotational velocity. Bolotin's method has been used to determine the resonance frequency which represents the boundaries of the instability region in the parametric plane. Modal response has been investigated at different locations of stable and unstable regions to validate the formulation. Based on the results obtained, Configuration-D has smallest width of instability region among all the tapered configurations considered and Configuration-A has largest width of instability region. After validation, various graphs have been plotted to study the effects of different parameters on the instability region by considering Configuration-A and Configuration-D. It has been observed that width of instability region increases with mean rotational velocity. Also, width of instability region increase as the hub radius increases. Increase of double-tapering both reduce the width of instability region. Unidirectional ply stacking sequence $[0]_{18s}$ has smallest width of the instability region while stacking sequence $[90]_{18s}$ has largest width of the instability region.

Chapter - 3

Free vibration and dynamic instability analyses of doubly-tapered rotating laminated composite beam for in-plane bending and axial vibrations

3.1 Introduction

A beam with two cross-sectional planes of symmetry (x-y and x-z planes, Figure 2.1) may undergo bending vibration in either on both of the two planes of symmetry. Bending with respect to x-y plane is called out-of-plane bending (as discussed in chapter-2) and bending with respect to x-z plane is called in-plane bending. In this chapter, free vibration and dynamic instability analyses for in-plane bending vibration and axial (stretching) vibration of a doubly-tapered rotating cantilever composite beam are conducted. Centrifugal loading component due to rotational velocity affects the in-plane bending vibration and the axial vibration. In addition to the rotation, tapering on the beam geometry brings significant change on the natural frequencies of in-plane bending and axial vibrations. In the first part of this chapter, free vibration analyses for in-plane bending and axial vibrations of doubly-tapered laminated composite beam are carried out using Rayleigh-Ritz method. Then, dynamic instability analysis is conducted applying Bolotin's method. Commercial Finite Element Analysis tool ANSYS is used for validation purpose. NCT-301 Graphite/Epoxy prepreg has been chosen as the material to perform the numerical analysis.

3.2 Energy formulation using Rayleigh-Ritz method

3.2.1 Strain energy

Based on the beam description given in section 2.2, following Figure 3.1 can be considered to determine the strain field in the case when the beam is deformed in the lamination plane (x-y plane). In Figure 3.1, M is any arbitrary point in the lamination plane of the beam and u_0, v_0 are axial and lateral mid-plane displacements, respectively. Using Classical Lamination Theory (CLT), strain in x-direction can be expressed by the mid-plane strain and the curvature in the x-y plane.
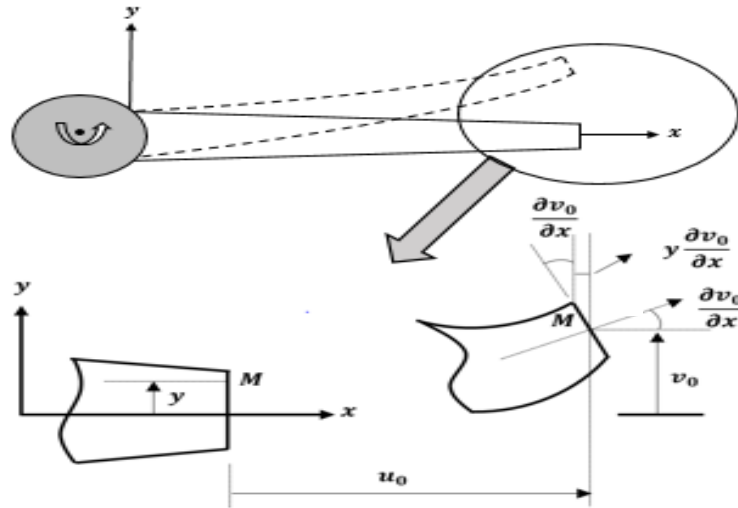
Figure 3.1 Deformation of beam in the lamination plane (x-y plane)

From Figure 3.1, strain in x-direction can be written as:

$$\varepsilon_{xx}{}^k = \frac{\partial u_0}{\partial x} - y \frac{\partial^2 v_0}{\partial x^2} \tag{3.1}$$

Substituting $\varepsilon_{xx}{}^k$ in equation (2.9) and neglecting $\varepsilon_{yy}{}^k$ and $\gamma_{xy}{}^k$, strain energy expression leads to:

$$U = \sum_{k=1}^{N} \frac{1}{2} \int_0^L \int_{-\frac{b(x)}{2}}^{\frac{b(x)}{2}} \int_{h_{k-1}}^{h_k} Q_{11}{}^k \left(\frac{\partial u_0}{\partial x} - y \frac{\partial^2 v_0}{\partial x^2}\right)^2 dz\, dy\, dx \tag{3.2}$$

From Classical Laminate Theory:

$$\sum_{k=1}^{N} \int_{h_{k-1}}^{h_k} Q_{11}{}^k dz = A_{11}(x) \tag{3.3}$$

where, $A_{11}(x)$ is the first coefficient of stretching stiffness matrix. Using equation (3.3) and due to cross sectional plane of symmetry in x-y plane, equation (3.2) leads to:

$$U = \frac{1}{2}\int_0^L \{A_{11}(x)b(x)\left(\frac{\partial}{\partial x}u_o(x,t)\right)^2 + A_{11}(x)\frac{(b(x))^3}{12}\left(\frac{\partial^2}{\partial x^2}v_0(x,t)\right)^2\}dx \tag{3.4}$$

Using the Rayleigh-Ritz method, mid-plane displacements u_0 and v_0 can be assumed as:

$$u_0(x,t) = \sum_{i=1}^{m} \emptyset_{2i}(x)q_{2i}(t) \tag{3.5}$$

$$v_0(x,t) = \sum_{i=1}^{m} \emptyset_{3i}(x)q_{3i}(t) \tag{3.6}$$

where, $\emptyset_{2i}$ and $\emptyset_{3i}$ are approximate shape functions for axial and in-plane bending displacements respectively and $q_{2i}(t)$ and $q_{3i}(t)$ are corresponding generalized coordinates. Substituting equations (3.5) and (3.6) in equation (3.4) one can get:

$$U = \sum_{i=1}^{m}\sum_{j=1}^{m}\frac{1}{2}\int_0^L \{A_{11}(x)b(x)\left(\frac{\partial}{\partial x}\emptyset_{2i}(x)\right)\left(\frac{\partial}{\partial x}\emptyset_{2j}(x)\right)q_{2i}(t)q_{2j}(t) +$$

$$A_{11}(x)\frac{(b(x))^3}{12}\left(\frac{\partial^2}{\partial x^2}\emptyset_{3i}(x)\right)\left(\frac{\partial^2}{\partial x^2}\emptyset_{3j}(x)\right)q_{3i}(t)q_{3j}(t)\}dx \tag{3.7}$$

Equation (3.7) can be written as:

$$U = \sum_{i=1}^{m}\sum_{j=1}^{m}\frac{1}{2}(q_{2i} K_{ij}{}^u q_{2j} + q_{3i} K_{ij}{}^v q_{3j}) \tag{3.8}$$

where,

$$K_{ij}{}^u = \int_0^L A_{11}(x)b(x)\emptyset'_{2i}(x)\emptyset'_{2j}(x)dx \tag{3.9}$$

$$K_{ij}{}^v = \int_0^L A_{11}(x)\frac{(b(x))^3}{12}\emptyset''_{3i}(x)\emptyset''_{3j}(x)dx \tag{3.10}$$

3.2.2 Work done by centrifugal force

In the case of in-plane bending vibration, rotating cantilever beam deflects laterally along with small axial displacement due to centrifugal force. By expressing small axial displacement in terms of lateral displacement (v_0), work done by this centrifugal force can be written as:

$$W = \frac{1}{2}\int_0^L P(x)(\frac{\partial}{\partial x}v_0(x,t))^2 dx \tag{3.11}$$

Here, $P(x)$ is given by equation (2.21). After applying the Rayleigh-Ritz approximate displacement function, equation (3.11) leads to:

$$W = \sum_{i=1}^m \sum_{j=1}^m \frac{1}{2}\int_0^L P(x)\frac{\partial}{\partial x}\emptyset_{3i}(x)\frac{\partial}{\partial x}\emptyset_{3j}(x)q_{3i}(t)q_{3j}(t)dx \tag{3.12}$$

Equation (3.12) can be written as:

$$W = \sum_{i=1}^m \sum_{j=1}^m \frac{1}{2}q_i K_{1ij}{}^{cv}q_j \tag{3.13}$$

where,

$$K_{1ij}{}^{cv} = \int_0^L P(x)\emptyset'_{3i}(x)\emptyset'_{3j}(x)dx \tag{3.14}$$

3.2.3 Kinetic Energy

Considering the velocity vector from equation (2.25) and neglecting displacement in z-direction one can get:

$$\vec{V} = (\frac{\partial u}{\partial t} - \Omega v)\hat{\imath} + (\frac{\partial v}{\partial t} + \Omega(R + x + u_0))\hat{\jmath} \tag{3.15}$$

Therefore, velocity components in x, y and z directions are:

$$V_x = \frac{\partial u}{\partial t} - \Omega v, V_y = \frac{\partial v}{\partial t} + \Omega(R + x + u_0) \text{ and } V_z = 0 \tag{3.16}$$

Using Figure 3.1, one can write:

$$u(x,t) = u_o(x,t) - y\frac{\partial}{\partial x}v_0(x,t) \tag{3.17}$$

$$v(x,t) = v_0(x,t) \tag{3.18}$$

72

Using equations (3.16), (3.17) and (3.18) into equation (2.25), kinetic energy equation of a doubly-tapered rotating composite beam can be written as:

$$T = \frac{1}{2}\int_0^L \int_{-b(x)/2}^{b(x)/2} \rho_L \left(\frac{\partial u_0}{\partial t} - y\frac{\partial^2 v_0}{\partial x \partial t} - \Omega v_0\right)^2 dy dx + \frac{1}{2}\int_0^L \int_{-b(x)/2}^{b(x)/2} \rho_L \left(\frac{\partial v_0}{\partial t} + \Omega(R + x + u_0)\right)^2 dy dx$$

(3.19)

Neglecting rotary inertia terms $(y\frac{\partial^2 v_0}{\partial x \partial t})$ and Coriolis term $(2\Omega\frac{\partial u_0}{\partial t}v_0)$, the kinetic energy equation simplifies to:

$$T = \frac{1}{2}\int_0^L b(x)\rho_L \left\{\left(\frac{\partial u_0}{\partial t}\right)^2 + \Omega^2 v_0{}^2\right\} dx$$

$$+ \frac{1}{2}\int_0^L b(x)\rho_L \left\{(\frac{\partial v_0}{\partial t})^2 + \Omega^2 u_0{}^2 + 2\Omega^2 u_0(R + x) + 2\Omega(R + x)\frac{\partial v_0}{\partial t} + \Omega^2(R + x)^2\right\} dx \qquad (3.20)$$

After applying the Rayleigh-Ritz approximate displacement function one can write:

$$T = \sum_{i=1}^m \sum_{j=1}^m (\frac{1}{2}\int_0^L \rho_L b(x)\emptyset_{2i}(x)\emptyset_{2j}(x)\frac{\partial q_{2i}(t)}{\partial t}\frac{\partial q_{2j}(t)}{\partial t} dx +$$

$$\frac{1}{2}\int_0^L \rho_L b(x)\emptyset_{3i}(x)\emptyset_{3j}(x)\frac{\partial q_{3i}(t)}{\partial t}\frac{\partial q_{3j}(t)}{\partial t} dx + \frac{1}{2}\int_0^L \rho_L b(x)\Omega^2\emptyset_{2i}(x)\emptyset_{2j}(x)q_{2i}(t)q_{2j}(t)dx +$$

$$\frac{1}{2}\int_0^L \rho_L b(x)\Omega^2\emptyset_{3i}(x)\emptyset_{3j}(x)q_{3i}(t)q_{3j}(t)dx + \int_0^L \rho_L b(x)\Omega^2(R + x)\emptyset_{2i}(x)q_{2i}(t)dx +$$

$$\int_0^L \Omega\rho_L b(x)(R + x)\emptyset_{3i}(x)\frac{\partial q_{3i}(t)}{\partial t} dx) + \frac{1}{2}\int_0^L \rho_L b(x)\Omega^2(R + x)^2 dx \qquad (3.21)$$

Equation (3.21) can be written as:

$$T = \sum_{i=1}^m \sum_{j=1}^m (\frac{1}{2}\,\dot{q}_{2i}\,M_{ij}{}^u\dot{q}_{2j} + \frac{1}{2}\,\dot{q}_{3i}\,M_{ij}{}^v\dot{q}_{3i} + \frac{1}{2}q_{2i}K_{ij}{}^{cu}q_{2j} + \frac{1}{2}q_{3i}K_{2ij}{}^{cv}q_{3j} + F_iq_{2i} +$$

$$\int_0^L \Omega\rho_L b(x)(R + x)\emptyset_{3i}(x)\dot{q}_{3i}dx) + \frac{1}{2}\int_0^L \rho_L b(x)\Omega^2(R + x)^2 dx \qquad (3.22)$$

where,

$$M_{ij}{}^u = \int_0^L \rho_L b(x)\emptyset_{2i}(x)\emptyset_{2j}(x)dx \qquad (3.23)$$

$$M_{ij}{}^v = \int_0^L \rho_L b(x)\emptyset_{3i}(x)\emptyset_{3j}(x)dx \qquad (3.24)$$

73

$$K_{ij}{}^{cu} = \int_0^L \rho_L b(x)\Omega^2 \emptyset_{2i}(x)\emptyset_{2j}(x)dx \tag{3.25}$$

$$K_{2ij}{}^{cv} = \int_0^L \rho_L b(x)\Omega^2 \emptyset_{3i}(x)\emptyset_{3j}(x)dx \tag{3.26}$$

$$F_i = \int_0^L \rho_L b(x)\Omega^2 (R + x)\emptyset_{2i}(x)dx \tag{3.27}$$

3.2.4 Equations of motion

To get the equations of motion for axial vibration and in-plane bending vibration, Lagrange's equation can be used. Using Lagrange's equation for two generalized coordinates, one can get two sets of matrix equations. For $q_{2i}(t)$, Lagrange's equation can be written as:

$$\frac{d}{dt}\left(\frac{\partial T}{\partial \dot{q}_{2i}}\right) - \frac{\partial T}{\partial q_{2i}} + \frac{\partial (U+W)}{\partial q_{2i}} = 0 \qquad , i = 1..m \tag{3.28}$$

and for $q_{3i}(t)$, Lagrange's equation can be written as:

$$\frac{d}{dt}\left(\frac{\partial T}{\partial \dot{q}_{3i}}\right) - \frac{\partial T}{\partial q_{3i}} + \frac{\partial (U+W)}{\partial q_{3i}} = 0 \qquad , i = 1..m \tag{3.29}$$

Substituting U, W and T from equations (3.8), (3.13) and (3.22), respectively, into the equations (3.28) and (3.29) and neglecting the load vector $\{F\}$ for free vibration analysis, one can get two sets of equations of motion in matrix form as follows:

$$[M^u]\{\ddot{q}_2\} + ([K^u] - [K^{cu}])\{q_2\} = \{0\} \tag{3.30}$$

$$[M^v]\{\ddot{q}_3\} + ([K^v] + [K_1{}^{cv}] - [K_2{}^{cv}])\{q_3\} = \{0\} \tag{3.31}$$

where, $[M^u]$, $[K^u]$, $[K^{cu}]$ and $\{q_2\}$ are mass matrix, global stiffness matrix, softening matrix due to centrifugal action and system displacement vector, respectively, for the axial vibration and $[M^v]$, $[K^v]$, $[K_1{}^{cv}]$, $[K_2{}^{cv}]$ and $\{q_3\}$ are mass matrix, global stiffness matrix, stiffness matrix due to centrifugal action, softening matrix due to centrifugal action and system displacement vector, respectively, for the in-plane bending vibration. Equations (3.30) and (3.31) can be written in matrix form as:

$$\begin{bmatrix} [M^u] & [0] \\ [0] & [M^v] \end{bmatrix} \begin{bmatrix} \{\ddot{q}_2\} \\ \{\ddot{q}_3\} \end{bmatrix} + \begin{bmatrix} [K^u] - [K^{cu}] & [0] \\ [0] & [K^v] + [K_1{}^{cv}] - [K_2{}^{cv}] \end{bmatrix} \begin{bmatrix} \{q_2\} \\ \{q_3\} \end{bmatrix} = \{0\} \qquad (3.32)$$

Shortly written as:

$$[M^{uv}]\{\ddot{\tilde{q}}\} + [K^{uv}]\{\tilde{q}\} = \{0\} \tag{3.33}$$

where, $[M^{uv}] = \begin{bmatrix} [M^u] & [0] \\ [0] & [M^v] \end{bmatrix}$, $[K^{uv}] = \begin{bmatrix} [K^u] - [K^{cu}] & [0] \\ [0] & [K^v] + [K_1{}^{cv}] - [K_2{}^{cv}] \end{bmatrix}$ and $\{\tilde{q}\} = \begin{bmatrix} \{q_2\} \\ \{q_3\} \end{bmatrix}$.

The solution of equation (3.33) can be assumed in the form

$$\{\tilde{q}\} = \{\tilde{Q}\}e^{\sqrt{-1}\omega t} \tag{3.34}$$

where, $\{\tilde{Q}\}$ is the mode shape (eigen) vector and ω is the natural frequency. Substituting equation (3.34) into the equation (3.33) yields:

$$([K^{uv}] - \omega^2[M^{uv}])\{\tilde{Q}\} = \{0\} \tag{3.35}$$

Equation (3.35) is an eigenvalue problem and can be solved to determine the natural frequencies of axial vibration and in-plane bending vibration for a doubly-tapered rotating cantilever laminated composite beam. The natural frequencies of axial vibration and natural frequencies of in-plane bending vibration determined from equation (3.35) can be distinguished by obtaining the corresponding mode shapes.

3.3 Boundary conditions and approximate shape functions

Rayleigh-Ritz method is the extension of Rayleigh's method that provides a means of obtaining a more accurate value for the fundamental frequency as well as approximations for the high frequencies and mode shapes. In this method single shape function is replaced by a series of shape functions. The success of the method depends on the choice of the shape functions that should satisfy the geometric boundary conditions.

In the case of axial vibration for a beam of length L, that is fixed at one end and free at the other end, boundary conditions are [10]:

$$u_{0(x=0)} = 0, u_{0(x=L)} \neq 0 \tag{3.36}$$

The approximate shape function for axial displacement that satisfies the boundary condition, is

$$\emptyset_{2i}(x) = \left(\frac{x}{L}\right)^i, i = 1,2,3 \ldots m \tag{3.37}$$

In the case of in-plane bending vibration for a beam of length L, that is fixed at one end and free at the other end, the boundary conditions are:

$$v_{0(x=0)} = 0, v_{0(x=L)} \neq 0, \left.\frac{\partial v_0}{\partial x}\right|_{(x=0)} = 0 \text{ and } \left.\frac{\partial v_0}{\partial x}\right|_{(x=L)} \neq 0 \tag{3.38}$$

The approximate shape function that satisfies the boundary condition given in equation (3.38), is

$$\emptyset_{3i}(x) = \left(\frac{x}{L}\right)^{i+1}, i = 1,2,3 \ldots m \tag{3.39}$$

3.4   Validation and results

The formulation described in section 3.2 has been developed using MATLAB for the validation of results and numerical analysis. Validation of results has been performed by comparing the existing results available in the literature and the results obtained using the FEA tool ANSYS. Due to absence of Coriolis term and due to the cross-sectional plane of symmetry being in x-y plane, natural frequencies obtained from equation (3.35) are for pure in-plane bending and pure axial vibrations. To validate the results obtained from Rayleigh-Ritz method, the first three in-plane bending and the first two pure axial natural frequencies are taken into account. In ANSYS, SHELL-181 element is used to discretize the beam. ANSYS Composite PrepPost (ACP) has been used to model the different taper configurations of the composite beam.

3.4.1 Validation step-1: Rotating uniform composite beam

In this validation step, natural frequencies of non-rotating and rotating uniform cantilever composite beams are validated. In Table 3.1, natural frequencies for non-rotating uniform cantilever composite beam obtained using Rayleigh-Ritz (R-R) method, ANSYS and existing results are listed and compared. The existing results obtained from [40], used an exact formula, which is based on Euler-Bernoulli beam theory [40]. In Table 3.1, length of the beam is 400 mm and width is 40 mm. The total thickness of the laminate is 3.2 mm and all the layers have same thickness. The result of R-R solution method converges for 7 terms in the approximate shape function. Mechanical properties of the material used are given in [40].

Table 3.1 Natural frequencies (Hz) of in-plane bending and axial vibrations for non-rotating uniform cantilever composite beam using different methods

Stacking sequence	Vibration type	Mode	R-R solution	Reference [40]	ANSYS
$[0/90]_{2s}$	In-plane bending	1st	158.47	156.50	154.63
		2nd	993.10	980.80	901.77
		3rd	2781.5	2747.0	2302.0
	Axial	1st	2452.5	-	2426.0
		2nd	7357.4	-	7286.6
$[45/-45/0/90]_{s}$	In-plane bending	1st	148.03	140.20	139.67
		2nd	927.67	879.00	842.25
		3rd	2598.3	2462.0	2236.8
	Axial	1st	2290.9	-	2176.5
		2nd	6872.7	-	6533.8

The mode shapes associated with the natural frequencies of the first three in-plane bending and first two axial vibrations of $[0/90]_{2s}$ laminated composite beam obtained using ANSYS, are illustrated in Figures 3.2 and 3.3, respectively. Mode shapes obtained using R-R method are given in section 3.5.

In Table 3.2, first three in-plane bending and first two axial natural frequencies for rotating clamped-free uniform composite beam have been compared with ANSYS results. In this case,

beam length, width, thickness of the lamina and hub radius are taken from Tables 2.3 and 2.4. Mechanical properties of composite material are given in Table 2.1.
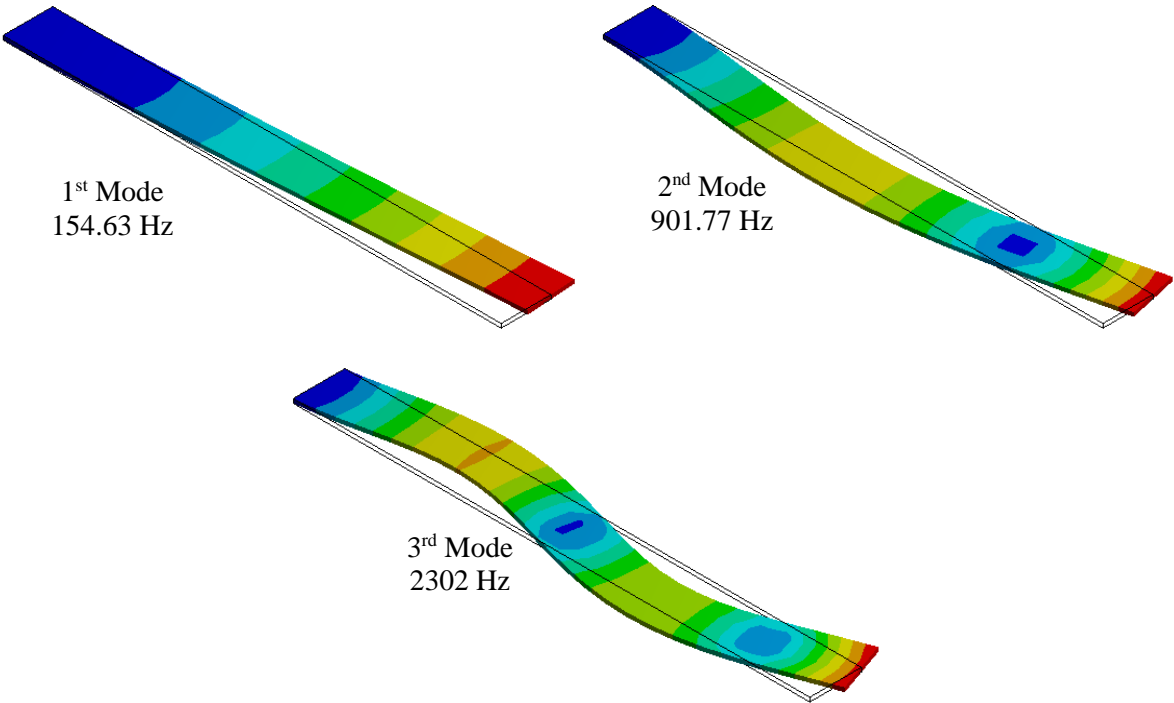
1st Mode
154.63 Hz

2nd Mode
901.77 Hz

3rd Mode
2302 Hz

Figure 3.2 First three in-plane bending vibration mode shapes of non-rotating uniform cantilever composite beam obtained using ANSYS

1st Mode
2426 Hz

2nd Mode
7286.6 Hz
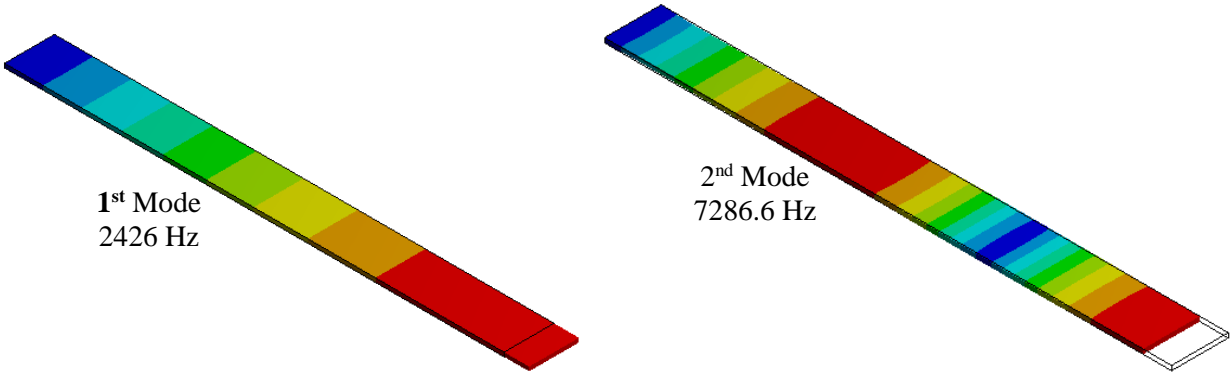
Figure 3.3 First two axial vibration mode shapes of non-rotating uniform cantilever composite beam obtained using ANSYS

Table 3.2 Natural frequencies (Hz) of in-plane bending and axial vibrations of rotating uniform cantilever composite beam

Stacking Sequence	Vibration type	Mode	R-R solution	ANSYS	R-R solution	ANSYS	R-R solution	ANSYS
			$\Omega = 0$ rad/s		$\Omega = 100$ rad/s		$\Omega = 200$ rad/s	
$[90]_{18s}$	In-plane bending	1st	120.35	120.04	120.72	120.40	121.81	121.48
		2nd	754.21	732.76	755.28	733.76	758.46	736.94
		3rd	2112.4	1980.6	2113.6	1981.0	2117.1	1985.2
	Axial	1st	2328.2	2323.2	2328.1	2323.1	2327.9	2322.7
		2nd	6984.5	6977.0	6984.4	6976.8	6984.4	6976.3

In Tables 3.1 and 3.2, natural frequencies of in-plane bending and axial vibrations of non-rotating and rotating cantilever uniform composite beams, respectively, show very good agreement between R-R method, ANSYS and existing results.

3.4.2 Validation step-2: Thickness-tapered rotating cantilever composite beam

In this validation step, natural frequencies of non-rotating and rotating thickness-tapered cantilever composite beams obtained using the R-R method are compared with ANSYS results for in-plane bending and axial vibrations. In Table 3.3, natural frequencies of non-rotating thickness-tapered cantilever composite beam are listed. Four different taper configurations with two different numbers of ply drop-off are considered to compare the results between R-R method and ANSYS. In Table 3.3, non-rotating condition is defined by '0 rad/s'. The beam length, width and hub radius are given in Table 2.4. Mechanical properties of composite and resin materials are given in Tables 2.1 and 2.2, respectively. Number of terms used in approximate shape function, in this case, is 7. Stacking sequence for the composite laminate is $[90]_{18s}$.

In Table 3.3, results for thickness-tapered composite beam show excellent agreement between R-R method and ANSYS. First three in-plane bending and first two axial vibration mode shapes of rotating (200 rad/s) thickness-tapered ($S = 10$, Configuration-A) cantilever composite beam obtained using ANSYS are illustrated in Figures 3.4 and 3.5, respectively.

Table 3.3 Natural frequencies (Hz) of in-plane bending and axial vibrations of non-rotating and rotating thickness-tapered cantilever composite beam for different taper configurations

Configuration	S		Mode	R-R	ANSYS	R-R	ANSYS	R-R	ANSYS
				$\Omega = 0$ rad/s		$\Omega = 100$ rad/s		$\Omega = 200$ rad/s	
A	6	In-plane	1st	123.69	123.70	124.09	124.06	125.29	125.11
			2nd	758.24	736.64	759.31	737.65	762.51	740.68
			3rd	2110.2	1976.2	2111.4	1977.3	2114.9	1980.6
		Axial	1st	2366.9	2365.8	2366.9	2365.7	2366.7	2365.3
			2nd	6970.2	6958.9	6970.1	6958.7	6970.1	6958.2
	10	In-plane	1st	125.78	126.81	126.20	127.16	127.47	128.20
			2nd	760.77	739.95	761.80	740.93	765.05	743.88
			3rd	2109.0	1972.9	2110.2	1974.0	2113.7	1977.2
		Axial	1st	2390.8	2401.3	2390.8	2401.2	2390.6	2400.8
			2nd	6962.4	6945.6	6962.4	6945.5	6962.3	6944.9
B	6	In-plane	1st	121.02	126.36	121.39	126.71	122.48	127.75
			2nd	758.44	742.65	759.50	743.64	762.67	746.61
			3rd	2124.3	1985.1	2125.4	1986.2	2128.9	1989.4
		Axial	1st	2332.5	2402.6	2332.5	2402.5	2332.2	2402.2
			2nd	6997.5	6987.6	6997.5	6987.4	6997.5	6986.9
	10	In-plane	1st	121.68	132.17	122.04	132.51	123.12	133.52
			2nd	762.55	753.11	763.60	754.06	766.75	756.89
			3rd	2135.8	1994.6	2136.9	1995.7	2140.4	1998.7
		Axial	1st	2333.3	2474.4	2333.3	2474.3	2333.1	2474.0
			2nd	7000.0	7013.7	6999.9	7013.5	6999.9	7013.0
C	6	In-plane	1st	120.57	126.36	120.94	126.70	122.03	127.75
			2nd	755.63	742.65	756.69	743.64	759.87	746.61
			3rd	2116.4	1985.1	2117.5	1986.2	2121.0	1989.4
		Axial	1st	2332.5	2402.6	2332.5	2402.5	2332.3	2402.2
			2nd	6997.5	6987.6	6997.5	6987.4	6997.5	6986.9
	10	In-plane	1st	120.62	132.17	120.98	132.51	122.07	133.52
			2nd	755.89	753.11	756.95	754.06	760.13	756.89
			3rd	2117.1	1994.6	2118.3	1995.7	2121.7	1998.7
		Axial	1st	2333.3	2474.4	2333.3	2474.3	2333.1	2474.0
			2nd	7000.0	7013.7	6999.9	7013.5	6999.9	7013.0
D	6	In-plane	1st	121.90	126.36	122.27	126.70	123.35	127.75
			2nd	764.00	742.65	765.00	743.64	768.15	746.61
			3rd	2139.7	1985.1	2140.9	1986.2	2144.3	1989.4
		Axial	1st	2193.1	2402.6	2193.0	2402.5	2192.8	2402.2
			2nd	6579.2	6987.6	6579.2	6987.4	6579.1	6986.9
	10	In-plane	1st	123.01	132.17	123.37	132.51	124.44	133.52
			2nd	770.86	753.11	771.90	754.06	775.02	756.89
			3rd	2159.1	1994.6	2160.2	1995.7	2163.6	1998.7
		Axial	1st	2159.4	2474.4	2159.3	2474.3	2159.2	2474.0
			2nd	6478.2	7013.7	6478.2	7013.5	6478.1	7013.0
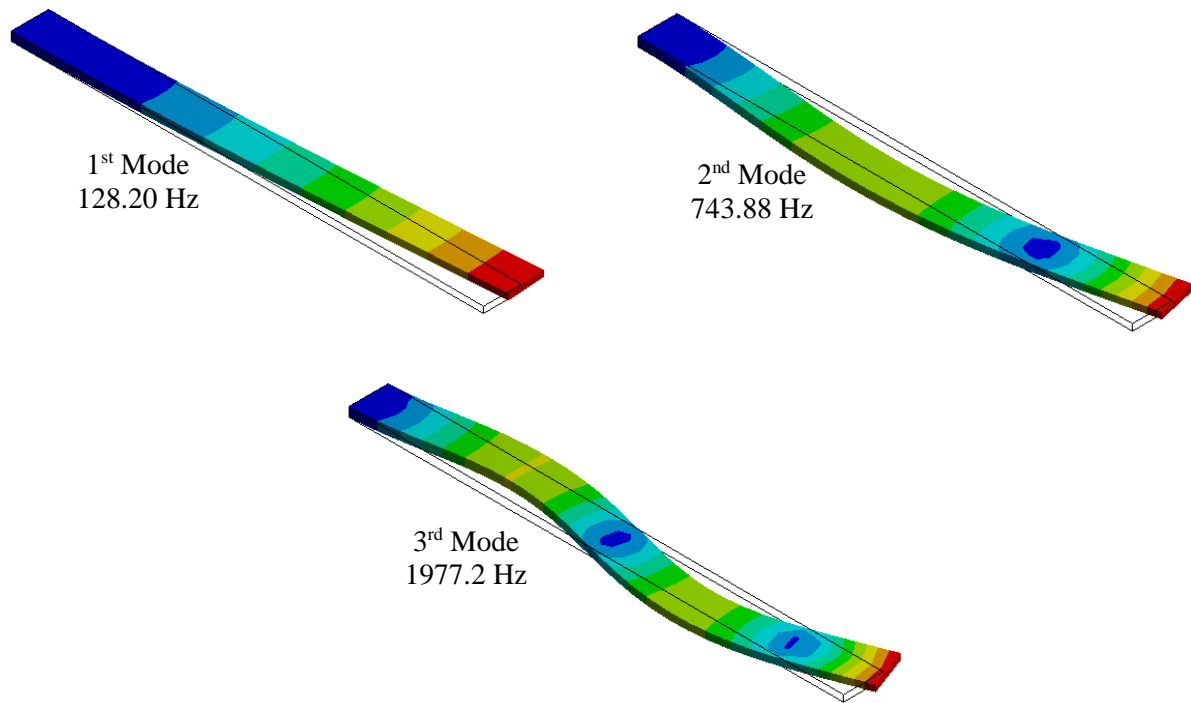
Figure 3.4 First three in-plane bending vibration mode shapes of rotating thickness-tapered cantilever composite beam obtained using ANSYS
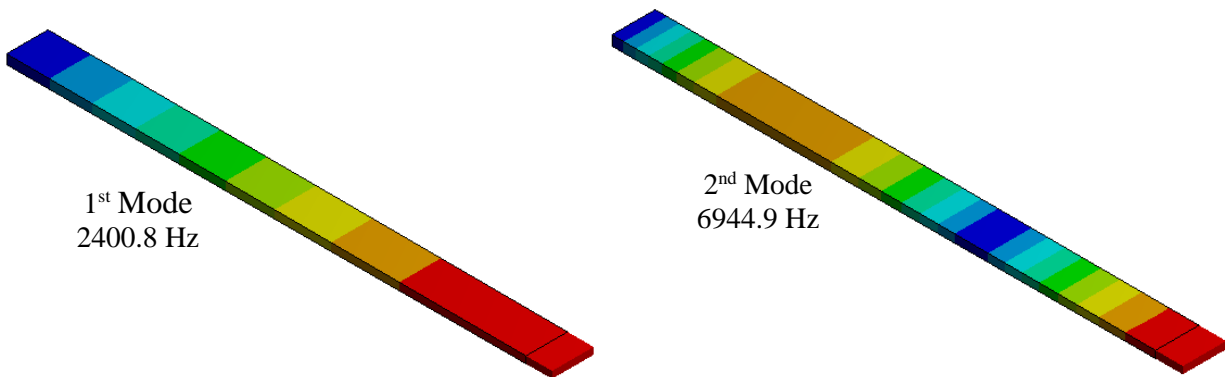
Figure 3.5 First two axial vibration mode shapes of rotating thickness-tapered cantilever composite beam obtained using ANSYS

3.4.3 Validation step-3: Doubly-tapered rotating cantilever composite beam

In this validation step, rotating doubly-tapered cantilever composite beam is considered to validate the R-R results with ANSYS results. Different values of width-ratio are considered for different thickness-taper configurations. The length of the cantilever beam is 25 cm and width at the fixed side is 2 cm. Stacking sequence is $[90]_{18s}$. Rotational velocity is 200 rad/s. In Tables 3.4 and 3.5, '0 rad/s' as rotational velocity is describing the non-rotating condition. In Table 3.4, unit width-ratio ($r_b = 1$) and '0' ply drop-off are describing the uniform-width and uniform-thickness in the composite beam, respectively. Table 3.4 validates the results for taper Configuration-A and Table 3.5 validates the results for Configurations B, C and D. For both tables, number of terms in approximate shape function is 8. Figures 3.6 and 3.7 show the mode shapes for in-plane bending and axial vibrations of rotating (200 rad/s) doubly-tapered ($r_b = 0.1, S = 18$) beam which has taper Configuration-A.

Table 3.4 Natural frequencies (Hz) of in-plane bending and axial vibrations of non-rotating and rotating doubly-tapered cantilever composite beam for Configuration-A

No. of ply drop-off, S			0				18			
r_b	Mode		R-R	ANSYS	R-R	ANSYS	R-R	ANSYS	R-R	ANSYS
			$\Omega = 0$ rad/s		$\Omega = 200$ rad/s		$\Omega = 0$ rad/s		$\Omega = 200$ rad/s	
0.1	In-plane	1st	158.50	159.23	160.15	161.14	167.87	175.02	169.77	176.87
		2nd	511.08	509.56	515.04	514.25	519.50	522.58	523.50	526.93
		3rd	1124.7	1116.6	1129.2	1121.7	1128.5	1118.8	1133.1	1123.6
	Axial	1st	3265.6	3257.0	3265.4	3256.6	3373.3	3430.9	3373.2	3430.6
		2nd	7637.8	7623.1	7637.7	7622.6	7630.1	7608.2	7630.0	7607.8
0.5	In-plane	1st	130.90	130.81	132.00	132.46	140.16	146.49	141.61	148.05
		2nd	627.00	621.02	630.82	625.39	636.70	635.76	640.57	639.65
		3rd	1618.1	1562.8	1622.4	1567.5	1617.8	1557.5	1622.2	1561.8
	Axial	1st	2659.0	2652.8	2658.8	2652.4	2768.8	2833.4	2768.6	2833.1
		2nd	7117.4	7106.2	7117.3	7105.6	7095.0	7067.1	7095.0	7066.6
1.0	In-plane	1st	120.35	120.04	121.81	121.48	129.70	135.68	131.51	137.01
		2nd	754.21	732.76	758.46	736.94	765.50	749.57	769.81	753.22
		3rd	2112.4	1980.6	2117.1	1985.2	2107.4	1965.8	2112.1	1969.8
	Axial	1st	2328.2	2323.2	2327.9	2322.7	2434.6	2499.2	2434.4	2498.8
		2nd	6984.5	6977.0	6984.4	6976.3	6950.2	6918.1	6950.1	6917.4

(Configuration-A)

Table 3.5 Natural frequencies (Hz) of in-plane bending and axial vibrations of non-rotating and rotating doubly-tapered ($S = 18$) cantilever composite beams for Configurations B, C and D

|	r_b		Mode	R-R	ANSYS	R-R	ANSYS
				0 rad/s		200 rad/s	
Configuration-B	0.1	In plane	1st	159.06	187.20	161.03	189.00
			2nd	512.90	541.34	517.61	545.50
			3rd	1128.7	1148.3	1133.9	1152.9
		Axial	1st	3277.1	3611.5	3276.9	3611.2
			2nd	7664.7	7815.5	7664.6	7815.1
	0.5	In plane	1st	134.97	158.13	136.06	159.62
			2nd	646.57	660.78	650.30	664.42
			3rd	1668.7	1601.2	1672.9	1605.1
		Axial	1st	2668.3	2997.1	2668.2	2996.7
			2nd	7142.4	7255.1	7142.4	7254.6
	1.0	In plane	1st	124.10	146.91	125.53	148.18
			2nd	777.79	780.49	781.91	783.86
			3rd	2178.5	2022.7	2182.9	2026.3
		Axial	1st	2336.5	2648.3	2336.1	2647.8
			2nd	7009.1	7100.8	7009.0	7100.2
Configuration-C	0.1	In plane	1st	159.06	186.17	160.70	187.99
			2nd	512.88	541.84	516.82	545.97
			3rd	1128.6	1138.7	1133.1	1143.3
		Axial	1st	3277.1	3614.7	3276.9	3614.4
			2nd	7664.7	7820.3	7664.6	7819.9
	0.5	In plane	1st	131.34	158.13	132.45	159.62
			2nd	629.19	660.78	633.01	664.42
			3rd	1623.8	1601.2	1628.1	1605.1
		Axial	1st	2668.4	2997.1	2668.2	2996.7
			2nd	7142.4	7255.1	7142.4	7254.6
	1.0	In plane	1st	120.77	146.91	122.22	148.18
			2nd	756.87	780.49	761.10	783.86
			3rd	2119.9	2022.7	2124.5	2026.3
		Axial	1st	2336.3	2648.3	2336.1	2647.8
			2nd	7009.0	7100.8	7009.0	7100.2
Configuration-D	0.1	In plane	1st	150.33	187.20	152.07	189.00
			2nd	484.70	541.35	488.90	545.50
			3rd	1066.7	1148.4	1071.5	1152.9
		Axial	1st	3097.2	3611.5	3097.1	3611.2
			2nd	7244.0	7815.5	7243.9	7815.1
	0.5	In plane	1st	124.13	158.13	125.31	159.62
			2nd	594.65	660.79	598.70	664.42
			3rd	1534.7	1601.2	1539.2	1605.1
		Axial	1st	2521.9	2997.1	2521.7	2996.7
			2nd	6750.4	7255.2	6750.3	7254.7
	1.0	In plane	1st	114.14	146.91	115.68	148.18
			2nd	715.32	780.49	719.80	783.87
			3rd	2003.5	2022.7	2008.4	2026.3
		Axial	1st	2208.1	2648.3	2207.9	2647.8
			2nd	6624.3	7100.8	6624.2	7100.3

83
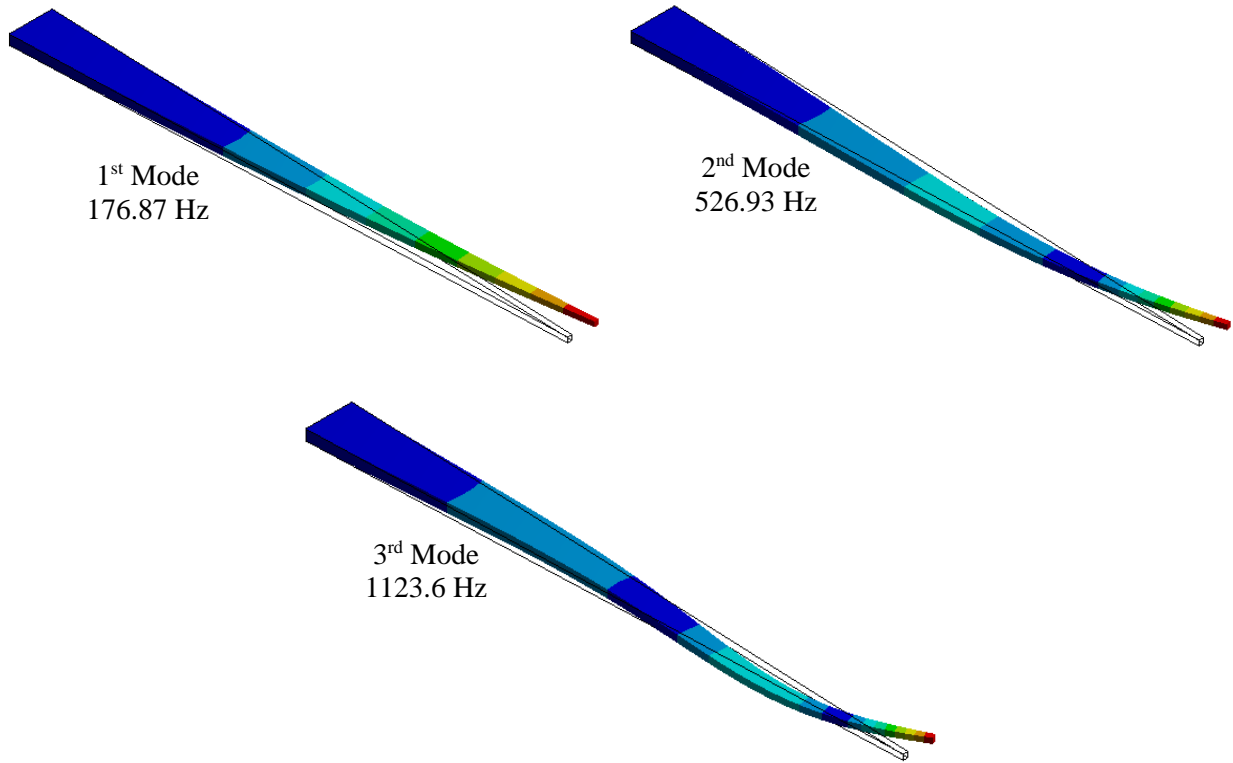
Figure 3.6 First three in-plane bending vibration mode shapes of doubly-tapered rotating cantilever composite beam (Configuration-A) obtained using ANSYS
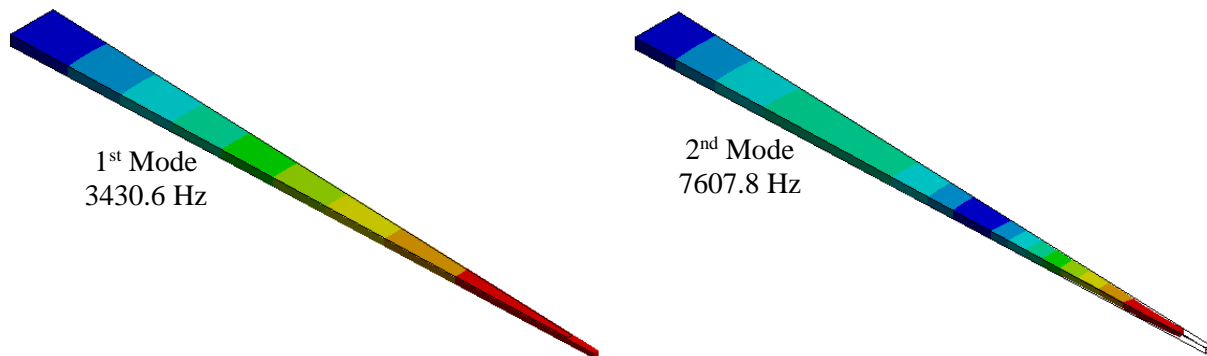
Figure 3.7 First two axial vibration mode shapes of doubly-tapered rotating cantilever composite beam (Configuration-A) obtained using ANSYS

3.5 Mode shapes determination

Having the eigenvectors obtained from equation (3.35), one can have the mode shapes of doubly-tapered $(L = 25 \text{ cm}, b_0 = 2 \text{ cm}, r_b = 0.1, S = 18)$ rotating cantilever laminated

($[90]_{18s}$) composite beams for in-plane bending and axial vibrations. In Figures 3.8 and 3.9, mode shapes of non-rotating and rotating (200 rad/s) uniform cantilever composite beams and doubly-tapered cantilever laminated composite beams (Configuration-A) are illustrated, respectively. They show that except the first mode, mode shapes are the same for non-rotating and rotating conditions. Also, one can observe that due to absence of Coriolis term and due to the cross-sectional plane of symmetry, mode shapes obtained are uncoupled and among the first six mode shapes obtained from equation (3.35), the first, second, third and fifth are in-plane bending vibration modes and fourth, sixth are axial vibration modes. Also, for doubly-tapered composite beam among the first eight mode shapes, the first, second, third, fourth, sixth and seventh are in-plane bending vibration modes and fifth and eighth are axial vibration modes. Also, it can be understood from Figures 3.8 and 3.9 that the maximum displacements for uniform beam are higher than that of the doubly-tapered beam in both non-rotating and rotating conditions.
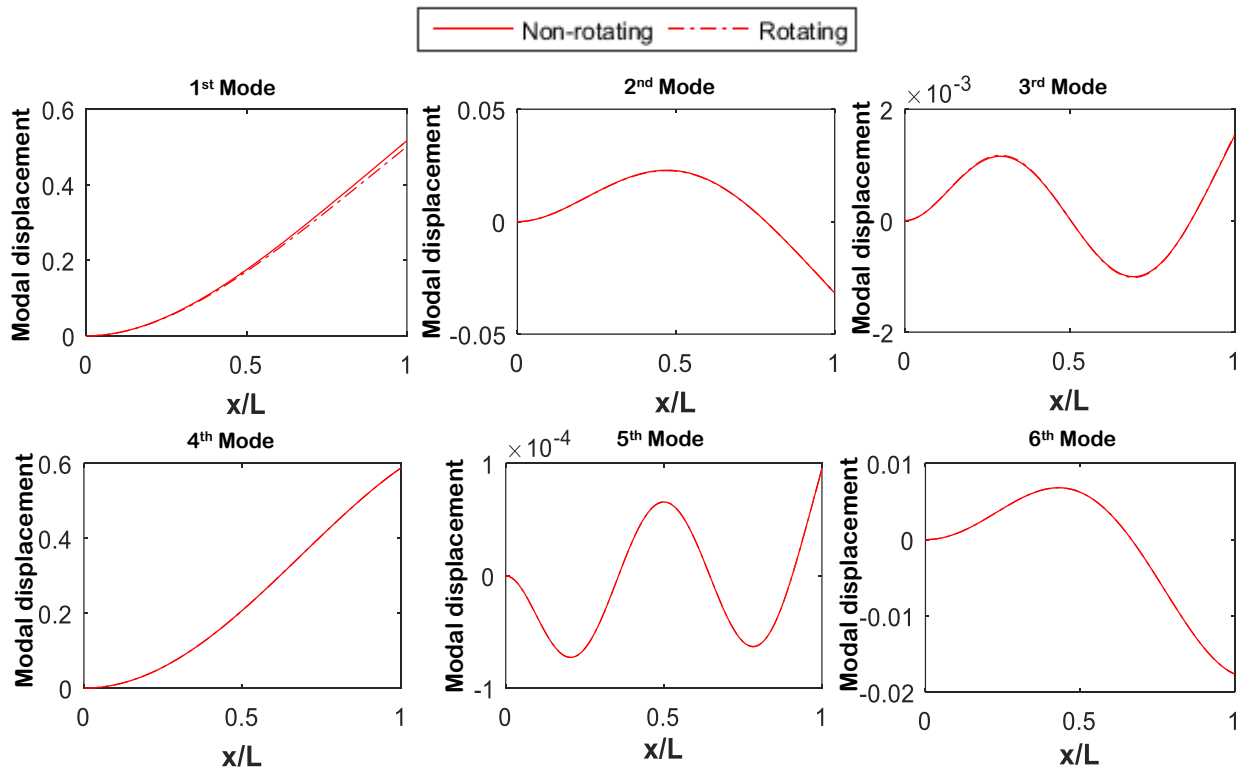
Figure 3.8 Mode shapes of non-rotating and rotating uniform cantilever composite beam

85
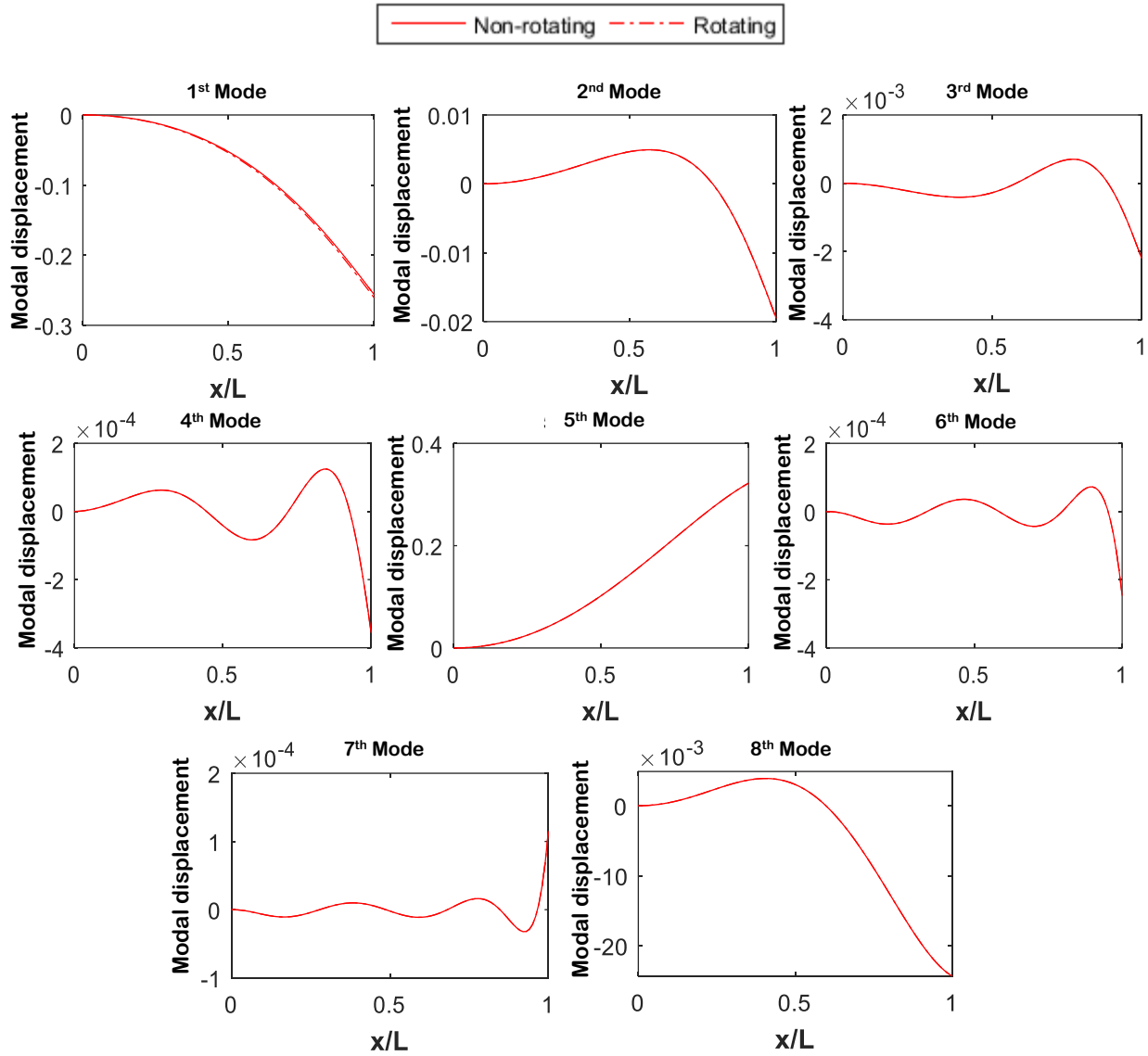
Figure 3.9 Mode shapes of non-rotating and rotating doubly-tapered cantilever composite beam

Figure 3.10 illustrates the first three in-plane bending and first two axial mode shapes for rotating (200 rad/s) doubly-tapered cantilevered laminated composite beam considering different taper configurations. It shows that for every mode, mode shapes are almost same for Configuration-B, C and D and maximum displacement for Configuration-A is the lowest among all the configurations considered.
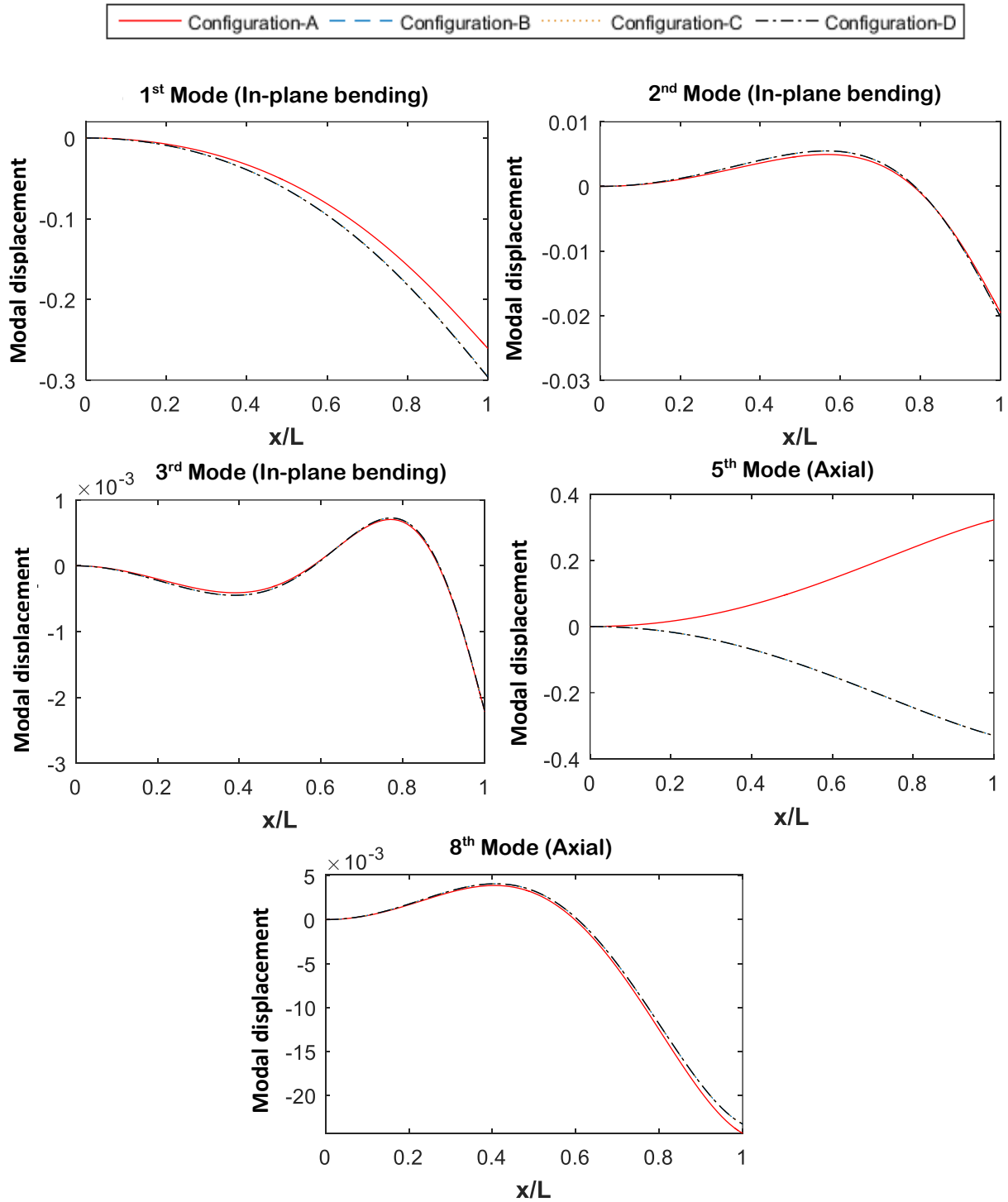
Figure 3.10 First three in-plane bending and first two axial vibrational mode shapes of rotating doubly-tapered beams for different taper configurations

3.6 Free vibration analysis

In this section, a set of graphs are plotted to understand the influences of different system parameters on the natural frequencies of in-plane bending and axial vibrations. Mechanical properties of materials used in this section are given in Tables 2.1 and 2.2.

3.6.1 Effect of rotational velocity

In order to understand the effect of rotational velocity on the natural frequencies of in-plane bending and axial vibrations, five different types of cantilever beams are considered where one has uniform-thickness and uniform-width, and four others are doubly-tapered ($S = 18, r_b = 0.1$) beams with four different taper configurations. The beam length, width at fixed side and hub radius are given in Table 2.3 and Table 2.4. The stacking sequence of the laminated beam is [90]$_{18s}$.

Figures 3.11 and 3.12, illustrate the variation of the first three in-plane bending and the first two axial natural frequencies, respectively, for various rotational velocities. It can be stated from the Figure 3.11 that for uniform or doubly-tapered beam, first three natural frequencies of in-plane bending vibration increase as the rotational velocity increases. Figure 3.12 for axial vibration illustrates that first two natural frequencies slightly decrease as the rotational velocity increases. Figure for first natural frequency of in-plane bending vibration and first two natural frequencies of axial vibrations show that doubly-tapered beam with any configuration has higher natural frequencies than uniform composite beam in both rotating and non-rotating conditions. Figure 3.11 for second and third natural frequencies of in-plane bending vibration shows that uniform composite beam has higher natural frequency than doubly-tapered beam in both rotating and non-rotating conditions. Also, it can be stated that, except for the second natural frequency of axial vibration, taper Configuration-A has the highest natural frequency and for both vibrational modes, Configuration-D has lowest natural frequency.
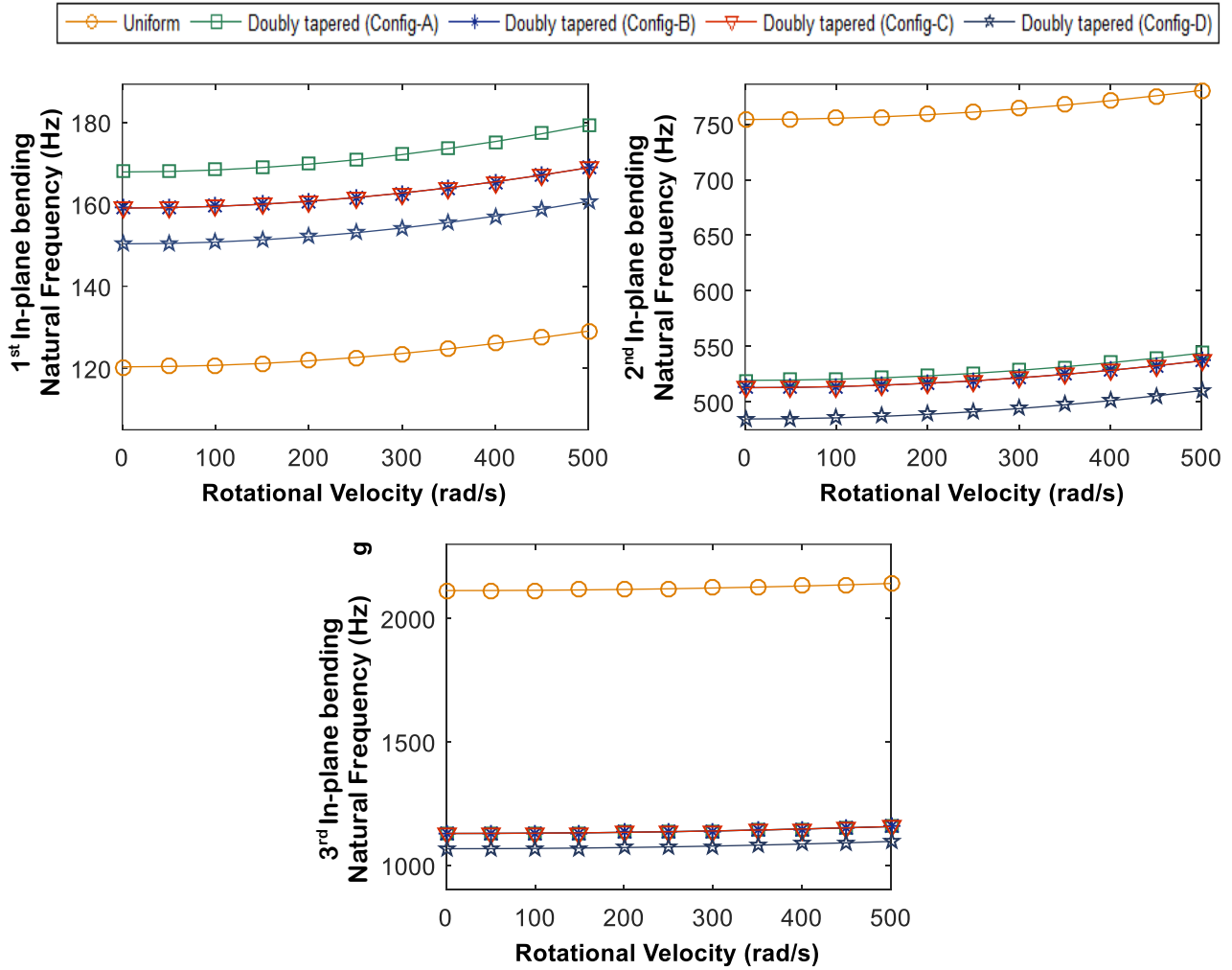
Figure 3.11 Effect of rotational velocity on the natural frequencies of in-plane bending vibration
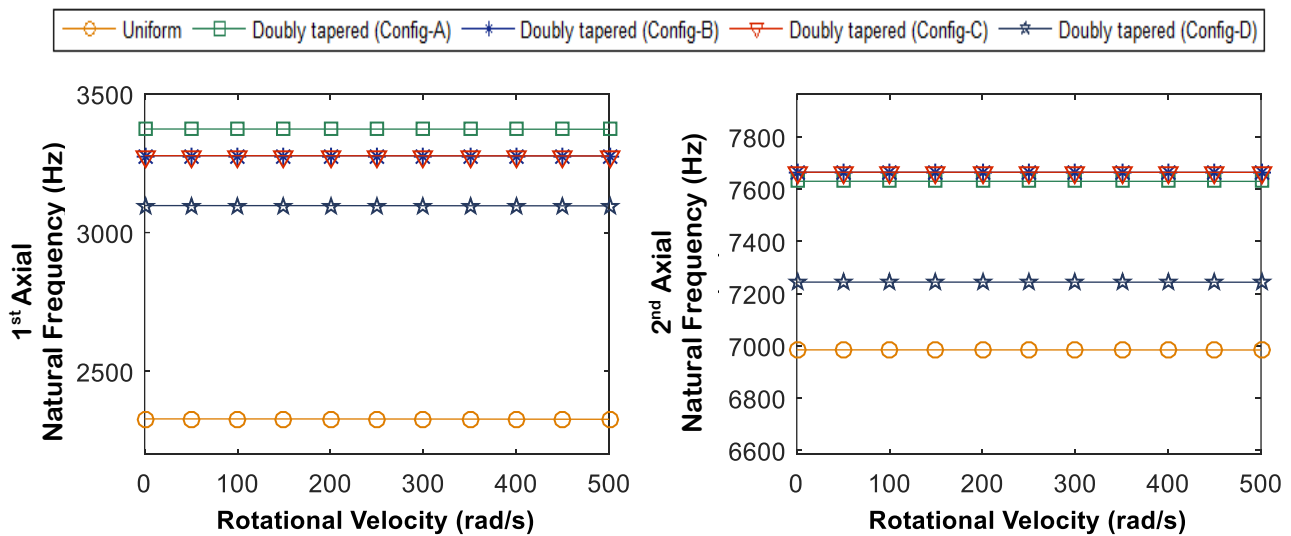
Figure 3.12 Effect of rotational velocity on the natural frequencies of axial vibration

3.6.2 Effect of hub radius to beam length ratio

In this section, doubly-tapered ($S = 18, r_b = 0.1$) rotating cantilever composite beams with four different taper configurations are considered to investigate the effect of hub radius to beam length ratio (R/L) on the natural frequencies of in-plane bending vibration. The rotating doubly-tapered beams have the same length, same stacking sequence and same width at the fixed side as that of section 3.6.1. The rotating velocity of the beam is 200 rad/s. In Figure 3.13, the variation of first three natural frequencies with respect to different values of hub radius to beam length ratio is illustrated. It can be understood from this figure that first three natural frequencies of in-plane bending vibration increase as the hub radius to beam length ratio increases.
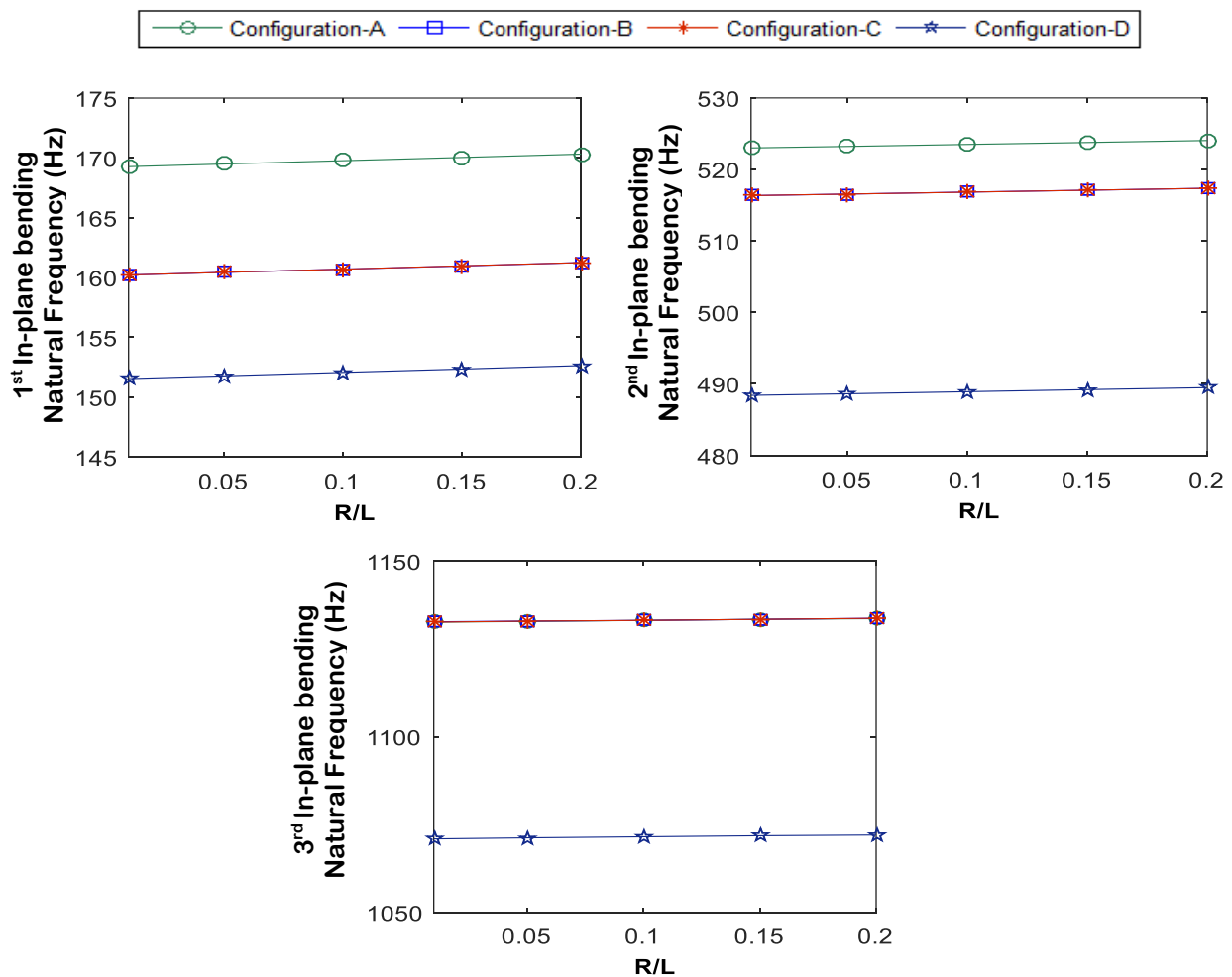
Figure 3.13 Effect of (R/L) on the natural frequencies of in-plane bending vibration

3.6.3 Effect of double-tapering

In this section, the effects of double-tapering on the natural frequencies of in-plane bending and axial vibrations of a rotating cantilever composite beam are studied. The beam length, width at fixed side, stacking sequence and rotating velocity are taken as that of previous section 3.6.2. Hub radius is taken as 0.025 m.

Figures 3.15 and 3.16 show that the first natural frequency of in-plane bending and first two natural frequencies of axial vibrations for all the configurations increase as the double-tapering increases. On the other hand, second and third natural frequencies of in-plane bending vibration decrease as the double-tapering increases. Among all the taper configurations, Configuration-A gives the highest natural frequencies of in-plane bending and axial vibrations for higher double-taper ratio.
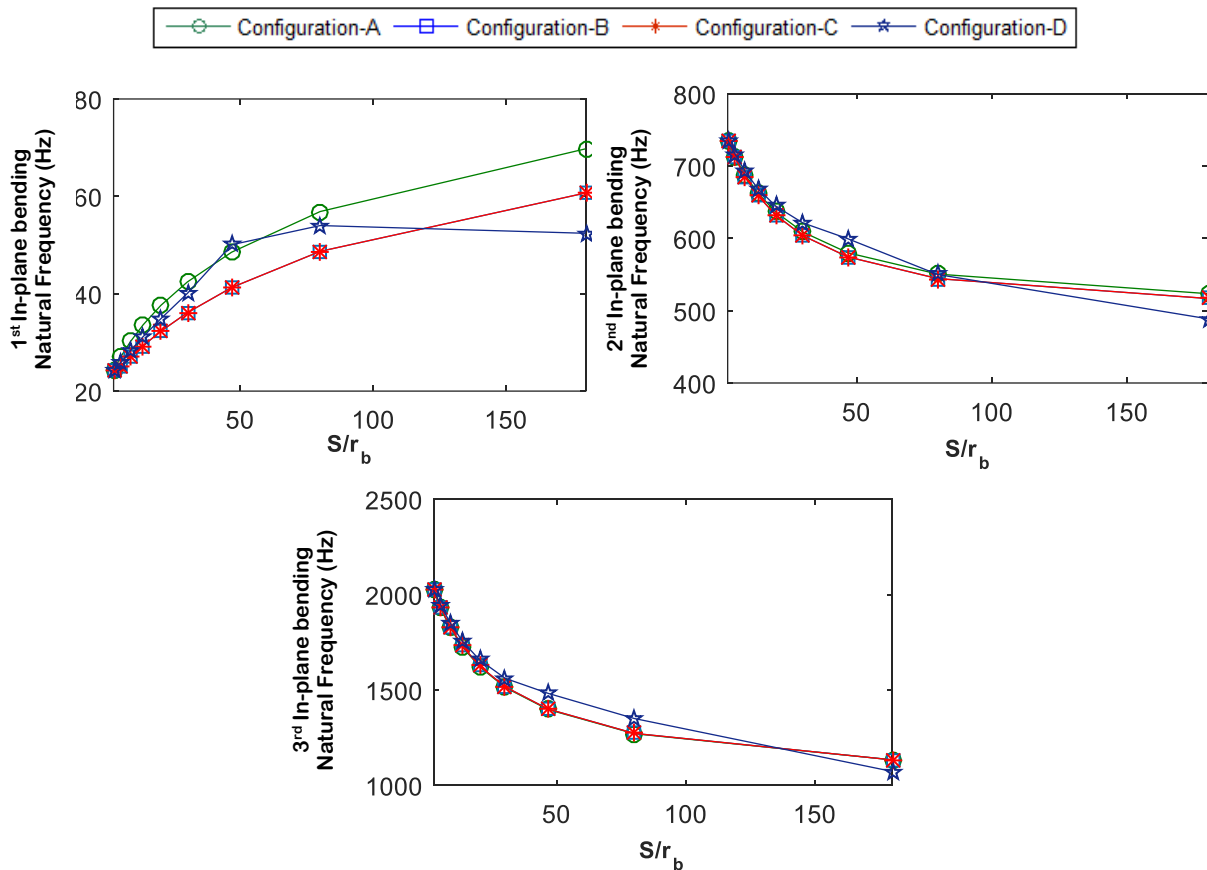
Figure 3.14 Effect of double-tapering on the natural frequencies of in-plane bending vibration
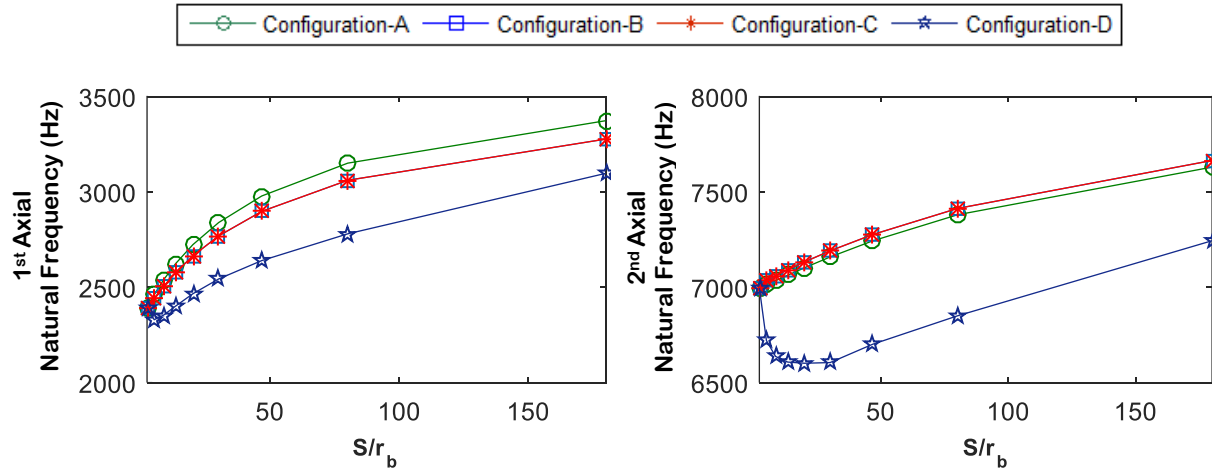
Figure 3.15 Effect of double-tapering on the natural frequencies of axial vibration

3.7   Critical speed determination

To obtain the critical speed of a doubly-tapered rotating cantilever composite beam for in-plane bending vibration, one can consider the equation (3.31) and follow the procedure discussed in section 2.8. Only the first natural frequency of in-plane bending vibration is considered to obtain the first critical speed as first natural frequency of axial vibration is much higher than the first natural frequency of in-plane bending vibration. In this section, Campbell diagram and the direct method both are considered to determine the critical speeds. To compare the critical speed of doubly-tapered cantilever composite beam, four different types of beams are taken as that of section 2.8.1.

In Figure 3.17 one can observe that doubly-tapered beam has highest critical speed that means operating speed for doubly-tapered beam is higher than other types of beams. From Figure 3.17, also, it can be stated that doubly-tapered beam with Configuration-A has the highest operating speed and consequently Configurations B, C and D take the other positions. Critical speeds obtained using the direct method and Campbell diagram are listed in Table 3.6.

92
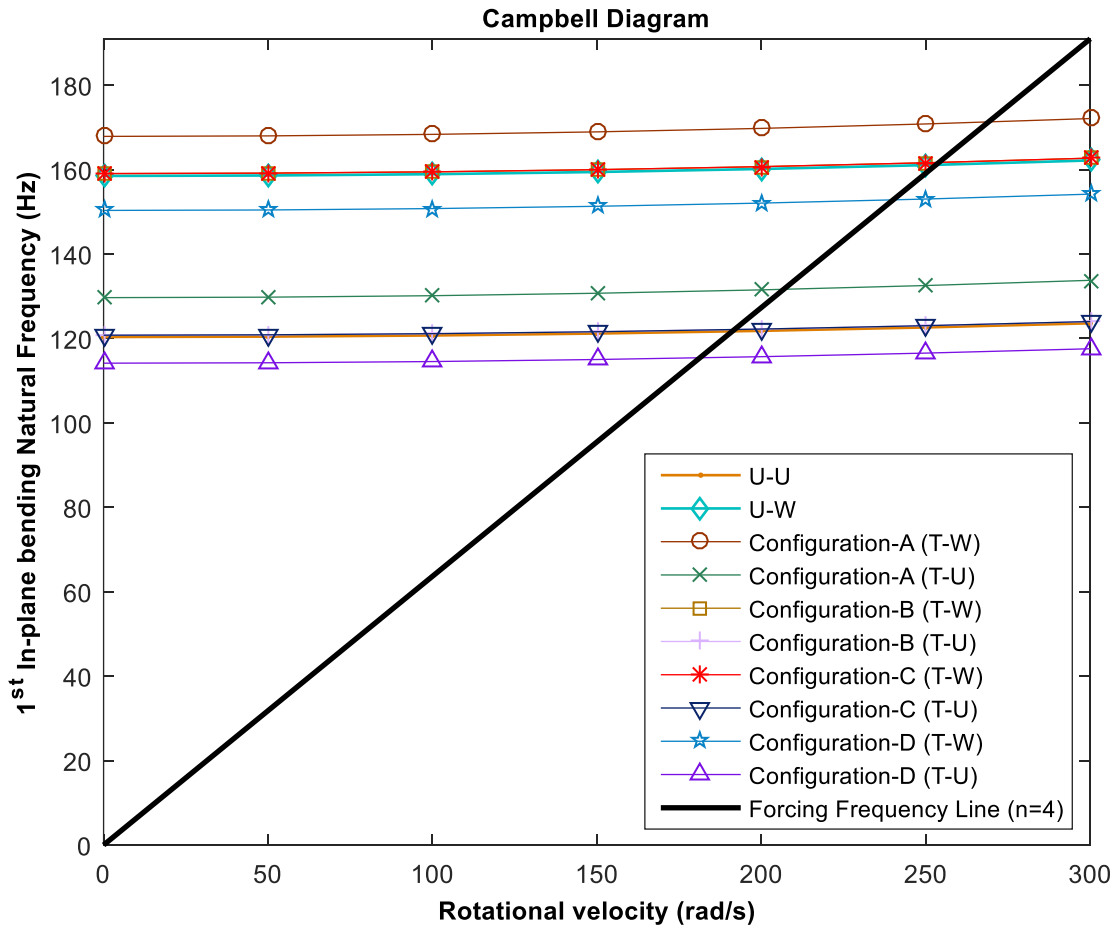
Figure 3.16 Critical speed determination from Campbell diagram for in-plane bending vibration

Table 3.6 Critical speeds (rad/s) calculated using different methods for in-plane bending vibration

Type of beam	Direct method	Campbell diagram
U-U	191.14	191.10
U-W	253.10	253.40
Configuration-A (T-W)	269.05	269.30
Configuration-A (T-U)	206.78	206.50
Configuration-B (T-W)	253.99	253.80
Configuration-B (T-U)	191.81	191.60
Configuration-C (T-W)	253.99	253.80
Configuration-C (T-U)	191.81	191.60
Configuration-D (T-W)	240.05	240.70
Configuration-D (T-U)	181.29	181.70

In Figure 3.18, only beam with configuration-A (T-W) is considered to understand the effect of laminate stacking sequence on critical speed. It can be understood from the Campbell diagram and results from direct method (listed in Table 3.7) that stacking sequence with unidirectional ply ($[0]_{18s}$) has the highest critical speed.
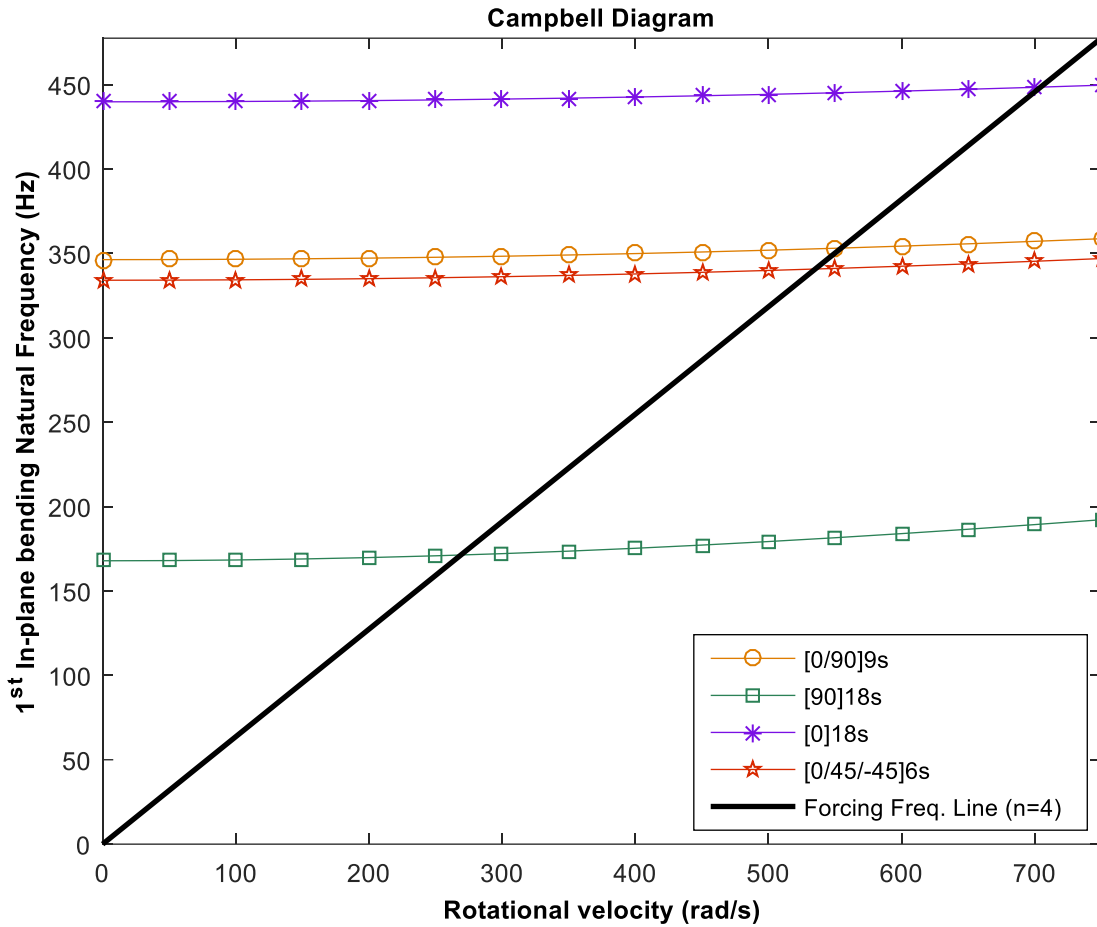
Figure 3. 17 Critical speed determination from Campbell diagram for in-plane bending vibration for different stacking sequences

Table 3.7 Critical speed (rad/s) for different stacking sequences for in-plane bending vibration

Stacking sequence	Direct method	Campbell diagram
$[0/90]_{9s}$	554.00	554.00
$[90]_{18s}$	269.05	269.30
$[0]_{18s}$	704.47	705.50
$[0/45/-45]_{6s}$	535.17	535.40

94

3.8 Dynamic instability analysis

Dynamic instability analysis can be carried out when a rotating structure experiences in-plane bending and axial vibrations. Periodic rotational velocity will result in a parametric excitation on the rotating beam. Periodic rotational velocity can be introduced into the equations of motion for in-plane bending and axial vibration problem, which is given in equation (3.33). The equation (3.33) can be expressed as:

$$[M^{uv}]\{\ddot{\tilde{q}}\} + ([K^{uv*}] + \Omega(t)^2[K_\Omega{}^*])\{\tilde{q}\} = \{0\} \tag{3.40}$$

where, $[K^{uv*}] = \begin{bmatrix} [K^u] & [0] \\ [0] & [K^v] \end{bmatrix}$ and $[K_\Omega{}^*] = \begin{bmatrix} -[K^{cu*}] & [0] \\ [0] & [K_1{}^{cv*}] - [K_2{}^{cv*}] \end{bmatrix}$

If periodic rotational velocity is employed in the system, dynamic instability can be observed. The region of dynamic instability can be found through Bolotin's method. Substituting $\Omega(t)$ from equation (2.54) into the equation (3.40) yields:

$$[M^{uv}]\{\ddot{\tilde{q}}\} + \left\{[K^{uv*}] + \left(\Omega_0{}^2 + 2\Omega_0{}^2\beta\sin\theta_p t + \frac{\Omega_0{}^2\beta^2}{2}\left(1 - \cos2\theta_p t\right)\right)[K_\Omega{}^*]\right\}\{\tilde{q}\} = 0 \tag{3.41}$$

In order to find the periodic matrix solution of this Mathieu type equation with period $2T$ one can take Bolotin's first approximation [31], and the periodic matrix solution with period $2T$ can be sought in the form:

$$\{\tilde{q}\} = \sum_{r=1,3,5\ldots}^{\infty}[\{a_r\}\sin\left(\frac{r\theta_p t}{2}\right) + \{b_r\}\cos\left(\frac{r\theta_p t}{2}\right)] \tag{3.42}$$

Taking one term solution and differentiating two times with respect to time t, leads to

$$\{\ddot{\tilde{q}}\} = [-\frac{\theta_p{}^2}{4}\{a_1\}\sin\left(\frac{\theta_p t}{2}\right) - \frac{\theta_p{}^2}{4}\{b_1\}\cos\left(\frac{\theta_p t}{2}\right)] \tag{3.43}$$

After substituting $\{\tilde{q}\}$ and $\{\ddot{\tilde{q}}\}$ in equation (3.41) and following the same procedure given in section 2.9, one can get two equations for resonance frequency:

$$\theta_p{}^2 = (4[K_\Omega{}^*]\Omega_0{}^2 + 4[K_\Omega{}^*]\Omega_0{}^2\beta + 2[K_\Omega{}^*]\Omega_0{}^2\beta^2 + 4[K^{uv*}])/[M^{uv}] \qquad (3.44)$$

$$\theta_p{}^2 = (4[K_\Omega{}^*]\Omega_0{}^2 - 4[K_\Omega{}^*]\Omega_0{}^2\beta + 2[K_\Omega{}^*]\Omega_0{}^2\beta^2 + 4[K^{uv*}])/[M^{uv}] \qquad (3.45)$$

Equations (3.44) and (3.45) can be solved as eigenvalue problems where each eigenvalue $\theta_p{}^2$ is the square of parametric resonance frequency which gives the boundary between stable and unstable regions in resonance frequency-driving amplitude plane for a system that experiences in-plane bending and axial vibrations. Equations (3.44) and (3.45) give upper and lower boundaries of the instability region, respectively.

3.9 Instability analysis considering different system parameters

Different system parameters (i.e. rotational velocity, hub radius, double-taper ratio and stacking sequence) and different taper conigurations have influences on the dynamic instability of a rotating structure that is vibrating in axial and in-plane bending motions. Following graphs illustrate the effects of various parameter on the width of instability region. The analysis is conducted using taper Configuration A and D. Also, the analysis is conducted considering first three in-plane bending and first two axial vibrational modes. Mechanical properties for composite and resin materials are given in Table 2.1 and 2.2, respectively.

3.9.1 Effect of different taper configurations

Figures 3.18 and 3.19 show the instability regions for first three in-plane bending and first two axial vibrational modes, respectively, for a doubly-tapered $(L = 25\ cm, b_0 = 2\ cm, S = 18, r_b = 0.1, R = .025\ m)$ rotating cantilever composite beam with different taper configurations. The mean value of angular velocity is 50 rad/s and the stacking sequence is [90]$_{18s}$. From Figure 3.18 for first three modes of in-plane bending vibration, it can be stated that beam with Configuration-D has largest width of instability region and Configuration-B has smallest width of instability region. Also, from Figure 3.19 for first two modes of axial vibration, it can be stated

that beam with Configuration-D has largest width of instability region and Configuration-A has smallest width of instability region.
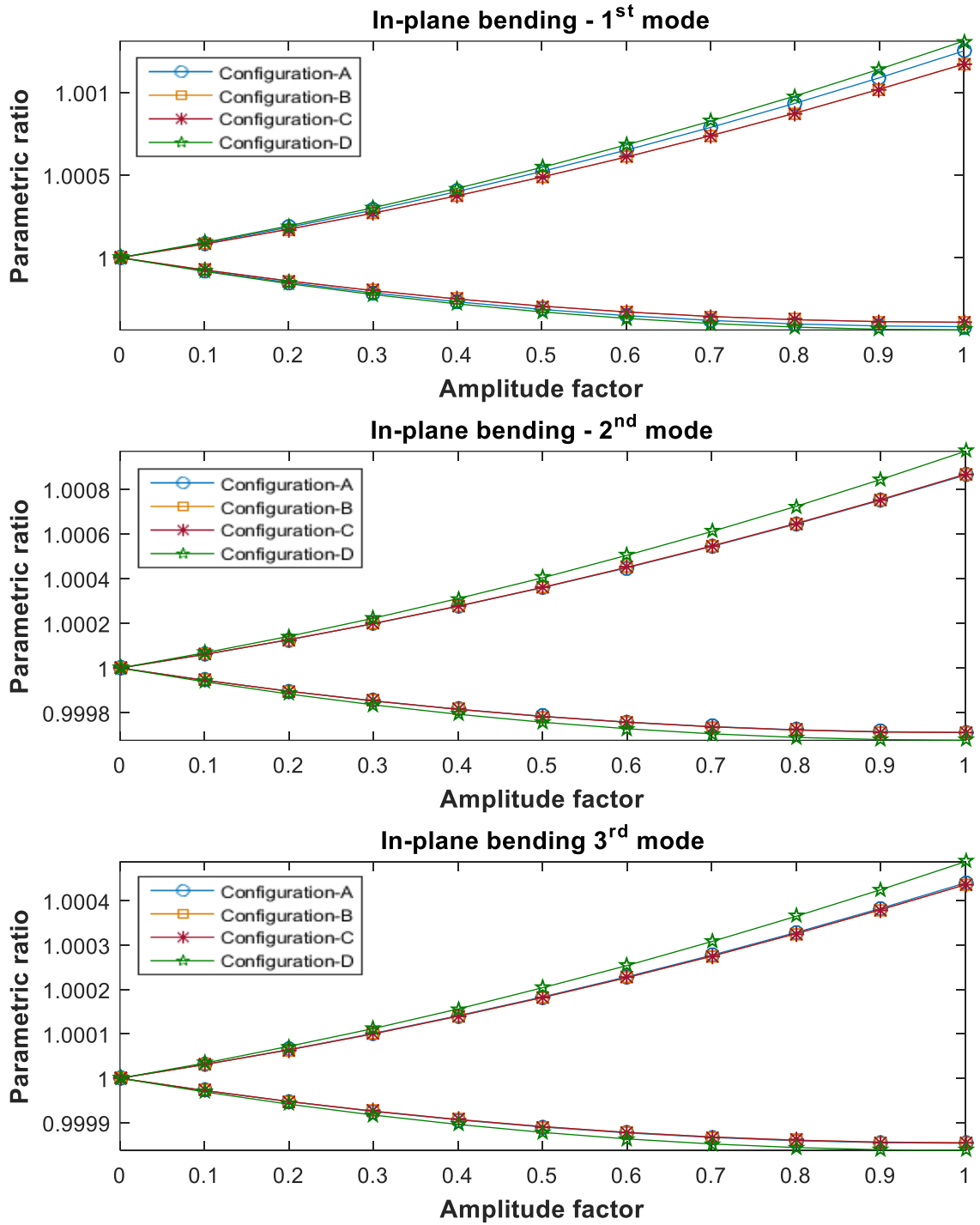
Figure 3.18 Effect of different taper configurations on the widths of instability regions for first three modes of in-plane bending vibration

97
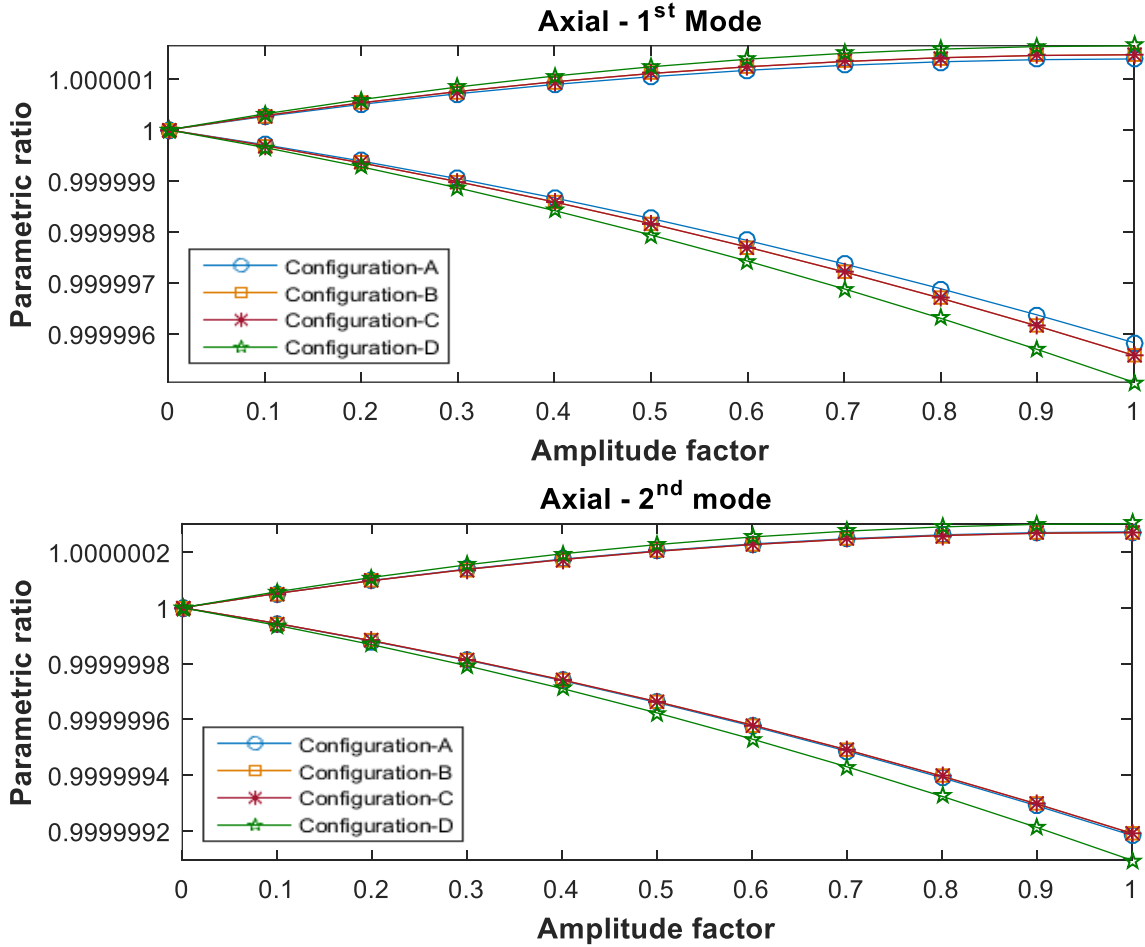
Figure 3.19 Effect of different taper configurations on the widths of instability regions for first two modes of axial vibration

3.9.2 Effect of mean rotational velocity

Figures 3.20 and 3.21 illustrate the behavior of the instability region due to increase of mean rotational velocity for first three modes of in-plane bending and first two modes of axial vibrations, respectively, for a doubly-tapered $(L = 25\ cm, b_0 = 2\ cm, S = 18, r_b = 0.1, R = .025\ m)$ cantilever composite beam. The stacking sequence is $[90]_{18s}$. From Figures 3.20 and 3.21, one can observe that for first three modes of in-plane bending and first two modes of axial vibrations, width of instability region increases as the rotational velocity increases and the width

of instability region for Configuration-A is less than the width of instability region for Configuration-D.

Figure 3.20 Effect of mean rotational velocity on the widths of instability regions for first three modes of in-plane bending vibration
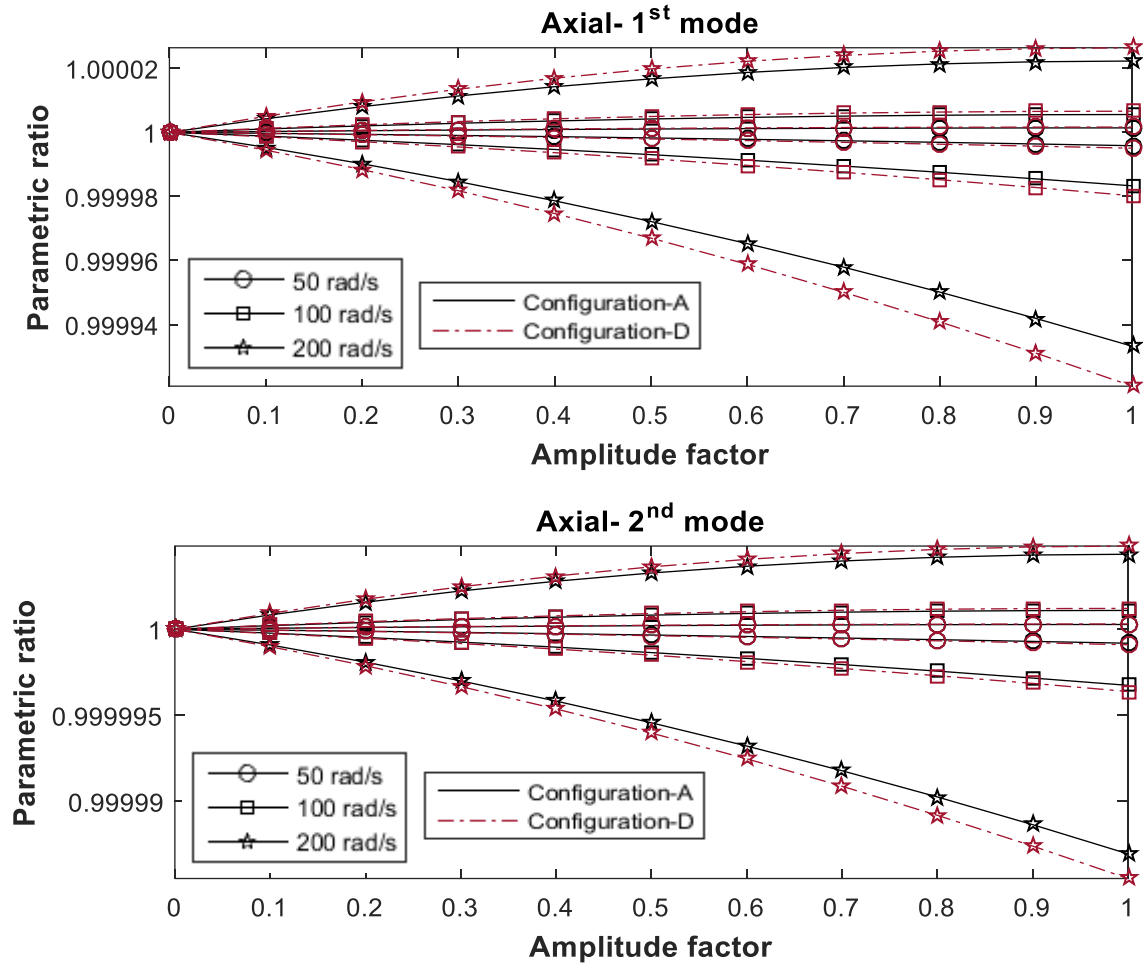
Figure 3.21 Effect of mean rotational velocity on the widths of instability regions for first two modes of axial vibration

3.9.3 Effect of hub radius to beam length ratio

Figures 3.22 and 3.23, illustrate the variation of width of instability region due to changes in the ratio of hub radius over beam length (R/L). The doubly-tapered $(S = 18, r_b = 0.1)$ rotating cantilever composite beam has the same length, same stacking sequence and same width at the fixed side as that of previous section 3.9.2. The mean value of rotational velocity is 50 rad/s. Figure 3.22 for first three modes of in-plane bending vibration shows that the width of instability region increases as the ratio of hub radius to beam length increases. Figure 3.23 for first two modes of axial vibration shows that hub radius has no effect on the dynamic instability of axial vibration.

Also, it can be understood from Figures 3.22 and 3.23, that the width of instability region for Configuration-A is less than the width of instability region for Configuration-D.

Figure 3.22 Effect of hub radius to beam length ratio on the widths of instability regions for first three modes of in-plane bending vibration
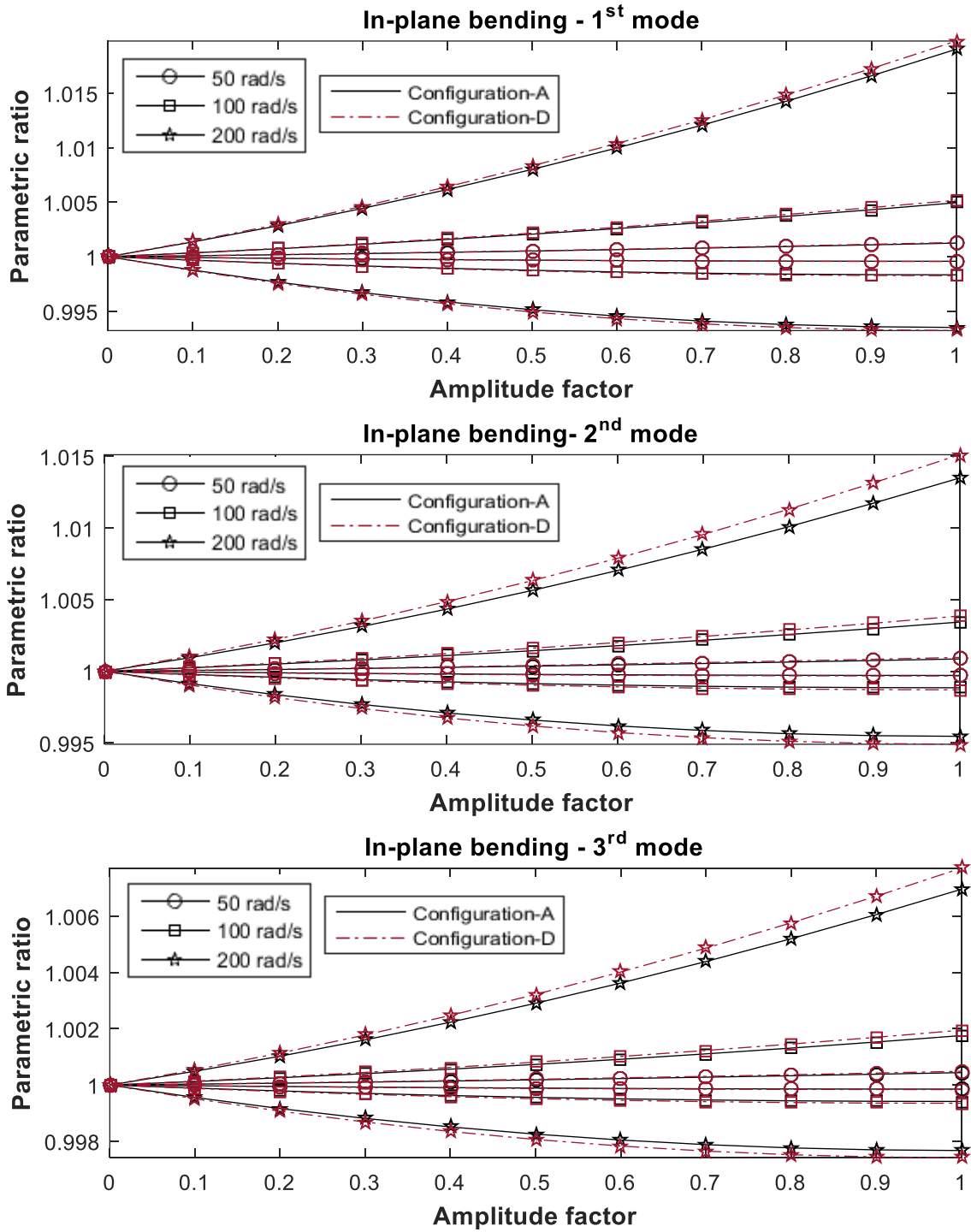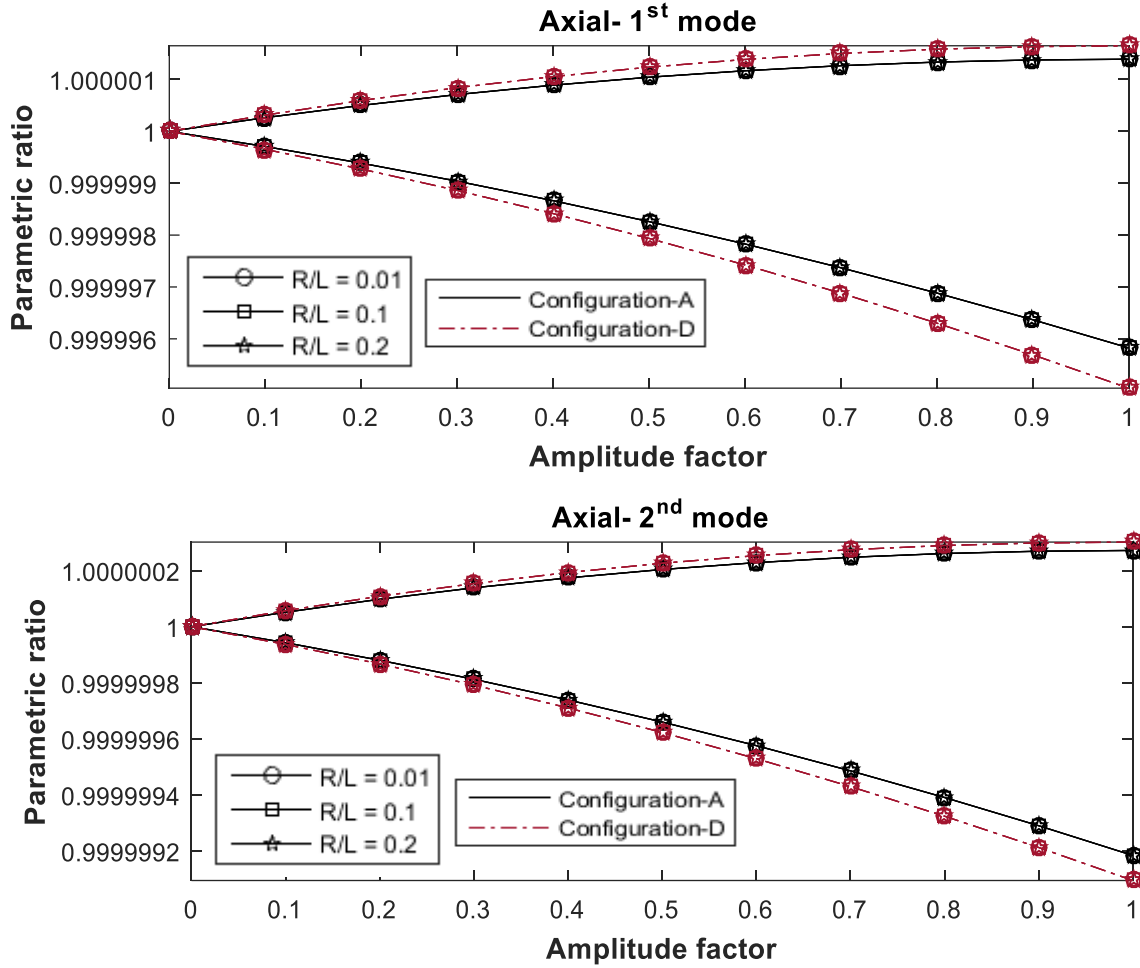
Figure 3.23 Effect of hub radius to beam length ratio on the widths of instability regions for first two modes of axial vibration

3.9.4 Effect of double-tapering

Figures 3.24 and 3.25 show the variation of width of instability region for three different values of double-taper ratio (S/r_b). The beam length, width at fixed side, stacking sequence and mean rotational velocity are taken as same as that of previous section 3.9.3. The hub radius, in this case, is 0.025 m. From Figure 3.24 for first three modes of in-plane bending vibration, it can be stated that increase of double-taper ratio (increase of double-tapering) increases the width of instability region. Figure 3.25 for the first two modes of axial vibration illustrates that increase of double-taper ratio decreases the width of instability region. Also, it can be understood from Figures

3.24 and 3.25, that the width of instability region for Configuration-A is less than the width of instability region for Configuration-D.
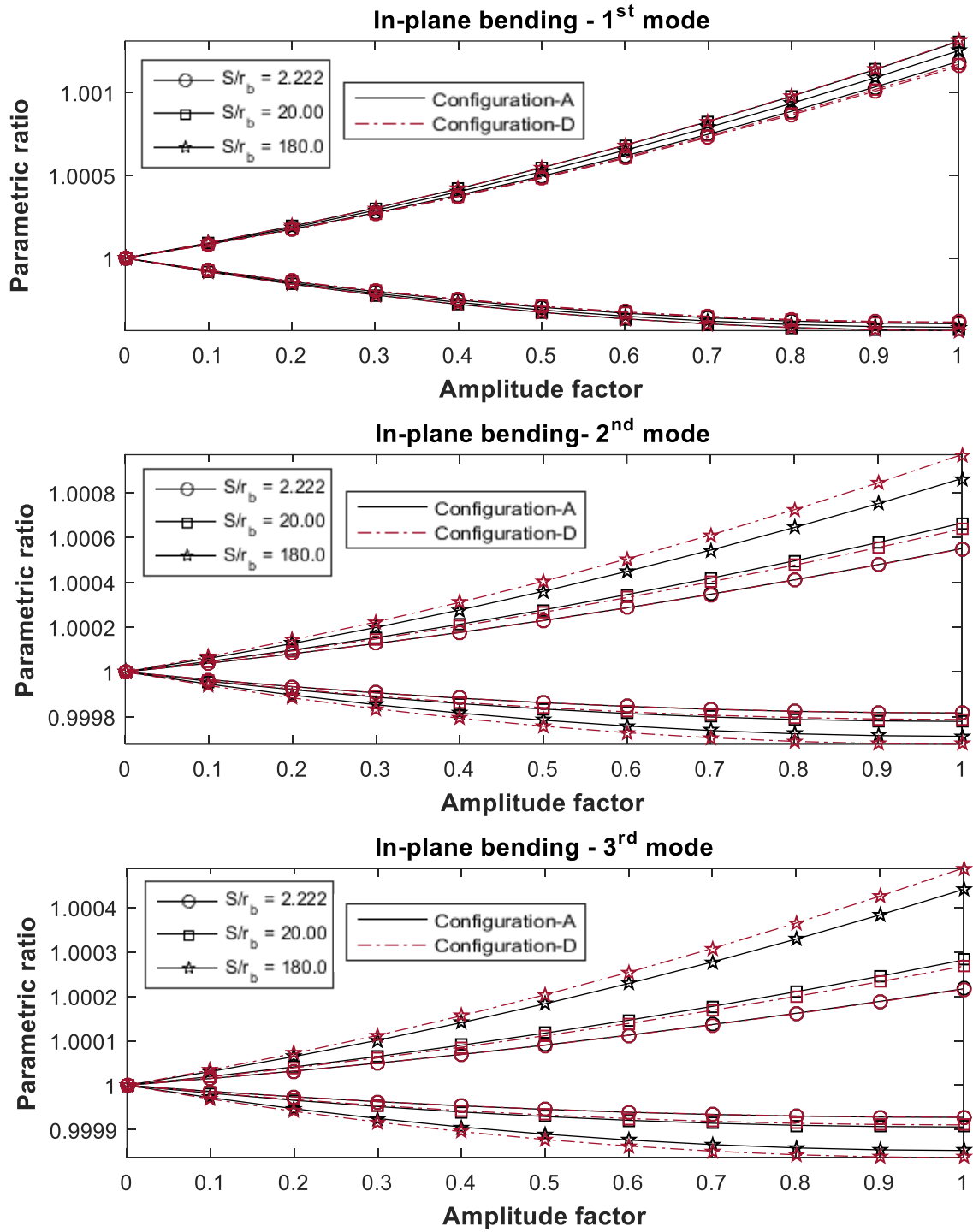
Figure 3.24 Double-tapering effect on the widths of instability regions for first three modes of in-plane bending vibration
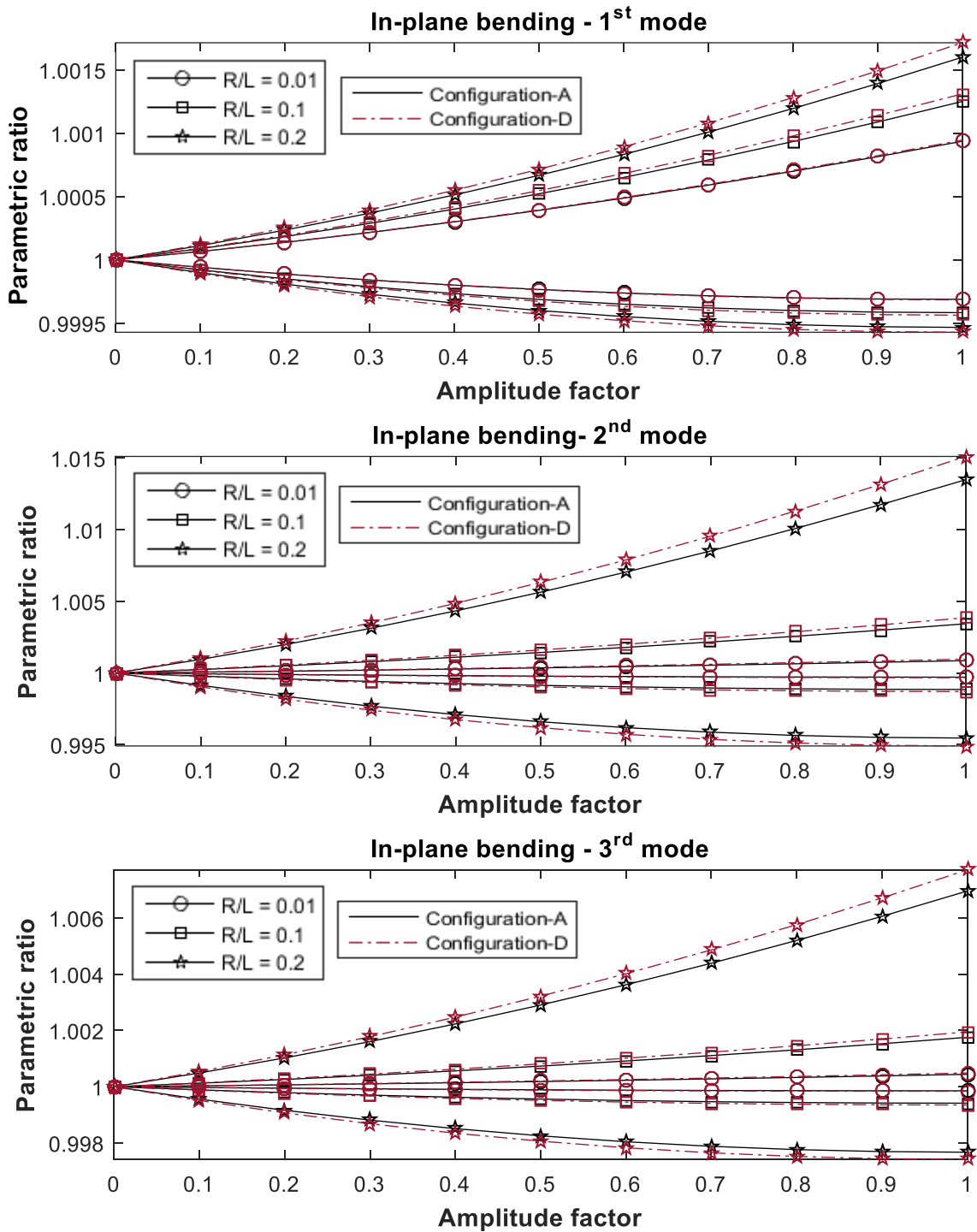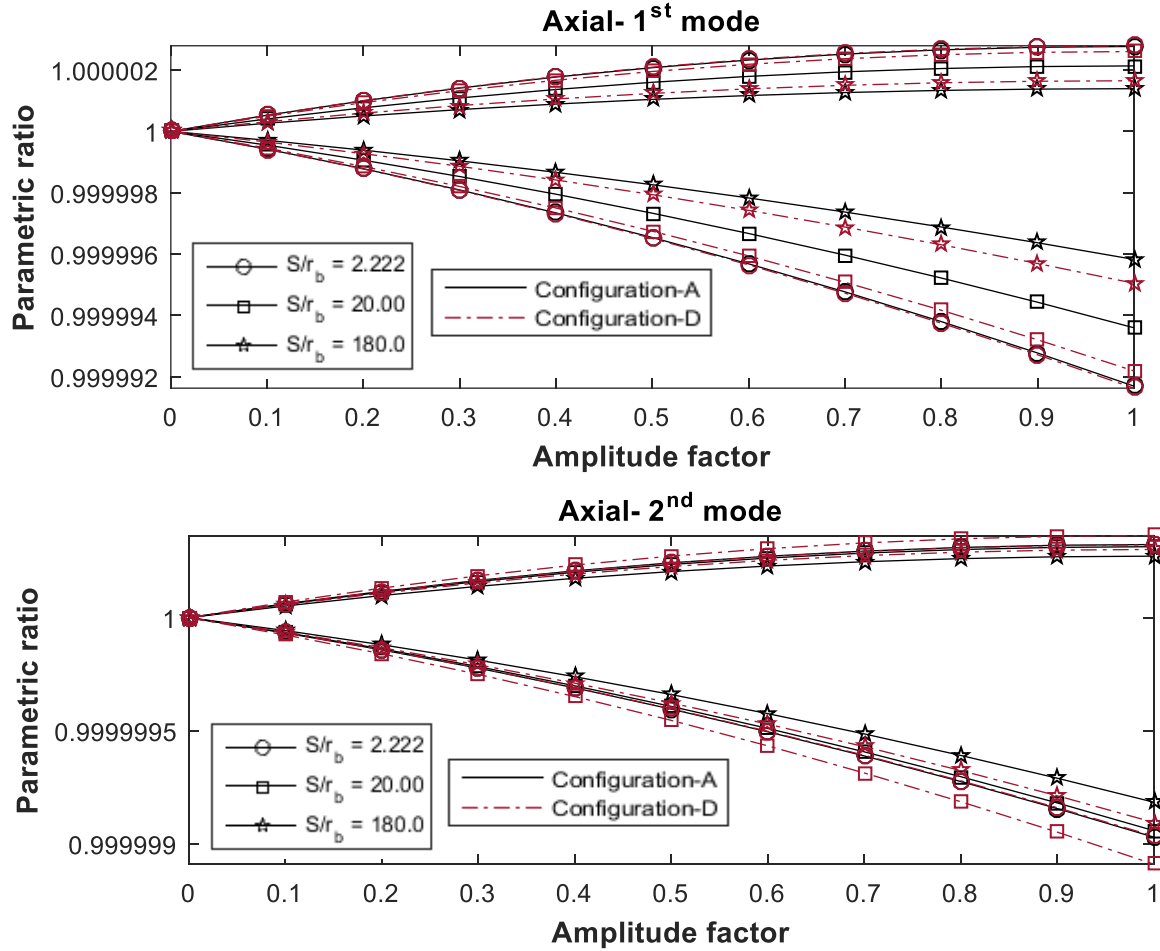
Figure 3.25 Double-tapering effect on the width of instability regions for first two modes of axial vibration

3.9.5 Effect of stacking sequence

In this section, effect of laminate stacking sequence on dynamic instability of in-plane bending and axial vibrations are studied. The doubly-tapered $(S = 18, r_b = 0.1)$ rotating cantilever composite beam has the same length, same width at fixed side, same hub radius and same mean rotational velocity as that of previous section 3.9.4. From Figure 3.26 for first two modes of axial vibration, it can be observed that Configuration-A follow the same consequence as that of in-plane bending vibration but in the case of Configuration-D, cross-ply stacking sequence $[0/90]_{9s}$ has smallest width of instability regions and on the other hand, stacking sequence $[90]_{18s}$

and [-45/45/0]$_{6s}$ have largest width of instability region. From Figure 3.27 for first three modes of in-plane bending vibration, it can be observed that unidirectional ply stacking sequence [0]$_{18s}$ has smallest width of instability regions and on the other hand, stacking sequence [90]$_{18s}$ has largest width of instability region. Cross-ply laminate stacking sequence [0/90]$_{9s}$ and angle-ply laminate stacking sequence [-45/45/0]$_{6s}$ have almost same width of instability region. Also, it can be noticed from Figure 3.27, that except for the stacking sequence [90]$_{18s}$, the width of instability region for Configuration-D is less than the width of instability region for Configuration-A.
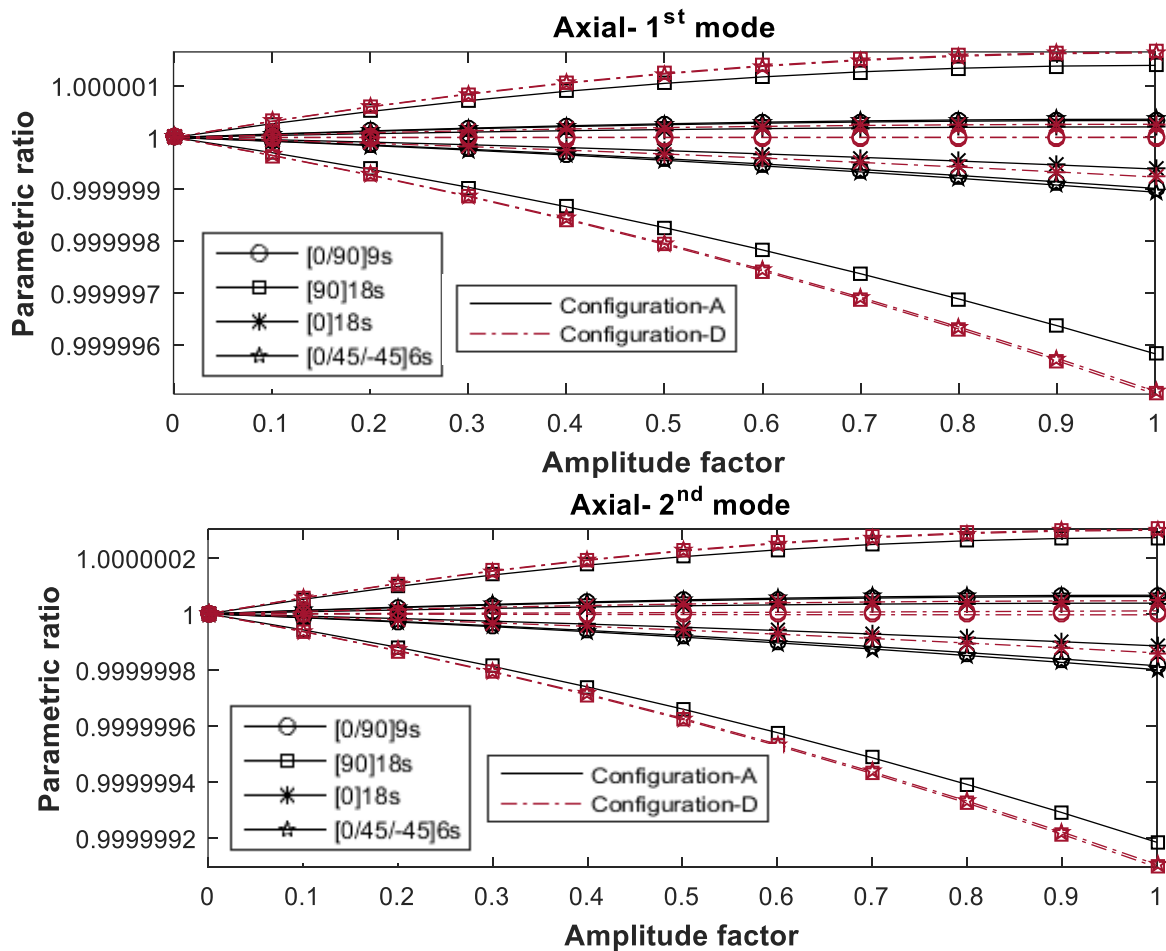
Figure 3.26 Effect of stacking sequence on the widths of instability regions for first two modes of axial vibration

105
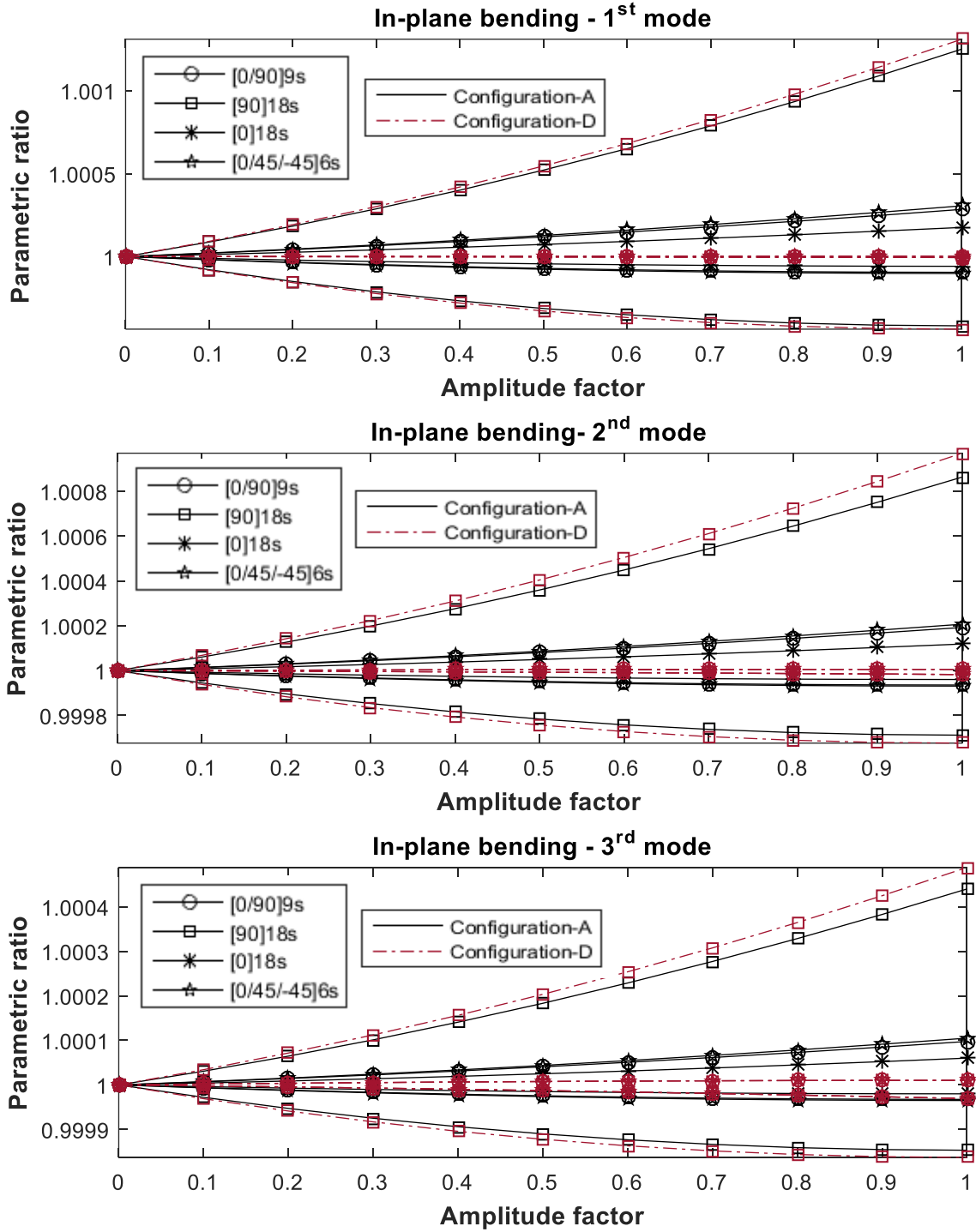
Figure 3.27 Effect of stacking sequence on the widths of instability regions for first three modes of in-plane bending vibration

3.10   Summary

In this chapter, in the first part, the free vibration analysis for in-plane bending and axial vibrations have been investigated for a doubly-tapered rotating cantilever composite beam. Rayleigh-Ritz method based on the Classical Lamination Theory was considered to formulate the problem. MATLAB was used to develop the formulation. The results from R-R method were validated with commercial FEA tool ANSYS. Upon completing the validation, effects of different parameters such as rotational velocity, hub radius, double-taper ratio and stacking sequence on the natural frequencies of in-plane bending and axial vibrations of composite beam are carried out. Based on the results obtained, Configuration-A has highest natural frequencies and Configuration-D has lowest natural frequencies for both in-plane bending and axial vibrations in non-rotating and rotating conditions. It has been observed that rotating velocity significantly increases the natural frequencies of in-plane bending vibration, but natural frequencies of axial vibration slightly decrease due to increase of the rotational velocity. Also, It has been observed that double-tapering increases natural frequencies of in-plane bending and axial vibrations. After the free vibration analysis, critical speed was determined for various types of beams. In this case, doubly-tapered beam has the highest critical speed (operating speed) than uniform beam. Also, beam with unidirectional ply stacking sequence $[0]_{18s}$ has highest critical speed.

In the second part of this chapter, dynamic instability analysis for in-plane bending and axial vibrations has been performed by considering the periodic rotational velocity. Bolotin's method was used to obtain the boundaries of instability region. Different graphs have been plotted to study the effects of different parameters and different taper configurations on the instability region. Based on the results obtained, for in-plane bending vibration, Configuration-B has smallest width of instability region and Configuration-D has largest width of instability region and for axial

vibration Configuration-D has largest width of instability region and Configuration-A has smallest width of instability region. The width of instability region increases with rotational velocity for both in-plane bending and axial vibrational modes. Also, the width of instability region increases with hub radius for in-plane bending vibration. Increase of double-tapering increases the width of instability region for in-plane bending vibration. On the other hand, increase of double-tapering decreases the width of instability region of axial vibration. Unidirectional ply stacking sequence $[0]_{18s}$ has the smallest width of instability region while stacking sequence $[90]_{18s}$ has largest width of instability region for both in-plane bending and axial vibrational modes.

Chapter - 4

Comparative study between out-of-plane bending and in-plane bending vibrations of doubly-tapered rotating composite beam

4.1   Introduction

In chapters 2 and 3, out-of-plane and in-plane bending vibrations of doubly-tapered rotating cantilever composite beam were analyzed, respectively. Chapters 2 and 3 were organized so as to focus on the effects of different parameters on the natural frequencies and instability regions of out-of-plane and in-plane bending vibrations, respectively. Moreover, critical speeds were also determined for both out-of-plane and in-plane bending vibrations.

In this chapter, a comparative study is conducted between out-of-plane and in-plane bending vibrations, in order to: 1) obtain the fundamental natural frequencies of the beam in non-rotating and rotating conditions, 2) identify the significant vibration to determine the first critical speeds, 3) compare the maximum displacements of out-of-plane bending and in-plane bending vibrations, and 4) compare the instability regions of out-of-plane bending and in-plane bending vibrations. To perform this comparative study, a doubly-tapered cantilever composite beam with four different taper configurations is considered. The length of the beam, width at fixed side, width ratio, number of ply drop-off, stacking sequence and the rotational velocity are mentioned in the respective sections. The hub radius is taken as 10 percent of the length of the beam. The material chosen is NCT/301 graphite-epoxy. The mechanical properties of the material are listed in Tables 2.1 and 2.2.

4.2   Fundamental frequency consideration

The fundamental frequency is defined as the lowest natural frequency of a structural system. To identify the fundamental frequencies in non-rotating and rotating doubly-tapered beams ($b_0 = 2\ cm, S = 18, r_b = 0.1, [90]_{18s}$), first natural frequencies of out-of-plane and in-plane bending vibrations are plotted with respect to different values of rotational velocity and different values of beam length. Only the first natural frequencies of out-of-plane bending and in-plane bending vibrations are considered to obtain the fundamental frequency as first natural frequency of axial vibration is much higher than the first natural frequencies of out-of-plane bending and in-plane bending vibrations.

In Figure 4.1, it is shown that in both non-rotating and rotating conditions, when the beam length is small, first natural frequency of in-plane bending vibration is much higher than the first natural frequency of out-of-plane bending vibration. That means for a small length of doubly-tapered beam, out-of-plane vibration is significant and that gives the fundamental frequency for non-rotating and rotating conditions. On the other hand, when the beam length is high (above 80 cm) and the rotational velocity is high, then the first natural frequency of out-of-plane bending vibration becomes higher than the first natural frequency of in-plane bending vibration. This implies that for higher beam length and for higher rotational velocity in-plane bending vibration is significant and that gives the fundamental frequency.
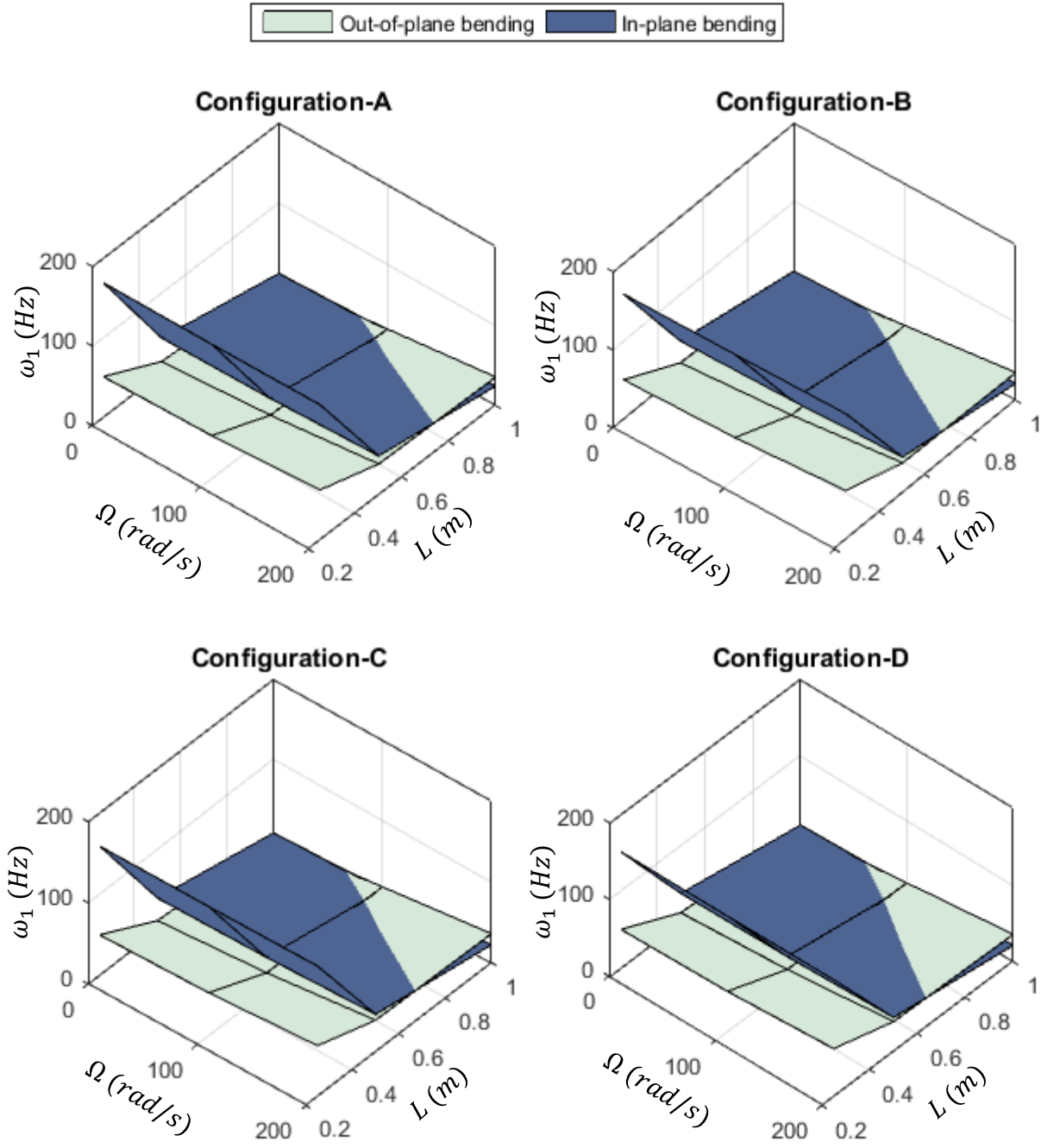
Figure 4.1 First natural frequencies of out-of-plane bending and in-plane bending vibrations with respect to rotational velocity and beam length

In Figures 4.2 and 4.3, second and third natural frequencies of out-of-plane bending and in-plane bending vibrations, respectively, are also plotted with respect to different values of rotational velocity and different values of beam length. From Figures 4.2 and 4.3, it can be

understood that increase of beam length decreases the second and third natural frequencies of out-of-plane and in-plane bending vibrations of doubly-tapered rotating cantilever composite beam.
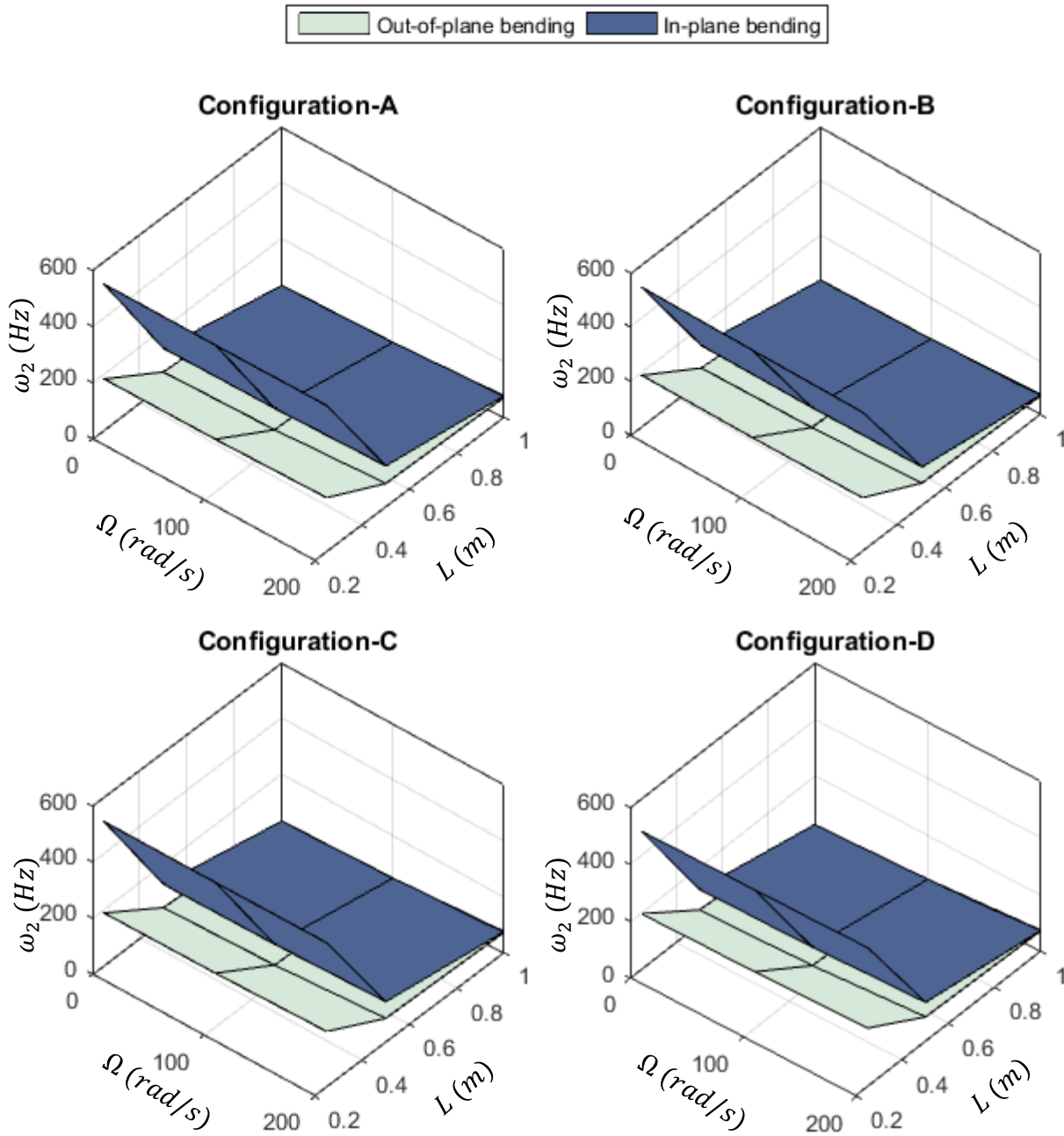
Figure 4.2 Second natural frequencies of out-of-plane bending and in-plane bending vibrations with respect to rotational velocity and beam length
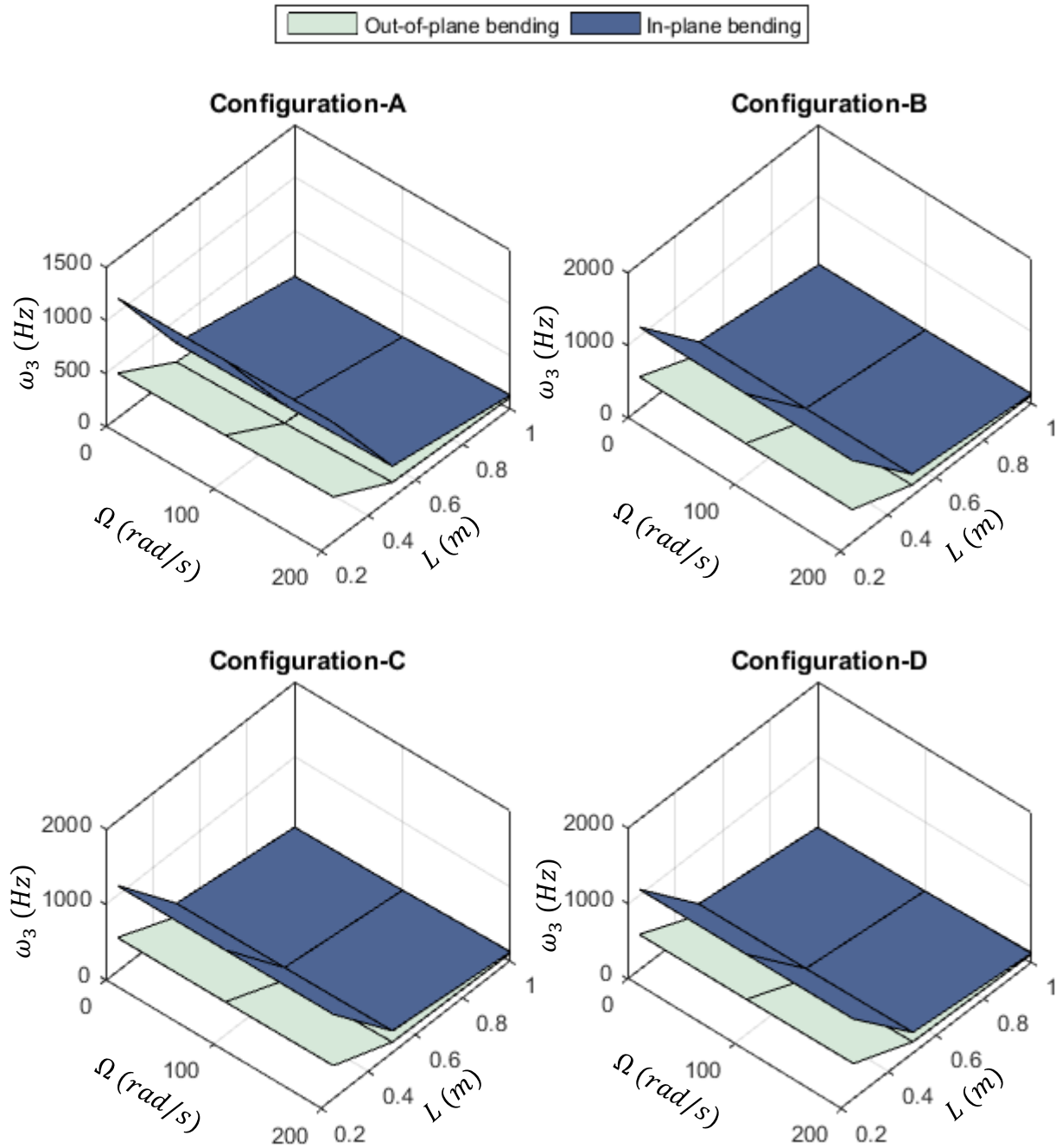
Figure 4.3 Third natural frequencies of out-of-plane bending and in-plane bending vibrations with respect to rotational velocity and beam length

In Figures 4.4 and 4.5, first and second natural frequencies of axial vibration are plotted, respectively, with respect to different values of rotational velocity and different values of beam length. From Figures 4.4 and 4.5, it can be understood that increase of beam length decreases the

first and second natural frequencies of axial vibration of doubly-tapered rotating cantilever composite beam.

Configuration-A

Configuration-B

Configuration-C

Configuration-D
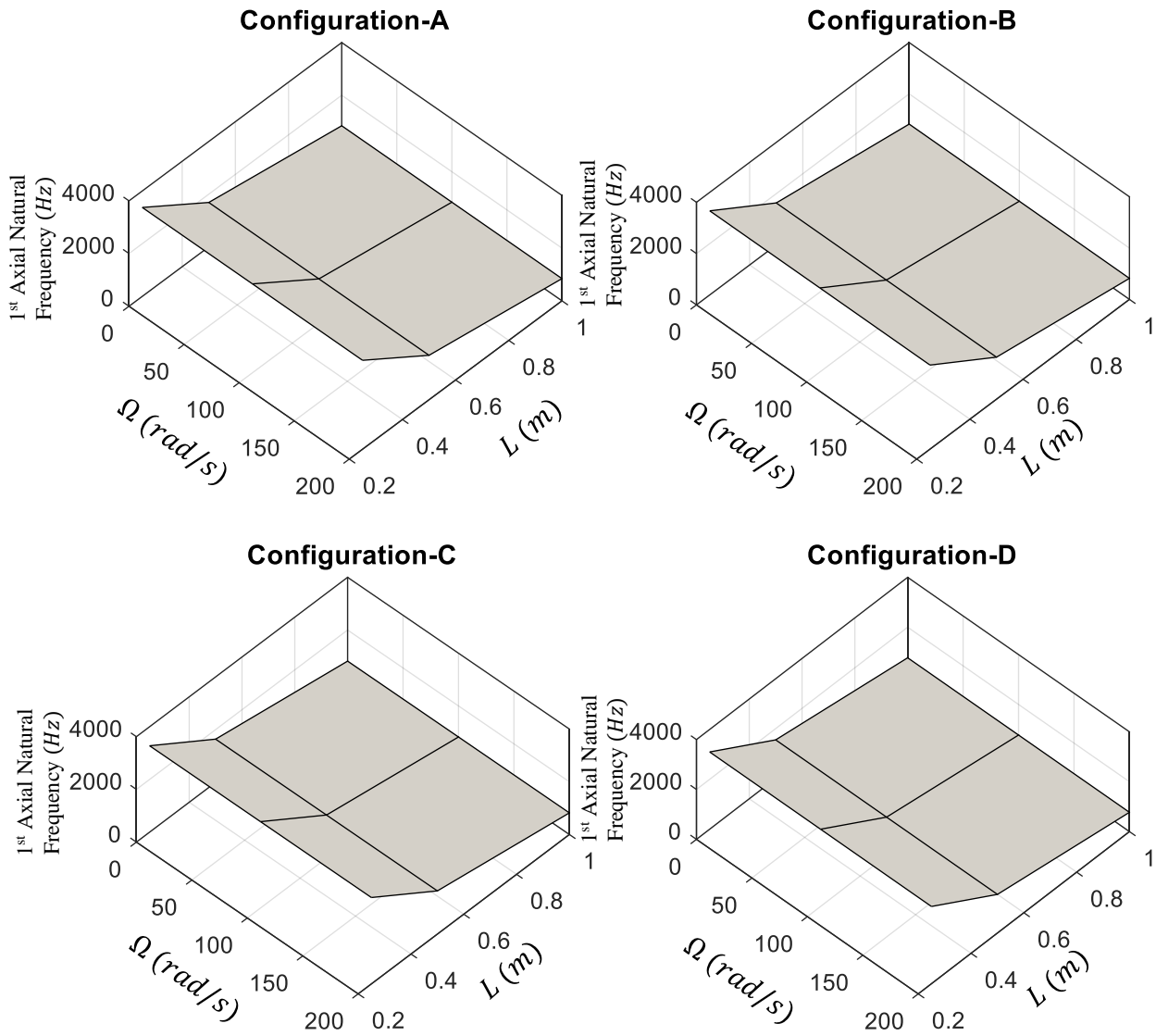
Figure 4.4 First natural frequency of axial vibration with respect to rotational velocity and beam length
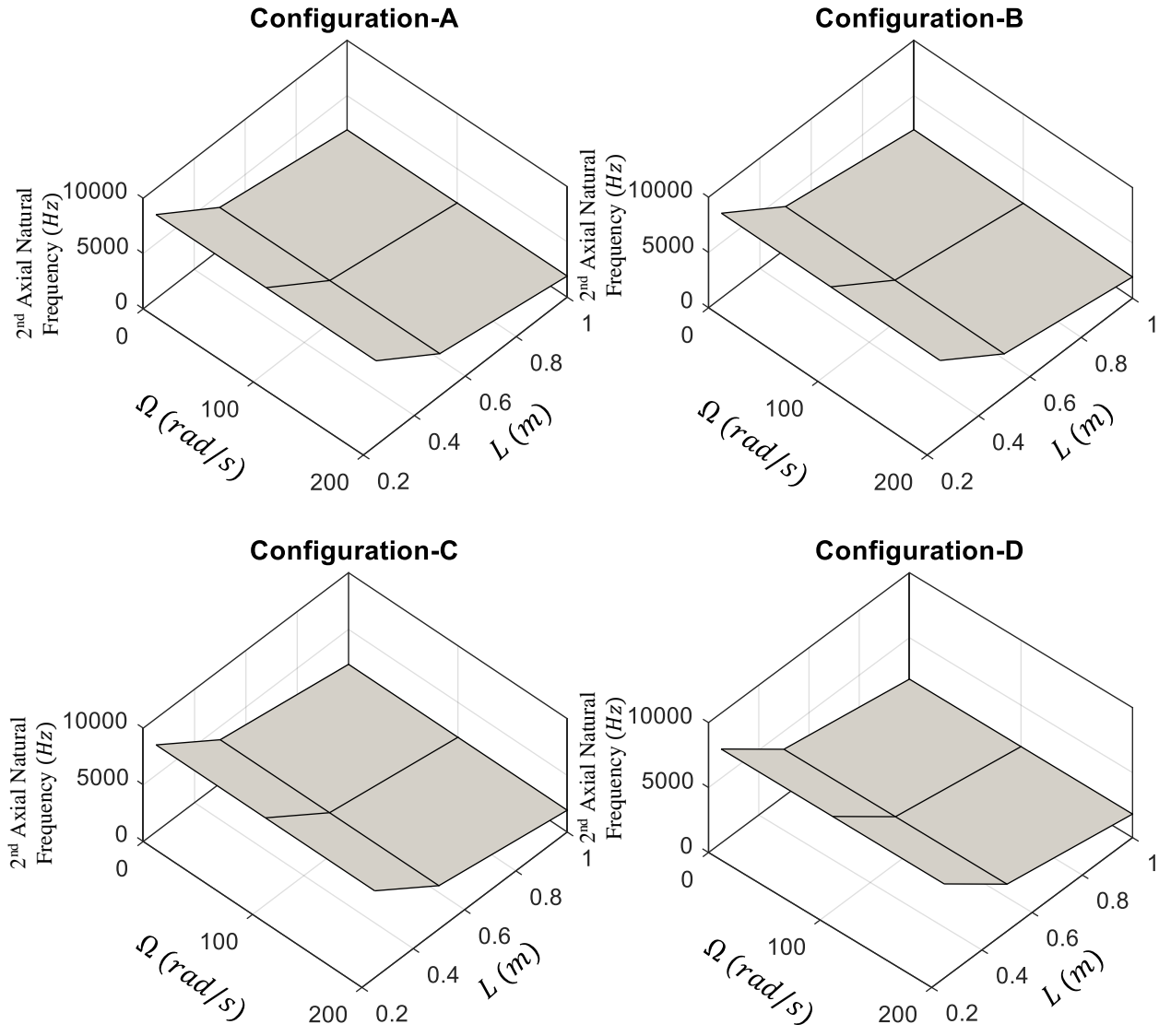
Figure 4.5 Second natural frequency of axial vibration with respect to rotational velocity and beam length

4.3 Critical speed consideration

In order to identify the significant vibrating motion for determining the critical speed of doubly-tapered rotating composite beam $(L = 2\,m, b_0 = 4\,cm\,r_b = 0.1, S = 18, [90]_{18s})$, a Campbell diagram is plotted by considering first natural frequencies of out-of-plane and in-plane bending vibrations.

In Figure 4.6, it is shown that out-of-plane bending vibration is significant to determine the first critical speed when multiple ($n = 2,3,4$ ...) rotating elements (i.e. blade in helicopter rotor system) are considered. On the other hand, for a single-bladed ($n = 1$) rotor system, in-plane bending vibration becomes significant. In Figure 4.6, OP denotes out-of-plane bending vibration and IP denotes in-plane bending vibration.
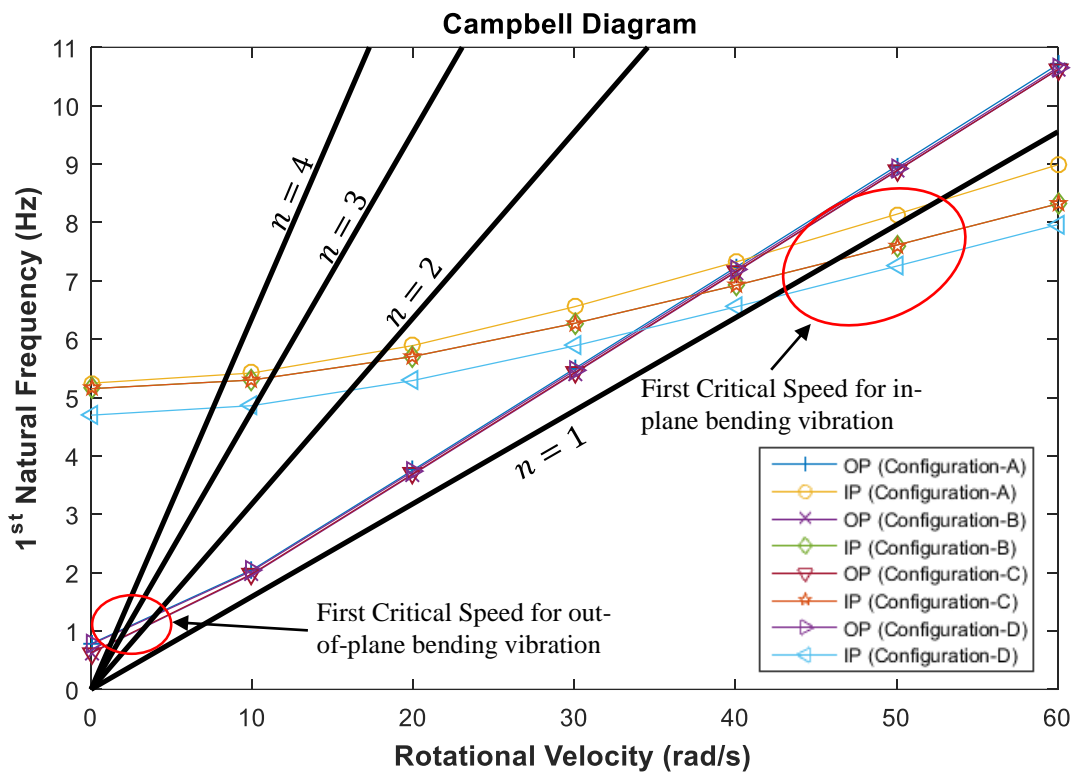
Figure 4.6 Campbell diagram for doubly-tapered composite beam considering out-of-plane (OP) and in-plane (IP) bending vibrations

4.4   Maximum displacement consideration

In Figures 4.7 and 4.8, first three mode shapes of non-rotating and rotating (50 rad/s) doubly-tapered cantilevered laminated composite beams $(L = 2\ m, b_0 = 4\ cm, r_b = 0.1, S = 18, [90]_{18s})$, are plotted, respectively, for out-of-plane and in-plane bending vibrations. From both figures, maximum displacements are observed from corresponding mode shapes of out-of-plane bending and in-plane bending vibrations.

From Figure 4.7, it is shown that in non-rotating condition except for the third modes of any configuration and second mode of Configuration-D, the maximum displacements of out-of-plane bending vibration are higher than the maximum displacements of in-plane bending vibration.

In Figure 4.8, it is shown that in rotating condition except for the second and third modes of Configuration-D, the maximum displacements of in-plane bending vibration are higher than the maximum displacements of out-of-plane bending vibration.
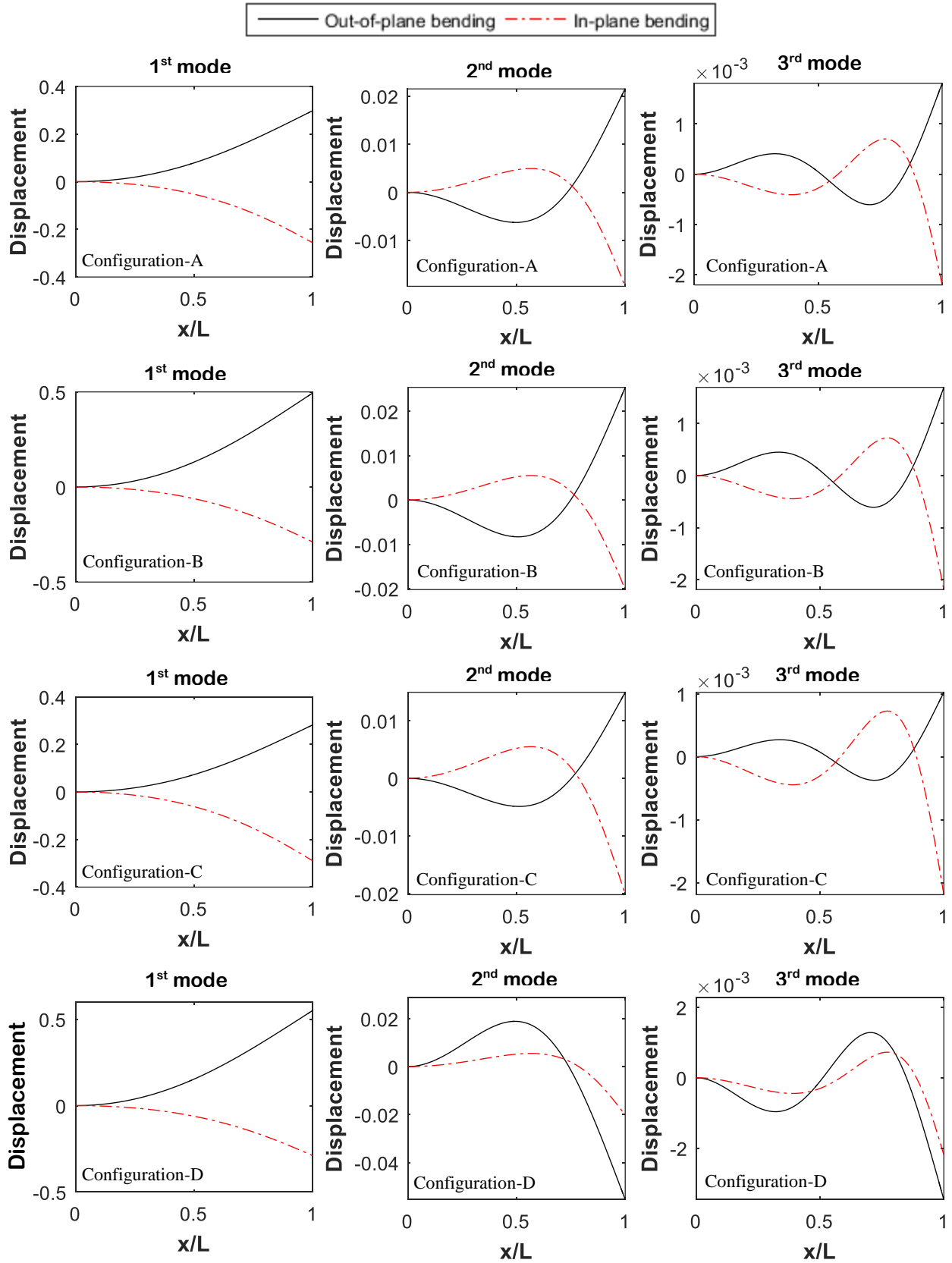
Figure 4.7 First three mode shapes of out-of-plane and in-plane bending vibrations (non-rotating)
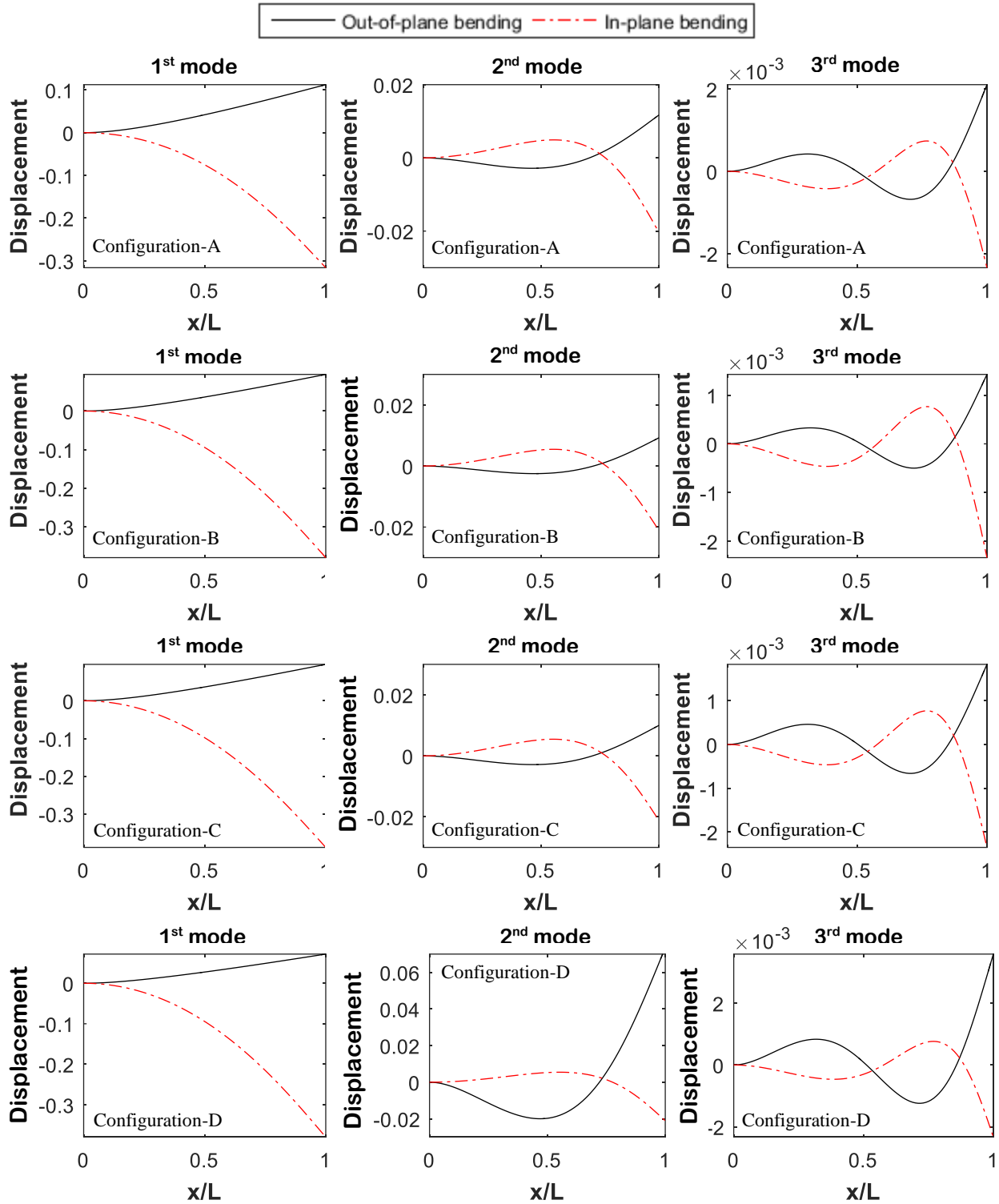
Figure 4.8 First three mode shapes of out-of-plane and in-plane bending vibrations for rotational speed of 200 rad/s

4.5 Instability region consideration

In Figures 4.9 to 4.11, first three instability regions of a doubly-tapered composite beam $(L = 2\ m, b_0 = 4\ cm, r_b = 0.1, S = 18, [90]_{18s})$, are plotted in a three-dimensional parametric plane for out-of-plane and in-plane bending vibrations. In Figures 4.9 to 4.11, it is shown that for all configurations and for all modes, the width of instability region increases as the amplitude factor (β) and mean rotational velocity (Ω_0) increase. Also, one can observe that instability region of out-of-plane bending vibration is much larger than that of the in-plane bending vibration. Based on the results obtained, for out-of-plane bending vibration, Configuration-D has the smallest width of instability region among all the tapered configurations considered and Configuration-A has the largest width of instability region (section 2.9.1) and for in-plane bending vibration, Configuration-B has the smallest width of instability region and Configuration-D has the largest width of instability region (section 3.9.1).

In Figure 4.12, spacing between the first three instability regions of out-of-plane bending vibration and first three instability regions of in-plane bending vibration are investigated by considering four different taper configurations. In this graph vertical axis represents the amplitude factor of periodic rotational velocity and the horizontal axis represents the resonance frequency. It is shown that for all the taper configurations, space between two consecutive instability regions of out-of-plane bending vibration is less than the spacing between two consecutive instability regions of in-plane bending vibration. Also, from Figure 4.12, it can be understood that first instability region of in-plane bending vibration has the smallest width of instability region and third instability region of out-of-plane bending vibration has the largest width of instability region.
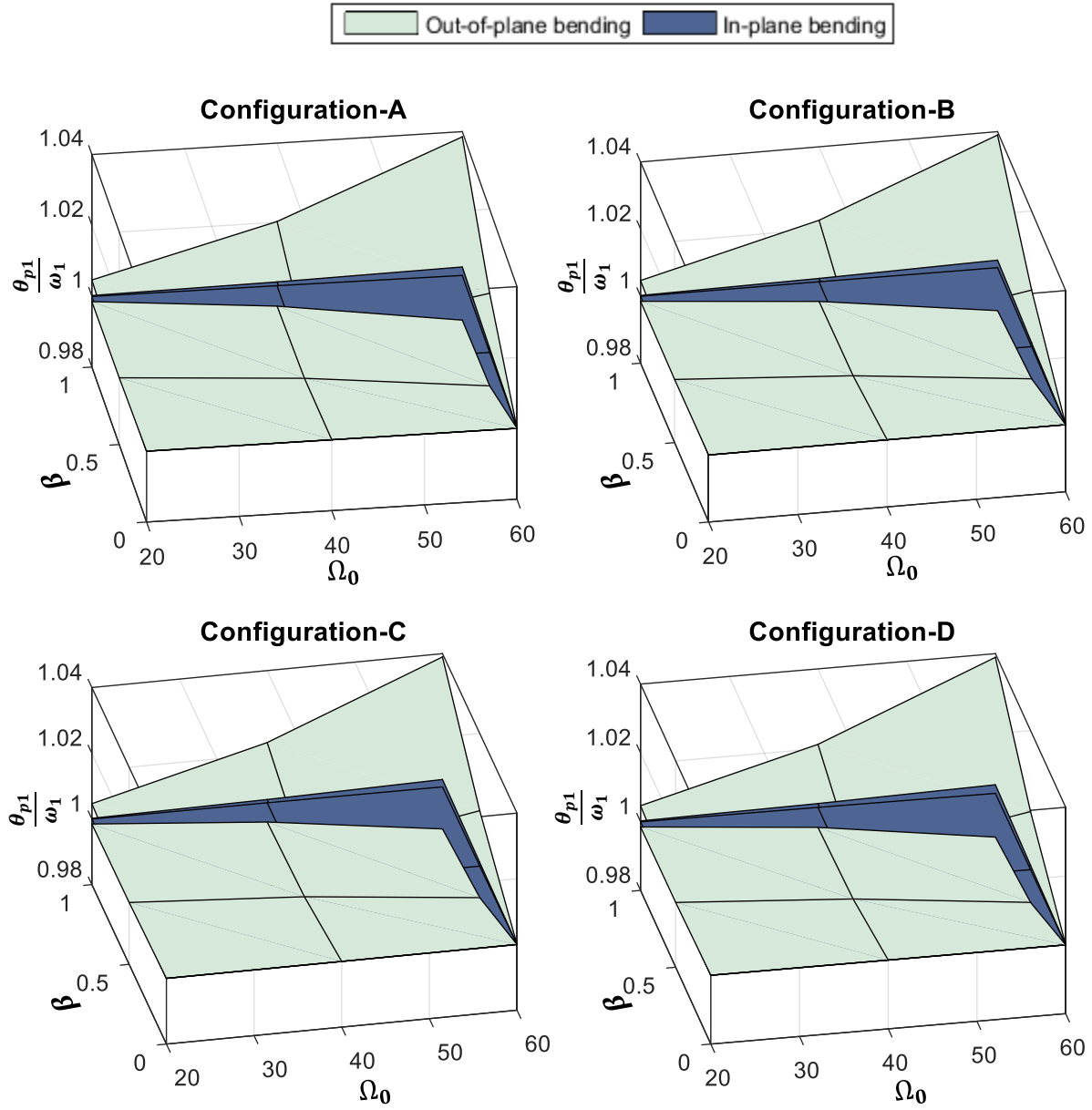
Figure 4.9 First instability regions of out-of-plane and in-plane bending vibrations for different taper configurations
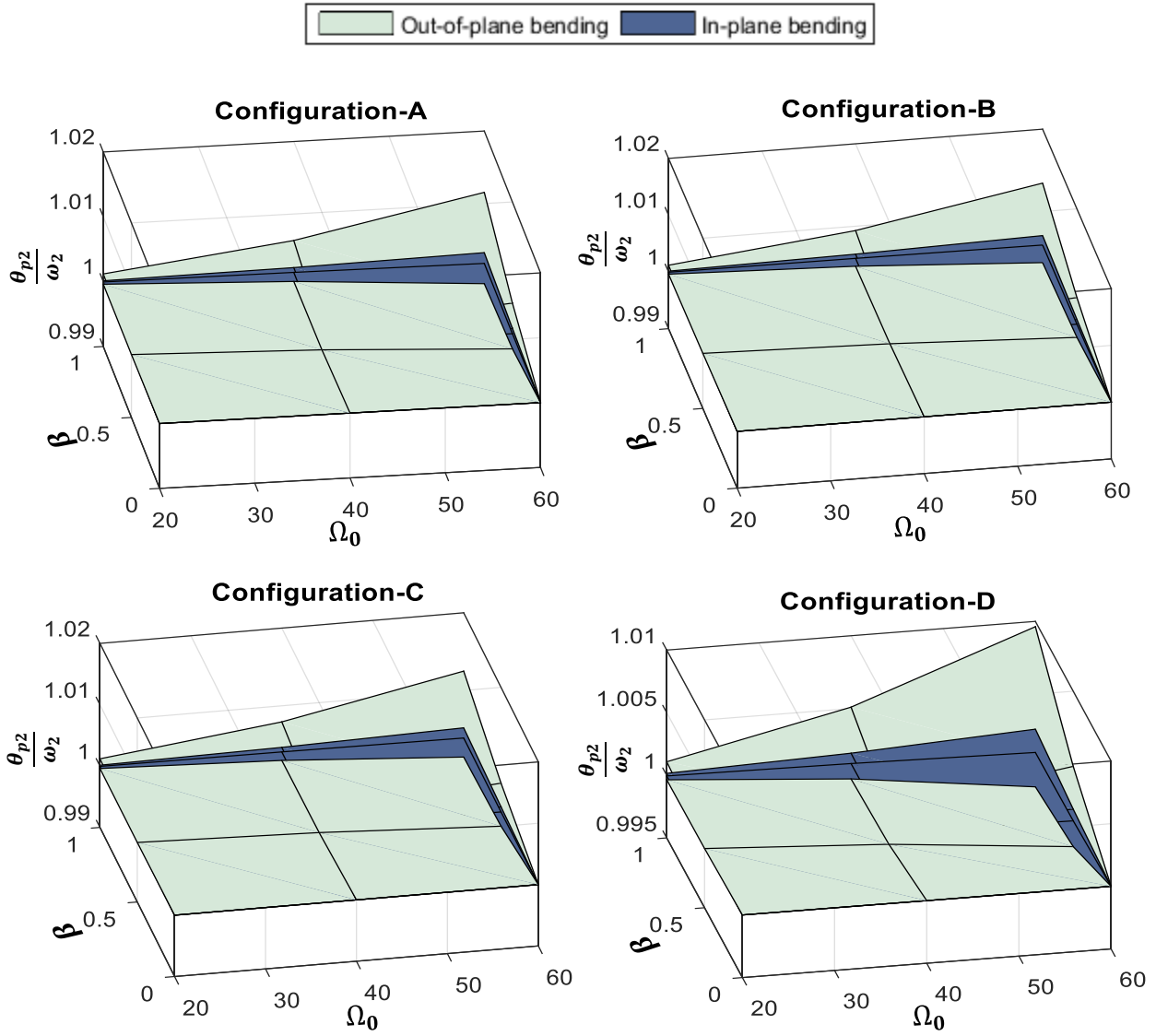
Figure 4.10 Second instability regions of out-of-plane and in-plane bending vibrations for different taper configurations
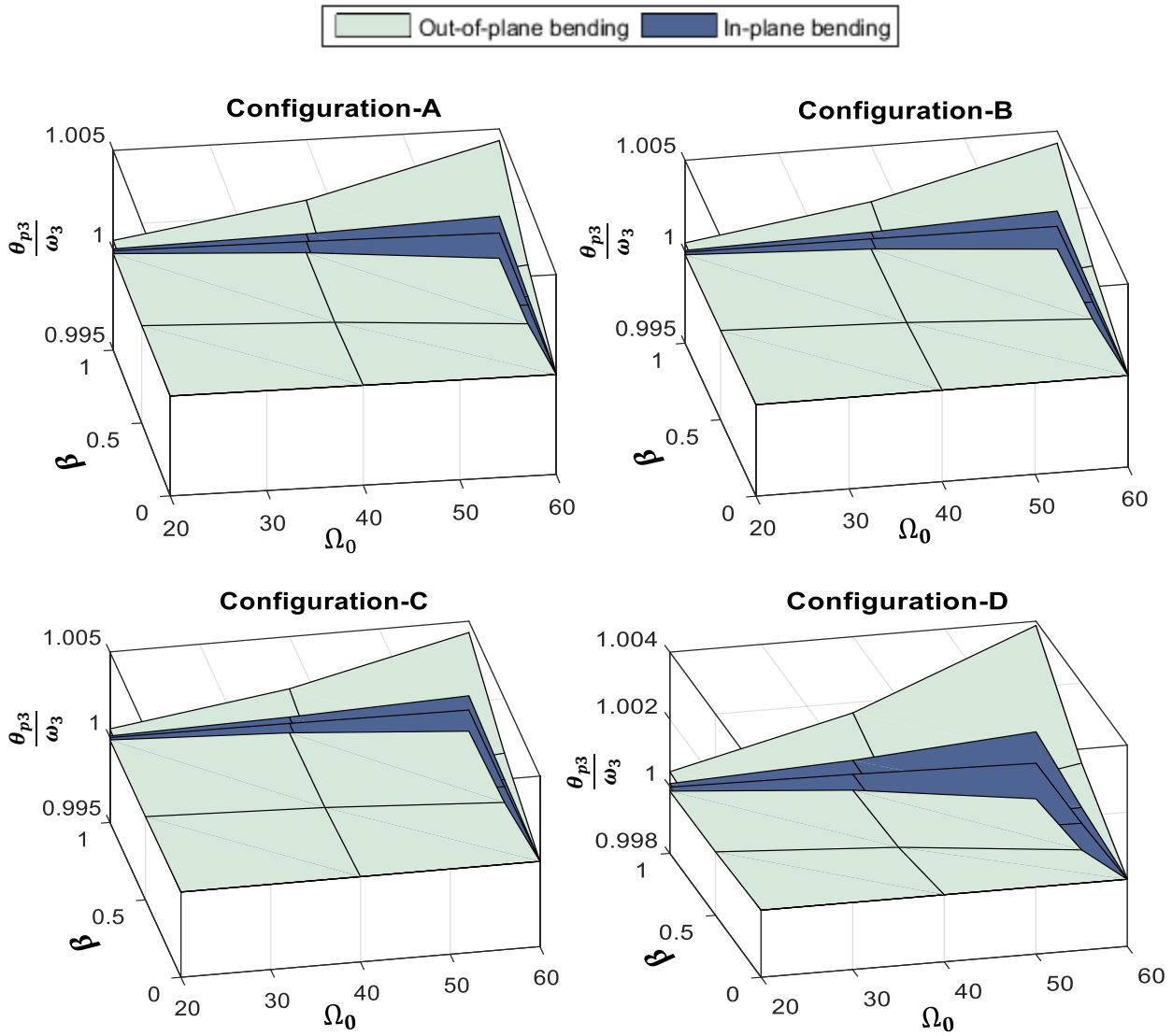
Figure 4.11 Third instability regions of out-of-plane and in-plane bending vibrations for different taper configurations
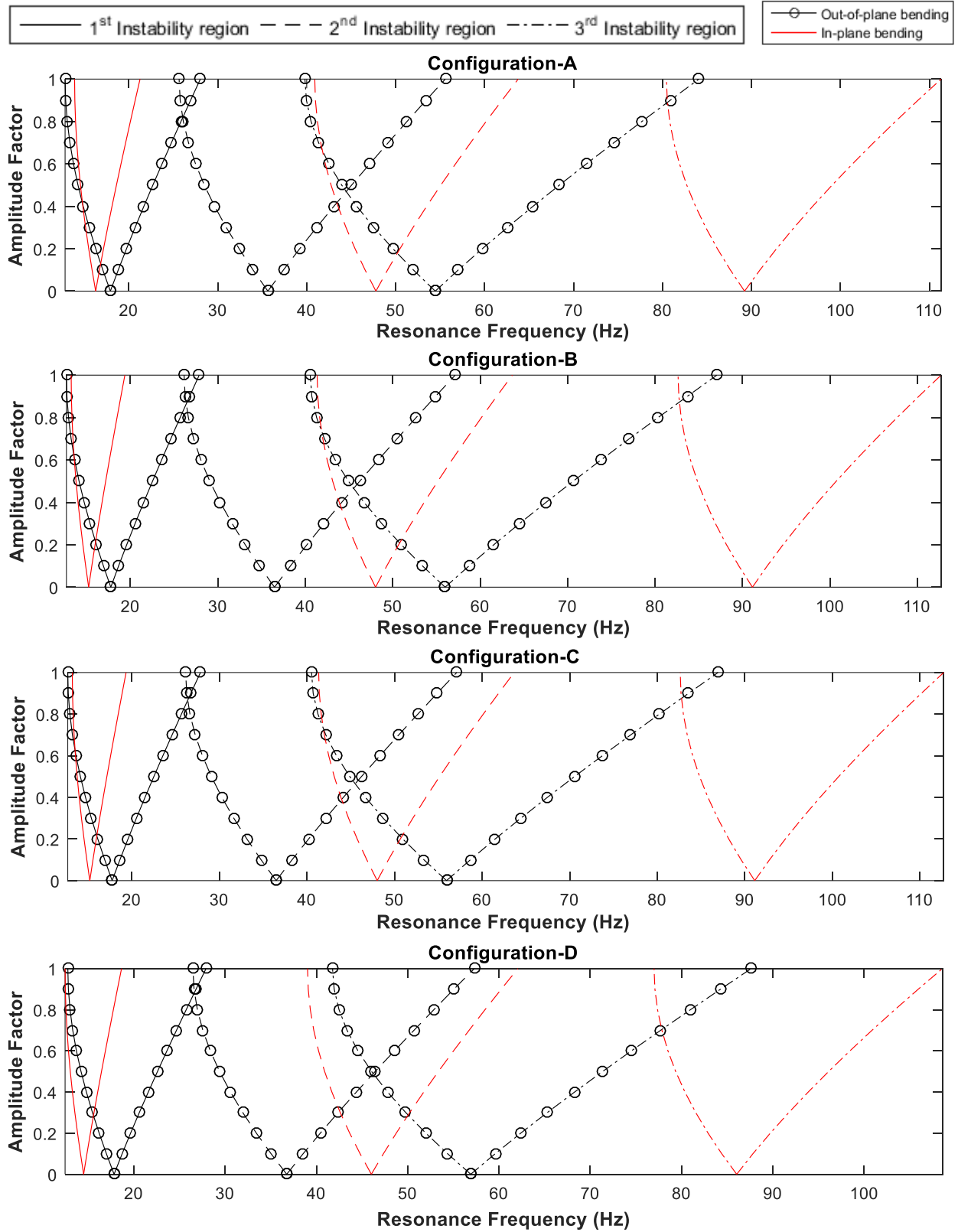
Figure 4.12 Spacing between the first three instability regions of out-of-plane and of in-plane bending vibration for different taper configurations.

4.6   Summary

In this chapter, a comparative study has been performed between out-of-plane and in-plane bending vibrations of a rotating doubly-tapered cantilever composite beam. The results for first three natural frequencies of out-of-plane and in-plane bending vibrations are compared for different cases. The results are extracted from the Rayleigh-Ritz method. Upon completing the investigation, it is shown that in non-rotating condition natural frequency of in-plane bending vibration is higher than the natural frequency of out-of-plane bending vibration, but with the increase of beam length and rotational velocity, the natural frequency of out-of-plane bending vibration becomes higher than the natural frequency of in-plane bending vibration. Also, it has been investigated that the first natural frequency of out-of-plane bending vibration is significant to determine the first critical speed, for a multi-bladed rotor system and first natural frequency of in-plane bending vibration is significant when the rotor system has a single blade. In non-rotating condition except for the third mode of any configurations and second mode of Configuration-D, maximum displacements of out-of-plane bending vibration are higher than the maximum displacements of in-plane bending vibration. In rotating condition except for the second and third modes of Configuration-D, maximum displacements of in-plane bending vibration are higher than the maximum displacements of out-of-plane bending vibration. It is shown that for all configurations and for all modes, the width of instability region increases as the amplitude factor and mean rotational velocity increase. Also, one can observe that width of instability region of out-of-plane bending vibration is larger than the width of instability region of in-plane bending vibration and spacing between two consecutive instability regions of out-of-plane bending vibration is less than the spacing between two consecutive instability regions of in-plane bending vibration.

Chapter - 5

Conclusion and future work

5.1   Major contribution

In the present thesis, free vibration and dynamic instability analyses of doubly-tapered rotating cantilever composite beams are conducted for three different types of vibrations (out-of-plane bending, in-plane bending and axial). Rayleigh-Ritz method based on classical lamination theory has been employed to formulate the free vibration problem. Bolotin's method is applied to determine the instability regions. Numerical and symbolic computations have been performed using MATLAB. The results for natural frequencies have been validated using FEA tool ANSYS.

A comprehensive parametric study is conducted in order to understand the effects of various parameters such as rotational velocity, hub radius, ply drop-off, double taper ratio and stacking sequence on the natural frequency of free vibration and instability regions of the doubly-tapered composite beams. Four different thickness-tapering configurations (Configurations A, B, C and D) were considered in the analysis.

Moreover, critical speed of a rotating doubly-tapered composite beam is determined and change of critical speed due to double-tapering is investigated. Also, change of maximum deflection due to rotational velocity and double-tapering is studied in this thesis. The material chosen in this thesis is NCT-301 graphite-epoxy prepreg, which is available in the laboratory of Concordia Centre for Composites (CONCOM).

5.2   Conclusions

The work done in this thesis has provided some conclusions on the performance and design of the rotating composite beam. The most important and principal conclusions of the study on free vibration analysis are given in the following:

➢ In order to obtain results using Rayleigh-Ritz method, it has shown that increase of the number of terms in approximate shape function increases the accuracy of results. In this thesis, results found with 7 and 8 terms in approximate shape functions of Rayleigh-Ritz method, matched well with the results obtained by using Conventional Finite Element Method, exact solution (for uniform beam) and ANSYS for uniform and doubly-tapered composite beams.

➢ Double-tapering increases the first natural frequencies of out-of-plane bending, in-plane bending and axial vibrations for both rotating and non-rotating cantilever composite beams.

➢ Increase of rotational velocity increases the natural frequencies of out-of-plane and in-plane bending vibrations, and on the other hand, increase of the rotational velocity slightly decreases the natural frequencies of axial vibration. In non-rotating condition, natural frequencies of in-plane bending vibration are higher than the natural frequencies of out-of-plane bending vibration, but at higher rotating speed and higher beam's length, natural frequencies of out-of-plane bending vibration becomes higher than the natural frequencies of in-plane bending vibration.

➢ It has been observed that the increase of the length of a doubly-tapered rotating cantilever composite beam decreases the natural frequencies of out-of-plane and in-plane bending vibrations.

➢ Increase of hub radius increases the natural frequencies of out-of-plane and in-plane bending vibrations for a constantly rotating doubly-tapered cantilever composite beam.

➢ For a doubly-tapered composite beam with different stacking sequences, it has been noticed that the laminate with only '0' degree fiber orientation gives highest natural frequencies and laminate with only '90' degree fiber orientation gives lowest natural frequency.

➢ Based on the results obtained for out-of-plane bending vibration of doubly-tapered rotating cantilever composite beam, Configuration D has the highest natural frequencies and is the most stiff configuration, Configuration C and Configuration B have the second highest and the third highest natural frequencies respectively. Configuration A has the lowest natural frequencies and is the least stiff configuration among all the considered configurations. In case of in-plane bending vibration, Configuration-A has the highest natural frequencies and Configuration-D has the lowest natural frequencies. Configuration-B and Configuration-C have almost same natural frequencies that lie in between natural frequencies of Configuration-A and Configuration-D.

➢ It has been observed that there is no significant change in the mode shapes when the beam starts to rotate from static condition. Based on the mode shapes plot it can be stated that for non-rotating condition maximum displacement of out-of-plane bending vibration is higher than the maximum displacement of in-plane bending vibration, and for rotating condition maximum displacement of in-plane bending vibration is higher than the maximum displacement of out-of-plane bending vibration.

➢ It has been investigated that, in order to determine the first critical speed, first natural frequency of out-of-plane bending vibration is significant for a multi-bladed rotor system and first natural frequency of in-plane bending vibration is important when the rotor system has a single blade.

The important conclusions of dynamic instability analysis due to time varying rotational velocity are given in the following:

➢ It has been seen that increase of mean rotational velocity increases the width of instability region for out-of-plane bending, in-plane bending and axial vibrations of a doubly-tapered cantilever composite beam. Also, for any specific mean rotational velocity, increase of amplitude of time varying rotational speed increases the width of instability regions for all three vibrational motions.

➢ From the parametric study, it has been found that increase of hub radius increases the widths of instability regions of out-of-plane and in-plane bending vibrations and hub radius has no effect on the dynamic instability of axial vibration.

➢ Double-tapering of the composite beam decreases the widths of instability regions of out-of-plane bending and axial vibrations, but on the other hand double-tapering increases the width of instability region of in-plane bending vibration.

➢ Based on the results obtained, Configuration-D has the smallest width of instability region and Configuration-A has the largest width of instability region for out-of-plane bending vibration. For in-plane bending vibration, Configuration-B has the smallest width of instability region and Configuration-D has the largest width of instability region. For axial vibration, Configuration-D has the largest width of instability region and Configuration-A has the smallest width of instability region.

➢ It has been noticed that the laminate with only '0' degree fiber orientation gives the smallest width of instability region and laminate with only '90' degree fiber orientation gives the largest width of instability region for any type of vibrational motion.

➢ It has been found that instability region of out-plane bending vibration is larger than the instability region of in-plane bending vibration.

➢ It has been studied that the spacing between two consecutive instability regions of out-of-plane bending vibration is less than the space between two consecutive instability regions of in-plane bending vibration.

5.3   Recommendations for future work

The study of free vibration and dynamic instability of doubly-tapered rotating composite beam can be continued in the future studies on these following recommendations:

➢ Free vibration and dynamic instability analyses of rotating doubly-tapered cantilever composite beam presented in this thesis can be performed for thick laminate considering First-order Shear Deformation Theory (FSDT).

➢ Damping can be introduced in the free vibration and dynamic instability analyses of doubly-tapered rotating composite beam.

➢ Transient and random vibration analyses can be performed on doubly-tapered rotating composite beam.

➢ Free vibration and dynamic instability analyses of rotating doubly-tapered cantilever composite beam presented in this thesis can be extended for rotating doubly-tapered open cylindrical shell.

References

[1] R. L. Bielawa, Rotary Wing Structural Dynamics and Aeroelasticity, Reston, VA: American Institute of Aeronautics and Astronautics, 2006.

[2] J. M. Bertholet, Composite Materials: Mechanical Behavior and Structural Analysis, New York: Springer, 1999.

[3] J. N. Reddy, Mechanics of Laminated Composite Plates and Shells: Theory and Analysis, CRC Press, 2003.

[4] R. M. Jones, Mechanics of Composite Materials, Washington: Scripta Book Co., 1975.

[5] A. K. Kaw, Mechanics of Composite Materials, Taylor and Francis group, 2006.

[6] K. He, S. V. Hoa and R. Ganesan, "The Study of Tapered Laminated Composite Structures: A Review, " *Composites Science and Technology*, vol. 60, pp. 2643-2657, 2000.

[7] F.-X. Irisarri, A. Lasseigne, F.-H. Leroy and R. Le Riche, "Optimal Design of Laminated Composite Structures with Ply Drops Using Stacking Sequence Tables," *Composite Structures*, vol. 107, pp. 559–569, 2014.

[8] B. Varughese, A. Mukherjee, "A Ply Drop-Off Element for Analysis of Tapered Layered Composites." *Composite Structures*, vol. 39, pp. 123–44, 1997.

[9] M. Geradin and D. J. Rixen, Mechanical Vibrations: Theory and Application to Structural Dynamics, John Wiley & Sons, Ltd, 1997.

[10] S. S. Rao, Mechanical Vibration, 5th ed., Pearson Education, Inc., 2004.

[11] R. Ganesan and A. Zabihollah, "Vibration Analysis of Tapered Composite Beams Using a Higher-order Finite Element; Part II: Parametric Study," *Journal of Composite Structures*, vol. 77, pp. 319-330, 2007.

[12] S. M. Akhlaque-E-Rasul, "Buckling Analysis of Tapered Composite Plates Using Ritz Method Based on Classical and Higher-order Theories," MASC Thesis, Concordia University, 2005.

[13] P. Salajegheh, "Vibrations of Thickness-and-width Tapered Laminated Composite Beams with Rigid and Elastic Supports," MASC Thesis, Concordia University, 2013.

[14] H. Eftakher, "Free and Forced Vibrations of Tapered Composite Beams Including the Effects of Axial Force and Damping," MASC Thesis, Concordia University, 2008.

[15] J.R. Banerjee, D.R. Jackson, "Free Vibration of A Rotating Tapered Rayleigh Beam: A Dynamic Stiffness Method of Solution," *Computers and Structures,* vol. 124, pp. 11–20, 2013.

[16] M. O. Kaya, "Free Vibration Analysis of a Rotating Timoshenko Beam by Differential Transform Method," *Aircraft Engineering and Aerospace Technology: An International Journal*, vol. 78, pp. 194–203, 2006.

[17] J. B. Gunda, A. P. Singh, P. S. Chhabra and R. Ganguli, "Free Vibration Analysis of Rotating Tapered Blades Using Fourier-P Super Element," *Structural Engineering and Mechanics*, vol. 27, No. 2, 2007.

[18] D. Ngo-Cong, N. Mai-Duy, W. Karunasena and T. Tran-Cong, "Free Vibration Analysis of Laminated Composite Plates Based on FSDT Using One-Dimensional IRBFN Method," *Computers and Structures*, vol. 89, pp. 1–13, 2011.

[19] H. Arvin, F. Bakhtiari-Nejad, "Nonlinear Free Vibration Analysis of Rotating Composite Timoshenko Beams, " *Composite Structures*, vol. 96, pp. 29–43, 2013.

[20] E. Carrera, M. Filippi, E. Zappino, "Free Vibration Analysis of Rotating Composite Blades via Carrera Unified Formulation," *Composite Structures*, vol. 106, pp. 317–325, 2013.

[21] O. O. Ozgumus, M. O. Kaya, "Energy Derivation and Extension- Flap wise Bending Vibration Analysis of a Rotating Piezolaminated Composite Timoshenko Beam," *Mechanics of Advanced Materials and Structures*, vol. 21:6, pp. 477-489, 2014.

[22] D.H. Hodges and E.H. Dowell, "Nonlinear Equations of Motion for The Elastic Bending and Torsion of Twisted Non Uniform Rotor Blades, " NASA TN D-7818, 1974.

[23] H.H. Yoo, S.H. Lee, and S.H. Shin, "Flap Wise Bending Vibration Analysis Of Rotating Multi-Layered Composite Beams," *Journal of Sound and Vibration*, vol. 286, pp. 745–761, 2005.

[24] S. Choi1, J. Park, J. Kim, "Vibration Control of Pre-Twisted Rotating Composite Thin-Walled Beams with Piezoelectric Fiber Composites," *Journal of Sound and Vibration,* vol. 300, pp.176–196, 2006.

[25] O. O. Ozgumus, M. O. Kaya, "Energy Expressions and Free Vibration Analysis of a Rotating Double Tapered Timoshenko Beam Featuring Bending–Torsion Coupling," *International Journal of Engineering Science*, vol. 45, pp. 562–586, 2007.

[26] N.K. Chandiramani, L. Librescu, C.D. Shete, "On The Free-Vibration of Rotating Composite Beams Using A Higher-Order Shear Formulation," *Aerospace Science and Technology.* Vol. 6 pp. 545–561, 2002.

133

[27] N. Baddour, "Hamilton's Principle for the Derivation of Equations of Motion", [http://www.academia.edu/164428/Hamiltons_Principle_for_the_Derivation_of_Equations_of_Motion]

[28] ANSYS[®] Academic Research, Release 15.0, Help system, Mechanical APDL Element Reference, Element Library.

[29] "http://www.matweb.com/index.aspx" [Online].

[30] M. A. Muslmani, "Rotordynamic Analysis of Tapered Composite Driveshaft Using Conventional and Hierarchical Finite Element Formulations," MASC Thesis, Concordia University, 2013.

[31] V. V. Bolotin, The Dynamic Stability of Elastic System, Holden-Day, INC., San Francisco, London, Amsterdam, 1964

[32] J. Xin, J. Wang, J. Yao & Q. Han, "Vibration, Buckling and Dynamic Stability of a Cracked Cylindrical Shell with Time-Varying Rotating Speed," *Mechanics Based Design of Structures and Machines: An International Journal*, vol. 39:4, pp. 461-490, 2011.

[33] F. Wang, W. Zhang, "Stability Analysis of A Nonlinear Rotating Blade with Torsional Vibrations," *Journal of Sound and Vibration*, vol. 331, pp. 5755–5773, 2012.

[34] C. M. Saravia, S. P. Machado, V. H. Cortínez, "Free Vibration and Dynamic Stability of Rotating Thin-Walled Composite Beams," *European Journal of Mechanics and A/Solids*, vol. 30, pp. 432-441, 2011.

[35] C. Lin, L. Chen, "Dynamic Stability of Rotating Composite Beams with A Viscoelastic Core," *Composite Structures*, vol. 58, pp. 185–194, 2002.

[36] A. Chattopadhyay, A. G. Radu, "Dynamic Instability Of Composite Laminates Using A Higher Order Theory," *Computers and Structures,* vol. 77, pp. 453-460, 2000.

[37] G. S-akar, M. Sabuncu, "Dynamic Stability Analysis of Pre Twisted Aerofoil Cross-Section Blade Packets Under Rotating Conditions," *International Journal of Mechanical Sciences*, vol. 50, pp. 1–13, 2008.

[38] J. Chung, D. Jung, H. H. Yoo, "Stability Analysis for The Flap Wise Motion of A Cantilever Beam With Rotary Oscillation," *Journal of Sound and Vibration*, vol. 273, pp. 1047–1062, 2004.

[39] W. Liu, "Dynamic Instability Analysis of Tapered Composite Plate Using Ritz and Finite Element Method," MASC Thesis, Concordia University, 2005.

[40] G. A. Hassan, M.A. Fahmy, I. G. Mohammed, "Effects of Fiber Orientation and Laminate Stacking Sequence on Out-of-plane And In-plane Bending Natural Frequencies of Laminated Composite Beams," *9th PEDAC conference*, Egypt, 2009.

[41] V. Yildirm, "Effect of The Longitudinal to Transverse Moduli Ratio on The In-plane Natural Frequency of Symmetric Cross Ply Laminated Beams By The Stiffness Method," *Composite Structures,* vol. 50, pp. 319-326, 2000.

[42] E, Kosko, "The Free Uncoupled Vibrations of Uniformly Rotating Beam," Institute of Aerophysics, University of Toronto, review no. 15. March 1960.

[43] D. C. D. Oguamanam and G. R. Heppler, "Vibration of Rotating Timoshenko Beams with Centrifugal Stiffening And Specified Torque or Velocity Profiles," *Transactions on the Built Environment*. vol. 19, 1996.

[44] M. Friswell, J. Penny, S. Garvey, and A. Lees, Dynamics of Rotating Machines, 1st ed., Cambridge University Press, 2010.

[45] Y. Huang, H. Lu, J. Fu, A. Liu, and M. Gu, "Dynamic Stability of Euler Beams Under Axial Unsteady Wind Force, " *Mathematical Problems in Engineering*, vol. 1, pp. 1-12, 2014.

[46] R. Southwell, and F. Gough, "The Free Transverse Vibration of Airscrew Blades," *British A.R.C. Reports and Memoranda*, No. 766, 1921.

[47] M. Scilhansl, "Bending Frequency of a Rotating Cantilever Beam," *Journal of Applied Mechanics*, vol. 25, pp. 28-30, 1958.

[48] S. Putter and H. Manor, "Natural Frequencies of Radial Rotating Beams," *Journal of Sound and Vibration*, vol. 56, pp. 175-185. 1978.

[49] C. Kuo, and S. Lin, "Modal Analysis and Control of a Rotating Euler-Bernoulli Beam Part I: Control System Analysis and Controller Design," *Mathematical and Computer Modelling*, vol. 27, No.5, pp.75-92. 1998.

[50] R. B. Abararcar and P. F. Cunniff, "The Vibration of Cantilever Beams of Fiber Reinforced Materials," *Journal of Composite Materials*, vol. 6, pp. 504-516, 1972.

[51] A. K. Miller and D. F. Adams, "An Analytic Means of Determining the Flexural and Torsional Resoant Frequencies of Generally Orthotropic Beams," *Journal of Sound and Vibration*, vol. 41, pp. 443-449, 1975.

[52] S. Krishnaswamy, K. Chandrashekhara and W. Z. B. Wu, "Analytical Solutions to Vibration of Generally Layered Composite Beams," *Journal of Sound and Vibration*, vol. 159, pp. 85-99, 1992.

[53] M. S. Nabi and N. Ganesan, "A Generalized Element for the Free Vibration Analysis of Composite Beams," *Journal of Computers and Structures*, vol. 51, pp. 607-610, 1994.

[54] K. B. Vijay, "Dynamic Response of Width- and Thickness-tapered Composite Beams Using Rayleigh-Ritz Method and Modal Testing," MASC Thesis, Concordia University, 2012.

[55] M. A. Fazili, "Vibration Analysis of Thickness-and Width-Tapered Laminated Composite Beams using Hierarchical Finite Element Method," MASC Thesis, Concordia University, 2013.

[56] S. H. Hyun, H. H. Yoo, "Dynamic Modeling and Stability Analysis of Axially Oscillating Cantilever Beams," *Journal of Sound and Vibration*, vol. 228, pp. 543–558. 1998.

[57] T.H. Tan, H.P. Lee, G.S.B. Leng, "Dynamic Stability of A Radially Rotating Beam Subjected to Base Excitation," *Computer Methods in Applied Mechanics and Engineering*, vol. 146, pp. 265–279. 1997.

[58] H.H. Yoo, R.R. Ryan, R.A. Scott, "Dynamics of Flexible Beams Undergoing Overall Motion," *Journal of Sound and Vibration*, vol. 181, pp. 261–278. 1995.

[59] L. W. Chen, W. K. Peng, "Dynamic Stability of Rotating Composite Shafts Under Periodic Axial Compressive Loads," *Journal of Sound and Vibration*, vol. 212, pp. 215-230. 1998.

APPENDIX-A

Configuration-A

In Figure A.1, taper Configuration-A is shown where drop-off composite plies are replaced with isotropic resin material. Figure A.2 shows the cross-sectional view of a beam has taper Configuration-A for 24 ply drop-off which is developed in ANSYS.
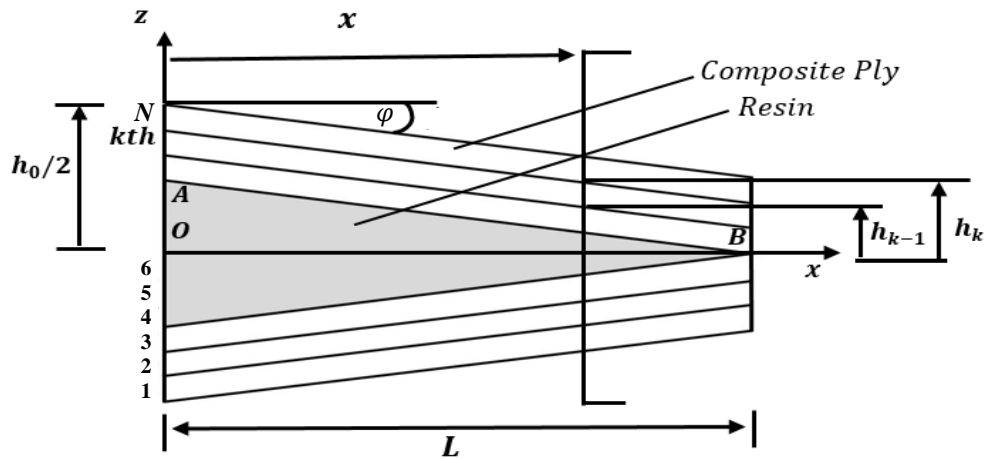
Figure A.1: Geometry of taper Configuration-A
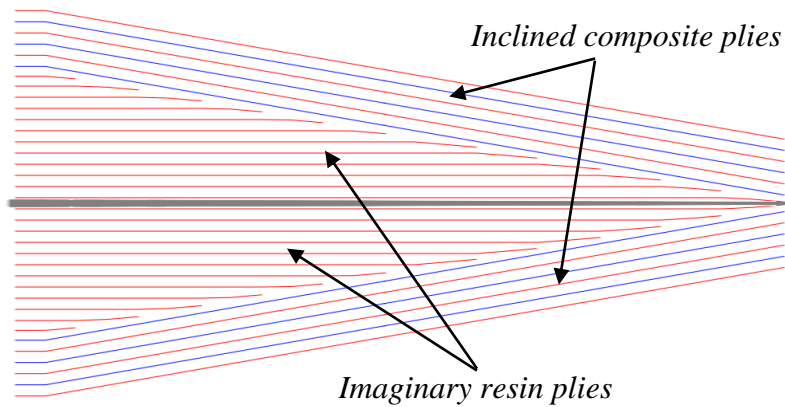
Figure A.2: Cross-sectional view of taper Configuration-A developed in ANSYS

In taper Configuration-A, expressions of h_k and h_{k-1} for composite plies are (Figure A.1):

$$h_k = -x * tan(\varphi) - \frac{h_0}{2} + h_{ply} * k \qquad (A.1)$$

139

$$h_{k-1} = -x * tan(\varphi) - \frac{h_0}{2} + h_{ply} * (k-1) \qquad (A.2)$$

Here, φ is the thickness-taper angle. Sign of φ can be 'positive' or 'negative' depends on the position of ply in top or bottom of z co-ordinate, respectively.

$k = 1,2,3 .... N$, where N is number of layers in the laminate

h_{ply} is thickness of lamina and $h_0 (= h_{ply} * N)$ is thickness of the laminate in thick side.

Resin pocket can be assumed as combination of imaginary resin plies which have same length as composite lamina but have variable thickness (Figure A.3). Expressions of h_k and h_{k-1} for imaginary resin plies are:

$$h_k = -x * tan \left(\frac{\varphi}{S/2} * (\frac{N}{2} - k) \right) - \frac{h_0}{2} + h_{ply} * k \qquad (A.3)$$

$$h_{k-1} = -x * tan \left(\frac{\varphi}{S/2} * (\frac{N}{2} + 1 - k) \right) - \frac{h_0}{2} + h_{ply} * (k-1) \qquad (A.4)$$

Here, sign of φ is positive and k lies between $(\frac{N-S}{2} + 1)$ to $(\frac{N+S}{2})$, where S is number of ply drop-off.
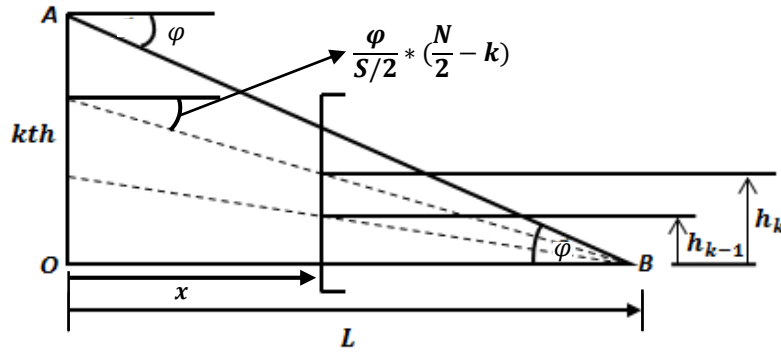
Figure A.3: Geometry of top half resin pocket in configuration-A

A graph can be plotted using equations (A.1)-(A.4) to validate these equations where x ranging from 0 to L. Figure A.4 illustrates a 25 cm long thickness-tapered composite laminate which has

12 plies at thick side, where 6 plies is dropped and replaced with resin material. Solid line represents thickness boundary of composite plies and dashed line represents thickness boundary of resin plies.
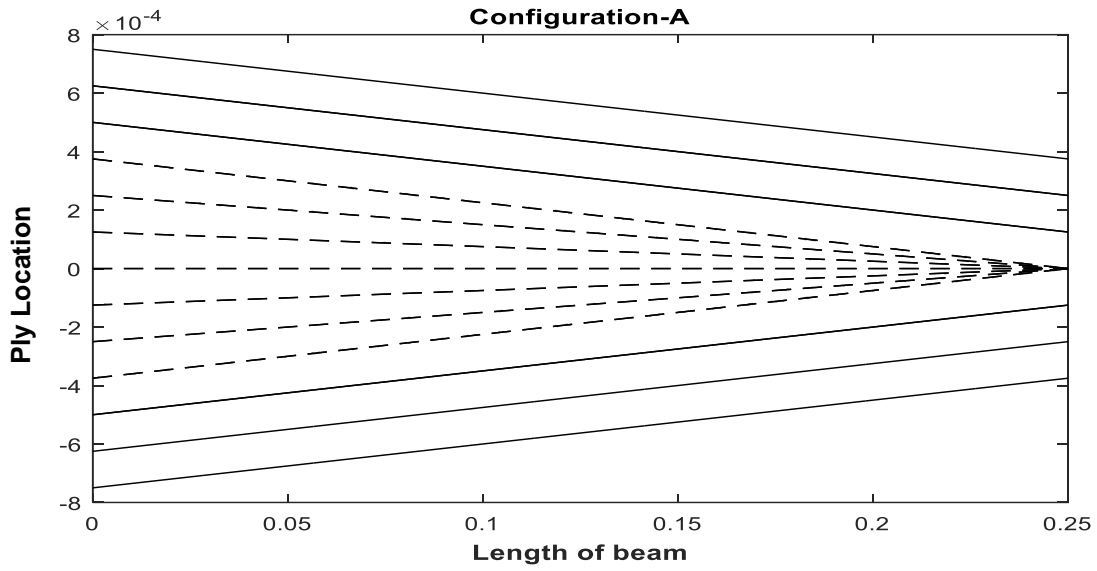
Figure A.4: Graphical representation of expressions for h_k and h_{k-1}
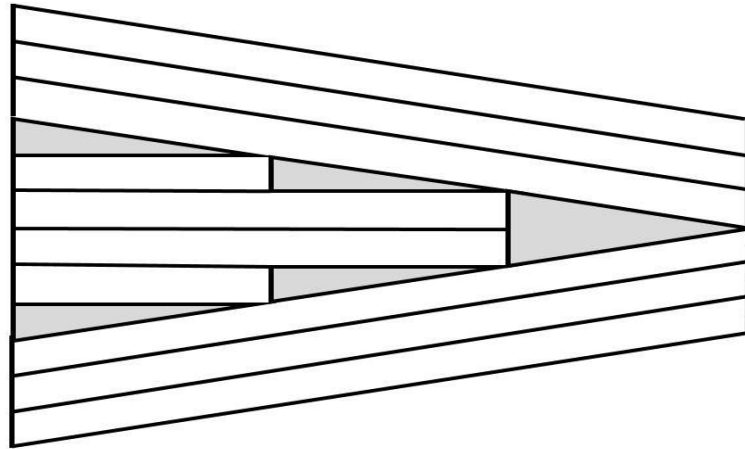
Figure A.5: Geometry of taper Configuration-B
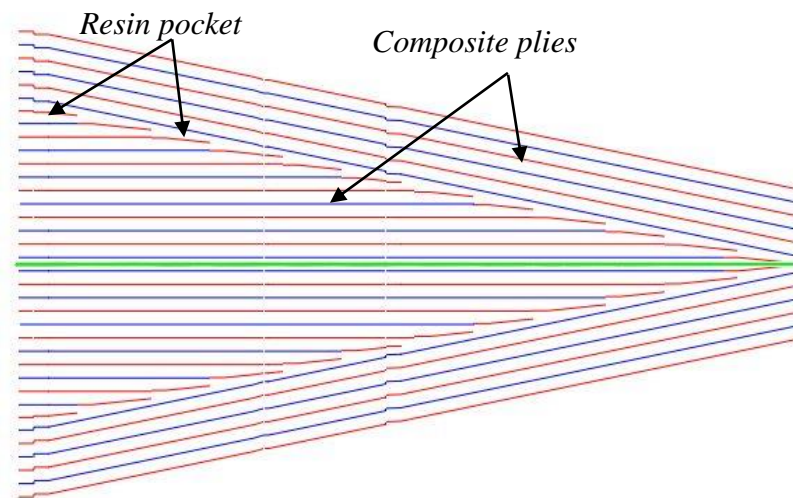
Figure A.6: Taper Configuration-B developed in ANSYS Composite PrepPost (ACP)
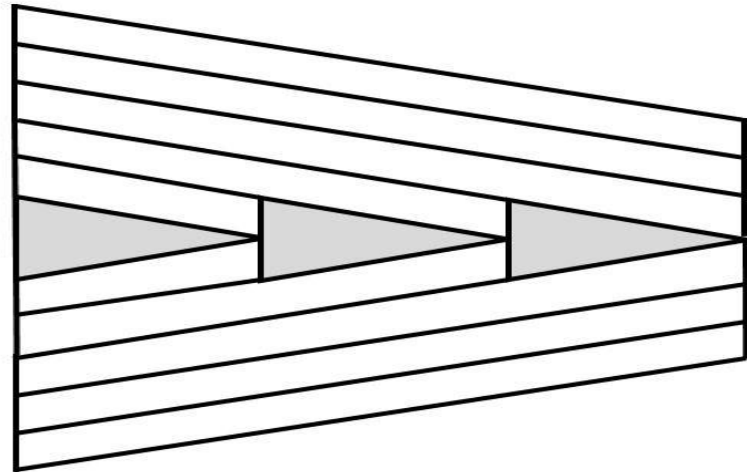
Figure A.7: Geometry of taper Configuration-C
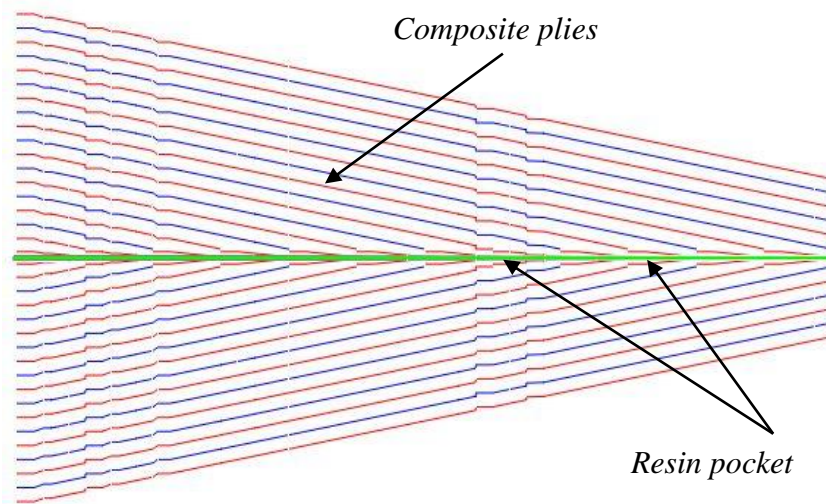
Figure A.8: Taper configuration-C developed in in ANSYS Composite PrepPost (ACP)
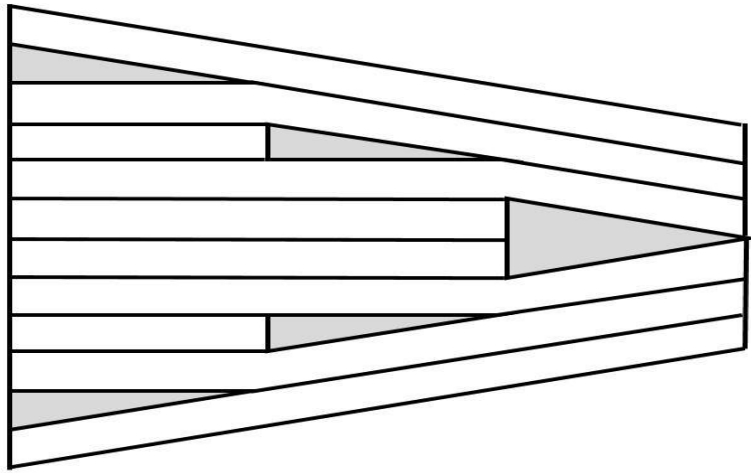
Figure A.9: Geometry of taper configuration-D
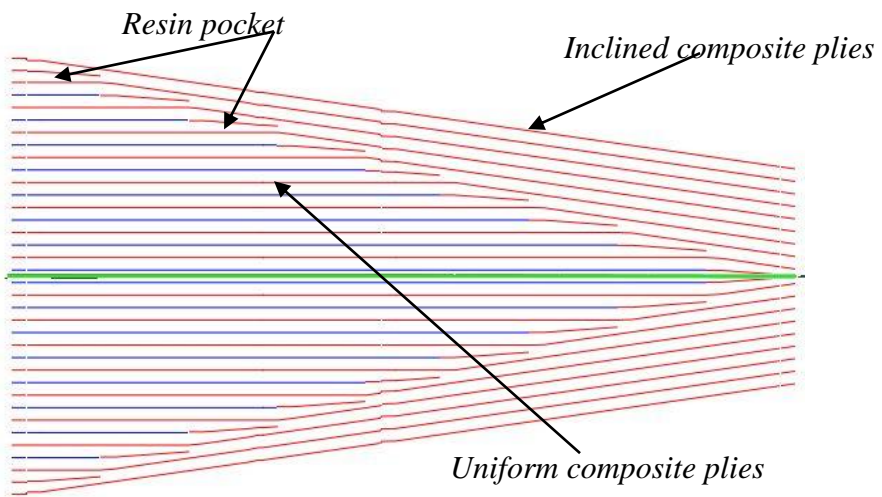
Figure A.10: Taper configuration-D developed in in ANSYS Composite PrepPost (ACP)

APPENDIX-B

After introducing periodic rotational velocity, equation of motion (2.36) becomes:

$$[M]\{\ddot{q}\} + ([K] + \Omega^2(t)[K^{*C}])\{q\} = \{0\} \qquad \text{B.1}$$

Here,

$[M]$ is mass matrix

$[K]$ is stiffness matrix due to elastic deformation

$\Omega^2(t)[K^{*C}]$ is time dependent stiffness matrix due to centrifugal action

$\{q\}$ is generalized coordinate vector

$\Omega(t)$ is periodic rotational velocity.

Now substituting periodic rotational velocity $\Omega(t) = \Omega_0 + \beta\,\Omega_0 sin\theta t$ in equation B.1 one can have:

$$[M]\{\ddot{q}\} + ([K] + \left(\Omega_0{}^2 + 2\Omega_0{}^2\beta sin\theta_p t + \frac{\Omega_0{}^2\beta^2}{2}\left(1 - cos2\theta_p t\right)\right)[K^{*C}])\{q\} = 0 \qquad \text{B.2}$$

To find the periodic solution with period $2T$ we will take Bolotin's first approximation [30], the periodic solutions with period $2T$ can be sought in the form:

$$\{q\} = \Sigma_{r=1,3,5\ldots}^{\infty}[\{a_r\}sin\left(\frac{r\theta_p t}{2}\right) + \{b_r\}cos\left(\frac{r\theta_p t}{2}\right)] \qquad \text{B.3}$$

Taking one-term solution and differentiating two times with respect to time t,

$$\{\ddot{q}\} = [-\frac{\theta_p{}^2}{4}\{a_1\}sin\left(\frac{\theta_p t}{2}\right) - \frac{\theta_p{}^2}{4}\{b_1\}cos\left(\frac{\theta_p t}{2}\right)] \qquad \text{B.4}$$

After substituting $\{q\}$ and $\{\ddot{q}\}$ in equation B.2 one can have:

$$[M]\{-\frac{\theta_p{}^2}{4}a_1 sin\left(\frac{\theta_p t}{2}\right) - \frac{\theta_p{}^2}{4}b_1 cos\left(\frac{\theta_p t}{2}\right)\} + \{[K] + (\Omega_0{}^2 + 2\Omega_0{}^2\beta sin\theta_p t + \frac{\Omega_0{}^2\beta^2}{2}(1 - $$

$$cos2\theta_p t))[K^C]\}\{a_1 sin\left(\frac{\theta_p t}{2}\right) + b_1 cos\left(\frac{\theta_p t}{2}\right)\} = 0 \qquad \text{B.5}$$

To compare the coefficient of $\sin\left(\frac{\theta_p t}{2}\right)$ and $\cos\left(\frac{\theta_p t}{2}\right)$ one can use following trigonometric formula:

$$\sin(\theta_p t)\sin\left(\frac{\theta_p t}{2}\right) = \frac{1}{2}\cos\left(\frac{\theta_p t}{2}\right) - \frac{1}{2}\cos\left(\frac{3\theta_p t}{2}\right) \qquad \text{B.6}$$

$$\sin(\theta_p t)\cos\left(\frac{\theta_p t}{2}\right) = \frac{1}{2}\sin\left(\frac{\theta_p t}{2}\right) + \frac{1}{2}\sin\left(\frac{3\theta_p t}{2}\right) \qquad \text{B.7}$$

$$\cos(2\theta_p t)\sin\left(\frac{\theta_p t}{2}\right) = -\frac{1}{2}\sin\left(\frac{3\theta_p t}{2}\right) + \frac{1}{2}\sin\left(\frac{5\theta_p t}{2}\right) \qquad \text{B.8}$$

$$\cos(2\theta t)\cos\left(\frac{\theta_p t}{2}\right) = \frac{1}{2}\cos\left(\frac{3\theta_p t}{2}\right) + \frac{1}{2}\cos\left(\frac{5\theta_p t}{2}\right) \qquad \text{B.9}$$

Using these formula from B.6 to B.9, one can write the equation B.5 as:

$$[M]\left\{-\frac{\theta_p^2}{4}a_1\sin\left(\frac{\theta_p t}{2}\right) - \frac{\theta_p^2}{4}b_1\cos\left(\frac{\theta_p t}{2}\right)\right\} + [K]\left\{a_1\sin\left(\frac{\theta_p t}{2}\right) + b_1\cos\left(\frac{\theta_p t}{2}\right)\right\} +$$

$$[K^C]\{\{\Omega_0{}^2 a_1\sin\left(\frac{\theta_p t}{2}\right) + \Omega_0{}^2 b_1\cos\left(\frac{\theta_p t}{2}\right)\} + 2\Omega_0{}^2\beta a_1\frac{1}{2}\cos\left(\frac{\theta_p t}{2}\right) - 2\Omega_0{}^2\beta a_1\frac{1}{2}\cos\left(\frac{3\theta_p t}{2}\right) +$$

$$2\Omega_0{}^2\beta b_1\frac{1}{2}\sin\left(\frac{\theta_p t}{2}\right) + 2\Omega_0{}^2\beta b_1\frac{1}{2}\sin\left(\frac{3\theta_p t}{2}\right) + \frac{\Omega_0{}^2\beta^2 a_1\sin\left(\frac{\theta_p t}{2}\right)}{2} + \frac{\Omega_0{}^2\beta^2 b_1\cos\left(\frac{\theta_p t}{2}\right)}{2} +$$

$$\frac{\Omega_0{}^2\beta^2 a_1\sin\left(\frac{3\theta_p t}{2}\right)}{4} - \frac{\Omega_0{}^2\beta^2 a_1\sin\left(\frac{5\theta_p t}{2}\right)}{4} - \frac{\Omega_0{}^2\beta^2 b_1\cos\left(\frac{3\theta_p t}{2}\right)}{4} - \frac{\Omega_0{}^2\beta^2 b_1\cos\left(\frac{5\theta_p t}{2}\right)}{4} = 0 \qquad \text{B.10}$$

Finally comparing the coefficient of $\sin\left(\frac{\theta t}{2}\right)$ and $\cos\left(\frac{\theta t}{2}\right)$ in the governing equation one can get two equations as below:

For $\sin\left(\frac{\theta_p t}{2}\right)$:

$$-\frac{\theta_p^2}{4}[M]\{a_1\} + [K]\{a_1\} + [K^C]\Omega_0{}^2\{a_1\} + [K^C]\Omega_0{}^2\beta\{b_1\} + \frac{\Omega_0{}^2\beta^2}{2}[K^C]\{a_1\} = 0 \qquad \text{B.11}$$

For $\cos\left(\frac{\theta_p t}{2}\right)$:

$$-\frac{\theta_p^2}{4}[M]\{b_1\} + [K]\{b\}_1 + [K^C]\Omega_0{}^2\{b_1\} + [K^C]\Omega_0{}^2\beta\{a_1\} + \frac{\Omega_0{}^2\beta^2}{2}[K^C]\{b_1\} = 0 \qquad \text{B.12}$$

Equations B.11 and B.12 can be written in the matrix form as

146

$$\begin{bmatrix} -\frac{\theta_p{}^2}{4}[M] + [K] + [K^C]\Omega_0{}^2 + \frac{\Omega_0{}^2\beta^2}{2}[K^C] & [K^C]\Omega_0{}^2\beta \\ [K^C]\Omega_0{}^2\beta & -\frac{\theta_p{}^2}{4}[M] + [K] + [K^C]\Omega_0{}^2 + \frac{\Omega_0{}^2\beta^2}{2}[K^C] \end{bmatrix} \begin{bmatrix} \{a_1\} \\ \{b_1\} \end{bmatrix} = \{0\}$$

<div align="right">B.13</div>

For non-trivial solution determinant of the matrix coefficients must be zero.

$$det\begin{bmatrix} -\frac{\theta_p{}^2}{4}[M] + [K] + [K^C]\Omega_0{}^2 + \frac{\Omega_0{}^2\beta^2}{2}[K^C] & [K^C]\Omega_0{}^2\beta \\ [K^C]\Omega_0{}^2\beta & -\frac{\theta_p{}^2}{4}[M] + [K] + [K^C]\Omega_0{}^2 + \frac{\Omega_0{}^2\beta^2}{2}[K^C] \end{bmatrix} = 0$$

<div align="right">B.14</div>

After expanding the determinant and solving for $\theta_p{}^2$, two equations can be found as:

$$\theta_p{}^2 = (4[K^C]\Omega_0{}^2 + 4[K^C]\Omega_0{}^2\beta + 2[K^C]\Omega_0{}^2\beta^2 + 4[K])/[M]$$

<div align="right">B.15</div>

$$\theta_p{}^2 = (4[K^C]\Omega_0{}^2 - 4[K^C]\Omega_0{}^2\beta + 2[K^C]\Omega_0{}^2\beta^2 + 4[K])/[M]$$

<div align="right">B.16</div>

Equations B.15 and B.16 can be solved as eigenvalue problems where each eigenvalue $\theta_p{}^2$ is the square of parametric resonance frequency which gives the boundary between stable and unstable regions in resonance frequency-driving amplitude plane. Equations B.15 and B.16 give upper and lower boundaries of the instability region, respectively.

APPENDIX-C

Example calculation of $[M], [K]$ and $[K^C]$:

Substituting $\emptyset_i(x) = (\frac{x}{L})^{i+1}$ and $\emptyset_j(x) = (\frac{x}{L})^{j+1}$ in $K_{ij}, K^C{}_{ij}$ and M_{ij} given in chapter-2, one can

get,

$$K_{ij} = \int_0^L b(x)D_{11}(x)\left(\frac{\partial^2}{\partial x^2}(\frac{x}{L})^{i+1}\right)\left(\frac{\partial^2}{\partial x^2}(\frac{x}{L})^{j+1}\right)dx = \frac{ij(ij+i+j+1)}{L^4}\int_0^L b(x)D_{11}(x)(\frac{x}{L})^{i+j-2}dx$$

(C.1)

$$K^C{}_{ij} = \int_0^L P(x)(\frac{\partial}{\partial x}(\frac{x}{L})^{i+1})(\frac{\partial}{\partial x}(\frac{x}{L})^{j+1})dx = \frac{(i+1)(j+1)}{L^2}\int_0^L P(x)(\frac{x}{L})^{i+j}dx \qquad \text{(C.2)}$$

$$M_{ij} = \int_0^L \rho_L b(x)(\frac{x}{L})^{i+1}(\frac{x}{L})^{j+1}dx = \int_0^L \rho_L b(x)(\frac{x}{L})^{i+j+2}dx \qquad \text{(C.3)}$$

For $m = 2$ in Rayleigh-Ritz approximate series, U, W and T (given in chapter-2) becomes:

$$U = \frac{1}{2}(q_{i=1}K_{11}q_{j=1} + q_{i=1}K_{12}q_{j=2} + q_{i=2}K_{21}q_{j=1} + q_{i=2}K_{22}q_{j=2}) \qquad \text{(C.4)}$$

$$W = \frac{1}{2}(q_{i=1}K^C{}_{11}q_{j=1} + q_{i=1}K^C{}_{12}q_{j=2} + q_{i=2}K^C{}_{21}q_{j=1} + q_{i=2}K^C{}_{22}q_{j=2}) \qquad \text{(C.5)}$$

$$T = \frac{1}{2}(q_{i=1}M_{11}q_{j=1} + q_{i=1}M_{12}q_{j=2} + q_{i=2}M_{21}q_{j=1} + q_{i=2}M_{22}q_{j=2}) \qquad \text{(C.6)}$$

Now using Lagrange's equation for $m = 2$, one can get:

$$\begin{cases} \frac{d}{dt}\left(\frac{\partial T}{\partial \dot{q}_{i=1}}\right) - \frac{\partial T}{\partial q_{i=1}} + \frac{\partial (U+W)}{\partial q_{i=1}} \\ \frac{d}{dt}\left(\frac{\partial T}{\partial \dot{q}_{i=2}}\right) - \frac{\partial T}{\partial q_{i=2}} + \frac{\partial (U+W)}{\partial q_{i=2}} \end{cases} = \begin{Bmatrix} 0 \\ 0 \end{Bmatrix} \qquad \text{(C.7)}$$

$$\begin{bmatrix} M_{11} & M_{12} \\ M_{21} & M_{22} \end{bmatrix}\begin{bmatrix} \ddot{q}_1 \\ \ddot{q}_2 \end{bmatrix} + \begin{bmatrix} K_{11} & K_{12} \\ K_{21} & K_{22} \end{bmatrix}\begin{bmatrix} q_1 \\ q_2 \end{bmatrix} + \begin{bmatrix} K^C{}_{11} & K^C{}_{12} \\ K^C{}_{21} & K^C{}_{22} \end{bmatrix}\begin{bmatrix} q_1 \\ q_2 \end{bmatrix} = \begin{bmatrix} 0 \\ 0 \end{bmatrix} \qquad \text{(C.8)}$$

Shortly written as:

$$[M]\{\ddot{q}\} + ([K] + [K^C])\{q\} = \{0\} \qquad \text{(C.9)}$$

Using equation C.1 to C.3, for N layers in composite laminate one can write:

$$[M] = \int_0^L \rho_L b(x) \begin{bmatrix} \dfrac{x^4}{L^4} & \dfrac{x^5}{L^5} \\ \dfrac{x^5}{L^5} & \dfrac{x^6}{L^6} \end{bmatrix} dx$$

$$[K] = \int_0^L b(x) D_{11}(x) \begin{bmatrix} \dfrac{4}{L^4} & \dfrac{12x}{L^5} \\ \dfrac{12x}{L^5} & \dfrac{36x^2}{L^6} \end{bmatrix} dx$$

$$[K^C] = \int_0^L P(x) \begin{bmatrix} \dfrac{4x^2}{L^4} & \dfrac{6x^3}{L^5} \\ \dfrac{6x^3}{L^5} & \dfrac{9x^4}{L^6} \end{bmatrix} dx$$

APPENDIX-D

Centrifugal force calculation

Centrifugal force calculation for composite ply and resin pocket (resin plies) in a doubly-tapered laminate are described below:

For composite ply:

From chapter-2 centrifugal force is

$$P(x) = \int_0^{L-x} b(\delta)\, \rho_L(\delta)\Omega^2 (R + x + \delta)d\delta \qquad \text{D.1}$$

$\rho_L(\delta) = \sum_{k=1}^N \rho_k\big(h_k(\delta) - h_{k-1}(\delta)\big)$, where $\big(h_k(\delta) - h_{k-1}(\delta)\big)$ is variable distance between top and bottom faces of a ply within x and L. For composite plies difference between top and bottom face does not vary along the length, which implies

$$h_k(\delta) - h_{k-1}(\delta) = h_k - h_{k-1}$$

Here, h_k and h_{k-1} for composite plies given at Appendix A. Substituting $b(\delta)$ (given in chapter-2) and $(h_k(\delta) - h_{k-1}(\delta))$ in equation D.1, finally one can get:

$$P(x) = \frac{1}{12}\rho_f\Omega^2(Lb_Lx + 3Rb_Lx + 2b_Lx^2 + 4Lb_L - Lb_0x + 6Rb_L - 3Rb_0x + 2b_Lx - 2b_0x^2 +$$

$$2Lb_0 + 6Rb_0 + 4b_0x)h_{ply}(L - x) \qquad \text{D.2}$$

Centrifugal force at any point x for a composite ply in taper laminate can be calculated using equation D.2. For example, if composite ply has following property:

Table D.1: Property of composite ply

Length of ply, L	0.25 m
Individual ply thickness, h_{ply}	0.000125 m
Width of ply, b_0	0.02 m
Width ratio, $r_b = \dfrac{b_L}{b_0}$	0.1 to 1
Rotational Velocity, Ω	200 rad/s
Hub radius, R	0.025 m
Density (ρ_f)	1480 kg/m^3

Then centrifugal force (P) can be plotted in 3D plane with respect to any point x and width-ratio in the ply:
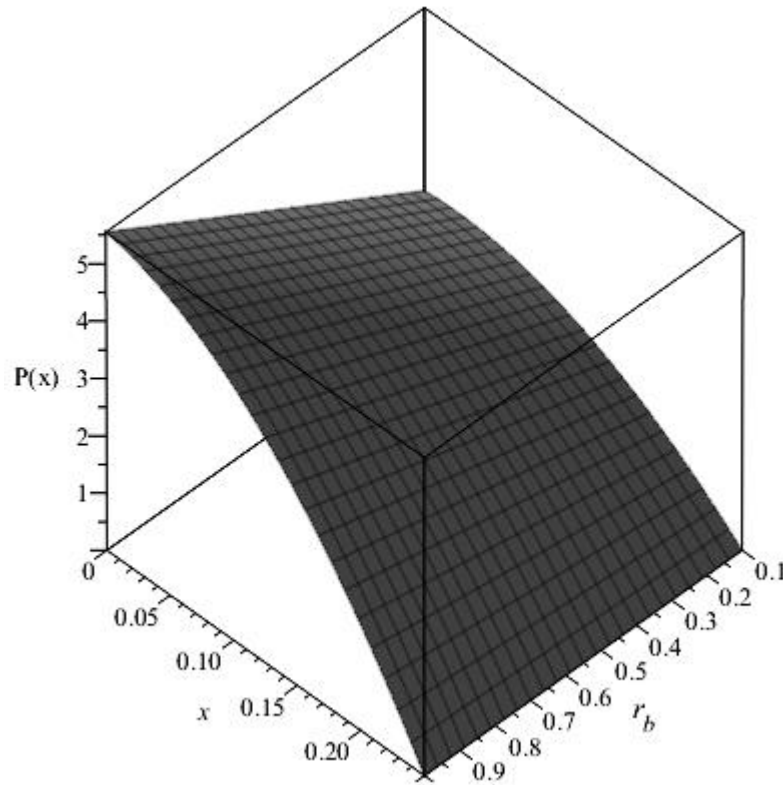
Figure D.1: Centrifugal force at any point x in the composite ply

Maximum centrifugal force $P(x = 0)$ for a uniform width $(r_b = 1)$ ply also can be calculated using exact formula of centrifugal force.

Exact formula of centrifugal force is

$$P = m\Omega^2 r = \rho * b_0 * h_{ply} * L * \Omega^2 * (R + \frac{L}{2}) \qquad \text{D.3}$$

Here,

$m(= \rho * b_0 * h_{ply} * L)$ is mass of the beam.

$r = (R + \frac{L}{2})$ is distance from center of rotation to center of mass.

Using the ply property given in table D.1 one can get, $P = 5.55\ N$. Which comply with figure D.1.

<u>For resin ply (Configuration-A):</u>

In resin ply difference between top and bottom faces vary along the length (See Appendix A).

Therefore

$$h_k(\delta) = -\delta \tan(A) + h_k \tag{D.4}$$

<u>and</u>
$$h_{k-1}(\delta) = -\delta \tan(B) + h_{k-1} \tag{D.5}$$

Here, $A = \dfrac{\emptyset}{S/2} * \left(\dfrac{N}{2} - k\right)$ and $B = \dfrac{\emptyset}{S/2} * \left(\dfrac{N}{2} + 1 - k\right)$

Finally

$$h_k(\delta) - h_{k-1}(\delta) = -(x + \delta)\tan(A) - (x + \delta)\tan(B) + h_{ply} \tag{D.6}$$

Substituting $h_k(\delta) - h_{k-1}(\delta)$ in equation D.1 one can get:

$$
\begin{aligned}
P(x) = \quad & \frac{1}{4} \frac{\rho\,\Omega^2\,b_0\left(L\,r_b - x\,r_b - L + x\right)(L-x)^3\left(\tan(B)-\tan(A)\right)}{L} \\[4pt]
& + \frac{1}{3}\left(\frac{\rho\,\Omega^2\,b_0\left(x\,r_b + L - x\right)\left(\tan(B)-\tan(A)\right)}{L} \right. \\[4pt]
& \left. + \frac{\rho\,\Omega^2\,b_0\left(L\,r_b - x\,r_b - L + x\right)\left(x\tan(B) - x\tan(A) + h_{ply}\right)}{L\,(L-x)} \right. \\[4pt]
& \left. + \frac{\rho\,\Omega^2\,b_0\left(L\,r_b - x\,r_b - L + x\right)\left(\tan(B)-\tan(A)\right)(R+x)}{L\,(L-x)} \right)(L-x \\[4pt]
& + \frac{1}{2}\left(\frac{\rho\,\Omega^2\,b_0\left(x\,r_b + L - x\right)\left(x\tan(B) - x\tan(A) + h_{ply}\right)}{L} \right. \\[4pt]
& + \left(\frac{\rho\,\Omega^2\,b_0\left(x\,r_b + L - x\right)\left(\tan(B)-\tan(A)\right)}{L} \right. \\[4pt]
& \left. \frac{\rho\,\Omega^2\,b_0\left(L\,r_b - x\,r_b - L + x\right)\left(x\tan(B) - x\tan(A) + h_{ply}\right)}{} \right)
\end{aligned}
\tag{D.7}
$$

Centrifugal force at any point x for a resin ply in tapered laminate can be calculated using equation D.7.

Validation of Rayleigh-Ritz solution for isotropic material

To validate the results for isotropic material, following exact solution can be used for non-rotating clamped-free uniform beam [10]:

$$\omega_i = \frac{\mu_i}{2\pi} \sqrt{\frac{EI}{\rho A L^4}} \tag{E.1}$$

where, $\mu_{i=1,2,3} = 3.516, 22.034, 61.701$ for first three natural frequencies, L is the length of the beam, $A(= b_0 h_0)$ is the cross sectional area of the beam, ρ is the mass density of the isotropic material, $I(= \frac{b_0 h_0{}^3}{12})$ is the moment of inertia of the beam cross section and E is the young modulus of isotropic material.

Table E.1 Mechanical properties of Steel and Aluminum [29]

Material ⟶	Steel (AISI 1059)	Aluminum
Elastic modulus (E)	200 GPa	68 GPa
Density (ρ)	7870 kg/m^3	2698 kg/m^3
Poisson's ratio (v)	0.29	0.36

The Rayleigh-Ritz energy formulation for composite material that described in section 2.3 can be used for isotropic material by considering same mechanical properties in all three directions ($e.g.$ $E_1 = E_2 = E_3 = E$ and $v_{12} = v_{21} = v$). In Table E.2, first three out-of-plane bending natural frequencies determined for non-rotating clamped-free uniform isotropic beam using Rayleigh-Ritz (R-R) method, are compared with the exact solution and ANSYS results. The beam is 25 cm long and width is 2 cm. The thickness of the beam is 4.5 mm.

Table E.2 Natural frequencies (Hz) of non-rotating clamped-free uniform isotropic beam

Material	Mode	R-R solution (8 terms)	Exact solution	ANSYS
Steel	1st	61.265	58.632	59.105
	2nd	383.94	367.44	369.91
	3rd	1075.4	1028.9	1034.0
Aluminum	1st	62.587	58.391	59.179
	2nd	398.23	365.92	370.40
	3rd	1098.6	1024.7	1035.5

As expected, results obtained from R-R method for non-rotating uniform isotropic beam is showing very good agreement with the results obtained from ANSYS and exact solution.

In Table E.3, first three out-of-plane bending natural frequencies determined for rotating clamped-free uniform isotropic beam using Rayleigh-Ritz (R-R) method, are compared with ANSYS results. The hub radius is taken as 2.5 cm.

**Table E.3** Natural frequencies (Hz) of rotating clamed-free uniform isotropic beam

Material	Mode	R-R	ANSYS	R-R	ANSYS	R-R	ANSYS
		$\Omega=0$ rad/s		$\Omega=100$ rad/s		$\Omega=200$ rad/s	
Steel	1st	61.265	59.105	63.99	61.941	71.535	69.735
	2nd	383.94	369.91	386.4	372.42	393.51	379.86
	3rd	1075.4	1034.0	1077.8	1036.5	1084.9	1043.9
Aluminum	1st	62.587	59.179	65.260	62.021	72.671	69.830
	2nd	392.23	370.40	394.59	372.91	401.60	380.36
	3rd	1098.6	1035.5	1100.9	1038.0	1107.9	1045.4

In Table E.4, first three out-of-plane bending natural frequencies determined for four different types of rotating clamped-free isotropic beams using Rayleigh-Ritz (R-R) method, are compared with ANSYS results. In this case, the width of the beam at fixed side is ($b_0 =$) 2 cm and the thickness at fixed side is ($h_0 =$) 4.5 mm.

Table E.4 Natural frequencies (Hz) of rotating clamped-free uniform isotropic beam

| Type of beam	Material	Mode	R-R	ANSYS	R-R	ANSYS
			$\Omega=0$ rad/s		$\Omega=200$ rad/s	
Uniform Thickness - Uniform width $(h_L = h_0, b_L = b_0)$	Steel	1st	61.265	59.105	71.535	69.735
		2nd	383.94	369.91	393.51	379.86
		3rd	1075.4	1034.0	1084.9	1043.9
	Aluminum	1st	62.587	59.179	72.671	69.830
		2nd	392.23	370.40	401.60	380.36
		3rd	1098.6	1035.5	1107.9	1045.4
Uniform Thickness - Tapered Width $(h_L = h_0 , b_L = \frac{b_0}{2})$	Steel	1st	75.190	72.474	83.946	81.557
		2nd	409.82	394.60	417.72	402.83
		3rd	1101.5	1058.3	1109.3	1066.4
	Aluminum	1st	76.813	72.531	85.403	81.637
		2nd	418.66	395.02	426.40	403.26
		3rd	1125.3	1059.6	1132.9	1067.7
Tapered Thickness - Uniform Width $(h_L = \frac{h_0}{2}, b_L = b_0)$	Steel	1st	66.626	64.140	76.761	74.653
		2nd	319.16	307.30	329.36	317.91
		3rd	823.55	792.61	833.58	803.04
	Aluminum	1st	68.064	64.126	78.014	74.673
		2nd	326.05	307.41	336.04	318.05
		3rd	841.32	793.23	851.14	803.69
Doubly-Tapered $(h_L = \frac{h_0}{2}, b_L = \frac{b_0}{10})$	Steel	1st	111.45	107.15	118.16	114.14
		2nd	396.89	381.56	403.28	388.23
		3rd	917.02	880.82	923.19	887.26
	Aluminum	1st	113.85	107.07	120.43	114.09
		2nd	405.45	381.45	411.71	388.14
		3rd	936.81	880.77	942.85	887.22

In Figures E.1 to E.3, first three natural frequencies of out-of-plane bending vibration are plotted for five different types of beams with respect to rotational velocity to compare the natural frequencies of the composite beam and isotropic beam. From Figures E.1 to E.3, it can be stated that, fiber orientation in the plies and double-tapering in the composite beam provide better design options compared to the beam made with isotropic material. Also, from Figures E.1 to E.2, one can see that natural frequencies of isotropic and composite beams increase with rotational velocity, which implies that rotational velocity (centrifugal force) increases the total stiffness of the composite and isotropic beams in case of out-of-plane bending vibration.
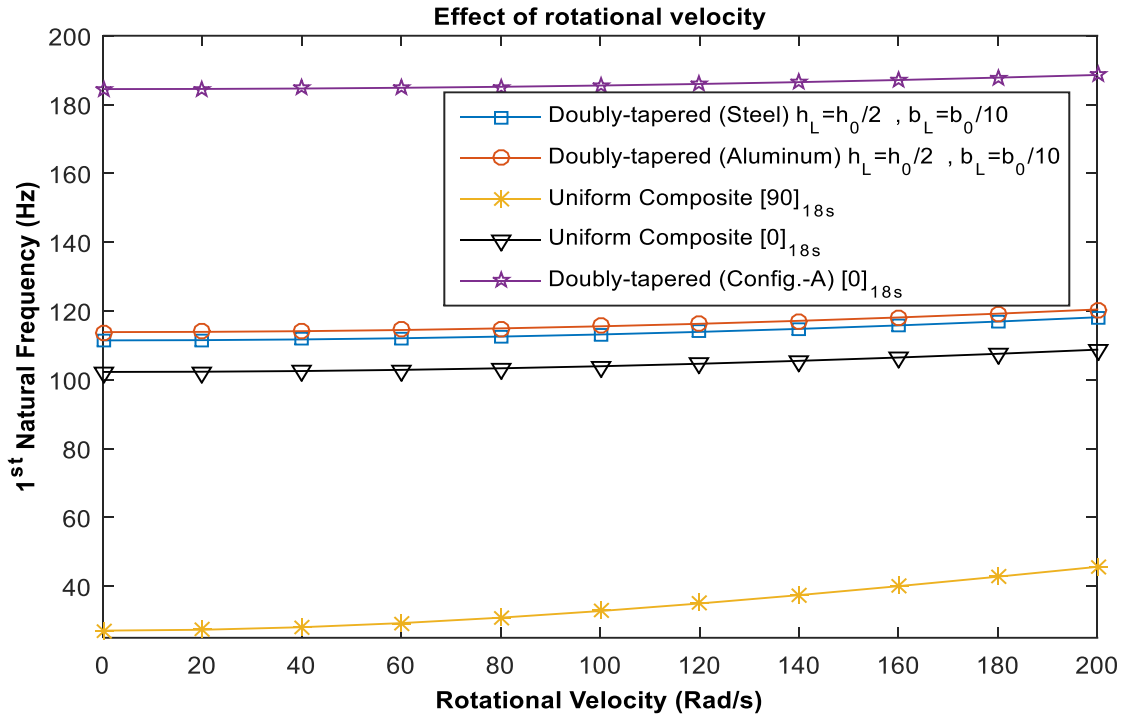
Figure E.1 Variation of first natural frequency of out-of-plane bending vibration for different types of rotating beams
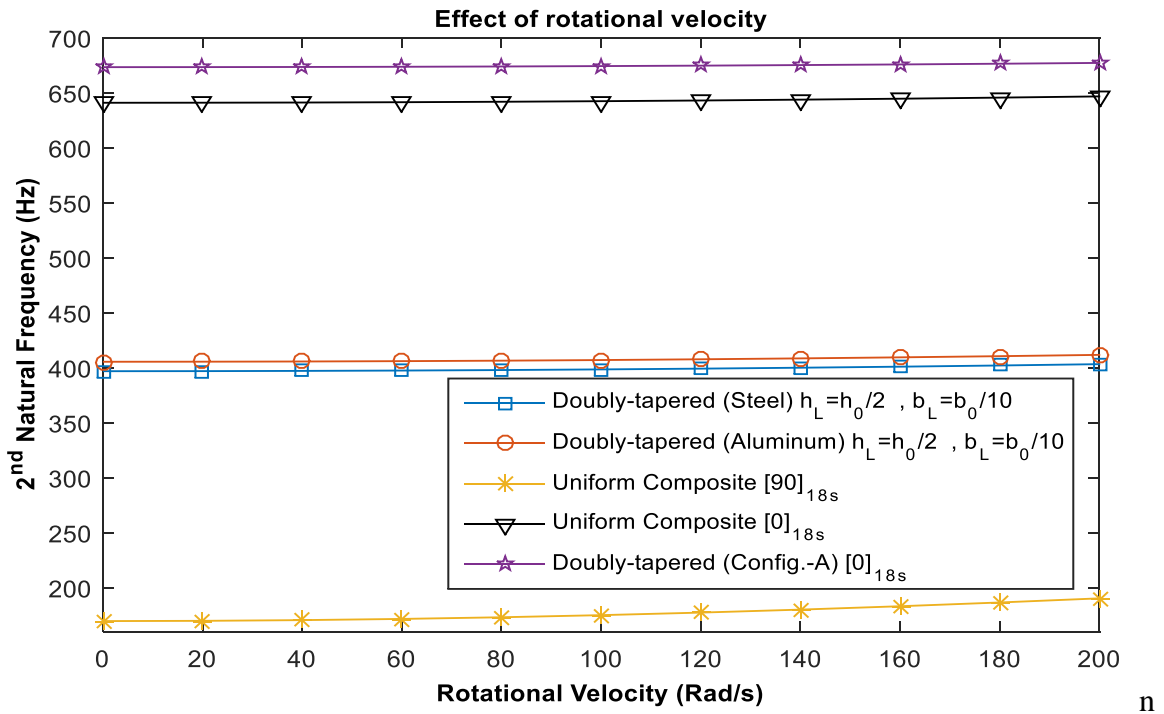

Figure E.2 Variation of second natural frequency of out-of-plane bending vibration for different types of rotating beams
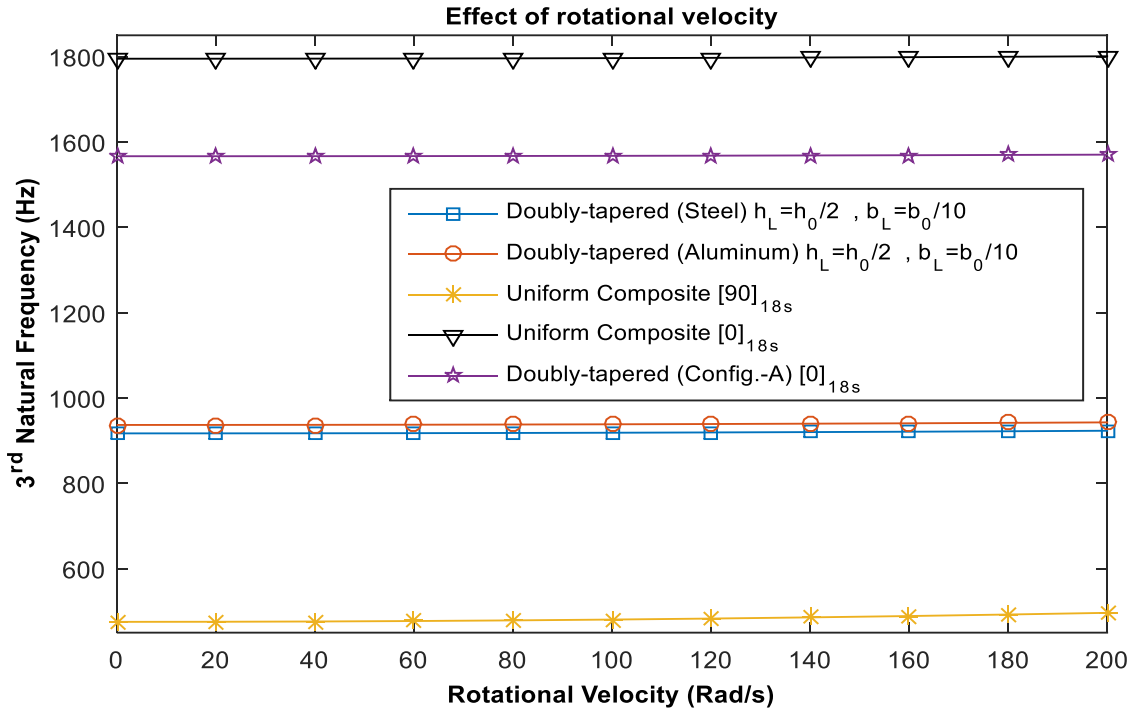
Figure E.3 Variation of third natural frequency of out-of-plane bending vibration for different types of rotating beams

In Figures E.4 to E.6, first three instability regions of out-of-plane bending vibration due to periodic rotational velocity, are plotted for three different types of doubly-tapered beams to compare the widths of instability regions for composite beam and isotropic beam. The mean value of rotational velocity is taken as 50 rad/s. From Figures E.4 to E.6, it can be stated that, doubly-tapered composite beam has less width of instability region compared to the doubly-tapered isotropic beam.
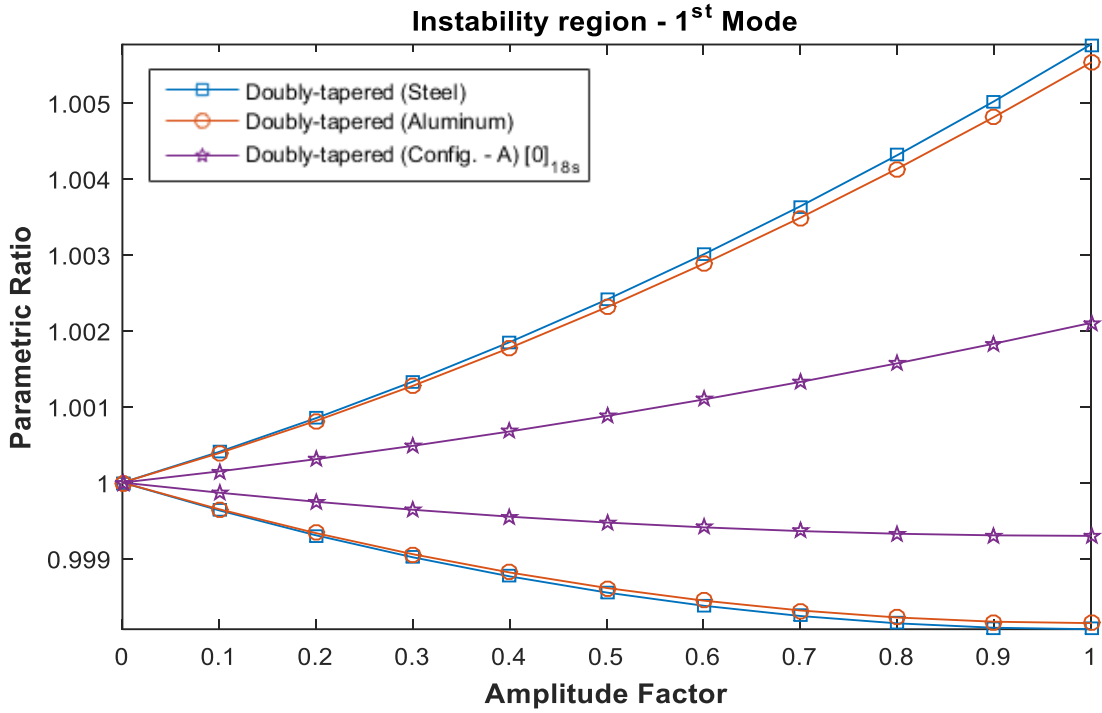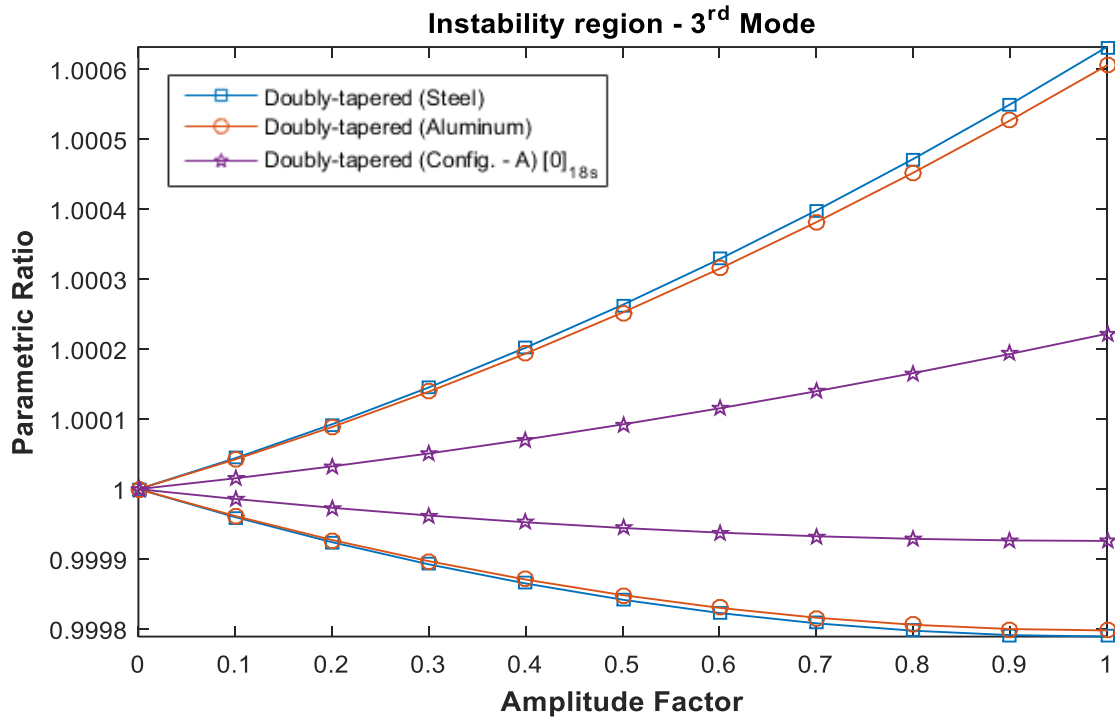
Figure E.4 First instability regions of out-of-plane bending vibration for different types of doubly-tapered beams
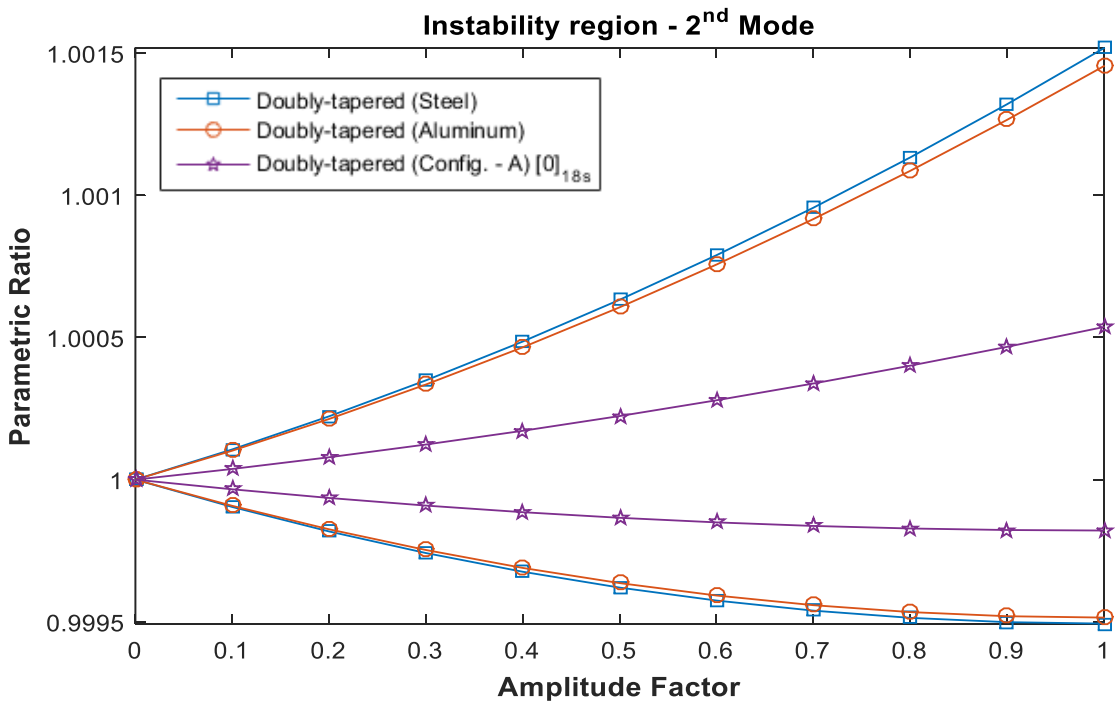
Figure E.5 Second instability regions of out-of-plane bending vibration for different types of doubly-tapered beams

Figure E.6 Third instability regions of out-of-plane bending vibration for different types of doubly-tapered beams